

School of Electrical Engineering, Computing and  
Mathematical Sciences

Curtin Institute of Radio Astronomy  
&  
International Centre for Radio Astronomy Research

An SKA precursor view of X-ray binary jets

Jaiverdhan Chauhan

This thesis is presented for the Degree of  
Doctor of Philosophy  
of  
Curtin University of Technology

June 2021



To the best of my knowledge and belief this thesis contains no material previously published by any other person except where due acknowledgement has been made. This thesis contains no material which has been accepted for the award of any other degree or diploma in any university.

A red rectangular box, likely a placeholder for a signature or stamp.

Jaiverdhan Chauhan



*“Dream is not that which you see while sleeping it is something that does not let you sleep.”*

— Dr. A. P. J. Abdul Kalam



# Acknowledgement to Country

I acknowledge that Curtin University works across hundreds of traditional lands and custodial groups in Australia, and with First Nations people around the globe. I wish to pay my deepest respects to their ancestors and members of their communities, past, present, and to their emerging leaders. My passion and commitment to work with all Australians and peoples from across the world, including the First Nations peoples are at the core of the work I do, reflective of my institutions' values and commitment to my role as leaders in the Reconciliation space in Australia.



# Acknowledgements

This PhD research journey of three years and around four months has been both incredible and challenging, which could not be possible without the help and support of many people.

First and foremost, I gladly express my wholehearted gratitude to my supervisor ***Prof. James Miller-Jones***. It's a matter of pride and honour for me to be your student. I will always be grateful to you for your invaluable guidance, immense knowledge and continuous encouragement throughout my research. As I have an X-ray astronomy background, it was initially challenging to adapt myself to the world of radio interferometers. It's all possible because of your endless efforts that I gradually picked up the necessary skills and knowledge required for this project. I really cannot express my sincere gratitude for everything you have done to me throughout my PhD in this single paragraph.

I also want to thank my co-supervisor, ***Dr. Gemma E. Anderson***, whose continuous inspiration and positive attitude has kept me confident and made my work realistic. I will always be thankful to you for introducing me to a great telescope, the Murchison Widefield Array. Your style of motivation and teaching is phenomenal, which always inspired me to learn more and more. You always checked that my project was going on the right track. I wholeheartedly appreciate your immeasurable support and help which you offered throughout my PhD.

My special thank goes to ***Dr. Arash Bahramian***, who always encouraged me during tough times and provided relief from seriousness. Although you were not a part of my supervisory panel, you cared about me as your very own student.

I have learned a lot from you, especially in Astrostatistics. No words can help me in expressing my gratitude for all the kind support I received from him throughout this thesis.

I also want to thank many people at CIRA Dr. Jess Broderick, Dr. Paul Hancock, Dr. Marcin Sokolowski and Dr. Natasha Hurley-Walker for scientific discussions and for tolerating my dumb questions. All of your support was invaluable in the progress of this project. My sincere thanks also goes to my CIRA internal review panel, Prof. Melanie Johnston-Hollitt, Dr. Adrian Sutinjo and Dr. Clancy James, their constructive suggestions helped me in evolving my project. I thank Asso. Prof. Cath Trott for taking the effort and encouraging me by appreciating me after my talks. I also thank Dr. Ramesh Bhat for healthy discussions. A huge thanks to the CIRA administration team, Tina Salisbury, Angela Dunleavy, Emily Johnson, Chamila Thrum and Ali Smith for their continuous support during my PhD project.

Thank you to my friends and colleagues at CIRA, Steve Raj Prabhu, Torrance Hodgson, Mike Kriele, Stefan Duchesne and Jun Tian, for your sincere encouragement, happy social times and healthy discussions. Your continuous support gave me strength and made me believe that I was not alone.

I also want to thank my outside CIRA colleagues and friends, Dr. Thomas D. Russell, Dr. Wasim Raja, Dr. James R. Allison, Dr. Chris Flynn and Prof. Roberto Soria. They helped me learning something new every time I talked to them and always listen to all my questions, sometimes they were silly.

This PhD journey had never been possible without the initial support and encouragement of Prof. H.M. Antia and Dr. Varsha Chitnis. Thank you for believing in me. Your help was invaluable to me.

I would not have made it so far in life without the support of my childhood friend Abhinav, who always believed in me and always encouraged me to achieve something extraordinary in life. During my PhD journey, when I was feeling low you were always with me to motivate me.

To my mother and father, thank you for always loving and caring. My father always encouraged me to follow my dreams. I would also like to thank Pari, who was always there to listen to my everyday stories of joy, disturbances and frustrations. She always encouraged me and made me believe that I will make it possible.



# Statement of Contribution by Others

Chapter 3 of this thesis, “An ASKAP distance constraint to MAXI J1535–571”, is a reproduction of an already published work by Chauhan et al. 2019 (‘An HI absorption distance to the black hole candidate X-ray binary MAXI J1535–571’, Monthly Notices of the Royal Astronomical Society, Letters, Volume 488, Issue 1, page L129–L133, DOI: <https://doi.org/10.1093/mnrasl/slz113>). This is my own work, except the following. W. Raja helped in finalising the inputs for the ASKAP data processing. A. Bahramian did the Line-of-sight hydrogen column density ( $n_{\text{H}}$ ) calculations. J. R. Allison helped in making the strategy for calculating the rms noise. Discussions on the data reduction and implications of the results were contributed by my supervisory panel – J. C. A. Miller-Jones and G. E. Anderson. Discussions were also contributed to by W. Raja, A. Bahramian, A. Hotan, B. Indermuehle, M. Whiting, J. R. Allison, C. Anderson, J. Bunton, B. Koribalski and E. Mahony. I wrote the draft of the manuscript and distributed copies to all co-authors for proofreading. All co-authors provided input during several iterations of feedback until the manuscript was finalised.

The content of Chapter 4 of this thesis, “Measuring a kinematic distance to MAXI J1348–630 using the SKA precursors ASKAP and MeerKAT”, has been adapted from an already published work by Chauhan et al. 2021 (‘Measuring the distance to the black hole candidate X-ray binary MAXI J1348–630 using HI absorption’, Monthly Notices of the Royal Astronomical Society,

Letters, Volume 501, Issue 1, page L60–L64, DOI: <https://doi.org/10.1093/mnrasl/slaa195>). This is my own work, except the following. W. Raja performed some initial testing and also helped in finalising the inputs for the final ASKAP data processing. The MeerKAT data was reduced by J. R. Allison and P. F. L. Jacob. F. Carotenuto provided the MeerKAT continuum flux densities. Discussions on the data reduction and implications of the results were contributed by my supervisory panel – J. C. A. Miller-Jones and G. E. Anderson. Discussions were also contributed to by W. Raja, J. R. Allison, P. F. L. Jacob, F. Carotenuto, S. Corbel, R. Fender, A. Hotan, M. Whiting, P. A. Woudt, B. Koribalski and E. Mahony. I wrote the draft of the manuscript and distributed copies to all co-authors for proofreading. All co-authors provided input during several iterations of feedback until the manuscript was finalised.

Chapter 5 of this thesis, “Using SKA precursors to study the transient jets in MAXI J1535–571”, is a reproduction of the already published manuscript by Chauhan et al. (‘A broadband radio view of transient jet ejecta in the black hole candidate X-ray binary MAXI J1535–571’, Publications of the Astronomical Society of Australia, Volume 38, eid e045, page e045, DOI: <https://doi.org/10.1017/pasa.2021.38>). This is my own work, except the following. Initial calibration of the MWA data was done by A. Paduano and M. Sokolowski. The LBA data was reduced by J. C. A. Miller-Jones. The UTMOST data was reduced by C. Flynn and V. Gupta. The ATCA data was reduced by T. D. Russell. The Bayesian code to fit the spectra was developed with the help of A. Bahramian. S. W. Duchesne helped in flux-calibration of the MWA data. R. Soria helped with the H II region analysis for the free-free absorption towards MAXI J1535–571. Discussions on the implications of the results were contributed by my supervisory panel – J. C. A. Miller-Jones and G. E. Anderson. Discussions were also contributed to by A. Paduano, M. Sokolowski, C. Flynn, P. J. Hancock, N. Hurley-Walker, D. L. Kaplan, T. D. Russell, A. Bahramian, S. W. Duchesne, D. Altamirano, S. Croft, H. A. Krimm, G. R. Sivakoff, R. Soria, C. M. Trott,

R. B. Wayth, V. Gupta, M. Johnston-Hollitt, S. J. Tingay. I wrote the draft of the manuscript and distributed copies to all co-authors for proofreading. All co-authors provided input during several iterations of feedback until the manuscript was finalised.

The content of Chapter 6 of this thesis, “Low-frequency MWA detections of compact jets in two black hole XRBs”, is as yet unpublished. It is my own work, excepting the following. High-frequency data for MAXI J1820+070 was provided by A. J. Tetarenko. The MeerKAT and ATCA data were reduced by F. Carotenuto. Discussions were contributed to by my supervisory panel – J. C. A. Miller-Jones and G. E. Anderson.



**(Signature of candidate)**



**(Signature of supervisor)**



# Abstract

This PhD thesis uses the Square Kilometre Array (SKA) precursor telescopes, including the Murchison Widefield Array (MWA), the Australian Square Kilometre Array Pathfinder (ASKAP) and MeerKAT, to study the jets of black hole low-mass X-ray binaries, through both continuum monitoring and neutral hydrogen absorption measurements. BH-XRB jets have been well studied at GHz radio frequencies over the past two decades, but their low-frequency properties have been poorly explored, especially at frequencies  $< 300$  MHz. Similarly, while the early 2000s saw a number of H I absorption studies of BH-XRBs, this technique has not since seen widespread adoption for distance determinations. In this PhD research, we monitored outbursting BH-XRBs and constrained their kinematic distances. We studied radio jets from BH-XRBs in the frequency band 80–2000 MHz with the SKA precursor telescopes MWA, ASKAP and MeerKAT, complemented by other facilities at high frequencies ( $> 2$  GHz).

The study of the H I absorption complex in the direction of BH-XRBs provides us with an opportunity to determine the kinematic distance to the source. In this PhD thesis, we used the SKA precursor telescope ASKAP to detect significant ( $> 3\sigma$ ) H I absorption complexes towards two BH-XRBs; MAXI J1535–571 and MAXI J1348–630. Using the H I absorption spectra, we determined the kinematic distances to both the sources, which were previously unknown. In the case of MAXI J1348–630, we also used MeerKAT to measure the H I absorption spectrum in the direction of the source, which was found to be consistent with the ASKAP spectrum and indicates the robustness of our distance estimates. The

wide field-of-view of the SKA precursor telescopes ASKAP and MeerKAT covered a number of comparison extragalactic sources in the same observation. The HI absorption spectra towards the comparison extragalactic sources help us in breaking the degeneracy between the near and the far kinematic distances. We used our distance measurements to calculate other key parameters of the two BH-XRBs, including the peak X-ray luminosity, the soft-to-hard X-ray spectral state transition luminosity, and the mass of the BH.

In the case of transient jets, observations below 2 GHz help constrain the evolving spectral shape and locate the low-frequency spectral turnover. In this thesis, we detected for the first time with the MWA a transient jet from a BH-XRB, MAXI J1535–571. The source was simultaneously monitored with a suite of Australian radio telescopes, and our MWA detections constrained the broadband spectrum in the low-frequency regime. We detected a low-frequency turnover, which we ascribe to synchrotron self-absorption (SSA). We fit the broadband radio spectrum with an SSA model and used size constraints from the Australian Long Baseline Array (LBA) to determine various physical quantities of the transient jet knot in MAXI J1535–571, including the jet opening angle, the magnetic field strength and the minimum energy.

We also used the MWA to observe the compact jets in two BH-XRBs in their hard X-ray spectral states. We detected the compact jets at 154 MHz in both MAXI J1820+070 and MAXI J1348–630. These are the first detections of BH-XRB compact jets at low radio frequencies ( $< 300$  MHz). We generated broadband spectra for both the sources and have not observed any signs of a low-frequency turnover, in contrast to what had been predicted by the theoretical internal shock model for compact jets. This suggests that the compact jets continue to dissipate energy further downstream from the black hole than had previously been believed.

Finally, this thesis has highlighted the value of broadband radio monitoring of X-ray binary jets, showing how SKA precursors can be used to study the jets,

testing observing strategies and demonstrating the science that can be done at low radio frequencies. It thereby paves the way for future studies with the more sensitive SKA.



# Contents

|  |             |
|--|-------------|
| <b>Acknowledgements</b>  | <b>ix</b>   |
| <b>Abstract</b>  | <b>xvii</b> |
| <b>1 Introduction</b>  | <b>1</b>    |
| 1.1 Introduction to radio transients . . . . .                                 | 1           |
| 1.2 Introduction to X-ray binaries . . . . .                                   | 3           |
| 1.2.1 Introduction to black hole low-mass X-ray binaries . . . . .             | 5           |
| 1.2.2 Quiescence . . . . .   | 8           |
| 1.2.3 Outburst . . . . .   | 10          |
| 1.2.3.1 X-ray spectral states . . . . .  | 12          |
| 1.3 All Sky X-ray monitors . . . . .   | 13          |
| 1.4 Jets . . . . .   | 14          |
| 1.4.1 Jet launching and collimation . . . . .                                  | 15          |
| 1.5 Observations of radio jets in black hole X-ray binaries . . . . .          | 18          |
| 1.5.1 Compact jets . . . . .   | 19          |
| 1.5.2 Transient jets . . . . .   | 23          |
| 1.6 HI absorption in X-ray binaries . . . . .                                  | 26          |
| 1.6.1 Kinematic distance to X-ray binaries . . . . .                           | 28          |
| 1.7 Background studies of low-frequency radio jets in X-ray binaries . . . . . | 33          |

|          |  |           |
|----------|--|-----------|
| 1.8      | The SKA precursor telescopes . . . . .                                 | 35        |
| 1.8.1    | The Murchison Widefield Array . . . . .                                | 35        |
| 1.8.2    | The Australian Square Kilometre Array Pathfinder . . . . .             | 36        |
| 1.8.3    | MeerKAT . . . . .  | 37        |
| 1.9      | Monitoring the BH-XRB jets with modern radio interferometers . . . . . | 37        |
| 1.10     | Structure of this thesis . . . . .                                     | 39        |
| <b>2</b> | <b>Research methodology</b>  | <b>41</b> |
| 2.1      | Radio Interferometry basics . . . . .                                  | 42        |
| 2.1.1    | The measurement equation . . . . .                                     | 45        |
| 2.1.1.1  | W-Projection . . . . .   | 48        |
| 2.1.1.2  | W-Stacking . . . . .   | 49        |
| 2.1.2    | $uv$ -coverage . . . . .   | 51        |
| 2.1.3    | Flagging and Calibration . . . . .                                     | 53        |
| 2.1.3.1  | Flagging . . . . .   | 53        |
| 2.1.3.2  | Calibration . . . . .  | 54        |
| 2.2      | Interferometric techniques . . . . .                                   | 55        |
| 2.2.1    | Flagging methods . . . . .   | 55        |
| 2.2.2    | Calibration techniques . . . . .                                       | 56        |
| 2.2.3    | Weighting . . . . .  | 58        |
| 2.2.3.1  | Natural weighting . . . . .  | 58        |
| 2.2.3.2  | Uniform weighting . . . . .  | 59        |
| 2.2.3.3  | Robust weighting . . . . .   | 59        |
| 2.2.4    | Imaging and gridding . . . . .   | 60        |
| 2.2.5    | Deconvolution . . . . .  | 60        |
| 2.2.5.1  | The CLEAN algorithm . . . . .  | 61        |

|          |  |           |
|----------|--|-----------|
| 2.2.6    | Self-calibration . . . . .   | 62        |
| 2.3      | MWA data processing . . . . .  | 64        |
| 2.3.1    | Flux calibration . . . . .   | 66        |
| 2.3.2    | Stacking . . . . .   | 67        |
| 2.4      | ASKAP data processing . . . . .  | 68        |
| 2.5      | Observing strategies for black hole X-ray binaries at radio frequencies                                | 71        |
| <b>3</b> | <b>An ASKAP distance constraint to MAXI J1535–571</b>  | <b>73</b> |
| 3.1      | MAXI J1535–571 . . . . .   | 74        |
| 3.2      | Observations and Data reduction . . . . .  | 76        |
| 3.3      | Results . . . . .  | 77        |
| 3.3.1    | H I absorption spectra . . . . .   | 78        |
| 3.4      | Discussion . . . . .   | 82        |
| 3.4.1    | Spectral state transition luminosity . . . . .   | 84        |
| 3.4.2    | Peak X-ray luminosity . . . . .  | 84        |
| 3.4.3    | Line-of-sight hydrogen column density . . . . .  | 85        |
| 3.4.4    | Radio/X-ray correlation and the source distance . . . . .  | 86        |
| 3.4.5    | Natal kick and the source distance . . . . .   | 86        |
| 3.5      | Summary . . . . .  | 88        |
| <b>4</b> | <b>Measuring a kinematic distance to MAXI J1348–630 using the<br/>SKA precursors ASKAP and MeerKAT</b> | <b>89</b> |
| 4.1      | MAXI J1348–630 . . . . .   | 90        |
| 4.2      | Observations and Data reduction . . . . .  | 91        |
| 4.2.1    | ASKAP . . . . .  | 91        |
| 4.2.2    | MeerKAT . . . . .  | 92        |
| 4.3      | Results . . . . .  | 94        |

|          |  |            |
|----------|--|------------|
| 4.3.1    | H I absorption spectra . . . . .                                       | 96         |
| 4.3.1.1  | Comparison with the MeerKAT spectrum . . . . .                         | 97         |
| 4.4      | Discussion . . . . .   | 100        |
| 4.4.1    | Comparison with other distance constraints . . . . .                   | 100        |
| 4.4.2    | Distance constraint and its implications . . . . .                     | 102        |
| 4.4.3    | Future X-ray binary monitoring . . . . .                               | 102        |
| 4.5      | Conclusions . . . . .  | 104        |
| <b>5</b> | <b>Using SKA precursors to study the transient jets in MAXI J1535–</b> |            |
|          | <b>571</b>   | <b>107</b> |
| 5.1      | MAXI J1535–571 . . . . .   | 108        |
| 5.2      | Observations and Data reduction . . . . .                              | 109        |
| 5.2.1    | MWA . . . . .  | 109        |
| 5.2.2    | UTMOST . . . . .   | 110        |
| 5.2.3    | LBA . . . . .  | 112        |
| 5.2.4    | ASKAP . . . . .  | 112        |
| 5.2.5    | ATCA . . . . .   | 113        |
| 5.3      | Results . . . . .  | 118        |
| 5.3.1    | Outburst evolution . . . . .   | 118        |
| 5.3.2    | Low-frequency radio detections of MAXI J1535–571 . . . . .             | 120        |
| 5.3.3    | Source size . . . . .  | 122        |
| 5.3.4    | Multi-frequency radio light curve . . . . .                            | 123        |
| 5.3.5    | Radio spectrum . . . . .   | 124        |
| 5.4      | Radio spectral analysis . . . . .                                      | 126        |
| 5.4.1    | The Tsytovitch-Razin Effect . . . . .                                  | 128        |
| 5.4.2    | Free-Free Absorption . . . . .   | 128        |

|          |  |            |
|----------|--|------------|
| 5.4.3    | Synchrotron Self-Absorption . . . . .                                      | 131        |
| 5.5      | Discussion . . . . .   | 133        |
| 5.5.1    | Magnetic field strength . . . . .  | 134        |
| 5.5.2    | Jet opening angle . . . . .  | 136        |
| 5.5.2.1  | Lorentz factor . . . . .   | 137        |
| 5.5.3    | Future studies with the SKA-Low . . . . .                                  | 139        |
| 5.6      | Conclusions . . . . .  | 139        |
| <b>6</b> | <b>Low-frequency MWA detections of compact jets in two black hole XRBs</b> | <b>143</b> |
| 6.1      | Introduction . . . . .   | 144        |
| 6.1.1    | MAXI J1820+070 . . . . .   | 144        |
| 6.1.2    | MAXI J1348–630 . . . . .   | 146        |
| 6.2      | Observations and Data reduction . . . . .                                  | 147        |
| 6.2.1    | MAXI J1820+070 . . . . .   | 147        |
| 6.2.1.1  | MWA . . . . .  | 147        |
| 6.2.1.2  | VLITE . . . . .  | 149        |
| 6.2.1.3  | High-frequency (> 5 GHz) observations . . . . .                            | 149        |
| 6.2.2    | MAXI J1348–630 . . . . .   | 155        |
| 6.2.2.1  | MWA . . . . .  | 155        |
| 6.2.2.2  | MeerKAT . . . . .  | 155        |
| 6.2.2.3  | ATCA . . . . .   | 156        |
| 6.3      | Results . . . . .  | 158        |
| 6.3.1    | MAXI J1820+070 . . . . .   | 159        |
| 6.3.1.1  | Low-frequency radio detections of MAXI J1820+070159                        |            |
| 6.3.1.2  | Radio and X-ray light curve . . . . .                                      | 159        |

|          |   |            |
|----------|---|------------|
| 6.3.1.3  | Broadband spectrum . . . . .                                | 162        |
| 6.3.2    | MAXI J1348–630 . . . . .                                    | 164        |
| 6.3.2.1  | Low-frequency radio detections of MAXI J1348–630            | 164        |
| 6.3.2.2  | Multi-frequency radio light curve . . . . .                 | 165        |
| 6.3.2.3  | Radio spectrum . . . . .                                    | 169        |
| 6.4      | Discussion . . . . .  | 169        |
| 6.4.1    | MAXI J1820+070 . . . . .                                    | 171        |
| 6.4.2    | MAXI J1348–630 . . . . .                                    | 173        |
| 6.4.3    | Compact jet spectrum . . . . .                              | 174        |
| 6.5      | Conclusions . . . . .                                       | 176        |
| <b>7</b> | <b>Discussion, Conclusions and Future work</b>              | <b>177</b> |
| 7.1      | Discussion . . . . .  | 177        |
| 7.1.1    | HI absorption distances to black hole XRBs . . . . .        | 177        |
| 7.1.2    | Low-frequency studies of transient jets . . . . .           | 182        |
| 7.1.3    | Detection of the compact jets at low-frequency . . . . .    | 186        |
| 7.1.4    | Strategies for SKA . . . . .                                | 188        |
| 7.2      | Conclusions . . . . .                                       | 190        |
| 7.2.1    | Kinematic distances to black hole XRBs . . . . .            | 190        |
| 7.2.2    | Physical properties of the transient jets in MAXI J1535–571 | 192        |
| 7.2.3    | Low-frequency study of compact jets in black hole XRBs .    | 193        |
| 7.3      | Future work . . . . .                                       | 193        |
| 7.3.1    | Small scale structures in neutral hydrogen . . . . .        | 193        |
| 7.3.2    | High cadence monitoring of transient jets . . . . .         | 194        |
| 7.3.3    | Fitting the compact jet spectrum with physical models . .   | 194        |
| 7.3.4    | Monitoring with the SKA . . . . .                           | 195        |

|  |            |
|--|------------|
| 7.4 Contribution of this thesis . . . . .              | 196        |
| <b>Appendices</b>                                      | <b>199</b> |
| <b>A Synchrotron radiation</b>                         | <b>201</b> |
| <b>B COTTER</b>  | <b>207</b> |
| <b>C Publications</b>                                  | <b>209</b> |
| C.1 Publications included in this thesis . . . . .     | 209        |
| C.2 Publications not included in this thesis . . . . . | 210        |
| <b>D Acknowledgement of facilities and funding</b>     | <b>213</b> |
| <b>E Statement of contribution by Co-authors</b>       | <b>215</b> |
| <b>Bibliography</b>                                    | <b>253</b> |



# List of Figures

|     |  |   |
|-----|--|---|
| 1.1 | An artist's view of a low-mass black hole X-ray binary. The key components of these systems are indicated on the image. The emission from these different components dominate in different parts of the spectrum (jets in radio, inner accretion disc in X-rays, and outer accretion disc in optical and UV), and their different temperatures are denoted with different colours. The radio jets and the donor star are shown in light blue color. The accretion disc is illustrated through the use of different colours from red (cool - optical/UV) through to white (hot - X-rays). Image credit: NASA / CXC / M.Weiss. . . . . | 6 |
|-----|--|---|

1.2 Top left panel: An X-ray light curve of the BH-LMXB GX 339–4 over its full 2002/2003 outburst observed by the RXTE satellite (Belloni et al., 2005). Bottom left panel: The hardness ratio for the same light curve (Belloni et al., 2005). The dotted vertical lines highlight the main X-ray spectral state transitions. The dashed horizontal line indicates the hardness ratio where the source evolves between the various intermediate states through the high/soft state in the hardness intensity diagram (HID; right panel). The letters (A, B, C, D) in red represent different stages of the outburst as described in the text. Right panel: The hardness intensity diagram (HID) corresponding to the left panel figures (Belloni et al., 2005). The transitions between the X-ray spectral states (labelled in the grey boxes) are indicated by the grey lines (Belloni, 2010). The inset in the bottom left corner represents the ideal ‘q-shaped’ evolution of the source outburst in the HID diagram. This figure is adapted from Belloni et al. (2005). . . . . 11

1.3 A schematic diagram showing the type of radio jet associated with different X-ray states during a BH-LMXB outburst. The radio jets are overlaid on the HID of GX 339–4 for the 2002/2003 outburst, which is also shown in the right panel of Figure 1.2. The various colours in the outer images demonstrate the corresponding contributions of the jet (green), the corona (black), and the accretion disc (red) during (a) quiescence, (b) the hard state, (c) the intermediate state when an internal shock is produced in the jet due to the launching of discrete ejecta, and (d) the soft state when the jets are quenched (Fender et al., 2004). This figure is adapted from Fender et al. (2004), Belloni et al. (2005), Belloni (2010) and Romero et al. (2017). . . . . 19

1.4 Left panel: An image of the compact jet in Cygnus X-1 at 8.4 GHz generated using data from Very Long Baseline Array (VLBA) and phased VLA (Stirling et al., 2001). The compact jet extends up to  $\sim 20$  AU. The beamsize is presented in the bottom left corner. The source has a peak flux density of  $9.0 \text{ mJy beam}^{-1}$ , whereas the lowest contour is at  $0.1 \text{ mJy}$ . The image is taken from Stirling et al. (2001). Right panel: A typical broad band spectrum for the compact jet resulting from the superposition of many overlapping self-absorbed synchrotron spectra (dashed line).  $a$  is the spectral index of the electron energy distribution.  $\nu_b$  is the transition/break frequency from optically-thick to optically-thin synchrotron regions.  $\nu_c$  represents the synchrotron cooling break. . . . . 20

1.5 Left panel: VLA Image of GRS 1915+105 at 8.4 GHz showing the evolution of discrete ejecta from 27 March to 30 April 1994, which are moving away from the core at apparently superluminal velocities. The beamsize is shown in the top right corner, and the contours are  $1, 2^n$  (where  $n$  ranges from 1 to 10) times  $0.2 \text{ mJy beam}^{-1}$  for all the observations presented in the figure, except for the 27 March epoch, where the contour flux density levels are multiples of  $0.6 \text{ mJy beam}^{-1}$  (Figure from Mirabel & Rodríguez 1994). Right panel: A typical broad band spectrum for the transient jet showing a low-frequency turnover and synchrotron cooling break. The low-frequency turnover is likely to be due to synchrotron self-absorption. The figure is adapted from Rybicki & Lightman (1979) and Longair (2011). . . . . 25

- 1.6 A plot showing a schematic of a sources motion in our Milky Way Galaxy, according to its location along the line of sight. The diagram also shows the parameters used in the derivation of the kinematic distance to the source, described in Section 1.6.1. The Sun is located at a distance  $R_0 = 8.34 \pm 0.16$  kpc from the Galactic centre (Reid et al., 2014). The source of interest is shown as a red star, and the near and far distances are indicated with  $A$  and  $C$ , respectively. Point  $B$  marks the position of the tangent point, and  $d$  is the distance between the source and the Sun. The distance between the source and the Galactic centre is  $R$ , which is the same for both the near and far kinematic distances. Additionally, the radial velocity is also the same for both the near and far distances. 27
- 1.7 A plot showing the predicted variation of the radial velocity (for circular rotation) of the local standard of rest ( $V_{LSR}$ ) with the line of sight distance from the Sun ( $d$ ), in the direction of a Galactic source with the Galactic coordinates  $l = 309.26407$  deg,  $b = -1.10297$  deg. The horizontal line at  $-30 \text{ km s}^{-1}$  highlights the assumed radial velocity of the source. The near, far and the tangent point distances (dashed vertical line) are indicated in the figure. The blue color around the main curve illustrates the uncertainties on  $V_0$  and  $R_0$ . Beyond  $d = 10.5$  kpc, where  $R > R_0$ ,  $V_{LSR}$  becomes positive. . . . . 32
- 2.1 Diagrammatic representation of the geometry associated with radio astronomy. With reference to the interferometer, the astrophysical source is located at  $R$ . If we are looking at a source outside the solar system,  $R$  is many orders of magnitude greater than the distance between two antenna elements (baseline). This figure is adapted from ESA/C. Carreau/ATG medialab and web.haystack.edu. 44

|     |   |    |
|-----|---|----|
| 2.2 | Coordinate system of the celestial sphere (red) and the baseline parameters (black). On the celestial sphere, the $n$ -axis is perpendicular to the two-dimensional tangent plane created by the direction cosines $l$ and $m$ . The baseline coordinates are located on the Earth, where the $w$ -axis is along the line-of-sight. Two antennas, denoted with A and B are in the same $uv$ -space, and receiving emission from an astrophysical source (indicated with star symbol) at an angle $\theta$ to the zenith. This figure is adapted from Cosmic-Watch and web.haystack.edu. . . . . | 46 |
| 2.3 | A schematic diagram representing the MWA data reduction workflow. Most of the data processing has been done using the <code>MWA-fast-image-transients</code> pipeline. We manually assess the quality of the initial image before deciding on the next step (shown in red diamonds). When we are happy with the image quality, we then correct for ionospheric effects using <code>fits_warp</code> and correct the absolute flux scale using <code>flux_warp</code> before using <code>ROBBIE</code> to create the final sensitive mean image. . . . .   | 66 |
| 3.1 | 1.34 GHz ASKAP continuum image of our 21 September 2017 observation centered at RA = 15:35:19.71, DEC = -57:13:47.58 with a size of $1.15^\circ \times 1.15^\circ$ . The positions of MAXI J1535-571 and the comparison extragalactic source MGPS J153358-564218 are indicated by the red circle and square, respectively. . . . .  | 78 |
| 3.2 | ASKAP light curve of MAXI J1535-571 at 1.34 GHz. The peak flux density of MAXI J1535-571 exceeded 500 mJy. . . . .  | 79 |

3.3 Hardness intensity diagram (HID) for the 2017 outburst of MAXI J1535–571. The HID is made from public *MAXI* data, where intensity is the count rate in the energy range 2.0–20.0 keV, and the hardness ratio is the ratio of count rates in the 4.0–20.0 keV and 2.0–4.0 keV energy bands (Tao et al., 2018). Those X-ray data-points with simultaneous radio detections are highlighted with circles, whose size and color correspond to the measured radio flux density (zoomed in the inset of the plot). The radio flare occurred during the hard-to-soft X-ray spectral state transition. . . . . 80

3.4 The HI absorption spectrum observed from MAXI J1535–571 on 21 September 2017, when the source was brightest ( $S_0 = 579.6 \pm 2.1$  mJy). Spectra of MAXI J1535–571 and the extragalactic source MGPS J153358–564218 (in the local standard of rest frame) are displayed in red and blue, respectively.  $S_\nu$  is measured from the data cube and  $S_0$  is determined from the continuum image. The solid black horizontal line shows the zero flux level. The red and blue dotted lines represent the  $3\sigma$  rms noise levels (calculated directly from individual channel image in the spectral cube) for MAXI J1535–571 and the extragalactic source, respectively. The latter is higher due to being located further out in the primary beam. The dashed vertical line shows the rest velocity. The maximum negative velocity of significant ( $> 3\sigma$ ) absorption in the MAXI J1535–571 spectrum (dash-dotted vertical line at  $-69 \text{ km s}^{-1}$ ) places a lower limit on the source distance of  $4.1_{-0.5}^{+0.6}$  kpc. The maximum negative velocity derived from the extragalactic source spectrum (dotted vertical line at  $-89 \text{ km s}^{-1}$ ) constrains the upper limit on the distance of MAXI J1535–571 to be that of the tangent point at  $6.7_{-0.2}^{+0.1}$  . . . . . 81

3.5 The variation of the predicted velocity (for circular rotation) of the local standard of rest ( $V_{\text{LSR}}$ ) as a function of distance from the Sun ( $d$ ), in the direction of MAXI J1535–571. The horizontal line shows the velocity of  $-69 \pm 4 \text{ km s}^{-1}$ , measured from the HI absorption complex of the first epoch. The vertical line displays the most likely distance ( $4.1_{-0.5}^{+0.6} \text{ kpc}$ ) to MAXI J1535–571. The shaded region across both the lines highlight the respective error regions, as derived from the Monte Carlo approach of Wenger et al. (2018). The dashed line displays the position of the tangent point, which is our robust distance upper limit of  $6.7_{-0.2}^{+0.1} \text{ kpc}$ . . . . . 83

3.6 The variation of  $V_{\text{LSR}}$  with distance from the Sun along the line of sight to MAXI J1535–571, overlaid on a schematic of the Milky Way. The Scutum-Centaurus arm of the Milky Way lies in-between the Sun and MAXI J1535–571. The colour bar displays the variation of the predicted velocity (for circular rotation) of the local standard of rest ( $V_{\text{LSR}}$ ) as a function of distance from the Sun ( $d$ ), in the direction of MAXI J1535–571. The thick and the dashed circles correspond to the most likely distance ( $4.1_{-0.5}^{+0.6} \text{ kpc}$ ) and the robust upper limit ( $6.7_{-0.2}^{+0.1} \text{ kpc}$ ), respectively. We place MAXI J1535–571 beyond the Scutum-Centaurus arm but within  $6.7_{-0.2}^{+0.1} \text{ kpc}$ . 85

3.7 Radio–X-ray luminosity correlations for BH-XRBs and other classes of accreting compact objects including, neutron star XRBs and outbursting cataclysmic variables. The plot is adapted from Bahramian et al. (2018) and the best-fit correlation for black hole LMXBs is shown with the dashed line ( $\beta = 0.61$ ; Gallo et al., 2014). The radio/X-ray correlation for MAXI J1535–571 determined by Russell et al. (2017b) using a source distance of 6.5 kpc is shown with the magenta cross symbol. The radio/X-ray correlation obtained using our distance estimates is indicated by the cyan plus symbol. Our distance constraints help in understanding the nature of the compact object. . . . . 87

4.1 A continuum mosaic of the field surrounding MAXI J1348–630, from our 1.34-GHz ASKAP observation on 2019 February 13. The image has a size of  $1.7^\circ \times 1.5^\circ$ , centered at  $RA = 13^{\text{h}}49^{\text{m}}19.78^{\text{s}}$ ,  $DEC = -63^{\text{d}}20'23.93''$ . The location of MAXI J1348–630 is highlighted with the red circle, and the comparison extragalactic sources (listed in Table 4.1) are indicated by the blue squares. . . . . 95

4.2 The time-resolved 1.34-GHz ASKAP light curve of MAXI J1348–630 (black stars) and the extragalactic sources, for beam 20 only. The flux density of MAXI J1348–630 varies on a  $\sim 1$ -hour time scale, whereas the extragalactic sources remain constant within error bars, demonstrating that the variability observed in MAXI J1348–630 is intrinsic to the source. . . . . 96

4.3 The H I absorption complex observed in the direction of MAXI J1348–630 using our ASKAP observation from 2019 February 13.  $S_\nu$  is calculated from the spectral cube, whereas  $S_0$  is measured from the continuum image. The red and blue curves show the H I absorption against MAXI J1348–630 and the stack of the eight extragalactic sources (Table 4.1), respectively. The corresponding dotted lines represent the respective per-channel  $3\sigma$  noise levels (normalized to the source continuum flux density), taken from nearby source-free regions. The black dashed vertical line represents the rest frequency of the H I line. The dotted ( $-31 \text{ km s}^{-1}$ ) and dot-dashed vertical ( $-50 \text{ km s}^{-1}$ ) lines highlight the ( $> 3\sigma$  significant) maximum negative radial velocities (with respect to the LSR) observed from the spectra of MAXI J1348–630, and the merged extragalactic sources, respectively. The maximum negative velocity of  $-31 \pm 4 \text{ km s}^{-1}$  towards MAXI J1348–630 determines the most probable distance as  $2.2^{+0.5}_{-0.6} \text{ kpc}$ , whereas the non-detection of more negative velocities sets a stringent upper limit of the tangent point at  $5.3 \pm 0.1 \text{ kpc}$ . . . . . 98

4.4 The expected variation of the radial velocity of the local standard of rest in the direction of MAXI J1348–630 with distance from the Sun, calculated using the Monte Carlo approach described by Wenger et al. (2018). The black line represents the expected curve, and the blue shaded region shows the effect of incorporating the  $1\sigma$  uncertainties on the Galactic rotation parameters from Reid et al. (2014). The horizontal solid line shows the maximum negative radial velocity (with respect to the LSR) measured from the HI absorption spectrum. The solid and dashed vertical lines show the most likely distance and the tangent point distance, respectively. The grey shaded regions show the  $1\sigma$  uncertainties. The most probable distance of MAXI J1348–630 is the near kinematic distance of  $2.2_{-0.6}^{+0.5}$  kpc. . . . . 99

4.5 The MeerKAT (blue) and rebinned ASKAP (red) HI absorption spectra towards MAXI J1348–630. The  $3\sigma$  rms noise levels for both instruments are shown as dotted lines. The two spectra match well within uncertainties. . . . . 100

4.6 The variation of the theoretically predicted velocity (for circular motion) of the local standard of rest ( $V_{\text{LSR}}$ ) with distance from the Sun in the direction of MAXI J1348–630, overlaid on a cartoon diagram of the Milky Way. MAXI J1348–630 lies tangential to the Scutum-Centaurus arm of the Milky Way. The colour bar shows the predicted variation of the  $V_{\text{LSR}}$  as a function of distance from the Sun ( $d$ ), along the line of sight to MAXI J1348–630. The thick and the dashed circles represent the most likely distance ( $2.2^{+0.5}_{-0.6}$  kpc) and the robust upper limit ( $5.3 \pm 0.1$  kpc), respectively. Our distance constraints also place MAXI J1348–630 in front of the Scutum-Centaurus arm of the Milky Way, which is also consistent with the low  $n_{\text{H}}$  ( $0.64 \times 10^{22} \text{ cm}^{-3}$ ; Zhang et al. 2020a) determined from the X-ray studies. . . . . 103

5.1 Top and Middle panels: One-day averaged *Swift*/BAT, *Swift*/XRT and *MAXI* light curves of MAXI J1535–571 in the energy ranges 15.0–50.0 keV, 0.3–10.0 keV and 2.0–20.0 keV, respectively. Blue vertical lines highlight the dates of the MWA observations, green vertical lines indicate the UTMOST observations, and the LBA observation is denoted by the magenta vertical line. We also plot the dates of the ASKAP and ATCA observations with cyan and orange vertical lines, respectively (Chapter 3, Russell et al., 2019c). The dashed brown vertical line indicates the 21 September 2017 observation when the source was brightest (reaching  $\sim 590$  mJy at 1.34 GHz in ASKAP observation), when we were able to measure a quasi-simultaneous broadband radio spectrum. Bottom panel: Variation of the hardness ratio (HR) calculated from *MAXI* on-demand public data. The HR is defined as the ratio of count rates in the 10.0–20.0 keV and 2.0–10.0 keV energy bands. Our observations were all taken during the soft–intermediate state. . . . . 119

5.2 MWA (186 MHz; left panel) and ASKAP (1.34 GHz; right panel) continuum images of MAXI J1535–571 taken during the bright radio flare on 21 September 2017. The image is centred at the position of MAXI J1535–571 (RA = 15:35:19.71, DEC = –57:13:47.58; Russell et al., 2019c) with a size of  $1.16^\circ \times 1.16^\circ$ . In the MWA image, the diagonal stripes are sidelobes associated with PKS 1610–60 that is present to the south-east of MAXI J1535–571. These deconvolution artefacts are due to imperfect calibration resulting from the MWA’s ongoing configuration change. MAXI J1535–571 is significantly detected in both images, and is indicated by the cross-hairs. . . . . 121

5.3 Multi-frequency radio light curve of MAXI J1535–571. Solid squares, crosses, stars and circles correspond to MWA, UTMOST, ASKAP and ATCA observations, respectively. Different colours indicate different observing frequencies, as indicated by the plot legend. In the case of MWA non-detections, downward-pointing arrows represent  $3\sigma$  upper limits on the radio flux density. The medium-dark shaded region highlights the HIMS, the SIMS is represented by the light shaded region, and the dark shaded region highlights the hard X-ray spectral state. At the start and end of the light curve, ATCA points indicate the quenching and reappearance of the compact jets (Russell et al., 2019c, 2020). The two peaks are highlighted with the vertical dashed lines. The best-sampled date was 21 September (MJD 58017), during the first peak in the light curve. . . . . 125

5.4 Short time-scale light curves of the ATCA observations on 21 September 2017. The vertical dash-dotted line indicates the time of the MWA observation. ASKAP/ATCA flux densities are interpolated/extrapolated to the time of the MWA observations, and shown with hollow markers. Each plotted symbol and its colour represents a different observing frequency, as indicated in the legend. The dashed lines represent the fitted power law models for the respective light curves (as described in Section 5.3.5). By extrapolating/interpolating the flux density decays seen with ATCA and ASKAP, we reconstructed a strictly simultaneous radio spectrum at the time of the MWA observation. . . . . 126

5.5 Top panel: Broadband radio spectrum of MAXI J1535–571 on 21 September 2017. The flux densities are from MWA (this work), UTMOST (this work), ASKAP (Chapter 3) and ATCA (Russell et al., 2019c), as indicated. The black solid line highlights the median of the posterior distribution for the SSA model (discussed in Section 5.4.3), whereas the black dashed line shows the median of the posterior distribution for the FFA model (described in Section 5.4.2). We have added systematic uncertainties on the flux densities measured by MWA (10%), ASKAP (5%) and ATCA (a conservative 5%, as appropriate for the higher frequencies; Partridge et al., 2016), to incorporate the cross-telescope uncertainties. The orange and blue traces show random draws from the posterior distributions of the best fits for the SSA and FFA models, respectively. Bottom panel: Residuals relative to the median of the posterior distributions for both the SSA and FFA models. The low-frequency residuals are lower for the SSA model. The low-frequency turnover allows us to estimate several of the physical parameters of the jet. . . . . 127

|     |   |     |
|-----|---|-----|
| 5.6 | Variation of the magnetic field strength ( $B_s$ ) with angular size ( $\theta_s$ ) of the jet knot, according to Equation (5.8). The red shaded region around the main curve highlights the $1\sigma$ uncertainties on the self-absorption turnover frequency $\nu_p$ , the corresponding radio flux density $S_0$ , and our calculated range for the Doppler factor $\delta_{bp}$ . The vertical line at 23.8 mas indicates the estimated source size on 21 September 2017 (derived from our LBA observation on 23–24 September 2017, assuming constant expansion speed). The solid horizontal line shows the magnetic field strength ( $104^{+80}_{-78}$ mG) corresponding to the inferred source size. The shaded regions across all the horizontal and vertical lines indicate the $1\sigma$ uncertainties. The dashed black horizontal line at 40 mG corresponds to the minimum energy field strength $B_{eq}$ . Our SSA modelling and LBA size constraint suggest that the jet knot is close to equipartition. . . . | 135 |
| 5.7 | The variation of the bulk Lorentz factor with the inclination angle. The solid and the dashed black lines highlight the expected curves for expansion speeds of $c$ and $c/\sqrt{3}$ , respectively. The orange (expansion speed $c$ ) and the blue (expansion speed $c/\sqrt{3}$ ) shaded regions show the effect of incorporating the $1\sigma$ uncertainty on the opening angle and the distance to the source ( $4.1^{+0.6}_{-0.5}$ kpc; Chapter 3). If the jet is freely expanding, we would predict a bulk Lorentz factor $\Gamma > 10$ . . . . .   | 138 |
| 6.1 | The MWA continuum image of MAXI J1820+070 at 186 MHz observed on 12 April 2018, centered at RA = 18:20:21.94, DEC = 07:11:07.16 with a size of $1.5^\circ \times 1.5^\circ$ . The location of the source is indicated by the red circle, and was detected with a significance $> 4\sigma$ . . . . .   | 160 |

|     |  |     |
|-----|--|-----|
| 6.2 | Top panel: One-day average <i>Swift</i> /BAT light curve for MAXI J1820+070 in the energy range 15–50 keV. Red vertical lines highlight the epochs of the MWA observations. MAXI J1820+070 was in the hard X-ray spectral state during the MWA monitoring. Bottom panel: The low-frequency MWA light curve of MAXI J1820+070. Throughout the MWA monitoring, the flux density of the source remains constant within the $1\sigma$ uncertainties. The MWA observation on 12 April 2018 indicated with the dashed magenta line was part of a large multi-wavelength monitoring campaign from radio, through optical to X-rays. . . . .   | 161 |
| 6.3 | Broadband spectrum of MAXI J1820+070 on 12 April 2018. The flux densities are from MWA (this work), VLITE (Polisensky et al., 2018), VLA (Tetarenko et al., 2021), and ALMA (Tetarenko et al., 2021), as indicated. The black line highlights the best-fit power-law. We also add extra uncertainty on the radio flux densities of MWA (10%), VLITE (5%), VLA (5%) and ALMA (a conservative 5%, as appropriate for the higher frequencies; Partridge et al., 2016), to account for the non-simultaneity and cross-telescope uncertainties. The red traces show 1000 random draws from the posterior distributions of the best fit for the power-law. The spectrum shows no evidence of a low-frequency turnover. . . . . | 163 |
| 6.4 | A corner plot displaying the posterior distribution of parameters derived from our spectral modelling. The dashed vertical lines and the contours show the 16 <sup>th</sup> , 50 <sup>th</sup> and 84 <sup>th</sup> percentiles of the probability distribution. A correlation between the power-law spectral index and the amplitude is observed, which suggests that for less steep spectrum the amplitude is larger. . . . .  | 165 |

- 6.5 The MWA continuum image of MAXI J1348–630 field at 216 MHz observed on 7 February 2019, centered at RA = 13:47:50.33, DEC = -63:03:54.73 with a size of  $1.5^\circ \times 1.5^\circ$ . The source was significantly detected ( $> 6\sigma$ ), and is indicated by the red circle. . . . . 166
- 6.6 Multi-frequency radio light curve of MAXI J1348–630. Different symbols and colours indicate different instruments and observing frequencies, as shown in the plot legend. The MWA non-detections are indicated with the downward-pointing arrows, which represent  $3\sigma$  upper limits on the radio flux density. The dark shaded region highlights the hard X-ray spectral state, the medium-dark shaded region indicates the IMS, with the soft X-ray spectral state represented by the light shaded region. The dashed vertical line highlight the broadband coverage of the compact jets on or around 7 February 2019. . . . . 168
- 6.7 Broadband radio spectrum of MAXI J1348–630 on 07 February 2019. The flux densities are from MWA (this work) and ATCA (Carotenuto et al., 2021a), as indicated. We interpolated ATCA flux densities for the MWA time. The black line indicates the best-fit power-law. We also add extra uncertainty on the radio flux densities of MWA (10%) and ATCA (a conservative 5%, as appropriate for the higher frequencies; Partridge et al., 2016), to incorporate the quasi-simultaneity and cross-telescope uncertainties. The red traces show 1000 random draws from the posterior distributions of the best fit for the power-law. In the broadband compact jet spectrum we have not observed any signature of a low-frequency turnover. . . . . 170

|     |  |     |
|-----|--|-----|
| 6.8 | Corner plots showing the results of the MCMC power-law spectral fit. The panels display the histograms of the posterior distribution (one-dimensional) for the free model parameters. The contours and the vertical lines represent the 16 <sup>th</sup> , 50 <sup>th</sup> and 84 <sup>th</sup> percentiles of the probability distribution. We observed a correlation between the fitted power-law spectral index and the amplitude. . . . . | 171 |
| A.1 | Synchrotron emission from a relativistic electron. $p$ is the pitch angle of the electron, and $B$ is the magnetic field strength. The synchrotron emission is restricted to the shaded region, and $\theta = 1/\gamma$ . The figure is taken from Rybicki & Lightman (1979). . . . .  | 202 |
| A.2 | The plot showing the synchrotron spectrum of a relativistic electron, which is proportional to $F(x)$ . We defined frequency in terms of the critical frequency ( $\nu_{crt}$ ), where $x = \omega/\omega_{crt} = \nu/\nu_{crt}$ . $F(x)$ is given by eq. A.5 and A.6. . . . .   | 204 |

# Chapter 1

## Introduction

### 1.1 Introduction to radio transients

Over the past several decades, probing the transient universe has become a high-profile astrophysical endeavor. These transient events are thought to originate from some dynamical or explosive phenomenon and provide excellent opportunities to study accretion and other related phenomena, such as particle acceleration in extreme gravitational and magnetic fields (Cordes et al., 2004). Such transient events are either Galactic or extragalactic. Examples of Galactic events include flare stars (e.g., Lynch et al., 2017; Tu et al., 2021), radio ejections from X-ray binaries (e.g., Miller-Jones et al., 2004; Russell et al., 2019c), magnetars (e.g., Coti Zelati et al., 2021), star-planet interaction (e.g., Vedantham et al., 2020). Extragalactic transients include supernovae (e.g., Anderson et al., 2017), gamma-ray bursts (GRBs; e.g., Chandra & Frail, 2012; Li et al., 2021), tidal disruption events (TDEs; e.g., Zauderer et al., 2011; van Velzen et al., 2016), gravitational wave events (GWEs; e.g., Abbott et al., 2016; Hallinan et al., 2017; Mooley et al., 2018), ultraluminous X-ray sources (ULXs; e.g., Middleton et al., 2013), unknown nature (e.g., Anderson et al., 2019a) and many more. The transient nature of the sky at high-energies (X-ray and  $\gamma$ -ray) has been extensively studied, since various all-sky monitor instruments in space are continuously scanning for exotic

transient events, resulting in the discovery of new sources such as magnetars (e.g., Mihara et al., 2020), GRBs (e.g., Malacaria et al., 2021; Troja et al., 2021) and X-ray binaries (e.g., Negoro et al., 2017a; Kennea et al., 2017a; Yatabe et al., 2019). In the optical band, the development of modern instruments such as the Palomar Transient Factory (PTF; Law et al., 2009), the All-Sky Automated Survey for Supernovae (ASAS-SN; Shappee et al., 2014; Kochanek et al., 2017) and the Zwicky Transient Facility (ZTF; Bellm et al., 2019) increased our probability of detecting phenomena such as Type Ia supernovae and gravitational lensing events. The situation at radio frequencies is completely different. Even though the sampling time resolution in radio astronomy is extremely high, the number of transient events detected is quite low (e.g., Hyman et al., 2005; Bower et al., 2007; Lazio et al., 2010; Mooley et al., 2016; Stewart et al., 2016; Murphy et al., 2017; Leung et al., 2021). One of the primary reasons behind fewer detections of transients in the radio band when compared to high frequencies has been due to the lack of sensitive wide-field radio instruments.

Over the past few decades, large numbers of efforts have been made to study radio transient events through blind (e.g., McGilchrist & Riley, 1990; Minns & Riley, 2000) as well as targeted surveys (e.g., Hyman et al., 2005; Bower et al., 2007) covering a large part of the sky, but the numbers of detections are extremely low. For example, Bower et al. (2007) monitored a particular patch of sky for 20 years at 5 and 8.4 GHz, and detected just two radio transients from the two month averages. The authors have not detected any radio transient from the one year averages (Bower et al., 2007). The detections are even fewer at low radio frequencies ( $< 500$  MHz). For example, Lazio et al. (2010); Jaeger et al. (2012); Bell et al. (2014); Polisensky et al. (2016); Stewart et al. (2016); Murphy et al. (2017); Bell et al. (2019); Hajela et al. (2019); Anderson et al. (2019b) have explored the low-frequency radio sky in the frequency range 60–325 MHz, but these six surveys report just two radio transients (of unknown nature) and six upper limits on the transient surface densities. Therefore, most

transient studies at radio frequencies have been followed up by monitoring of high-energy transient events, from gamma-ray bursts to tidal disruption events to X-ray binaries.

## 1.2 Introduction to X-ray binaries

X-ray binaries (XRBs) are a special class of binary stars where one of the stars ran out of its nuclear fuel required for nuclear reactions and collapsed under the immense gravitational pressure to form a compact object (black hole or neutron star). The secondary star (donor star) of the binary system is less evolved and still producing energy by nuclear fusion. The compact object is accreting matter from the donor star (companion), and some special conditions are required for accretion to start (Illarionov & Sunyaev, 1975). For the constant flow of matter, the two members of the binary must be at a specific separation such that they should not merge, but at the same time allow the mass transfer from the companion to the compact object. The conditions required for stable accretion depend on factors including, the evolutionary phase of the donor star, the orbital parameters of the binary system, and the masses of the two objects. These conditions are fulfilled by only a small group of binary stars, and make XRBs a relatively rare class of binary system. Although, a large number of stars exist in binary systems, according to population synthesis models, only a few thousand X-ray binary systems are expected in the Milky Way (Dalton & Sarazin, 1995; Iben et al., 1995a,b).

XRBs play an important role in understanding the universal phenomenon of accretion because they evolve on humanly-observable timescales when compared to accretion onto more massive objects such as supermassive black holes (SMBHs), which typically take millions of years to evolve. XRBs are bright in all bands of the electromagnetic spectrum, with their spectral energy distribution peaking in X-rays. XRBs also show other highly energetic phenomena like relativistic jets.

Multi-wavelength studies of XRBs help in understanding some of the fundamental open questions related to accretion/ejection such as:

- What is the underlying physical process connecting the accretion inflow with the outflow (jet or winds)?
- What is the relative importance of radiation and kinetic outflows in carrying energy away from the system, and how does this change as the accretion geometry changes?
- How is the environment of the source influenced by the jets?

In an XRB system, the compact object is formed when the star runs out of nuclear fuel and starts collapsing under its own gravity (Carroll & Ostlie, 2017). It is not easy to determine whether the compact object will be a black hole or a neutron star. The nature of the compact object not only depends on the initial mass of the collapsing star but is also controlled by the stellar and binary evolution of the star in question (Carroll & Ostlie, 2017). If the initial mass of the star ( $M_{\text{star}}$ ) is  $> 8 M_{\odot}$ , it will finally evolve to form a neutron star or a black hole. After the supernova, if the mass of the remaining core ( $M_{\text{core}}$ ) is  $1.4 M_{\odot} < M_{\text{core}} < 3.0 M_{\odot}$ , the neutron degeneracy pressure balances the gravitational pull at the core of the star, resulting in a neutron star (Carroll & Ostlie, 2017). If  $M_{\text{core}} > 3 M_{\odot}$ , then a black hole is likely formed (Carroll & Ostlie, 2017). The research presented in this thesis focuses on XRBs where the compact object is a black hole or black hole candidate.

Depending on the nature of the donor star, XRBs can be further classified into three main classes; High-Mass X-ray Binaries (HMXBs), Intermediate-Mass X-ray Binaries (IMXBs), and Low-Mass X-ray Binaries (LMXBs). In HMXBs, the donor star is massive with a typical mass of  $> 10 M_{\odot}$  and is usually an evolved early-type star of spectral type O or B. In these systems, the mass transfer mainly happens through strong stellar winds. In IMXBs, the donor is usually a late B or A-type star, with the mass in the range 2 to  $10 M_{\odot}$ . These systems

are hard to observe because they are short-lived with high accretion rates (Podsiadlowski & Rappaport, 2000). For LMXBs, the mass of the companion star is  $< 2 M_{\odot}$ , usually of spectral type F or later, and typically belongs to an old stellar population ( $\gtrsim 5$  Gyr). The main mode of accretion in LMXB systems is Roche-lobe overflow, and it is thought that some of the present LMXBs evolved from the IMXB systems (Podsiadlowski et al., 2002). The research presented in this thesis focus on LMXBs.

### 1.2.1 Introduction to black hole low-mass X-ray binaries

In Figure 1.1, we present a cartoon diagram of a black hole LMXB. As discussed in the previous section, the primary mode of accretion in black hole LMXBs is Roche-lobe overflow. Given the orbital motion of the components, the matter falling in towards the black hole from the donor star has got significant angular momentum. Therefore, instead of directly falling onto the black hole, it spirals around the compact object in nearly circular orbits and forms a differentially rotating disc (Figure 1.1) called an accretion disc (Pringle & Rees, 1972). The radiation spectrum and the geometrical structure of the accretion disc depends on parameters including the size and the mass of the system (the compact object and the donor star), and the mass accretion rate at the external boundary of the disc (Shakura & Sunyaev, 1973).

According to the thin disc model, the angular velocity ( $\Omega_{\text{ang}}$ ) of the spiraling matter can be calculated using the Keplerian approach (Frank et al., 2002), and has the form

$$\Omega_{\text{ang}}(R) = \left( \frac{GM}{R^3} \right)^{1/2}, \quad (1.1)$$

where  $G$  is Newton's gravitational constant,  $M$  is the mass of the accreting compact object, and  $R$  is the distance of the matter from the compact object. After deriving  $\Omega_{\text{ang}}$  from equation 1.1, the circular velocity ( $V_{\text{circ}}$ ) can be determined (Frank et al., 2002) as

$$V_{\text{circ}} = R\Omega_{\text{ang}}(R) \propto R^{-1/2}. \quad (1.2)$$

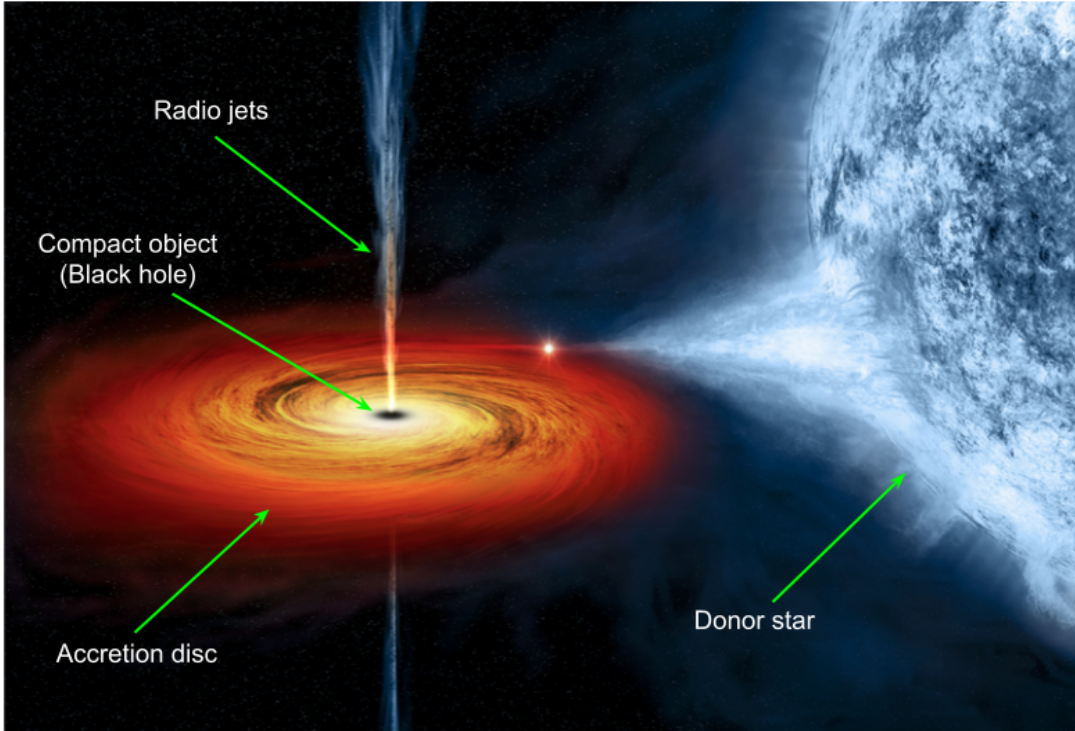


Figure 1.1: An artist's view of a low-mass black hole X-ray binary. The key components of these systems are indicated on the image. The emission from these different components dominate in different parts of the spectrum (jets in radio, inner accretion disc in X-rays, and outer accretion disc in optical and UV), and their different temperatures are denoted with different colours. The radio jets and the donor star are shown in light blue color. The accretion disc is illustrated through the use of different colours from red (cool - optical/UV) through to white (hot - X-rays). Image credit: NASA / CXC / M.Weiss.

For the matter to move inwards towards the black hole, it needs to lose angular momentum. In this context, the viscous forces acting between the neighbouring rings of the matter play an important role. They redistribute the angular momentum in such a way that some fraction of the matter loses angular momentum and moves towards the compact object. The rest of the matter gains angular momentum and moves outwards (Pringle & Rees, 1972).

In this process, some gravitational energy ( $E_G$ ) is released locally, and its dissipation rate can be calculated from the rate of viscous energy dissipation. A small fraction of the dissipated gravitational energy is used to increase the

rotational kinetic energy. The remaining gravitational energy is converted to thermal energy ( $E_{Th}$ ), which is emitted from the surface of the accretion disc (Shakura & Sunyaev, 1973). The temperature of the matter in the accretion disc can reach up to  $10^7$  K when the matter reaches the innermost stable circular orbit (ISCO), beyond which the accreted matter will eventually fall onto the black hole without any significant emission of radiation.

In the accretion disc, energy is mostly generated by viscous heating and the reprocessing of X-ray photons, which are produced in the inner part of the disc (Shakura & Sunyaev, 1973; van Paradijs & McClintock, 1995; Frank et al., 2002). The reprocessing of X-ray photons is mostly dominant in the outer part of the accretion disc, which is bright in optical/UV emission. The energy spectrum of the inner disc can be best described as a multicolor blackbody, where the effective temperature ( $T_{eff}$ ) scales with the disc radius (Shakura & Sunyaev, 1973) as

$$T_{\text{eff}}(R) \propto R^{-3/4}, \quad (1.3)$$

so the closer the material gets to the compact object, the hotter it gets. In the outer part of the accretion disc, which is irradiation-dominated, the effective temperature varies (Frank et al., 2002) as

$$T_{\text{eff}}(R) \propto R^{-1/2}. \quad (1.4)$$

In the canonical model, a temperature-inversion layer is formed in the disc chromosphere due to X-ray irradiation in the outer part of the disc. We therefore observe absorption and emission lines from the accretion disc (van Paradijs & McClintock, 1995). The black hole LMXBs are bright over the broad electromagnetic spectrum and their accretion disc peaks in X-rays.

## 1.2.2 Quiescence

Most black hole LMXBs spend the majority of their time in quiescence (indicated with ‘A’ in Figure 1.2), where the X-ray luminosity is  $<10^{-5.5}$  times the Eddington luminosity<sup>1</sup> (Plotkin et al., 2017). In this case, the gas density in the accretion disc is believed to be comparatively low, and therefore, the energy radiated from the accretion disc is significantly small. In quiescence, the energy produced by viscous heating is advected inwards towards the compact object along with the accreted matter. As a result, the accretion disc is truncated at some large radius, and we have a more tenuous, geometrically thick, and radiatively inefficient hot inflow.

It is believed that the accretion flow onto the black hole may be composed of two zones; an outer optically thick, geometrically thin disc and an inner advection dominated accretion flow (ADAF) region (Narayan et al., 1996, 1997a,b; Esin et al., 1997). When the inner mass accretion rate ( $\dot{m}$ ) is considerably small as compared to the critical mass accretion rate<sup>2</sup> ( $\dot{m}_{\text{crit}}$ ),  $\dot{m} \ll \dot{m}_{\text{crit}}$ , the optically thick and geometrically thin accretion disc is truncated at a comparatively large transition radius, which is suggested to be associated with the angular momentum of the accreted matter from the donor star (Esin et al., 1997). Therefore, the inner accretion flow is dominated by ADAFs (Esin et al., 1997). The model for describing the advection dominated accretion flows was initially proposed by Ichimaru (1977), and further elaborated by Narayan & Yi (1994) and Abramowicz et al. (1995). The theory of ADAFs is important to understand the quiescent state because during that time  $\dot{m} \ll \dot{m}_{\text{crit}}$ . According to ADAFs theory, an appreciable

---

<sup>1</sup>This is a theoretical limit on the maximum luminosity ( $L_{\text{Edd}}$ ), which can be achieved when there is a balance between the inward gravitational force and the outward radiation pressure created by photons.

<sup>2</sup>The critical mass accretion rate can be defined as (Fukue, 2004)

$$\dot{m}_{\text{crit}} \equiv \eta \dot{m}_{\text{Edd}} \equiv \frac{L_{\text{Edd}}}{c^2}, \quad (1.5)$$

where  $\dot{m}_{\text{Edd}}$  is the Eddington accretion rate,  $L_{\text{Edd}}$  is the Eddington luminosity and  $\eta$  is the accretion efficiency.

portion of the liberated accretion energy is advected onto the black hole through the event horizon (e.g., Ichimaru, 1977; Narayan & Yi, 1994; Abramowicz et al., 1995).

In this low-density quiescent state, the Coulomb transfer between the electrons and the ions becomes ineffective. While the ions attain the virial temperature and acquired most of the viscous energy, electrons have a much lower temperature as compared to the ions because they are radiating efficiently. As a result, the gas acquires two different temperatures, and the accretion flow becomes a nearly spherical flow with sub-Keplerian rotation. Therefore, instead of disc-like, the ADAFs onto the black hole turned to be nearly spherical, and the energy generated due to viscous heating is advected with the accreted matter. Therefore, the gas in the accretion disc cannot cool down (Frank et al., 2002).

There are various alternative theories to explain quiescence, including the advection dominated inflow-outflow solutions (ADIOS; Blandford & Begelman 1999), the convection dominated accretion flows (CDAFs; Quataert & Gruzinov 2000), and the magnetically dominated accretion flows (MDAFs; Meier 2005), which suggest that when the mass accretion rate is significantly small the accretion flow becomes considerably less luminous. In the case of the ADIOS model, only a small portion of the accreted material is accreted onto the compact object, and the radiated energy moves radially outward, which may drag along the remaining accreted gas in the form of winds. In quiescence, the inner mass accretion rate is lower than the mass transfer rate from the donor. That builds up matter in the disc until the surface density is high enough to trigger a disc instability and an outburst (Blandford & Begelman, 1999). Quataert & Gruzinov (2000) suggest that in the CDAFs model a large amount of the energy is propagated outwards through convection. However, in the MDAFs theory, the outer part of the accretion disc is proposed to be optically thick and geometrically thin. The flow of matter in the inner part of the accretion disc is significantly inefficient because in the inner disc region the magnetic forces are much stronger than the

radiation and the thermal forces (Meier, 2005).

### 1.2.3 Outburst

The build up of matter in the disc in the quiescent state causes an LMXB to undergo an episode of rapid brightening observed across the electromagnetic spectrum known as an outburst (see Figure 1.2, e.g., Frank et al. 2002; Belloni et al. 2005; Belloni 2010). The duration of an outburst varies from a few weeks to a few years (e.g., Tetarenko et al., 2016). The exact mechanism that triggers the beginning of an outburst is still unknown, however, the best explanation is given by the disc instability model, which suggests that a thermal-viscous instability in the accretion disc is responsible for the onset of an outburst (see Dubus et al. 2001, for a review).

According to the disc instability model, the cyclic process of outburst and quiescence for an LMXB may proceed in the following way. In quiescence, the inner mass accretion rate is lower than the mass transfer rate from the donor. Therefore, the cold accretion disc continues accumulating matter from the donor star through Roche lobe overflow until it attains a critical density. The accretion disc temperature also increases to the critical value, which is necessary to ionise the hydrogen. When both disc temperature and disc surface density reach their critical limit, it causes a heating front that propagate through the accretion disk. This event changes the accretion disc into a hot and bright state that commences the outburst (Menou et al., 1999). When the accretion disc depletes, the outburst decays, and the system returns to quiescence. The system again starts accumulating matter in the accretion disc for the next outburst.

During the outburst, as  $\dot{m}$  increases ( $\dot{m} \leq \dot{m}_{\text{crit}}$ ), the hot ADAF region starts radiating quite efficiently, which shrinks the size of the ADAF region. As a result, the inner edge of the optically thick, geometrically thin accretion disc starts moving towards the ISCO (Esin et al., 1997). When  $\dot{m}$  reaches its maximum limit ( $\dot{m} \approx \dot{m}_{\text{crit}}$ ), the inner edge of the disc approaches the ISCO (Esin et al.,

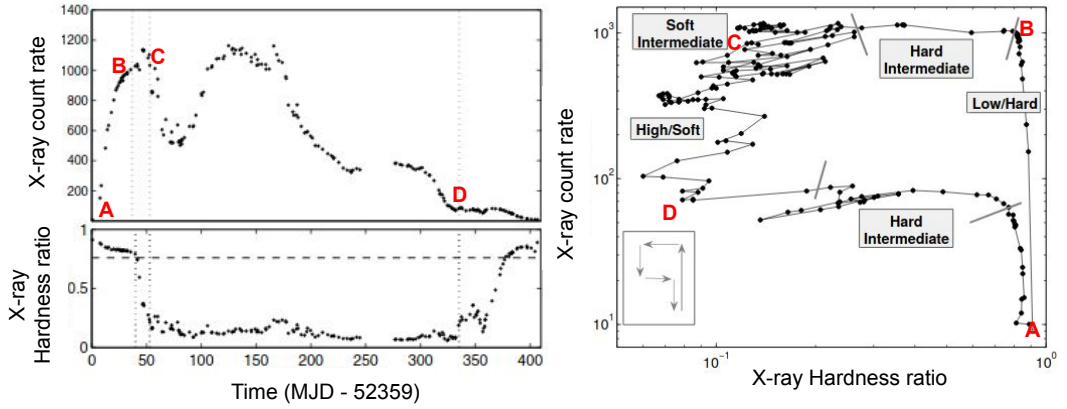


Figure 1.2: Top left panel: An X-ray light curve of the BH-LMXB GX 339–4 over its full 2002/2003 outburst observed by the RXTE satellite (Belloni et al., 2005). Bottom left panel: The hardness ratio for the same light curve (Belloni et al., 2005). The dotted vertical lines highlight the main X-ray spectral state transitions. The dashed horizontal line indicates the hardness ratio where the source evolves between the various intermediate states through the high/soft state in the hardness intensity diagram (HID; right panel). The letters (A, B, C, D) in red represent different stages of the outburst as described in the text. Right panel: The hardness intensity diagram (HID) corresponding to the left panel figures (Belloni et al., 2005). The transitions between the X-ray spectral states (labelled in the grey boxes) are indicated by the grey lines (Belloni, 2010). The inset in the bottom left corner represents the ideal ‘q-shaped’ evolution of the source outburst in the HID diagram. This figure is adapted from Belloni et al. (2005).

1997), and the ADAF region nearly completely disappears. The remnant traces of the ADAF zone can be found as a low-density corona<sup>3</sup> above the inner disc (Esin et al., 1997).

<sup>3</sup>Corona is thought to be located in the inner part of the accretion disc close to the black hole, where most of the accretion energy is liberated. Corona is conceptualized to be formed of quasi-thermal electrons, which have mean energy ( $kT_e$ ) in between 50 — 100 keV (e.g., Haardt & Maraschi, 1991, 1993). Corona is not emitting a large amount of photons in itself, but interacts with a small fraction of the thermal photons ( $< 10$  keV) from the accretion disc (e.g., Haardt & Maraschi, 1991, 1993). The thermal photons gain energy from the corona through inverse Compton scattering, and give rise to non-thermal, power-law emission (e.g., Walter & Courvoisier, 1992).

### 1.2.3.1 X-ray spectral states

The evolution of a typical BH-LMXB during its outburst is shown in Figure 1.2. Throughout their outburst cycles, BH-XRBs show characteristic X-ray spectral states (shown in Figure 1.2), namely hard, hard-intermediate (HIMS), soft-intermediate (SIMS), and soft (Belloni et al., 2005; Remillard & McClintock, 2006; Belloni, 2010), which are thought to be related to the geometry of the accretion flow (Meyer-Hofmeister et al., 2009).

Generally, the canonical BH-LMXBs spend most of their life span in the quiescent state (indicated by ‘A’ in Figure 1.2), which is by definition extremely hard to study because of its low luminosity ( $< 10^{-5.5} L_{\text{Edd}}$ ; e.g., Gallo et al. 2014; Plotkin et al. 2017). During this state, the X-ray energy spectrum is best described by a dominant broadband non-thermal power-law component, where the X-ray photon index ( $\Gamma$ ) is  $\gtrsim 2.1$  (Plotkin et al., 2013). A weak thermal blackbody component may also be present, which is associated with the truncated accretion disc. In this state, the inner regions of the inflow become optically thin, geometrically thick, and radiatively inefficient (Narayan & Yi, 1995), see Section 1.2.1 for more detail. The donor star also dominates the optical emission from the system (White et al., 1995).

In the initial phase of a canonical outburst, the source emerges from the quiescent state and enters the hard state, which corresponds to the right vertical branch in Figure 1.2 (right panel). The canonical hard X-ray state is also observed in the decaying phase of the outburst. The X-ray energy spectrum is still dominated by the non-thermal power-law component ( $> 80\%$  contribution to the total X-ray flux), with  $1.4 < \Gamma < 2.1$  (e.g., Remillard & McClintock, 2006).

Following the counterclockwise movement in Figure 1.2 (right panel), the source first enters the hard-intermediate state (HIMS), and then moves into the soft-intermediate state (SIMS) as the thermal blackbody component increases and the non-thermal power-law component decreases (increase in  $\Gamma$  value with  $\Gamma > 2.4$ ), due to the increase in inner mass accretion rate. The two intermediate

states can also be differentiated by the drop in fractional rms (root mean square) variability, which is a quantity used to measure the X-ray variability (Belloni et al., 2005; Belloni, 2010).

As the outburst evolves, the mass accretion rate further increases and the optically thick, geometrically thin disc further extends towards the black hole. The system enters the soft X-ray spectral state shown in the left of Figure 1.2 (right panel). In the soft state, the X-ray energy spectrum is dominated by the soft, thermal blackbody component, with a disc temperature  $kT \lesssim 1$  keV. The optically thick, geometrically thin accretion disc extends up to the ISCO. In some cases, a weak non-thermal power-law continuum is also observed ( $< 25\%$  contribution to the total X-ray flux, Remillard & McClintock 2006).

After attaining its maximum value, the mass accretion rate starts decreasing with the source simultaneously evolving back through the intermediate states, which corresponds to the lower horizontal branch in Figure 1.2 (right panel). As the mass accretion rate further decreases, the BH-LMXB enters the hard state again. Finally, the source returns to its quiescence state when the mass accretion rate drops below the critical value ( $\dot{m}_{\text{crit}}$ ).

### 1.3 All Sky X-ray monitors

In recent times the probability of detecting X-ray binaries in outburst has dramatically improved due to the advent of modern all-sky X-ray monitors such as the Monitor of All-sky X-ray Image<sup>4</sup> (*MAXI*; Matsuoka et al., 2009), and the Burst Alert Telescope (BAT) onboard the Neil Gehrels Swift Observatory<sup>5</sup> (*Swift*/BAT; Gehrels et al., 2004; Barthelmy et al., 2005), which are continuously scanning the sky.

*MAXI* is an X-ray telescope mounted on the International Space Station (ISS). The X-ray telescope consists of two instruments: a Gas Slit Camera (GSC) and

---

<sup>4</sup><http://maxi.riken.jp/top/index.html>

<sup>5</sup><https://swift.gsfc.nasa.gov/>

Solid-state Slit Camera (SSC), which together work in the 0.5 to 30 keV energy range, and have a field-of-view of  $\sim 240 \text{ deg}^2$  (Matsuoka et al., 2009). *MAXI* can therefore scan nearly all of the sky at X-ray wavelengths for every 90 minute orbit of the ISS (Matsuoka et al., 2009).

While the primary goal of the *Swift*/BAT<sup>6</sup> is to provide Gamma Ray Burst (GRB) triggers, the telescope discovers and monitors other high-energy transient events (Barthelmy et al., 2005). The instrument has a FOV of 1.4 steradian, and can provide a positional accuracy of 4-arcmin. *Swift*/BAT operates in the 15–150 keV energy range (Barthelmy et al., 2005).

## 1.4 Jets

The previous section describes the observable emission caused by the inflow or accretion of matter on black hole X-ray binaries. However, we also observe the ejection of highly energetic plasma in the form of collimated outflows known as jets (e.g., Fender, 2006; Fender & Gallo, 2014). These jets are accelerated from the inner accretion flow and are launched from the accretion disc at velocities close to the speed of light. Jets extract a considerable amount of power from the accretion flow or potentially from the black hole spin, which is then deposited into the surrounding medium (e.g., Gallo et al., 2005; Tetarenko et al., 2018a). Although it is thought that accretion and ejection are interconnected (e.g., Tananbaum et al., 1972; Corbel et al., 2003; Gallo et al., 2003; Fender et al., 2004; Gallo et al., 2012; Corbel et al., 2013; Gallo et al., 2014), the true relation is still not fully understood. Jets are mostly observed in the radio to the infrared frequency band, but in some cases have also been detected in the optical (e.g., Han & Hjellming, 1992; Kanbach et al., 2001; Fender, 2001; Uemura et al., 2004; Russell & Fender, 2010), ultraviolet (Curran et al., 2010) and X-ray regime (Pe’er & Markoff, 2012; Russell et al., 2013; Shahbaz et al., 2013). Radio jets emit energy through synchrotron radiation. The theory of Synchrotron radiation is described

---

<sup>6</sup>[https://swift.gsfc.nasa.gov/about\\_swift/bat\\_desc.html](https://swift.gsfc.nasa.gov/about_swift/bat_desc.html)

in detail in Appendix A.

### 1.4.1 Jet launching and collimation

Although it is known that accretion and ejection are interconnected (e.g., Tananbaum et al., 1972; Corbel et al., 2003; Gallo et al., 2003; Fender et al., 2004; Gallo et al., 2012; Corbel et al., 2013; Gallo et al., 2014), the exact mechanism behind the jet launch and collimation is still not fully understood. However, various theories suggest that the magnetic field from the accretion disc plays a crucial role (e.g. Blandford & Znajek, 1977; Blandford & Payne, 1982). While it has been confirmed that most of the detected jet emission is due to energetic  $e^-/p^+$  or  $e^-/e^+$  particles (Corbel et al., 2015), but the true composition (whether leptonic, baryonic or both) of the jet is still under debate. The commissioning of the Event Horizon Telescope and other multi-wavelength instruments have increased our capability of monitoring an outburst from the X-ray to the radio band. Hence, the composition of the jets can be precisely constrained by modeling their broadband SED (spectral energy distribution; Croston et al., 2018; EHT MWL Science Working Group et al., 2021), because a particular peak in the SED can signify the presence of specific particles. In some cases, the interaction of the jet with the surroundings can also help us in determining their constitution (Heinz, 2006, 2008). Additionally, the polarization observations with the EHT can also provide some insight on the jet composition, because polarization depends on the plasma composition (e.g., Wardle et al., 1998; Romero et al., 2017). The detection of circular polarization suggests the presence of  $ep$  plasma, because in the case of  $e^-e^+$  plasma circular polarization cancels due to symmetry (e.g., Romero et al., 2017). However, caution should be taken because the polarization technique is still under debate (e.g., Ruszkowski, 2003).

Various models have been proposed to understand the jet launching mechanism, some of them are described here. In a model proposed by Blandford & Znajek (1977), it is suggested that the spin of the black hole plays an important

role in powering the jets. When the black hole spins, the ergosphere also rotates with the black hole, which powers the jets. The magnetic field lines present in the accretion disc move towards the black hole along with the accreted matter. As the density of the in-flowing matter increases close to the black hole, so does the intensity of the magnetic field lines also. When the accreted matter falls on the black hole through the event horizon, the magnetic field lines remain threaded with the ergosphere. The space-time in the vicinity of the event horizon is therefore forced to rotate with the black hole, which twist the magnetic field lines into helical magnetic springs. Further out from the central engine, these magnetic springs expand under their own pressure, and plasma attached to these magnetic field lines get accelerated, which we observe as relativistic jets (Blandford & Znajek, 1977). However, this model suffers limitations because it only applies to black holes and not to other accreting compact objects such as neutron stars.

Blandford & Payne (1982) proposed a model that suggests that the strong magnetic fields confined in the differentially rotating accretion disc are responsible for the acceleration of the jets. The magnetic field lines emerge out of the accretion disc and spread to large distances in space. Additionally, they take energy and angular momentum out of the accretion disc through ionised matter. The coronal matter in the accretion disc is accelerated upward and outward through a combination of the co-rotating magnetic field lines attempting to uncoil, and the magnetic energy density also being sufficiently larger than the kinetic and thermal energies above the accretion disc. When the kinetic energy density becomes equivalent to the magnetic field density, the acceleration of the particles stops but collimation persists (Livio et al., 1999). The tension between the magnetic field lines enables the toroidal component of the magnetic field to collimate the accretion flow into a pair of bipolar jets, which point in a direction perpendicular to the plane of the accretion disc (Blandford & Payne, 1982). In this model, the radio jets are launched with the help of magnetic fields from the accretion disc, hence, can be applied to any system with an accretion disc.

Narayan et al. (2003) proposed the concept of a magnetically arrested disc (MAD) to explain the jet launching from a non-spinning black hole. The authors have suggested that the accreted plasma drags in the poloidal magnetic field, which is strong and coherent and can not escape from the accretion disc due to the continuous accretion flow (Narayan et al., 2003). Therefore, the poloidal magnetic field grows in strength and eventually disrupts the accretion flow at a particular distance from the black hole known as the magneto-spheric radius (Narayan et al., 2003). Inside the magneto-spheric radius, the accretion flow breaks up into discrete blobs that can only move towards the black hole through magnetic reconnection. The velocity of the blobs is significantly less than the free-fall velocity (Narayan et al., 2003), and the entire rest-mass energy is liberated to infinity in the form of heat, radiation and magnetic energy (Narayan et al., 2003). Tchekhovskoy et al. (2011) have broadly validated the fundamental predictions of the model presented by Blandford & Znajek (1977), and also extended the model given by Narayan et al. (2003) to include highly spinning black holes. Later, Narayan et al. (2012) performed sophisticated, general-relativistic magneto-hydrodynamic (GRMHD) simulation with two different topologies of the magnetic field; SANE (standard and normal evolution, weak and turbulent magnetic field) and MAD, to understand the jet launching mechanism. The authors found that even in the SANE configuration, 60% of the inflowing matter flows out of the system. Therefore, a significant amount of matter is flowing out of the system. In all the theoretical approaches magnetic field plays a crucial role in jet launching.

The spatial scales on which the aforementioned models work is far smaller than could be probed by mas-level images. Currently, the Event Horizon Telescope is capable of providing high angular resolution, of the order of  $\mu\text{as}$ , and capable of probing the sub-lightday structures (e.g.; Janssen et al., 2021). These high-resolution images provide crucial information of the jets, for example the jet bases are detected to be much wider, which is contrary to theoretical expectations

(Punsly, 2021; Punsly & Chen, 2021; Punsly et al., 2021). In future, these high-resolution observations will help us in constraining the aforementioned models for jet launching. Additionally, polarimetric imaging with the EHT will help us in understanding the structure of the magnetic field in the vicinity of the black hole, which will provide extra constraints on jet launching models (Romero et al., 2017). Finally, the sub-mm/IR observations that probe the optically-thin parts of the jet base (certainly in XRBs) can help shed some light on jet launching and acceleration, particularly when compared with the predictions of GRMHD models.

## 1.5 Observations of radio jets in black hole X-ray binaries

During a canonical black hole LMXB outburst, we observe dramatic changes in the intensity of the X-rays when the source undergoes transitions between various characteristic X-ray spectral states (discussed in Section 1.2.3.1). We observe similar behaviour from BH-XRBs in the radio band, as a particular X-ray spectral state is connected to a specific kind of radio ejection (Figure 1.3; e.g., Fender et al., 2004; Remillard & McClintock, 2006; Belloni, 2010).

Over the course of a single outburst, two types of radio jets are observed (Figure 1.3); a compact jet and a transient jet, which can be distinguished on the basis of their spectral indices ( $\alpha$ , where  $S_\nu \propto \nu^\alpha$ ;  $S_\nu$  is the radio flux density and  $\nu$  is the frequency) and morphology (e.g., Fender, 2006). Both types of jets have been detected at high ( $> 1$  GHz; e.g., Russell et al., 2019c; Carotenuto et al., 2021a) as well as at low radio frequencies ( $< 1$  GHz; e.g., Chapter 5, Broderick et al., 2018a; Polisensky et al., 2018; Chauhan et al., 2019a). The most plausible explanation for the two types of radio jets was given by Fender et al. (2004). According to the authors, a continuous flow assumed to be conical is responsible for the compact jets, whereas an internal shock in the continuous conical flow

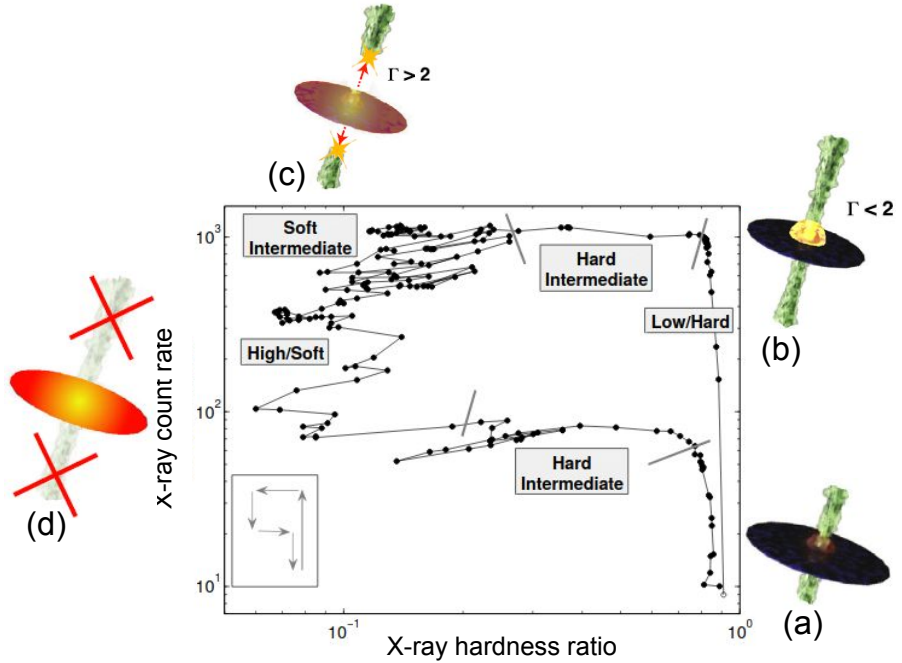


Figure 1.3: A schematic diagram showing the type of radio jet associated with different X-ray states during a BH-LMXB outburst. The radio jets are overlaid on the HID of GX 339–4 for the 2002/2003 outburst, which is also shown in the right panel of Figure 1.2. The various colours in the outer images demonstrate the corresponding contributions of the jet (green), the corona (black), and the accretion disc (red) during (a) quiescence, (b) the hard state, (c) the intermediate state when an internal shock is produced in the jet due to the launching of discrete ejecta, and (d) the soft state when the jets are quenched (Fender et al., 2004). This figure is adapted from Fender et al. (2004), Belloni et al. (2005), Belloni (2010) and Romero et al. (2017).

produces transient jets. Owing to their rapid evolution, studies of BH-XRBs can allow us to probe the causal connection between changes in the accretion flow and subsequent changes in the jets.

### 1.5.1 Compact jets

Optically thick, flat or slightly inverted spectra ( $0 \lesssim \alpha \lesssim 0.6$ , Figure 1.4 right panel) from partially self-absorbed, steady, compact jets (Stirling et al., 2001) are observed during the hard X-ray spectral state (Figure 1.3 left vertical branch, Corbel et al. 2000; Dhawan et al. 2000; Fender et al. 2000; Fender 2001; Stirling

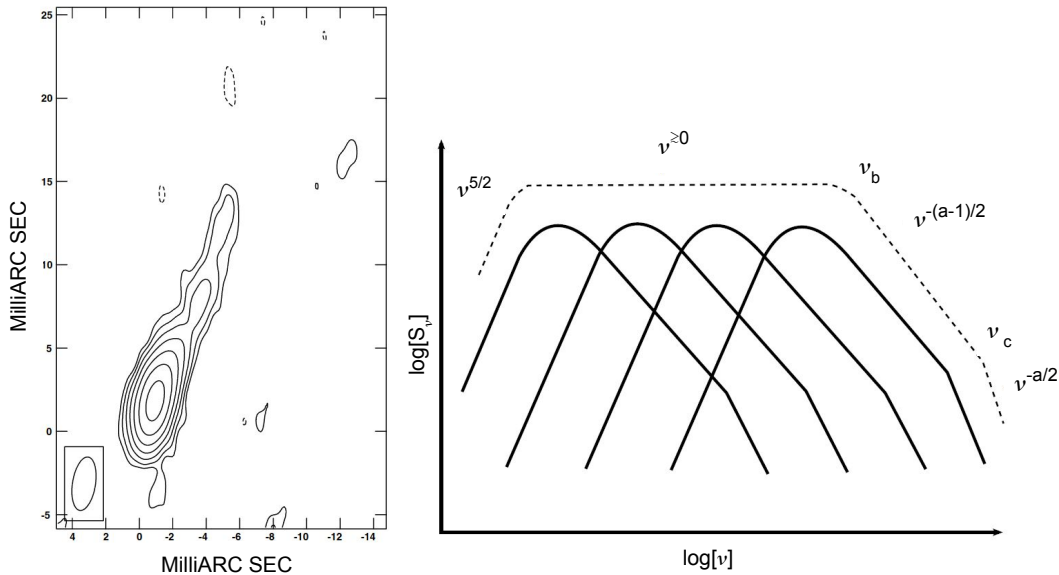


Figure 1.4: Left panel: An image of the compact jet in Cygnus X-1 at 8.4 GHz generated using data from Very Long Baseline Array (VLBA) and phased VLA (Stirling et al., 2001). The compact jet extends up to  $\sim 20$  AU. The beamsize is presented in the bottom left corner. The source has a peak flux density of  $9.0 \text{ mJy beam}^{-1}$ , whereas the lowest contour is at  $0.1 \text{ mJy}$ . The image is taken from Stirling et al. (2001). Right panel: A typical broad band spectrum for the compact jet resulting from the superposition of many overlapping self-absorbed synchrotron spectra (dashed line).  $a$  is the spectral index of the electron energy distribution.  $\nu_b$  is the transition/break frequency from optically-thick to optically-thin synchrotron regions.  $\nu_c$  represents the synchrotron cooling break.

et al. 2001), which is associated with a dominant non-thermal (hard power-law) component in the X-ray spectrum (Fender et al., 2004; Fender, 2010; Narayan & Yi, 1995; Remillard & McClintock, 2006). In high-resolution observations, compact jets appear as continuous threads with a bright core (Figure 1.4 left panel, Dhawan et al. 2000; Stirling et al. 2001).

In general, the persistent compact jets become increasingly more optically thin in the low-frequency band as the particles move away from the jet base. The compact jets are believed to be moderately relativistic, and have bulk Lorentz factors of  $\leq 2$  (Fender et al., 2004). Note that some recent work has suggested that the Lorentz factors may be significantly higher ( $> 5$ ; e.g., Casella et al., 2010; Tetarenko et al., 2019, 2021). Owing to their compact nature, only in

GRS 1915+105 (Dhawan et al., 2000), MAXI J1836–194 (Russell et al., 2015), and Cygnus X–1 (Stirling et al. 2001, see Figure 1.4 left panel, and Miller-Jones et al. 2021), and MAXI J1820+070 (Tetarenko et al., 2021) have these jets been spatially resolved, showing typical sizes of the order of a few tens of AU (astronomical units). The electron populations present at different distances (along the axis of the jet) from the compact object produce self-absorbed synchrotron spectra with peaks shifting to lower frequencies on moving downstream, which can give rise to flat spectra (Figure 1.4 right panel). At a particular frequency ( $\nu_b$ ), the synchrotron jet spectrum changes from optically thick to optically thin, above which the jet is no-longer self-absorbed. The frequency corresponding to the point of transition/break ( $\nu_b$ ) is related to the most compact region of the jet where the particles are first accelerated and start to follow a power-law distribution (Markoff et al., 2001, 2005). It is thought that diffusive shock acceleration is responsible for the particle acceleration (e.g. Bell, 1978; Drury, 1983). In general, the break frequency is observed in the GHz band for AGNs (Ho, 1999), and in the IR regime for LMXBs (e.g. Corbel & Fender, 2002; Gandhi et al., 2011; Russell et al., 2013). The physical distance from the compact object and the compact object mass determines the break frequency ( $\nu_b$ ), which lies in the range 10–1000  $R_g$  (where  $R_g = GM/c^2$  is the gravitational radius) for the brighter hard states (e.g. Markoff et al., 2001, 2003, 2005; Migliari et al., 2007; Gallo et al., 2007; Markoff et al., 2008; Maitra et al., 2009).

It has also been observed that the break frequency can vary between BH-LMXBs (Russell et al., 2013) and can also change with time (Gandhi et al., 2011). According to the standard jet model for all steady jets from LMXBs and AGNs, a positive correlation can be observed between the source luminosity and the break frequency provided that the break is connected with the same physical distance (i.e. normalised to  $R_g$ ) of the jet at all times (Falcke & Biermann, 1995; Markoff et al., 2003; Heinz & Sunyaev, 2003; Falcke et al., 2004). Assuming that a fixed amount of the accretion power is channelled into the outflows (Falcke &

Biermann, 1995),  $\nu_b$  can be related to the mass accretion rate ( $\dot{m}$ ) as  $\nu_b \propto \dot{m}^{2/3}$ . If the source is in a radiatively inefficient hard state (Heinz & Sunyaev, 2003), then the X-ray luminosity of the source ( $L_X$ ) scales with  $\dot{m}$  as  $L_X \propto \dot{m}^2$ . Therefore,  $\nu_b \propto L_X^{1/3}$  (Russell et al., 2013).

At frequencies higher than  $\nu_b$ , we can further observe a turnover or break ( $\nu_c$ ) in the jet spectrum (Figure 1.4 right panel). This break is due to the high-energy electrons, which are losing a substantial portion of their energy through radiation because timescales of the emission being much shorter than the dynamical timescale of the source (Sari et al., 1998). This break has only been observed once by Russell et al. (2014).

In addition to observational studies, there have been many theoretical efforts to understand the physics of the compact radio jets in BH-XRBs. The theorists have proposed two basic models; the single acceleration model and the internal shock model. Pe'er & Casella (2009) studied the origin of flat-spectrum compact radio jets arising from a single acceleration event. The authors considered a Maxwellian distribution of particles and above the peak of the Maxwellian distribution the particles have a power-law distribution. According to the model, electrons gained kinetic energy only once at the base of the jet. When these accelerated particles propagate, they lose their energy through synchrotron emission and adiabatic expansion. A flat radio spectrum is observed due to losses in the particle energy and decay of the magnetic field strength along the axis of the jet. The authors predict turnovers at both low and high frequencies. The low-frequency turnover is due to a change in the plasma density from optically thick to optically thin, whereas the high-frequency turnover corresponds to emission from particles at the peak of the Maxwellian distribution. Pe'er & Casella (2009) also explored the possibility of a non-conical jet giving rise to a flat spectrum.

On the other hand, Jamil et al. (2010) proposed an internal shock model to understand the physics behind the compact jets where the collisions between the continuously emitted ejecta (shells) generate internal shocks necessary to

replenish the losses due to synchrotron emission and adiabatic cooling. The authors considered power-law distributed electrons in a conical jet and also predict turnovers at low and high frequencies. They suggest that the low-frequency turnover (at  $\sim 1$  GHz) is connected to the extent of the jet in space while the high-frequency turnover (at  $\sim 1$  THz) is correlated with the jet power ( $\nu \propto L^{\sim 0.6}$ ). The authors predict that the low-frequency turnover depends on the number of shells and the distance downstream where these shells collide. Later, Malzac (2014) extended this model by considering a more physical scenario of a variable Lorentz factor. This model suggests that the Lorentz factor fluctuations are driven by the accretion flow fluctuations, such that the power spectrum of the X-ray variations provide the power spectrum of the Lorentz factor fluctuations (Malzac, 2014). The internal shocks are the outcome of fluctuations in the velocity of the outflow and the spectral energy distribution is connected to the dynamics of the internal shocks (Jamil et al., 2010; Malzac, 2014). Malzac (2014) also mentioned that a flat spectrum is observed when the power spectral density of the Lorentz factor fluctuations changes as  $1/f$  (where  $f$  is the frequency of fluctuation). All the theoretical models postulate a low-frequency turnover/break/cutoff in the compact jet spectrum.

### 1.5.2 Transient jets

When the mass accretion rate increases, the inner edge of the accretion disc is thought to move in towards the compact object causing the X-ray luminosity to increase to  $\gtrsim 10^{37}$  erg  $s^{-1}$  (Remillard & McClintock, 2006). We observe transient jets during the intermediate X-ray spectral states near the peak of the outburst. This occurs when a BH-XRB is transitioning from the hard to the soft X-ray spectral state (Figure 1.3, Fender et al. 2004) as the X-ray spectrum becomes progressively more dominated by the thermal emission from the accretion disc (Remillard & McClintock, 2006). The transient jets are bright, relativistically-moving, discrete (Figure 1.5 left panel), expanding ejecta (e.g., Mirabel & Rodríguez, 1994;

Hjellming & Rupen, 1995; Tingay et al., 1995; Miller-Jones et al., 2012), which are likely ejected on both sides of the compact object (relative to the accretion disc). The jets often appear one-sided, likely owing to Doppler boosting, although the possibility of intrinsic asymmetry has been raised (e.g., Fendt & Sheikholeslami, 2013).

These transient ejecta are optically thin (above a certain frequency, Figure 1.5 right panel), having a steep radio spectrum ( $-1 \leq \alpha \leq -0.2$ ). A turnover in the radio spectrum (Figure 1.5 right panel) is sometimes observed (e.g., Miller-Jones et al., 2004; Chandra & Kanekar, 2017), which moves to lower frequencies as the emission region expands (van der Laan, 1966a). Such a spectral turnover could either be caused by synchrotron self-absorption (SSA), the Tsytovich-Razin (T-R) effect, a low-energy cutoff in the electron energy distribution, or through free-free absorption (FFA) by thermal plasma (see Gregory & Seaquist, 1974; Miller-Jones et al., 2004, and references therein). SSA is thought to be the most plausible explanation as it implies the physical parameters of the jet (i.e. magnetic field strength and the radius of the emitting region) set the low-frequency turnover in XRBs. All the above mentioned models are explained in detail in Chapter 5.

van der Laan (1966b) proposed a model to explain the evolution of the synchrotron-emitting plasma with time. According to the author, the plasma cloud expands gradually in time and loses energy adiabatically. The energy loss rate due to adiabatic expansion of a plasma cloud filled with relativistic particles is defined as

$$\dot{E} = -\frac{1}{3} (\nabla \cdot v) E, \quad (1.6)$$

where  $E$  is the energy of the particle, and  $v$  is the particle velocity. If we consider the radius of the plasma blob is  $R$ , which is expanding uniformly, then the distribution of the radial velocity inside the sphere is given by

$$v = \dot{R} \left( \frac{r}{R} \right), \quad (1.7)$$

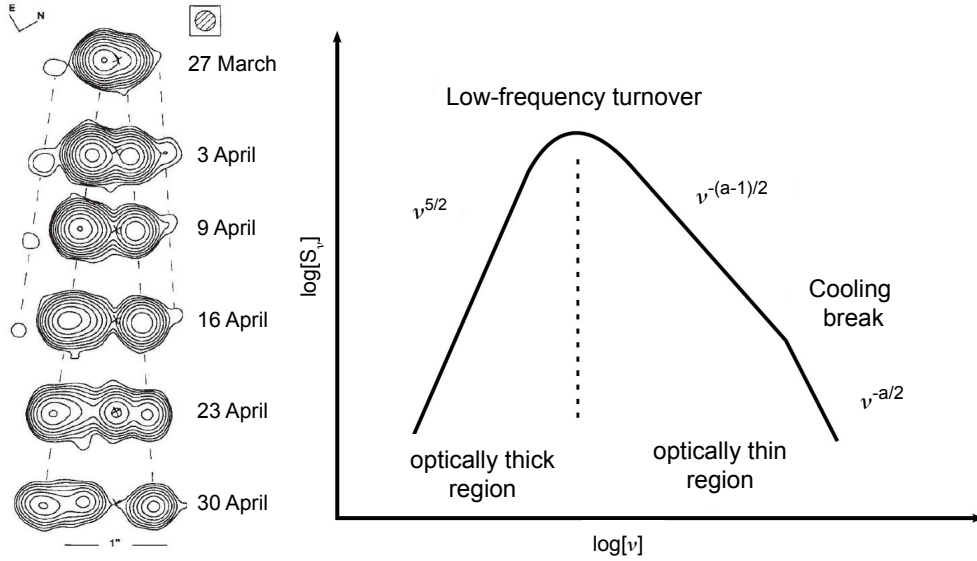


Figure 1.5: Left panel: VLA Image of GRS 1915+105 at 8.4 GHz showing the evolution of discrete ejecta from 27 March to 30 April 1994, which are moving away from the core at apparently superluminal velocities. The beamsize is shown in the top right corner, and the contours are  $1, 2^n$  (where  $n$  ranges from 1 to 10) times  $0.2 \text{ mJy beam}^{-1}$  for all the observations presented in the figure, except for the 27 March epoch, where the contour flux density levels are multiples of  $0.6 \text{ mJy beam}^{-1}$  (Figure from Mirabel & Rodríguez 1994). Right panel: A typical broad band spectrum for the transient jet showing a low-frequency turnover and synchrotron cooling break. The low-frequency turnover is likely to be due to synchrotron self-absorption. The figure is adapted from Rybicki & Lightman (1979) and Longair (2011).

so that

$$\dot{E} = - \left( \frac{\dot{R}}{R} \right) E. \quad (1.8)$$

The above equation highlights that the rate of energy loss is proportional to the particle energy ( $E$ ). Therefore, the expansion is self-similar, maintaining the same spectral shape as it evolves (e.g. van der Laan, 1966b).

There are various studies (e.g. Miller-Jones et al., 2004; Broderick et al., 2018b), which highlight that the canonical jet geometry model proposed by van der Laan (1966b) has limitations in explaining the sharp rise in the radio flux density of the source as the model predicts only a gradual increase in the radius of the plasma cloud. As a result, other models were proposed to explain this ob-

served phenomenon by considering the variable nature of the jet expansion. For example, Hjellming & Johnston (1988) proposed that during the transient event, twin relativistic spherical clouds of plasma evolve and expand with the sound velocity. The authors also explained the geometry of the ejection and suggest that for a system like SS 433 (where the environment is very dense from the donor star’s wind), initially the jet expansion is slowed due to the dense environment but later the jets can begin to freely expand when they have escaped the dense environment. In another approach, Marti et al. (1992) presented a twin jet model with particle injection. The model considers synchrotron radiation from twin jets expanding adiabatically in the lateral direction, with particle injection causing the rapid increase in the flux density. The authors also assumed that initially the radius of the plasma cloud increases exponentially in the lateral direction, and later the expansion becomes constant. These models were mainly proposed to explain the results from a few specific systems such as Cygnus X–3 and SS 433. Therefore, to study the behaviour of transient jets in BH-LMXBs at low-radio-frequencies, we need to observe these jets with high cadence, and finally perform rigorous testing of aforementioned models with the broadband observations.

## 1.6 H I absorption in X-ray binaries

The radio jets from black hole low-mass X-ray binaries may also provide us with an opportunity to study the distribution of neutral hydrogen along the line-of-sight, which is abundantly distributed in our Milky Way Galaxy. In general, the radio jets give rise to broadband continuum emission. The H I clouds between us and the jets absorb that emission at their rest frequency. Since the H I clouds are moving with different velocities with respect to us, that imprints absorption at a range of velocities on the background continuum emission from the XRB. These absorption spectral lines can be used to determine the kinematic distance to the source (e.g., Chapter 3, Chapter 4, Goss & Mebold, 1977; Dickey, 1983; Dhawan et al., 2000). Given that the jets from BH-LMXBs move at velocities close to

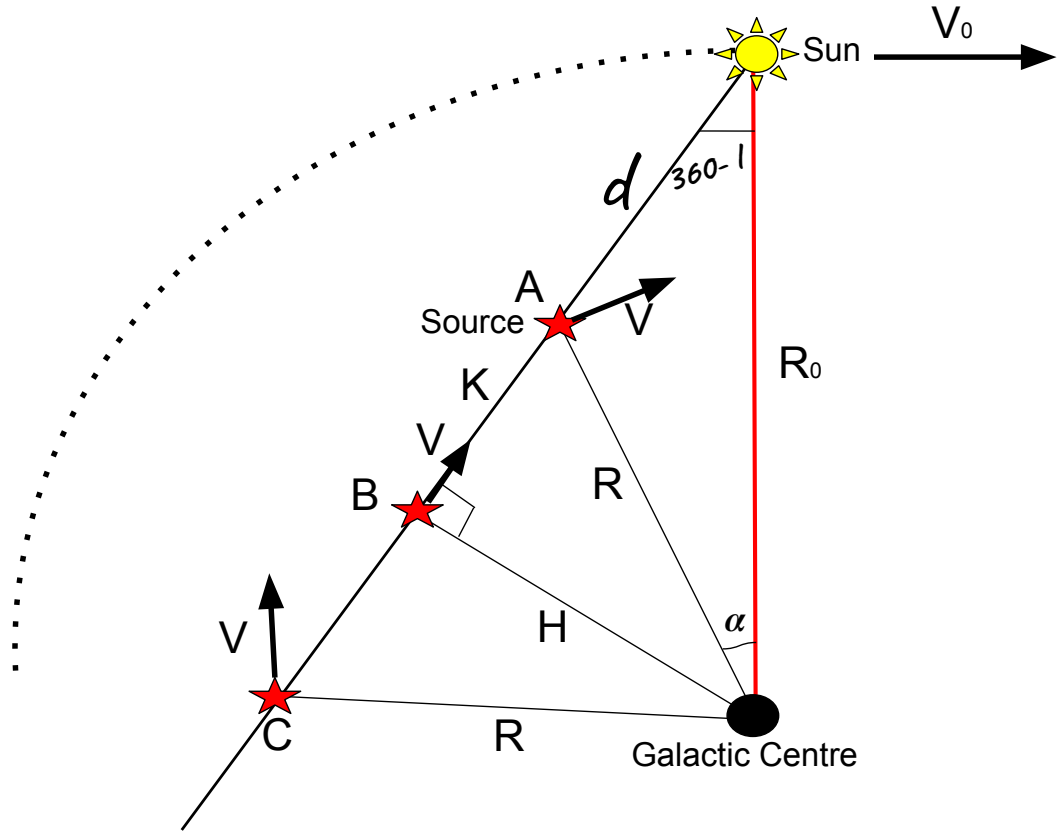


Figure 1.6: A plot showing a schematic of a sources motion in our Milky Way Galaxy, according to its location along the line of sight. The diagram also shows the parameters used in the derivation of the kinematic distance to the source, described in Section 1.6.1. The Sun is located at a distance  $R_0 = 8.34 \pm 0.16$  kpc from the Galactic centre (Reid et al., 2014). The source of interest is shown as a red star, and the near and far distances are indicated with  $A$  and  $C$ , respectively. Point  $B$  marks the position of the tangent point, and  $d$  is the distance between the source and the Sun. The distance between the source and the Galactic centre is  $R$ , which is the same for both the near and far kinematic distances. Additionally, the radial velocity is also the same for both the near and far distances.

the speed of light, the line of sight towards the jets also changes slightly each time we observe the event (around daily). We can therefore expect variation in the HI absorption lines, which allows us to probe small-scale fluctuations in the interstellar neutral hydrogen (e.g. Dhawan et al., 2000).

### 1.6.1 Kinematic distance to X-ray binaries

The distance to an astrophysical object is a key physical parameter as it provides us with a way to determine physical quantities from observables, such as luminosity from flux density, physical separation from angular separation, and velocity from proper motion. However, the BH-XRBs distances are often poorly constrained and suffer large uncertainties that can in some cases exceed 50% (Jonker & Nelemans, 2004).

For BH-XRBs in our Galaxy, parallax is the most fundamental and model-independent method for estimating stellar distances. The main caveat of this method is that for typical XRB distances, the measured parallax is extremely small (1 milliarcsec for 1 kpc). Therefore, instruments capable of probing sub-milliarcsecond scales are required. Such studies are possible only with very long baseline interferometry (VLBI) or with dedicated missions such as *Gaia* (Gaia Collaboration et al., 2018), and only for a handful of XRBs (e.g. Miller-Jones et al., 2009; Reid et al., 2011; Gandhi et al., 2019; Atri et al., 2020).

High-precision trigonometric parallax measurements are not possible for most black hole XRBs. In such cases, the distance is commonly estimated by comparing the inferred absolute magnitude of the donor star (as determined from its spectral type) with the apparent magnitude, after considering the maximum contribution from the accretion disk (Jonker & Nelemans, 2004). The main limitations of this technique are the uncertainties associated with the disk contribution and the extinction along the line of sight. Distances can also be constrained by using the proper motions of the jet ejecta (Mirabel & Rodríguez, 1994) or by studying the interstellar extinction (Zdziarski et al., 1998).

If the companion star is too faint (e.g. if the system is highly extinguished) and other approaches are not available then other technique must be used, one of which uses the Doppler shifted 21-cm absorption line of neutral hydrogen (HI; e.g., Chapter 3, Chapter 4, Goss & Mebold 1977; Dickey 1983; Dhawan et al. 2000). Intervening interstellar HI clouds are presumed to follow the rotation of

the Milky Way and their absorption features allow us to constrain the kinematic distance to the source (Gathier et al., 1986; Kuchar & Bania, 1990). If the source is beyond the solar orbit, this method provides an accurate kinematic distance estimation. However, the method suffers from ambiguities if the source lies within the solar orbit (Wenger et al., 2018).

If we consider that the matter in our Milky Way Galaxy is rotating around the Galactic centre in purely circular orbits, then the resultant radial velocity ( $V_r^T$ ) for an object (in the fourth quadrant) with Galactic coordinates  $l$  (longitude) and  $b$  (latitude) is defined as

$$V_r^T = V_0 \sin(l - \alpha) - V_0 \sin l, \quad (1.9)$$

where  $V_0$  is the rotational velocity of our Milky Way Galaxy ( $= 240 \pm 8 \text{ km s}^{-1}$ ; Reid et al. 2014), and  $\alpha$  is the angle formed between the lines connecting the Galactic centre and the source, and the Galactic centre and the Sun (see Figure 1.6). All the objects (outside the  $\sim 1 \text{ kpc}$  region of the Galactic Centre) in our Milky Way Galaxy are assumed to be rotating with the velocity  $V_0$  in their own rest frame.

From Figure 1.6, we can see that

$$\sin(l - \alpha) = -\frac{H}{R}. \quad (1.10)$$

The distance of the source (point A in Figure 1.6) from the tangent point (point B in Figure 1.6) is given as

$$K = R \cos(l - \alpha). \quad (1.11)$$

The distance of the tangent point (point B in Figure 1.6) from the Galactic point is defined as

$$H = -R_0 \sin l. \quad (1.12)$$

And the distance of the tangent point (point B in Figure 1.6) from the Sun is given as

$$d + K = R_0 \cos l. \quad (1.13)$$

From equation 1.10 and 1.12, we get

$$\sin(l - \alpha) = \frac{R_0}{R} \sin l. \quad (1.14)$$

Now using equation 1.14 in equation 1.9, we find

$$V_r^T = -V_0 \sin l + V_0 \frac{R_0}{R} \sin l, \quad (1.15)$$

$$V_r^T = V_0 \sin l \left( -1 + \frac{R_0}{R} \right). \quad (1.16)$$

After using Pythagora's theorem in Figure 1.6 we get

$$R^2 = K^2 + H^2. \quad (1.17)$$

Using equation 1.12 and 1.13 in equation 1.17

$$R^2 = (R_0 \cos l - d)^2 + (R_0 \sin l)^2, \quad (1.18)$$

$$R = \sqrt{R_0^2 + d^2 - 2 R_0 d \cos l}. \quad (1.19)$$

Substituting the value of  $R$  from equation 1.19 into equation 1.16, the value of  $V_r^T$  is found to be

$$V_r^T = V_0 \sin l \left( -1 + \frac{R_0}{\sqrt{R_0^2 + d^2 - 2 R_0 d \cos l}} \right). \quad (1.20)$$

After rearranging the terms, we get

$$\frac{R_0}{\sqrt{R_0^2 + d^2 - 2 R_0 d \cos l}} = \left( \frac{V_r^T}{V_0 \sin l} + 1 \right), \quad (1.21)$$

$$R_0^2 + d^2 - 2 R_0 d \cos l = \frac{R_0^2}{\left(\frac{V_r^T}{V_0 \sin l} + 1\right)^2}. \quad (1.22)$$

Finally, the distance to the source can be expressed as

$$d^2 - 2 R_0 d \cos l + R_0^2 \left(1 - \frac{1}{\left(\frac{V_r^T}{V_0 \sin l} + 1\right)^2}\right) = 0. \quad (1.23)$$

equation 1.23 is a quadratic equation in  $d$ , which is the distance to the source along the line of sight. On comparing the equation 1.23 with a standard quadratic equation of the form  $a d^2 + b d + c = 0$ , we define

$$a = 1; b = -2 R_0 \cos l; c = R_0^2 \left(1 - \frac{1}{\left(\frac{V_r^T}{V_0 \sin l} + 1\right)^2}\right), \quad (1.24)$$

$$d = \frac{-b \pm \sqrt{b^2 - 4ac}}{2a}. \quad (1.25)$$

On solving the quadratic equation 1.23, we get two solutions for the distance (near and far, see Fig 1.7) for a single velocity measurement ( $V_r^T$ ), which are equidistant from the tangent point. The radial velocity attains its maximum value at the tangent point (see Fig 1.7), which is fixed for a given Galactic longitude ( $l$ ). Once an object is at or beyond the tangent point, velocities of its absorption spectrum are independent of its distance until  $R > R_0$ . Therefore, caution should be taken because the use of H I absorption to derive a distance to an X-ray binary system is useful only for objects closer than the tangent point. Once absorption is observed at the tangent point velocity, then unless we see absorption at positive velocities (corresponding to the object lying outside the solar circle at  $R > R_0$ ), then the only distance constraint that we can place would be that the object lies beyond the tangent point.

Previously, this approach was used to constrain the distance of two black hole XRBs; GRS 1915+105 (Dhawan et al., 2000) and SS 433 (Lockman et al.,

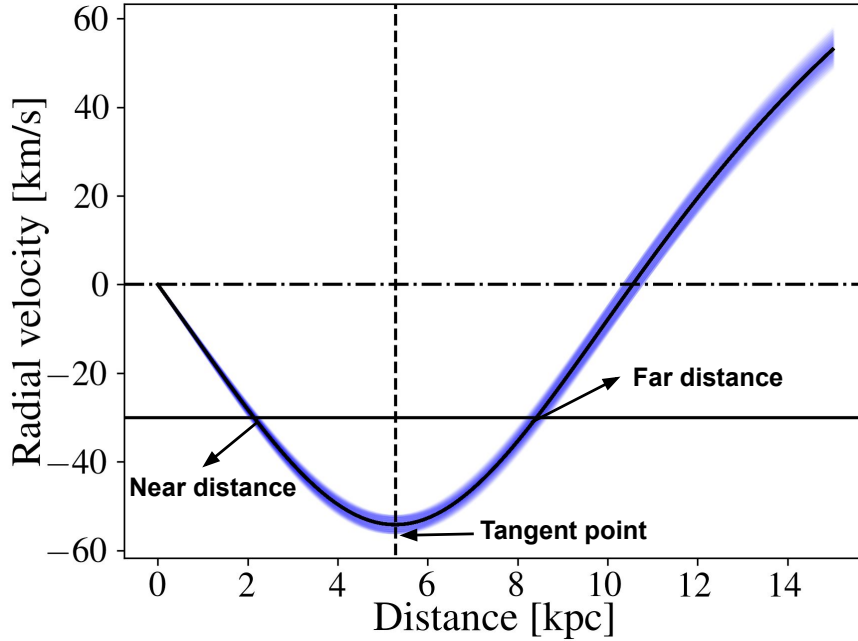


Figure 1.7: A plot showing the predicted variation of the radial velocity (for circular rotation) of the local standard of rest ( $V_{LSR}$ ) with the line of sight distance from the Sun ( $d$ ), in the direction of a Galactic source with the Galactic coordinates  $l = 309.26407$  deg,  $b = -1.10297$  deg. The horizontal line at  $-30 \text{ km s}^{-1}$  highlights the assumed radial velocity of the source. The near, far and the tangent point distances (dashed vertical line) are indicated in the figure. The blue color around the main curve illustrates the uncertainties on  $V_0$  and  $R_0$ . Beyond  $d = 10.5 \text{ kpc}$ , where  $R > R_0$ ,  $V_{LSR}$  becomes positive.

2007). The uncertainties reported on the XRBs distances are of the order of  $\sim 50\%$  (Jonker & Nelemans, 2004), which is considerably higher than the mean difference (21%) between the distances calculated using the parallax method and the Doppler shifted H I absorption line technique (Wenger et al., 2018). Therefore, the kinematic distance estimates obtained from the aforementioned method are fairly accurate (at least for circular rotation) when the source is located beyond the Solar orbit. They suffer ambiguities if the source is located within the Solar circle (e.g. Reid et al., 2014; Wenger et al., 2018).

## 1.7 Background studies of low-frequency radio jets in X-ray binaries

Our description of compact and transient jets in Sections 1.5.1 and 1.5.2 demonstrate that low-frequency observations are important for understanding their physics. For the compact jets, the prevailing theoretical models (e.g., Pe’er & Casella, 2009; Jamil et al., 2010; Malzac, 2014, described in detail in Section 1.5.1) explained the observed flat spectrum in different ways. Both models predict a turnover in the high-frequency regime [ $> 1$  THz, this break moves to lower frequencies as the spectrum softens (e.g., Russell et al., 2013)]. However, model given by Jamil et al. (2010) and Malzac (2014) also predicts a low-frequency ( $< 1$  GHz) turnover. The detection of a low-frequency turnover (at  $< 1$  GHz) in the compact jets would help in determining the extent of the compact jet in the space away from the black hole (explained in Section 1.5.1). The low-frequency turnover and the slope of the spectrum below the turnover could also put observational constraints on several key properties including the electron energy distribution (power-law or Maxwellian or both), the magnetic field strength (constant or variable), and the energy losses (radiative or adiabatic or both) predicted by various theoretical models.

The lateral expansion of the transient jet dictates the temporal variation of the flux density. High-cadence low-frequency radio monitoring together with simultaneous high-frequency observations helps in studying the evolution of the low-frequency turnover (discussed in Section 1.5.2). The variation of the turnover frequency with time is crucial to understand the corresponding variation in the magnetic field strength and the minimum energy of the transient jet, which ultimately provide information on energy imparted by the transient jet to the ambient surroundings.

As early as the 1970s, radio studies of XRB jets were conducted but mainly at high frequencies ( $\geq 1$  GHz). Only a few studies were performed in the low-

frequency regime ( $\leq 1$  GHz). For example, in 1972, the HMXB Cygnus X-3 underwent an extraordinary bright radio flare that was extensively monitored at high frequencies (Branson et al., 1972; Hjellming & Balick, 1972) but observed just twice at low frequencies (365 and 408 MHz: Anderson et al., 1972; Bash & Ghigo, 1973). In 2001, the same source experienced another major outburst. Miller-Jones et al. (2004) monitored it at both low (73.8 & 327.5 MHz) and high ( $>1$  GHz) frequencies. With the help of low-frequency observations, Miller-Jones et al. (2004) clearly observed a synchrotron self-absorption (SSA) turnover, which helped in calculating the magnetic field strength of the radio jets.

During June 2015, the LMXB V404 Cygni underwent a powerful outburst following 26 years of quiescence. The source was monitored in all bands of the electromagnetic spectrum, involving a large fraction of the X-ray binary community. The Low Frequency Array (LOFAR) detected V404 Cygni at 150 MHz with a flux density of  $\sim 30$  mJy ( $8\sigma$ ; Broderick et al., 2015). The GMRT also monitored the source at four different frequencies; 235, 325, 610 and 1280 MHz (Chandra & Kanekar, 2017). During the outburst phase, the source was bright at low frequencies ( $470 \pm 49$  and  $188 \pm 27$  mJy at 610 and 235 MHz, respectively) and displayed a rapid decay in the radio flux density. The radio intensity dropped by factors of  $\approx 15$  and  $\approx 50$  at 235 and 610 MHz, respectively, in four days. Using high frequency ( $>1$  GHz) data from other instruments, including the Radio Astronomical Telescope Academy Nauk 600 (RATAN-600) and the Northern Extended Millimeter Array (NOEMA), Chandra & Kanekar (2017) observed a SSA turnover at  $\approx 1.5$  GHz. The authors used the turnover frequency and the corresponding flux density to constrain the jet's parameters, including the magnetic field strength, the minimum total energy, the transient jet power, and the jet radius (Chandra & Kanekar, 2017).

Recently, LOFAR observed SS 433, an XRB located in the supernova remnant (SNR) W 50, in the 115–189 MHz frequency range (Broderick et al., 2018b). The authors detected 0.5–1 Jy variability in the radio flux density at 150 MHz

in  $<200$  days, which is hard to explain via the expanding synchrotron bubble model given by van der Laan (1966b). While the model seems to explain the high-frequency observations of XRBs (Tetarenko et al., 2017), it has limitations in explaining the low-frequency results presented by Miller-Jones et al. (2004) and Broderick et al. (2018b). Therefore, high-cadence observations of the radio jets with SKA precursors covering a wide frequency range from MHz to GHz, will provide new observational data necessary to model the emission geometry. Finally, from the above studies, it is evident that low-frequency observations can improve our understanding of the jets in BH-LMXBs.

## 1.8 The SKA precursor telescopes

In the past, one of the biggest obstacles to low-frequency radio astronomy was the lack of sensitive instruments, especially at frequencies below 1 GHz. At the present time, many efforts are underway to understand the technological challenges in constructing the world’s most sensitive radio telescope, the Square Kilometre Array (SKA). The technology required for building the SKA has been tested in the form of SKA precursors. Currently, there are four SKA precursors: the Murchison Widefield Array (MWA), the Australian SKA Pathfinder (ASKAP), MeerKAT, and the Hydrogen Epoch of Reionization (HERA). Summarised below are those SKA precursors that I have used for my Ph.D. project. These precursors provide new capabilities that can be used to study the radio properties of XRBs.

### 1.8.1 The Murchison Widefield Array

The Murchison Widefield Array (MWA) is located at the Murchison Radio-astronomy Observatory (MRO) in Western Australia. The MWA operates in the frequency range 80-300 MHz, with a processing bandwidth of 30.72 MHz. It provides unprecedented survey efficiency due to its  $\sim 2752$  m<sup>2</sup> collecting area

and 610 deg<sup>2</sup> field of view at 150 MHz. The instrument also provides an angular resolution of  $\sim 3$  arcmin at 150 MHz with 3 km baselines in Phase I (Tingay et al., 2013).

Recently the telescope underwent a major upgrade, and in Phase II the telescope has two different configurations; the compact hex configuration and the extended configuration (Wayth et al., 2018). Both the configurations have 128 tiles, but in the hex configuration, most of the baselines are  $< 200$  m, whereas MWA has its longest baseline length of  $\sim 5.3$  km in the extended configuration. Therefore, in the extended configuration, the telescope has double the angular resolution when compared to Phase I. This upgrade also significantly improved the classical confusion noise, which decreased by a factor of 5-10 when compared to Phase I (1.7 mJy at 154 MHz). Hence, the sensitivity also increased by a factor of 4, due to the associated reduction in the confusion noise (Wayth et al., 2018).

### 1.8.2 The Australian Square Kilometre Array Pathfinder

The Australian Square Kilometre Array Pathfinder<sup>7</sup>(ASKAP) is a synthesis radio telescope also located at the MRO (Johnston et al., 2007; Hotan et al., 2014, 2021). The telescope operates over the frequency range of 0.7–1.8 GHz and has a processing bandwidth of 300 MHz. ASKAP provides a resolution of 10 arcsec with the wide field of view (FOV) of 30 deg<sup>2</sup> at 1.4 GHz, which is made possible by the phased array feed (PAF) receivers (Hampson et al., 2012). The telescope consists of thirty-six dishes of 12 m diameter each, resulting in a total collecting area of 4000 m<sup>2</sup>, with a maximum baseline of length 6 km. At 1.34 GHz, the telescope has a processed bandwidth of 300 MHz, which is further divided into 16384 fine channels, each of which has a frequency resolution of 18.519 kHz (Hotan et al., 2014, 2021). ASKAP also provides a continuum sensitivity of 37  $\mu$ Jy (300 MHz bandwidth and 1 hour observation) at 1.34 GHz (Hotan et al., 2021).

---

<sup>7</sup><http://www.atnf.csiro.au/projects/askap/index.html>

### 1.8.3 MeerKAT

MeerKAT<sup>8</sup> is currently the most sensitive and largest radio telescope in the southern hemisphere, located in the Karoo desert in South Africa (de Blok et al., 2010; Jonas & MeerKAT Team, 2016; Camilo et al., 2018). The telescope consists of 64 identical dishes, each with a diameter of 13.5 m, and has offset Gregorian feeds to provide an unblocked aperture. MeerKAT is currently operating in the frequency range of 0.9–1.67 GHz (L-band) with a processed bandwidth of 860 MHz (Camilo et al., 2018). Earlier, MeerKAT was functioning in a low-resolution mode with 4096 fine channels that each had a frequency resolution of 209 KHz (Camilo et al., 2018). Recently, MeerKAT underwent a correlator upgrade, which provides 32768 equivalent 26.123 kHz channels (Gupta et al., 2017, 2021). The MeerKAT array configuration has a dense core, with a maximum baseline length of 8 km, and a large FOV of 1.69 deg<sup>2</sup> and a resolution of  $\sim 5$  arcsec (Camilo et al., 2018; Carotenuto et al., 2021a). MeerKAT achieves a sensitivity of  $\sim 9 \mu\text{Jy beam}^{-1}$  (in 1 hour) at 1.01 GHz (Taylor & Jarvis, 2017).

## 1.9 Monitoring the BH-XRB jets with modern radio interferometers

The advent of modern telescopes such as the SKA precursors including MWA, ASKAP and MeerKAT, and other instruments in the low-frequency regime ( $< 1.5$  GHz) including the Low Frequency Array (LOFAR; van Haarlem et al., 2013), the VLA Low Band Ionospheric and Transient Experiment (VLITE; Clarke et al., 2016), the Long Wavelength Array (LWA; Ellingson et al., 2009), and the upgraded Giant Metre-wave Radio Telescope (uGMRT; Gupta et al., 2017; Reddy et al., 2017) have increased our ability (due to higher sensitivity and better UV coverage) to detect XRB outbursts at low radio frequencies.

These new and upgraded facilities, especially ASKAP and MeerKAT, oper-

---

<sup>8</sup><https://www.astron.nl/telescopes/square-kilometre-array/>

ating around 1.4 GHz provide new opportunities to study H I absorption in the direction of black hole XRBs, which can be used to constrain the kinematic distances of sources (Chapters 3 and 4). The importance of the distance to an astrophysical source has already been discussed in Section 1.6.1. Therefore, when other methods are not available to determine the distance to a BH-LMXB, the H I absorption technique has proven to be highly useful. Additionally, the wide field of view of modern telescopes such as ASKAP provides us with an opportunity to study comparison extragalactic sources in the same observation, which is essential to break the degeneracy of near and far distances (Chapters 3 and 4). Due to its low system temperature, MeerKAT can be used to study H I absorption in the direction of faint black hole XRBs.

Observations from modern low-frequency interferometers can further help us in constraining the spectra of BH-LMXB jets in the low-frequency regime, which can provide us an opportunity to detect a low-frequency turnover in the spectra of both compact and transient jets. In the case of transient jets, the turnover frequency along with the source size help in determining physical parameters such as the magnetic field strength and the minimum energy, which ultimately help us in understanding the energetics of the jets. The low-frequency turnover in the compact jet spectrum provides information on the downstream distance at which the jet dissipates energy via internal shocks.

The studies of various XRBs described in Section 1.7, highlight the importance of high-cadence, low-frequency radio observations of XRB jets. At present, Australia has a suite of complementary radio telescopes to study jets in XRBs over a broad radio spectral range (0.08–110 GHz). This suite comprises the Murchison Widefield Array (MWA; Tingay et al., 2013; Wayth et al., 2018), the upgraded Molonglo Observatory Synthesis Telescope (UTMOST; Bailes et al., 2017), the Australian Square Kilometre Array Pathfinder (ASKAP; Hotan et al., 2014, 2021), the Australia Telescope Compact Array (ATCA: Frater et al., 1992; Wilson et al., 2011), the Parkes Radio Telescope (e.g., Edwards, 2012; Hobbs

et al., 2020), and the Australian Long Baseline Array (LBA; Preston et al., 1989; Preston & SHEVE Team, 1993; Jauncey et al., 1994). The combined capabilities of these telescopes have never before been simultaneously deployed to study radio jets in BH-XRBs.

Until now, there have been few studies of compact jets in the low-frequency band. Recently, the hard state observations of MAXI J1820+070 by VLITE (with a radio flux density of  $33.0 \pm 5.3$  mJy at 339 MHz; Polisensky et al. 2018) and LOFAR (with radio flux density of  $42 \pm 5$  mJy at 146 MHz; Broderick et al. 2018a), provide the best (one-off) low-frequency measurements of the compact jets. These results highlight the capabilities of modern radio interferometers in detecting radio jets in BH-XRBs. In this PhD research, I have used a variety of SKA precursors (MWA, ASKAP and MeerKAT), and other Australian telescopes to study radio jets in XRBs.

## 1.10 Structure of this thesis

This thesis presents a study of radio jets from Galactic BH-LMXBs in the low-frequency regime using the SKA precursor telescopes, including MWA, ASKAP and MeerKAT. We targeted three BH-LMXBs: MAXI J1535–571, MAXI J1820+070 and MAXI J1348–630. We measured the kinematic distances to MAXI J1535–571 and MAXI J1348–630. We detected the transient jets in MAXI J1535–571 and MAXI J1348–630, and presented the broadband spectral modelling of the transient jet in MAXI J1535–571. We detected the compact jets in MAXI J1820+070 and MAXI J1348–630. In fact this latter case represents the first detection of compact jets at frequencies  $< 300$  MHz in BH-LMXBs with MWA.

Chapter 2 provides a brief overview of the theory of interferometry, observing strategy, calibration and data reduction. I have also discussed issues specific to the MWA and ASKAP. In the same chapter, I also described the intricacies of the data and the reduction strategies that are specific to MWA and ASKAP. In Chapters 3 and 4, I present kinematic distance constraints to the black hole candidates

LMXBs MAXI J1535–571 and MAXI J1348–630, along with the implications of the estimated distance constraints. Chapter 5 discusses a broadband study of the transient radio jets in MAXI J1535–571 using the Australian suite of complementary radio telescopes. I also present the modelling of the broadband radio spectrum and place constraints on the jet physical parameters, including the jet opening angle, the magnetic field strength, and the equipartition energy. Chapter 6 presents the first-time MWA detection of the compact jets in BH-LMXBs in the low-frequency regime ( $< 300$  MHz). I also discuss modelling of the broadband compact jet spectrum, along with the implications of the low-frequency detection. My discussion and conclusions of the obtained results are presented in Chapter 7. I also discuss my future work plans in the same chapter.

# Chapter 2

## Research methodology

Radio telescopes are fundamentally different to optical or X-ray telescopes, in that they utilise the wave nature of the incoming radiation. The radio telescopes collect and record information about the amplitude and phase of the radio wave to characterise the visibility properties. A visibility is sensitive to all regions of the sky to which the telescope responds, due to the Fourier transform nature of the relationship between sky brightness and visibility. Because of their long wavelengths, radio waves can propagate through dense regions of the universe, which are obscured by gas and dust. Additionally, the 5-15 GHz radio band is not heavily influenced by Earth's atmosphere. Therefore, radio waves provide us with an opportunity to explore that part of the universe, which is not accessible to optical and X-ray wavelengths.

The resolving power of a single radio telescope is given as  $\approx 1.22 \lambda/D$ , where  $\lambda$  is the observing wavelength and  $D$  is the aperture diameter. The capability of a single dish radio telescope to resolve sources in crowded regions of the universe is significantly restricted by the mechanical structure we can construct to hold a single-dish telescope. Note that the Five-hundred-meter Aperture Spherical radio Telescope (FAST) is the biggest single aperture telescope in the world at present, with a diameter of 500 m, and a resolution of  $2.9'$  in the L-band (Nan et al., 2011). The necessity to achieve high angular resolution led to the evolution of radio

interferometry, where signals from multiple single radio telescopes distributed over large distances are combined to get an extremely high angular resolution (even up to microarcsec; and now resolution is  $\approx 1.22 \lambda/B_{\max}$ , where  $B_{\max}$  is the maximum distance between two antennas). This methodology enables us to synthesise a radio telescope like the Event Horizon Telescope (EHT), which virtually transform Earth in to a radio telescope, and provide an angular resolution sufficient to resolve the event horizon of a supermassive black hole (Event Horizon Telescope Collaboration et al., 2019a,b,c,d,e,f). In this chapter, I have given a brief overview of the fundamentals of radio interferometry. Then, I discussed our observing strategy. Finally, I explained the data reduction procedure for the SKA precursor radio telescopes; MWA and ASKAP, which are the main telescopes used in this PhD research.

## 2.1 Radio Interferometry basics

Modern radio interferometers consist of several single radio telescope elements distributed over few kilometers to thousands of kilometres. The advancement of high-performance computing facilities has appreciably increased our ability to process signals from a substantially large number of single elements, which increased the total collecting area and therefore sensitivity by a considerable amount. Additionally, the baseline (the distance between two single elements) of the order of thousands of kilometres provides an angular resolution of the order of  $\mu\text{arcsec}$  at hundreds of GHz frequencies. Therefore, 21st-century radio interferometers have high sensitivity, along with considerably high-resolution in comparison to single-dish telescopes (Baars et al., 2009).

Irrespective of the location, design and main science goals, the fundamental theory behind all the interferometers remains the same. In this Section, I have briefly discussed the principles of radio interferometry and aperture synthesis, along with the data reduction procedures. The detailed theory for these techniques can be found in Clark (1999) and Thompson et al. (2001).

In the case of radio interferometry, we combine the electromagnetic radiation collected by two or more radio antennas separated by some distance, and compute the spatial coherence function of the incident electric field. Under some specific assumptions, this could be interpreted as a Fourier transform of the sky brightness, which is modified by atmospheric and instrumental effects. If the spatial coherence function is well sampled, we can invert it to calculate the distribution of the sky brightness, and therefore generate an image of the observed sky.

If there are  $N_e$  single antenna elements in a radio interferometer, then the number of independent pairs or baselines is given by  $N_e(N_e - 1)/2$ .

We assume  $E_\nu(r)$  is the quasi-monochromatic component of a time-varying electric field ( $E_\nu(r, t)$ ) created on a random pair of antennas by the astrophysical source of interest, which is different for different pair of antennas. Following the prescription given in Clark (1999), at frequency  $\nu$  the time-averaged cross-correlation ( $V_\nu$ ) of the two electric fields, or visibilities, by antennas located at  $r_a$  and  $r_b$  (see Figure 2.1) is defined as

$$V_\nu(r_a, r_b) = \langle E_\nu(r_a) E_\nu^*(r_b) \rangle, \quad (2.1)$$

where  $E_\nu^*$  is the complex conjugate of  $E_\nu$ , and time averaging is indicated by  $\langle \rangle$ .

There are various fundamental assumptions in radio interferometry to simplify Equation 2.1. As the astrophysical sources are located at considerably large distances, we can only obtain the information on the structure of a source in two dimensions, with no details about its depth. Moreover, we also presume there is no contaminating additional source between us (observer) and the celestial sphere, and the intervening space is empty. Under these assumptions, the visibility function takes the form

$$V_\nu(r_a, r_b) \approx \int \mathcal{I}_\nu(s) e^{-2\pi i \nu s \cdot (r_a - r_b)/c} d\Omega, \quad (2.2)$$

where  $\mathcal{I}_\nu(s)$  is the observed intensity or surface brightness of a small area on the

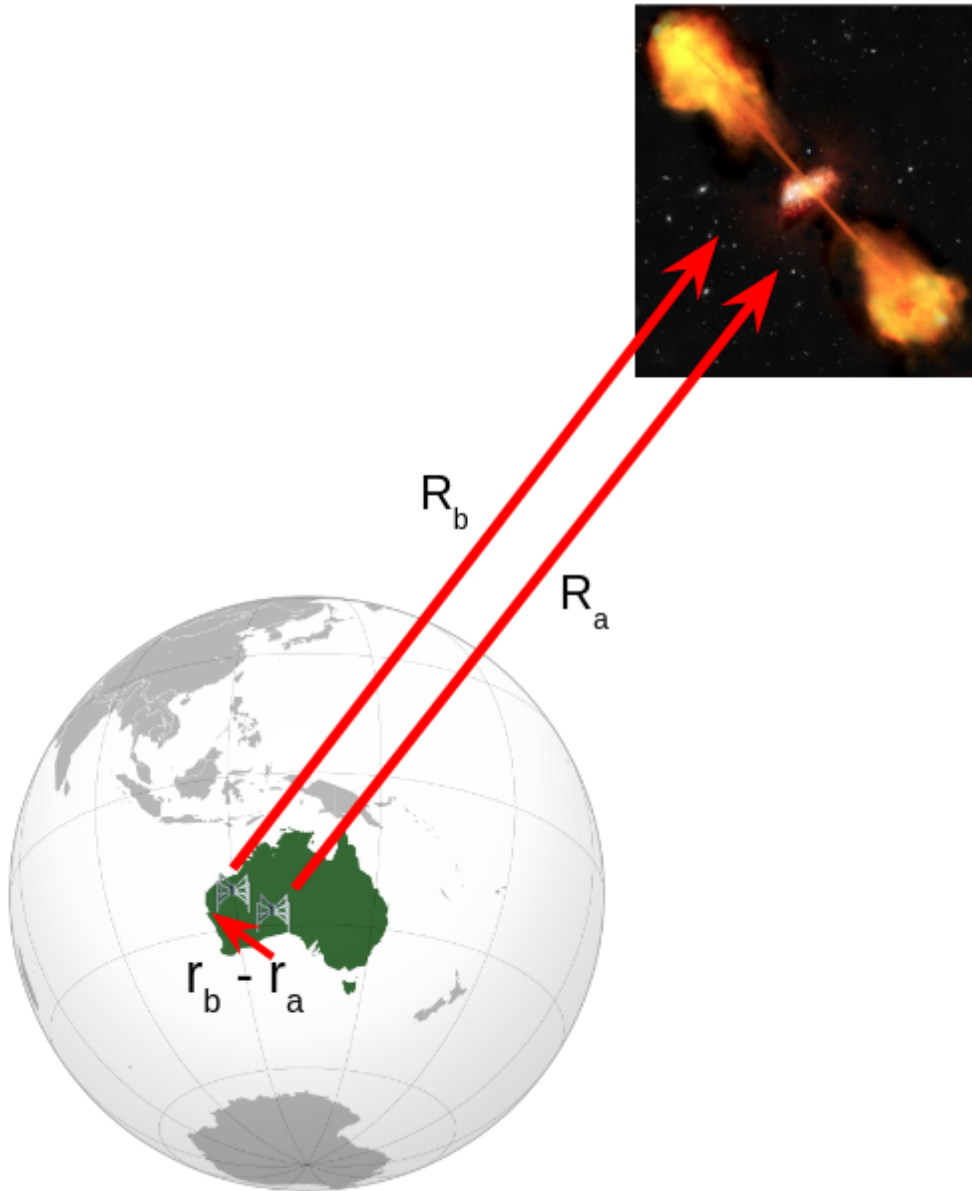


Figure 2.1: Diagrammatic representation of the geometry associated with radio astronomy. With reference to the interferometer, the astrophysical source is located at  $R$ . If we are looking at a source outside the solar system,  $R$  is many orders of magnitude greater than the distance between two antenna elements (baseline). This figure is adapted from ESA/C. Carreau/ATG medialab and [web.haystack.edu](http://web.haystack.edu).

celestial sphere (Fig 2.2) with solid angle element  $d\Omega$ , which is defined as

$$d\Omega \equiv \frac{dl dm}{n} = \frac{dl dm}{\sqrt{1 - l^2 - m^2}}, \quad (2.3)$$

Equation 2.2 represents the visibility in terms of baseline length (antenna separation  $(r_a - r_b)$ ), and provides the spatial coherence function, which is also known as the van Cittert-Zernike Theorem (van Cittert, 1934; Zernike, 1938). Using Equation 2.2 we can retrieve the surface brightness of the sky  $\mathcal{I}_\nu$ .

### 2.1.1 The measurement equation

The astronomical object (highlighted with a star symbol in Figure 2.2) is so far away from us that we can assume all radiation coming from the source to us can be represented by a plane-parallel wave, and reaches antennas A and B (Figure 2.2) at different times, resulting in geometric delay. To compensate for the geometric delays, the observers add timing delays (either through software or physical cables) to the signal from different elements of the interferometer.

Each of the interferometric visibilities can be placed on the  $uv$ -plane (see Figure 2.2), where axes  $u$  and  $v$  are perpendicular to the line of sight, and the third  $w$  axis is parallel to the line of sight. When we project the baseline  $b = r_a - r_b$  (antenna spacing) onto the  $uv$ -plane, we get the quantities  $u$  and  $v$ , which are in units of wavelength  $\lambda$ . We can define a baseline in the  $uv$ -plane as

$$b = r_a - r_b = \lambda(u, v, w \equiv 0). \quad (2.4)$$

Following the assumption that the emission is being radiated from a small area of the sky we can consider it to be emitted from a 2D plane, allowing us to set  $w = 0$ . In this framework, we can define the unit vector  $s$  in terms of its components as  $(l, m, n = \sqrt{1 - l^2 - m^2})$ , where  $l$ ,  $m$  and  $n$  are direction cosines, see Figure 2.2). Using this relation in Equation 2.2, we get

$$V_\nu(u, v, w \equiv 0) = \iint \mathcal{I}_\nu(l, m) \frac{e^{-2\pi i(ul+vm)}}{\sqrt{1 - l^2 - m^2}} dl dm. \quad (2.5)$$

Using the same aforementioned assumption of a small emitting sky area,  $l$  and  $m$  will be significantly small, and  $\sqrt{1 - l^2 - m^2} \approx 1$ . However, given that

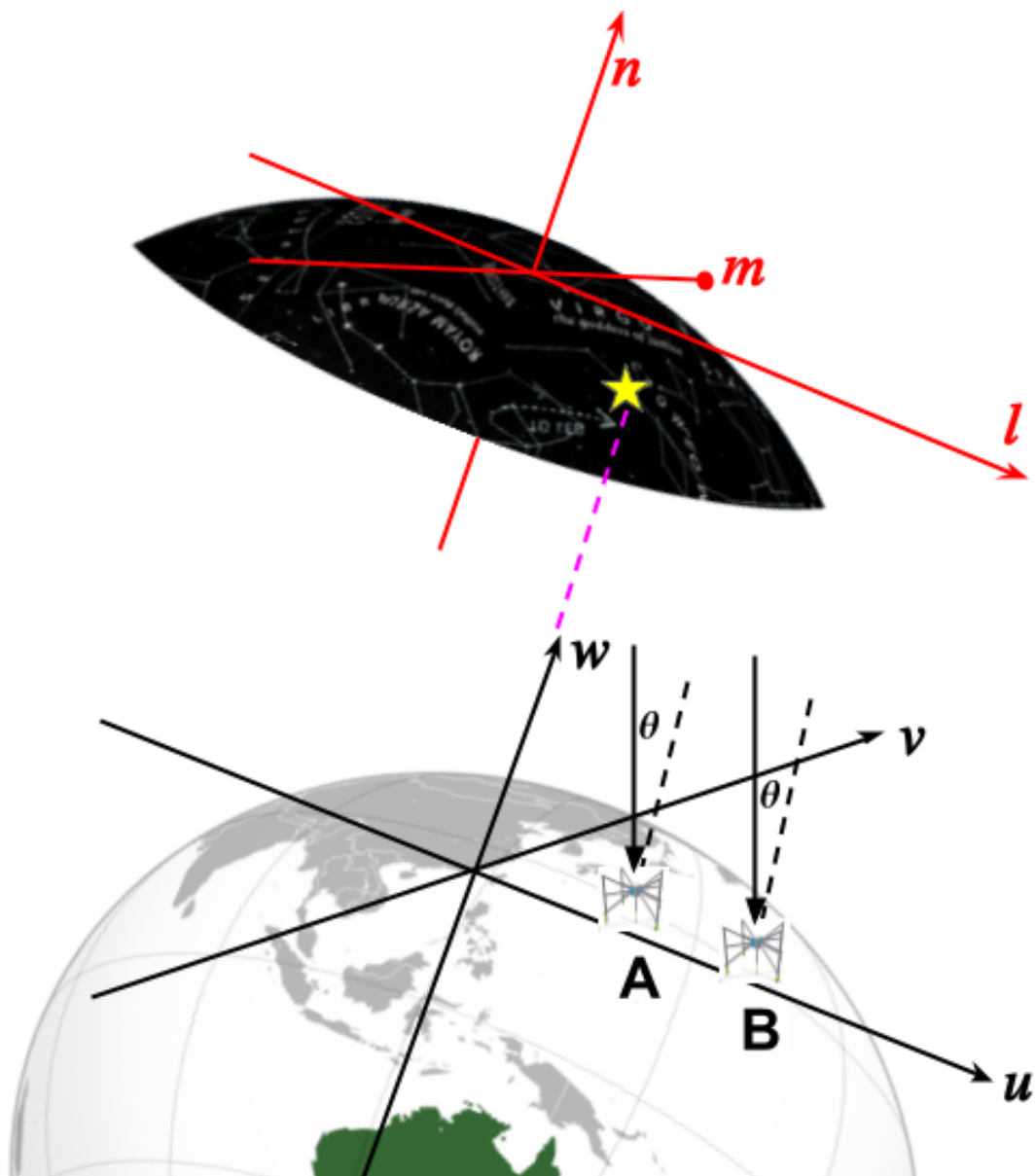


Figure 2.2: Coordinate system of the celestial sphere (red) and the baseline parameters (black). On the celestial sphere, the  $n$ -axis is perpendicular to the two-dimensional tangent plane created by the direction cosines  $l$  and  $m$ . The baseline coordinates are located on the Earth, where the  $w$ -axis is along the line-of-sight. Two antennas, denoted with A and B are in the same  $uv$ -space, and receiving emission from an astrophysical source (indicated with star symbol) at an angle  $\theta$  to the zenith. This figure is adapted from Cosmic-Watch and [web.haystack.edu](http://web.haystack.edu).

the antenna elements of the interferometer are not dimensionless point probes but have finite sizes and exhibit direction-dependent sensitivity, the observed visibility

(the spatial coherence function) is attenuated by the normalised antenna response (primary beam)  $\mathcal{A}_\nu(s)$ . Equation 2.5 is now written as

$$V_\nu(u, v, w \equiv 0) = \iint \mathcal{A}_\nu(l, m) \mathcal{I}_\nu(l, m) e^{-2\pi i(ul+vm)} dl dm, \quad (2.6)$$

where  $V_\nu(u, v)$  is generally referred to as the complex visibility.  $\mathcal{A}_\nu(s)$  is a direction dependent parameter, which rapidly drops to zero when we move away from the pointing centre. We restrict our analysis to a small field-of-view (FOV) in a single pointing. In general,  $\mathcal{A}_\nu(s)$  can be precisely measured and enforces the basic assumptions described earlier, that the emission is coming from a small patch of the celestial sphere.

The true brightness of the targeted source can be estimated by taking the inverse Fourier transform of Equation 2.6 and then dividing by  $\mathcal{A}_\nu(l, m)$ . The resultant quantity is the true sky intensity convolved with the Fourier transform of the  $uv$ -sampling function (described in Section 2.1.2). To obtain the true image of the sky we need to perform deconvolution.

In the case of modern low-frequency wide field-of-view radio interferometers like the SKA precursor telescopes MWA and ASKAP, Equation 2.6 is not directly applicable, because the  $w$  term ( $\neq 0$ ) can not be ignored. For these interferometers, Equation 2.6 is modified as

$$V_\nu(u, v, w) = \iint \mathcal{A}_\nu(l, m) \mathcal{I}_\nu(l, m) e^{-2\pi i(ul+vm+w(\sqrt{1-l^2-m^2}-1))} \frac{dl dm}{\sqrt{1-l^2-m^2}}, \quad (2.7)$$

where angular coordinate  $(l, m, n)$  defines a position on the celestial sphere, and  $n = \sqrt{1-l^2-m^2}$ .

To handle the data from such wide field-of-view radio interferometers a two-dimensional inverse Fourier transform is not suitable, so we require additional algorithms discussed below.

### 2.1.1.1 W-Projection

The W-Projection method projects the various  $W$ -terms onto the  $w = 0$  plane, so that it is still possible to use a two-dimensional Fourier transform to reconstruct the sky image (Cornwell et al., 2003; Cornwell et al., 2005, 2008), which is computationally efficient and easy to solve. We can rewrite Equation 2.7 in terms of the  $w$  free term and  $w$ -term as

$$V_\nu(u, v, w) = \iint \mathcal{A}_\nu(l, m) \mathcal{I}_\nu(l, m) e^{-2\pi i(ul+vm)} e^{-2\pi iw(\sqrt{1-l^2-m^2}-1)} \frac{dl dm}{\sqrt{1-l^2-m^2}}, \quad (2.8)$$

The exponential component carrying the  $w$ -term is represented with  $G(l, m, w)$ , such that

$$G(l, m, w) = e^{-2\pi iw(\sqrt{1-l^2-m^2}-1)}, \quad (2.9)$$

Now, we can rewrite equation 2.8 as

$$V_\nu(u, v, w) = \iint \mathcal{A}_\nu(l, m) \mathcal{I}_\nu(l, m) e^{-2\pi i(ul+vm)} G(l, m, w) \frac{dl dm}{\sqrt{1-l^2-m^2}}, \quad (2.10)$$

The above equation can be further simplified as

$$V_\nu(u, v, w) = \mathcal{F}_{2D} \left[ \frac{\mathcal{A}_\nu(l, m) \mathcal{I}_\nu(l, m)}{\sqrt{1-l^2-m^2}} G(l, m, w) \right], \quad (2.11)$$

where  $\mathcal{F}_{2D}$  is the 2-D Fourier transform operator,

$$V_\nu(u, v, w) = \mathcal{F}_{2D} \left[ \frac{\mathcal{A}_\nu(l, m) \mathcal{I}_\nu(l, m)}{\sqrt{1-l^2-m^2}} \right] \otimes \mathcal{F}_{2D} [G(l, m, w)], \quad (2.12)$$

$$V_\nu(u, v, w) = V_\nu(u, v, w = 0) \otimes \mathcal{F}_{2D} [G(l, m, w)], \quad (2.13)$$

$$V_\nu(u, v, w) = V_\nu(u, v, w = 0) \otimes \tilde{G}(u, v, w), \quad (2.14)$$

The above equation demonstrates that the visibilities with the non-zero  $w$ -term can be presented as a convolution between the visibilities projected onto the  $w = 0$  plane and the convolution function  $\tilde{G}(u, v, w)$ , where  $\tilde{G}(u, v, w)$  is the 2-D

Fourier transform of the function  $G(l, m, w)$  defined as

$$\tilde{G}(u, v, w) = \iint e^{-2\pi i(ul+vm)} G(l, m, w) dl dm, \quad (2.15)$$

$$\tilde{G}(u, v, w) = \iint e^{-2\pi i(ul+vm)} e^{-2\pi iw(\sqrt{1-l^2-m^2}-1)} dl dm, \quad (2.16)$$

After following Cornwell et al. (2003) and Cornwell et al. (2005, 2008), we can use the small angle approximation in Equation 2.16 and expanding  $[1 - (l^2 + m^2)]^{1/2} \approx [1 - \frac{1}{2}(l^2 + m^2)]$ , we get

$$\tilde{G}(u, v, w) = \iint e^{-2\pi i(ul+vm)} e^{\pi iw(l^2+m^2)} dl dm, \quad (2.17)$$

$$\tilde{G}(u, v, w) = \frac{i}{w} e^{-i\pi\left(\frac{u^2+v^2}{w}\right)}, \quad (2.18)$$

The following steps can then be used to perform a FFT of the visibilities  $V_\nu(u, v, w)$  with a non-zero  $w$ -term to obtain a dirty image.

1. Use the measured visibilities  $V_\nu(u, v, w)$  to calculate the projection of the visibilities onto the  $w = 0$  planes ( $V_\nu(u, v, w = 0)$ ).
2. Use a gridding function to grid the visibilities  $V_\nu(u, v, w = 0)$ , and then perform inverse FFT.
3. Obtain the dirty image.

To recover the true sky brightness from the dirty image we need to perform a deconvolution as described in Section 2.2.5.

### 2.1.1.2 W-Stacking

W-Stacking is another important technique to handle the  $W$ -term (Humphreys & Cornwell, 2011; Offringa et al., 2014), which is an order of magnitude computationally faster than W-Projection. In the case of the W-Stacking algorithm, the visibilities are gridded on different  $w$ -layers, and  $w$ -corrections are applied after

performing the inverse Fourier transform on gridded visibilities (Humphreys & Cornwell, 2011; Offringa et al., 2014).

Again starting from Equation 2.7, and rewriting the right-hand side in terms of  $w$ -term independent and dependent components,

$$V_\nu(u, v, w_i) = \iint \mathcal{A}_\nu(l, m) \mathcal{I}_\nu(l, m) e^{-i2\pi(ul+vm)} e^{-i2\pi[w_i(\sqrt{1-l^2-m^2}-1)]} \frac{dl dm}{\sqrt{1-l^2-m^2}}, \quad (2.19)$$

For every given  $w$ -term (where  $w_i \neq 0$ ), Equation 2.19 is basically a 2-D Fourier transform. After taking the inverse of the transform in the Equation 2.19, we get

$$\frac{\mathcal{A}_\nu(l, m) \mathcal{I}_\nu(l, m)}{\sqrt{1-l^2-m^2}} = e^{i2\pi[w_i(\sqrt{1-l^2-m^2}-1)]} \iint V_\nu(u, v, w_i) e^{i2\pi(ul+vm)} du dv, \quad (2.20)$$

By integrating both sides of Equation 2.20 along the  $w$  axis between the minimum ( $w_{\min}$ ) and maximum ( $w_{\max}$ )  $w$  value, this equation can be written as

$$\frac{\mathcal{A}_\nu(l, m) \mathcal{I}_\nu(l, m)(w_{\max} - w_{\min})}{\sqrt{1-l^2-m^2}} = \int_{w_{\min}}^{w_{\max}} e^{i2\pi[w(\sqrt{1-l^2-m^2}-1)]} dw \iint V_\nu(u, v, w_i) e^{i2\pi(ul+vm)} du dv, \quad (2.21)$$

Through this process the  $w$  values are discretized into  $N_w$  terms along the  $w$  axis and therefore specify the number of  $w$ -layers that are handled. We can therefore write Equation 2.21 as

$$\frac{\mathcal{A}_\nu(l, m) \mathcal{I}_\nu(l, m)(w_{\max} - w_{\min})}{\sqrt{1-l^2-m^2}} = \sum_{n=0}^{N_w-1} e^{i2\pi[w_n(\sqrt{1-l^2-m^2}-1)]} \iint V_\nu(u, v, w_n) e^{i2\pi(ul+vm)} du dv, \quad (2.22)$$

Offringa et al. (2014) suggested that the difference between the two subsequent  $w$  values  $\delta w [= (w_B - w_A)]$  should be less than one radian.

$$|\delta w 2\pi(\sqrt{1-l^2-m^2}-1)| \ll 1, \quad (2.23)$$

Therefore, the total number of  $w$ -layers required is

$$N_w \gg 2\pi(w_{\max} - w_{\min}) \max_{l,m} (1 - \sqrt{1 - l^2 - m^2}), \quad (2.24)$$

Depending on the observation, the real values for the right-hand side of Equation 2.24 can be significantly different. The value of  $w_{\max} - w_{\min}$  is governed by the wavelength, the coplanarity of the array, and the zenith angle (ZA; Offringa et al., 2014), and the value of the  $\max_{l,m}$  term depends on the angular size of the image (Offringa et al., 2014).

For gridding the visibilities, the  $w$ -values are increased or decreased by a small amount to match the  $w$ -value of the closest  $w$ -layer. The rounding off the  $w$ -values can create aliasing if the number of  $w$ -layers are significantly less than the required  $w$ -layers defined by Equation 2.24 (Offringa et al., 2014). This  $w$ -aliasing can cause “ghost” sources to appear in the image. Therefore, the number of  $w$ -layers should be accurately predicted (Offringa et al., 2014). After gridding the visibilities to the various  $w$ -layers, we perform an inverse FFT and apply a phase shift to these data to generate an image corresponding to a particular  $w$ -layer. We repeat this process  $N_w$  times to generate images corresponding to all the  $w$ -layers. Therefore, using Equation 2.22, the true sky image can be recreated as

$$\mathcal{A}_\nu(l, m) \mathcal{I}_\nu(l, m) = \frac{\sqrt{1 - l^2 - m^2}}{(w_{\max} - w_{\min})} \sum_{n=0}^{N_w-1} e^{i2\pi[w_n(\sqrt{1-l^2-m^2}-1)]} \mathcal{F}_{2D}^{-1} [V_\nu(u, v, w_n)], \quad (2.25)$$

where  $\mathcal{F}_{2D}^{-1}$  represents the two-dimensional inverse Fourier transform process.

### 2.1.2 $uv$ -coverage

Our retrieval of the true sky brightness is restricted by our capability to sample the  $uv$ -plane. Even with hundreds of antennas in modern radio interferometers,

it is not possible to completely sample the  $uv$ -plane; there are both gaps in the interior (minimum baseline length), and ultimately a maximum baseline length. This places limits both on the maximum resolution of our observations as well as the instrument's ability to detect large scale structures above a certain angular extent, commonly referred to 'resolving out'. The holes between baselines, and a sudden jump to a region with no data after the maximum baseline create sidelobes in the point source response.

Designing an ideal interferometer with optimal  $uv$ -coverage is a complex relationship between FOV, sensitivity and cost, which depends on the maximum baseline and the computational power required for the number of baselines. Additionally, various science themes require different  $uv$ -coverage and therefore have a different meaning of an ideal  $uv$ -coverage. Hence, we can never recover the true brightness of the sky.

A sampling function ( $S(b)$ ) is defined to describe the limited  $uv$ -coverage, which is essential when we try to recover the sky brightness through the Fourier transform of our measurements. The sampling function can be written as

$$S(b \equiv (u, v)) = \sum_{m=0}^M \delta(u - u_m) \delta(v - v_m), \quad (2.26)$$

where  $M$  is the total number of baselines, and each Dirac-delta function represents a different baseline in the  $uv$ -plane.

The sampled visibility function  $V_\nu^S(b)$  can be defined as product of  $V_\nu(b)$  and  $S(b)$

$$V_\nu^S(b) = S(b) V_\nu(b), \quad (2.27)$$

therefore,

$$\mathcal{I}_{\text{dirty}}(s, \nu) = \mathcal{F} [S(b) V_\nu(b)], \quad (2.28)$$

where  $\mathcal{F}$  is the Fourier operator and  $\mathcal{I}_{\text{dirty}}$  is the dirty image, which is not a true image of the sky. The dirty image is the convolution of the sampling function and the spatial coherence function.

We use the convolution theorem ( $\mathcal{F}[A.B] = \mathcal{F}[A] \otimes \mathcal{F}[B]$ , where  $\otimes$  represents convolution) to calculate its impact on the dirty image, and then try to remove it.

$$\mathcal{I}_{\text{dirty}}(s, \nu) = \mathcal{I}_{\text{true}}(s, \nu) \otimes \tilde{S}(s), \quad (2.29)$$

where  $\tilde{S}(s)$  is the Fourier transform of the sampling function.

From Equation 2.29, we found that when we directly Fourier transform our measurements from the  $uv$ -plane to the image plane, the recovered sky brightness is the true sky brightness convolved with  $\tilde{S}(s)$ , which is known as the dirty image.  $\tilde{S}(s)$  is also described as the dirty beam, and is the PSF (Point Spread Function) of the interferometer. To recover the true sky brightness, we require deconvolution to remove the artefacts generated due to the incomplete sampling of the  $uv$ -plane. The process of deconvolution can be done using the CLEANing algorithms discussed in Section 2.2.5.

### 2.1.3 Flagging and Calibration

In order to determine the true brightness of our source, the observed data must first be flagged to remove the visibilities contaminated by radio frequency interference (RFI). Then it should be calibrated to rectify the effects created by the instrument and the atmosphere. In the following sections, we describe these two steps in further detail, drawing from the approach of Fomalont & Perley (1999).

#### 2.1.3.1 Flagging

Flagging is the process in which we carefully examine (manually or through automated algorithms) the raw data in order to identify and consecutively remove/ignore the corrupted data. The data could be corrupted by radio frequency interference (RFI), damaged hardware such as broken antennas or dipoles, hardware or software malfunction, antenna shadowing, recording memory failure, and in some cases scheduling errors. Such bad data will prevent us from determining the actual antennas response, and eventually, result in incorrect calibration.

### 2.1.3.2 Calibration

The radio signal from our target astrophysical source becomes corrupted by the atmosphere and the instrument. The process by which we recover the actual source signal and remove the atmospheric propagation and instrumental errors is known as calibration.

The calibration formalism can be mathematically realised as follows. Suppose we observed a source at time  $t$ , the measured visibilities are  $\tilde{V}_{ij}(t)$  from a pair of antennas with baseline  $ij$ , which are different from the true visibilities  $V_{ij}(t)$ . The differences could be due to the source elevation dependent antenna gains, pointing and tracking errors, time-varying atmospheric effects, and arbitrary stochastic noise. In the case of an ideal interferometer, the relation between  $\tilde{V}_{ij}(t)$  and  $V_{ij}(t)$  is linear. The individual antennas have enough separation that there is no mutual coupling, so the response related to one antenna pair does not impact the output of any other pair. The relation between the observed visibilities and the true visibilities can be defined as

$$\tilde{V}_{ij}(t) = \mathcal{G}_{ij}(t)V_{ij}(t) + \epsilon_{ij}(t) + \eta_{ij}(t), \quad (2.30)$$

where  $\mathcal{G}_{ij}(t)$  is the baseline-dependent complex gain,  $\epsilon_{ij}(t)$  is the baseline-dependent complex offset factor, and  $\eta_{ij}(t)$  represents contributions due to stochastic noise. We can further broadly define  $\mathcal{G}_{ij}(t)$  as the product of the two antenna-dependent complex gains  $g_i(t)$  and  $g_j(t)$

$$\mathcal{G}_{ij}(t) = g_i(t)g_j^*(t)g_{ij}(t), \quad (2.31)$$

or

$$\mathcal{G}_{ij}(t) = a_i(t)a_j(t)a_{ij}(t)e^{i(\phi_i(t)-\phi_j(t)+\phi_{ij}(t))}, \quad (2.32)$$

where  $a(t)$  is the antenna-dependent amplitude correction,  $\phi(t)$  is the antenna-dependent phase correction factor, and  $g_{ij}(t)$ ,  $a_{ij}(t)$  and  $\phi_{ij}(t)$  are baseline-dependent

residual gains (which are  $< 1\%$  for an ideal interferometer).

The antenna-dependent complex gains  $g_i(t)$  and  $g_j(t)$  can be determined by the observations of a standard calibrator source. In general, two calibrator sources, flux (primary) and phase (secondary), are observed. The radio flux density of the flux calibrator source is well-established and constant with time. The same source could be used for delay and bandpass calibration. This is because it is typically nice and bright, so a channel-based response has plenty of signal-to-noise. Whereas, time-dependent amplitude and phase corrections are determined using the secondary calibrator source, which should be unresolved and bright (need not be as bright as the flux calibrator, as we don't need channel-by-channel solutions), along with highly constrained position coordinates and needs to be close to the target source. The complex gains are calculated as a function of time and interpolated and/or extrapolated to the target source over the full observation. Nevertheless, a few small residual errors may still persist due to the spatial and timing differences between the source and the calibrator observations, which leads to some variations that can be corrected by self-calibration (Section 2.2.6).

## 2.2 Interferometric techniques

### 2.2.1 Flagging methods

Various methods have been proposed for RFI mitigation and flagging, which can be done in the hardware (pre-correlation) as well as in the software (post-correlation) domain. Hardware-based approaches generally use either some dedicated hardware such as extra antennas to remove sources of interference (e.g., Kocz et al., 2010) or use some standard signal to determine the interference and remove it from the observed science data (e.g., Barnbaum & Bradley, 1998; Briggs et al., 2000; Fridman & Baan, 2001; Hellbourg et al., 2014). Software based techniques search for anomalous bright bursts (RFI) in antenna, time, and frequency space (e.g., Golap et al., 2005; Athreya, 2009; Pen et al., 2009; Offringa et al.,

2012; Sekhar & Athreya, 2018). After detecting these spurious signals, the corrupted data are discarded from further processing. The software based tools have a benefit that they can be used for both archival as well as new data.

The automatic flagging using software-based tools has been found to be highly effective for continuum observations. This approach shows limitations when working with spectral line data because bright spectral lines are mistakenly identified as RFI. In this situation, we take advantage of the concept that the polarization characteristics of RFI and the astrophysical source are significantly different. In radio astronomy, the polarisation state of the radiation from the sky can be fully characterised by four Stokes polarisation parameters, namely Stokes I, Q, U and V (Stokes, 1852). The Stokes I corresponds to the total intensity, whereas Stokes Q and U represent linear polarisation, and the circular polarisation is denoted by the Stokes V (Stokes, 1852). The majority of the radio sky is free from circularly polarised sources, and therefore, a Stokes V image of the sky from the telescope should in many cases be thermal noise. Hence, RFI is observed as a bright source in Stokes V image, which is confined to a narrow frequency range. Thus for spectral line observations, flagging should be performed in Stokes V.

In this PhD research, we used the **AOFLAGGER** software (Offringa et al., 2012) for flagging RFI in the MWA data, and the **CFLAG** tool is used for discarding corrupted data from the ASKAP observations. Once the data are accurately flagged and become free from all spurious signals, we move on to the next step of calibration.

### 2.2.2 Calibration techniques

We can broadly explain the process of calibration in the following steps:

- Ideally, the antenna gains are constant over the processed bandwidth of the observation, but factors like incorrect antenna timing and position can create inadequacies in the correlator model, which can lead to a linear phase slope in the frequency space and constant in time. This phase slope is

defined as a delay, which is detected for a single baseline and in the correlated visibilities. In continuum imaging when we average the frequencies an uncorrected delay creates de-correlation of the continuum signal.

Apart from delay, irregularities also happen in the phase response and amplitude response as a function of frequency, which are a property of bandwidth. The instrument and the atmosphere insert a spurious frequency dependence to the measured visibilities, which needs to be determined and corrected. While working with continuum data, averaging the frequencies with these errors results in limited dynamic range and signal-to-noise.

To correct for these errors we need to perform delay and bandpass calibration, where calibration solutions are determined using a bright source observed for a short time interval.

- In the correlator, signals from different antennas at specific frequencies are combined into visibilities. The correlator processes only electronic voltages in terms of relative phase and signal strength. Hence, it is crucial to correct the correlator products to recover the actual flux density from the sky visibilities. For this purpose, we need to apply flux calibration (Baars et al., 1977; Scaife & Heald, 2012; Perley & Butler, 2013).

In the flux calibration, we map the instrumental response to the incoming radio emission to an established flux density scale. The most effective method of performing flux calibration is by observing a standard calibrator that has a well-established flux density and comparing it to our target source (Baars et al., 1977; Scaife & Heald, 2012; Perley & Butler, 2013).

- The complex gain calibration (also known as antenna gain calibration) is used to correct for time varying properties that arise due to dynamic conditions of the telescope such as receiver power level settings, receivers removal and corrupted baseband samplers. Antenna gain calibration also traces changes due to environmental conditions such as the ionospheric conditions

(which are particularly problematic at low radio frequencies  $< 300$  MHz), atmospheric phase and opacity, the troposphere (at high frequencies) and occasional event like solar flares. Using proper antenna gain calibration, we can calibrate some of them. For complex gain calibration, the calibrator source should be unresolved<sup>1</sup> and must have constant flux density over the observation time. This allows the variation in gain to be directly calculated.

### 2.2.3 Weighting

Each sampled visibility data point ( $V_\nu^S(u_m, v_m)$ ; defined in Section 2.1.2) is multiplied by a weight  $w_m$  before gridding defined as:

$$W(u, v) = \sum_{m=0}^M w_m \delta(u - u_m) \delta(v - v_m), \quad (2.33)$$

where  $W(u, v)$  is the weighting function, which is incorporated to enhance the fidelity and dynamic range of the restored sky image. To meet various science goals different weighting functions are defined, which are discussed below.

#### 2.2.3.1 Natural weighting

This weighting scheme assigns constant weight to each visibility, equivalent to the inverse noise variance on that visibility data point,

$$w_m = \frac{1}{\sigma_m^2}, \quad (2.34)$$

where  $\sigma_m$  is the rms noise of the visibility point  $m$ .

Natural weighting maximizes the point source sensitivity in the sky image. It in some way provides the natural resolution of the telescope. We can then trade off some sensitivity to get extra resolution by upweighting the longer baselines.

---

<sup>1</sup>In fact we just need a known sky brightness distribution (a good source model). An unresolved source has a particularly simple model (point source at the phase centre has zero phase and fixed amplitude with baseline length), but resolved sources can be used if we have a good model for them

Natural weighting is most suitable for extended source sensitivity, as it tends to upweight the (usually more densely populated) short baseline regions of the  $uv$ -plane.

### 2.2.3.2 Uniform weighting

In the uniform weighting recipe, the weights are equal to the inverse of the sampling density function, which is defined as

$$w_m = \frac{1}{\sigma_m^2 \rho_m(u_m, v_m)}, \quad (2.35)$$

where  $\rho_m$  is the local density of the  $(u, v)$  points.

This weighting scheme typically gives higher resolution and minimizes side-lobe level, but significantly increases the rms noise level (double that of natural weighting, but it depends on the array configuration and the balance between long and short baselines) in the image.

### 2.2.3.3 Robust weighting

As we have noticed natural weighting minimises the noise level, whereas uniform weighting suppresses sidelobes. A robust weighting scheme provides a trade-off between the two. Robust weighting changes smoothly from uniform to natural weighting as a function of robustness ( $R$ ), which is a real value parameter (Briggs, 1995).

In the Common Astronomy Software Application (CASA v5.1.2-4: McMullin et al., 2007) package notation the robustness parameter ( $R$ ) varies from -2 (nearly uniform weighting) to +2 (close to natural weighting), and  $R = 0$  provides an appropriate compromise between sensitivity and resolution (Briggs, 1995).

## 2.2.4 Imaging and gridding

When we are dealing with the small field-of-view coplanar telescopes,  $w \equiv 0$  and can be ignored. Therefore, the visibilities can be considered to lie on a plane. In this case, we can perform a two-dimensional inverse Fourier transform of the calibrated visibility data (Equation 2.6) to obtain a dirty image. We further apply a deconvolution algorithm to recover the true sky image.

While observing the sky with low-frequency radio interferometers having wide field-of-view, we cannot reconstruct the sky image using the assumption that the visibilities lie on a plane as  $w \neq 0$  (e.g. MWA and ASKAP; Tingay et al., 2013; Hotan et al., 2014; Wayth et al., 2018; Hotan et al., 2021). To handle the  $w$ -term, various techniques have been proposed such as the three-dimensional Fourier transform (Perley, 1989), warped snapshot (Perley, 1989), W-Projection (Cornwell et al., 2003; Cornwell et al., 2005, 2008), W-Stacking (Humphreys & Cornwell, 2011; Offringa et al., 2014) and W-Snapshot (Cornwell et al., 2012). All radio telescopes I have used in my PhD research are widefield so I will not outline the 2D approximation. In Section 2.1.1, I discussed only those methods which are broadly used in my PhD work.

As the W-Stacking and W-Snapshot method produces the dirty sky image, we then need to perform the deconvolution process (Section 2.2.5) to recreate the true sky image.

## 2.2.5 Deconvolution

Deconvolution is the process to reconstruct the accurate sky image ( $\mathcal{I}_{\text{true}}$ ) from the dirty image ( $\mathcal{I}_{\text{dirty}}$ ). As discussed in Cornwell & Fomalont (1999) and Venkata (2010), a non-linear deconvolution technique is necessary to recover the actual sky brightness from an observation with a limited  $uv$ -coverage. Further, a primary beam correction is generally required to normalize the attenuated source fluxes in the recovered sky image (Cornwell et al., 2008).

### 2.2.5.1 The CLEAN algorithm

Various algorithms are proposed for the purpose of deconvolution, but I discuss the CLEAN algorithm because it is most commonly used (Högbom, 1974; Clark, 1980; Schwab & Cotton, 1983; Cornwell et al., 2008), and I have also used it in my PhD research.

CLEAN makes an assumption that there are just point sources in the image field. This algorithm applies an iterative procedure to obtain a list of strengths and positions of the point sources also called CLEAN components (which forms the model image). Except Högbom’s CLEAN (Högbom, 1974), all other variants generally include two cycles: the major (on the visibility plane) and the minor (on the image plane) cycle.

In Högbom CLEAN (Högbom, 1974), at every iterative step a scaled point spread function (dirty beam) is subtracted from the dirty image (or the subtracted dirty image) at the highest peak position. The magnitude and location of the subtracted brightest point source are recorded and added to an image model (CLEAN components). The iterative process of subtraction stops when the number of iterations exceeds the defined maximum number or the brightest point source in the residual image is below a specified threshold. The final dirty image known as the residual image should contain only noise. Therefore, the ‘CLEANed’ image, or recovered image, can be generated by convolving the most recent stacked CLEAN components with an idealised ‘CLEAN restoring beam’ (typically an elliptical Gaussian), and further adding back the final residual image.

To reduce the computational time, Clark (1980) proposed a more efficient CLEAN algorithm based on the Fast-Fourier transform (FFT), which operates in  $uv$ -space and includes both major and minor cycles. In this approach, instead of using the full dirty beam, a small section of the dirty beam including the highest exterior sidelobe is selected during a minor cycle. The point sources are then determined in the dirty image if their magnitude is higher than the maximum exterior sidelobe. A standard CLEAN is executed using the dirty beam fraction

and the selected point sources from the dirty image. The CLEANing process continues until there are no further elements to be picked-up in the dirty image. In a major cycle, the model image (or CLEAN components) is Fourier transformed to the  $uv$ -space, and then subtracted from the visibilities. Finally, the ‘CLEANed’ image is reconstructed by transforming the model image back to the image plane, and then subtracted it from the residual image.

Schwab & Cotton (1983) developed a modified version of the Clark CLEAN algorithm, where CLEAN components (or model image) are subtracted from the degridded visibility data. This approach reduces gridding errors and eliminates aliasing noise. Recently, a new variant of the CLEAN algorithm called multi-scale CLEAN proposed by Cornwell et al. (2008), where emission from the large scale structures is deconvolved first. The finer details are determined later as the iteration process progresses.

## 2.2.6 Self-calibration

As discussed in Section 2.1.3.2, initially, the true structure or surface brightness of the targeted field is unknown. Therefore, for preliminary calibration of the visibilities, a standard calibrator must be monitored to calculate and transfer the gains from the calibrator to the targeted field. However, the calibrator observations are different from the source observation both in time and pointing direction.

We are looking through different pieces of the ionosphere, which varies with time, so it is unlikely that separate calibrator observations can fully correct the data. To handle these calibration errors, when there is enough flux density in the field (at MWA and ASKAP frequencies, there almost always will be), we can use self-calibration.

The primary focus of the self-calibration process is to determine the actual complex antenna gains in the direction of the primary source and at the time of monitoring. Self-calibration is an iterative approach where the initial starting

point is the model of the source field itself, which we continue to iterate over and thus improve the complex antenna gain solutions with each iteration. In the self-calibration technique, the difference ‘ $\mathcal{S}$ ’ between the measured visibilities ( $\tilde{V}$ ) and the model visibilities ( $\hat{V}$ ) is minimised by the least squares approach (Cornwell & Fomalont, 1999).

$$\mathcal{S} = \sum_k \sum_{\substack{i,j \\ i \neq j}} w_{ij}(t_k) \left| \tilde{V}_{ij}(t_k) - g_i(t_k)g_j^*(t_k)\hat{V}_{ij}(t_k) \right|^2, \quad (2.36)$$

where  $w_{ij}(t_k)$  are the weights corresponding to the baseline  $i - j$  at a particular time  $t_k$ . As described earlier, the self-calibration process generally uses the initial image of the source field as the model image. The antenna gains  $g(t)$  are determined by dividing measured visibilities with the initial model, which are then used to further calibrate the visibilities according to

$$\mathcal{S} = \sum_k \sum_{\substack{i,j \\ i \neq j}} w_{ij}(t_k) \left| \hat{V}_{ij}(t_k) \right|^2 \left| X_{ij}(t_k) - g_i(t_k)g_j^*(t_k) \right|^2, \quad (2.37)$$

where  $X_{ij}$  is the ratio of observed to model visibilities, and is described as

$$X_{ij}(t) = \frac{\tilde{V}_{ij}(t)}{\hat{V}_{ij}(t_k)}. \quad (2.38)$$

If the model is accurate,  $X_{ij}$  is independent of  $u$  and  $v$  but proportional to the antenna gains. We can then determine the gains for each integration period. This process continues until it converges (i.e. when there is no obvious improvement), and finally an acceptable intensity map is created. The self-calibration process fails if the signal-to-noise (SNR) is not adequately high, or the source structure is significantly complex to model. This method also shows limitations if the total number of variables is greater than the number of independent visibility measurements (Cornwell & Fomalont, 1999).

In the case of wide field-of-view low-frequency interferometers the ionosphere

is not same in two different directions on the sky, so the gains will differ. But as our target sources are point sources, so the impact of ionosphere is minimal. However, we observe a shift in the position of the sources due to ionospheric distortions. We used the `fits_warp` (Hurley-Walker & Hancock, 2018) software package to deal with such effects (discussed in Section 2.3).

## 2.3 MWA data processing

MWA is not a tracking telescope but rather has a fixed number of sky pointings. It therefore needs to repoint every 2-min to keep up with the Earth’s rotation, which means that throughout an observation the MWA’s primary beam is also changing every 2-min (Offringa et al., 2014). We can assume a constant beam for a period of 2-min, and hence, the data are recorded and imaged in 2-min snapshots (Offringa et al., 2014).

For processing the MWA data, we have primarily relied on the `MWA-fast-image-transients` pipeline<sup>2</sup>. The various steps taken to create a clean image from the MWA raw data are highlighted in Figure 2.2, and described below

1. We download the `CASA` measurement sets from the MWA All-Sky Virtual Observatory<sup>3</sup> (ASVO) server. ASVO acquires GPU box files from the magnetic storage tapes at Pawsey Supercomputing Centre, and automatically runs `COTTER` (described in Appendix B) on their server and provides `CASA` measurement sets.
2. The target source observation is calibrated using an observation of a bright, non-variable calibrator source such as Hydra A, Hercules A, Centaurus A or Pictor A. We relied on a single source for calibration as at the time of processing, no MWA sky model exists for the Galactic plane that would allow us to perform an in-field calibration. Self-calibration is also applied,

---

<sup>2</sup><https://github.com/PaulHancock/MWA-fast-image-transients>

<sup>3</sup><https://asvo.mwatelescope.org/>

as described in Section 2.2.6.

3. The measured visibilities are weighted using the Briggs (1995) robustness parameter  $R = 0.0$ , which is a compromise between sensitivity and resolution (described in Section 2.2.3.1). Imaging is performed using `WSClean` (Offringa et al., 2014), which applies  $w$ -corrections using the W-stacking (Section 2.1.1.2) approach. We created  $9000 \times 9000$  pixel images, where each pixel is 16 arcsec. We manually check the image for evidence of side lobes and bright source artefacts, which can be removed through self-calibration (Section 2.2.6) or variations in the imaging parameters. If we continue observing large scale sidelobes due to bright extended sources and degraded resolution due to corrupted long baselines tiles, we simply discard that 2-min snapshot.
4. After creating a good quality image, we apply the `fits_warp` (Hurley-Walker & Hancock, 2018) software package to correct for the spatial warping of the image due to the Earth’s ionosphere, which is significant at low radio frequencies. The radio waves from astrophysical sources incident on an interferometer are refracted by the ionosphere, which induces a shift in the measured position of the source. This shift should be corrected to obtain the correct position of the sources.
5. The absolute flux scale is calibrated using the `flux_warp` software package (Duchesne et al., 2020). The methodology is described below in Section 2.3.1.
6. Once we apply the aforementioned corrections to the 2-min snapshot images, we create a mean image using the `ROBBIE` software package (Hancock et al., 2019). The detailed approach of stacking is illustrated in Section 2.3.2.

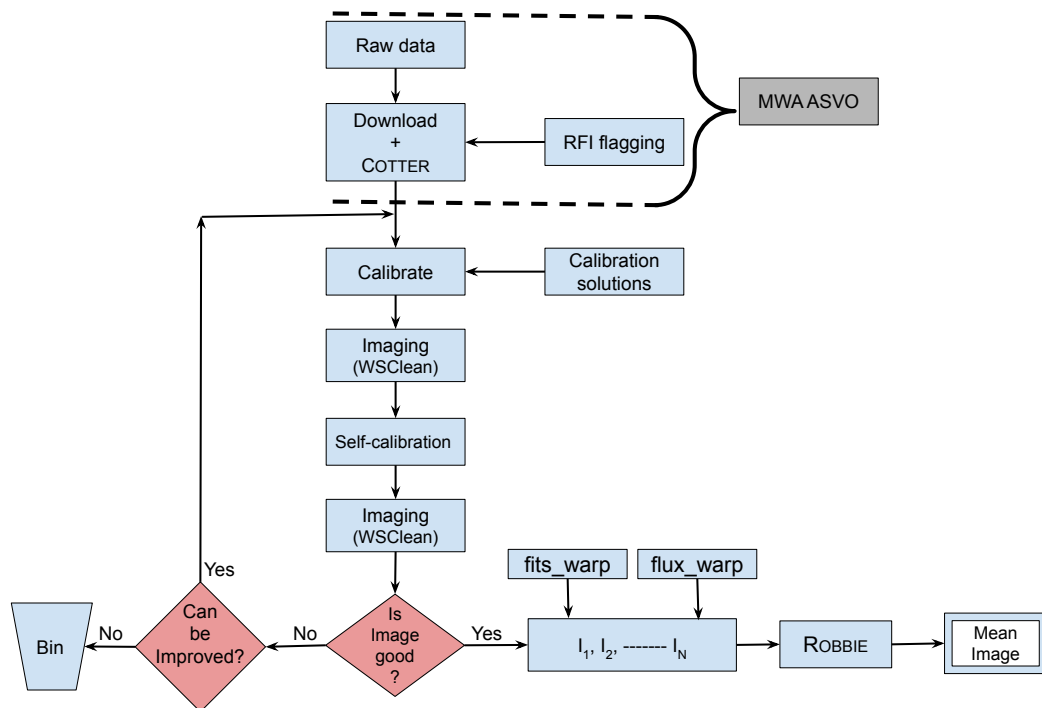


Figure 2.3: A schematic diagram representing the MWA data reduction workflow. Most of the data processing has been done using the `MWA-fast-image-transients` pipeline. We manually assess the quality of the initial image before deciding on the next step (shown in red diamonds). When we are happy with the image quality, we then correct for ionospheric effects using `fits_warp` and correct the absolute flux scale using `flux_warp` before using `ROBBIE` to create the final sensitive mean image.

### 2.3.1 Flux calibration

In general, during the calibration process (Section 2.2.2), a primary calibrator source is used to calibrate the flux density of the target field. This procedure worked reasonably well for most of the interferometers such as `UTMOST`, `ASKAP`, `ATCA`, and `LBA` used in this PhD research. But in the case of `MWA`, this approach has limitations, where the flux scales in the final images can be off by  $\leq 50\%$  in comparison to the input amplitude calibration model (Duchesne et al., 2020). The reasons behind the failure of this method could be: 1) the models used for bright sources are from Phase I of the `MWA`, where the angular resolution is  $\sim 3$  arcmin at 154 MHz, which improved by a factor of  $\sim 2$  in the `MWA` Phase II upgrade. Therefore, the models defined for the bright calibrator

sources are not accurate. 2) the data have residual primary beam model errors (Duchesne et al., 2020). 3) the primary calibrator does not dominate the field, in the way that it might do at lower frequencies. There are always bright sources in an MWA field of view.

To correct the absolute flux calibration of the MWA images, we used the `flux_warp`<sup>4</sup> software package developed by Duchesne et al. (2020). The authors found that the flux scale offsets are much more prominent in low-elevation observations where the primary beam model incorporated for correction is less accurate. Due to earth rotation, every 2-min snapshot has a different pointing centre, hence a slightly different primary beam correction is required between the snapshots. The inputs to the `python` code `flux_warp` are a Stokes I MWA image of our field, a catalogue derived from this image that lists the sources in the field and their radio flux densities, and a standard catalogue of the sky for comparison (Duchesne et al., 2020). The `flux_warp` tool creates a flux scaling screen, which is then multiplied with the Stokes I image to correct the absolute flux scale. The screen used to perform the flux correction is created by assuming a function which is then fit to the flux offsets in the image. Some examples of useful functions include a mean or median fit to the flux offset, or a one-dimensional polynomial fit to the elevation or declination of the image (Duchesne et al., 2020).

### 2.3.2 Stacking

In a 2-min snapshot image, we found an rms noise level between 30 to 40 mJy at 154 MHz in the extended configuration close to the Galactic Plane. At this rms noise level, it is hard to detect a relatively faint ( $\sim 30$  mJy) radio jet from a black hole XRB with high confidence ( $> 3\sigma$ ). Given that black hole XRB radio jets in the low-frequency band ( $< 300$  MHz) are unlikely to vary over the 30 minutes of monitoring at each frequency, we can increase the signal-to-noise ratio by stacking together the 2-min snapshot images.

---

<sup>4</sup>[https://gitlab.com/Sunmish/flux\\_warp](https://gitlab.com/Sunmish/flux_warp)

In order to stack the 2-min snapshot images we used the **ROBBIE**<sup>5</sup> software package (Hancock et al., 2019). This software joins the individual images together to create an image cube, where the observation time is the third axis of the image cube. This cube is subsequently used to generate a mean image (Hancock et al., 2019). For example, if we create an image cube using ‘N’ 2-min snapshot images, each with an equal rms noise level of  $r_{noise}$  mJy beam<sup>-1</sup>, then the rms noise level of the mean image will be improved by a factor of  $\sqrt{N}$ . By stacking the 2-min snapshots we detected relatively faint ( $\sim 60$  mJy at 154 MHz) compact jets in the BH-XRBs MAXI J1820+070 and MAXI J1348–630 (Chapter 6).

## 2.4 ASKAP data processing

To process ASKAP data, we use the standard ASKAP data analysis software, **ASKAPsoft**<sup>6</sup> (Guzman et al., 2019). The pipeline includes all the necessary steps (discussed in Section 2.1) for flagging, correcting for ionospheric Faraday rotation, bandpass, flux and gain calibration, and creating a clean image. After inspecting the preliminary image, the image quality was then improved through changes in the weighting scheme, the self-calibration loops and the number of clean minor cycles. The standard pipeline also creates an image cube (also known as a spectral cube). We summarize the ASKAP data processing workflow in the following steps, which are part of the **ASKAPsoft** pipeline.

1. The anomalous samples from the calibrator and the source data sets are flagged using the tool **CFLAG**, which is part of the pipeline. The flagging has two steps:
  - (a) The corrupted channels, antennas and baselines, time intervals, and autocorrelations are flagged following predefined criteria such as amplitude maximum value. Sometimes a basic flat amplitude level is also

---

<sup>5</sup><https://github.com/PaulHancock/Robbie>

<sup>6</sup><http://www.atnf.csiro.au/computing/software/askapsoft/sdp/docs/current/index.html>

used for detecting and flagging RFIs.

(b) In the second step, Stokes-V and dynamic amplitude flagging is performed for HI absorption line imaging (explained in Section 2.2.1).

2. Further, the tool **CBPCALIBRATOR**, included in **ASKAPsoft**, is used to determine the bandpass solutions. PKS B1934–638 (Reynolds, 1994a) is used as a bandpass and absolute flux density calibrator. The calibrator solutions are applied using the tool **CCALAPPLY**.
3. The initial imaging is done using the tool **CIMAGER**, which uses the W-Projection algorithm (Cornwell et al., 2008). **ASKAPsoft** uses **preconditioning** for weighting the visibility measurements (Venkata, 2010), where this approach optimises the processing by reducing the data access load. We used a preconditioning value that is equivalent to a robustness parameter  $R = 0.5$  in the Briggs (1995) robust weighting scheme (Section 2.2.3.1). We then self-calibrate, which is also a part of **ASKAPsoft**.
4. We used the **SIMAGER** task to generate spectral-line cubes. The spectral line imaging can be broadly described in the following way.
  - (a) The Earth revolves around the Sun and also rotates around its own axis. The Sun is also rotating around the Galaxy. Therefore, our velocity with respect to the astrophysical source is not constant in direction or in time. Hence, we need to apply Doppler corrections to the spectral line. Otherwise, the spectral line will slowly move outside the covered frequency range.
  - (b) Then, from various velocity frames such as Geocentric, Barycentric and Local Standard of Rest (LSR) a velocity frame is selected. We selected LSR velocity frame for our observations. The relativistic velocity ( $V_{\text{rev}}$ ) can be expressed in terms of the rest frequency of the line ( $\nu_0$ ) and the

observing frequency ( $\nu$ ) with the following relation

$$V_{\text{rev}} = \frac{\nu_0^2 - \nu^2}{\nu_0^2 + \nu^2} c, \quad (2.39)$$

where  $c$  is the speed of light.

In radio astronomy, the above equation can be approximated as

$$V^{\text{radio}} = \frac{\nu_0 - \nu}{\nu_0} c, \quad (2.40)$$

where  $V^{\text{radio}}$  is the radial velocity. The above equation is used to convert observing frequency to velocity.

- (c) Further, a continuum is subtracted from the image cube, generated after imaging every channel. For continuum subtraction, it is first essential to recognize which channels contain only continuum signal, and which contain both line and continuum signal. The channels containing entirely continuum are known as line-free channels. Differentiation between the line-free channels and the line signal containing channels is done by creating an initial cube. If the spectral line signal is significantly weak in-comparison to the continuum, it is usually crucial to clean the cube (Westpfahl, 1999).

The continuum subtraction can be done in the image plane or in the  $uv$ -plane. In the case of image plane based continuum subtraction, a continuum map is created after imaging and averaging the line-free channels. The continuum map is subtracted from all the channels carrying spectral line signal. To recover the final cube cleaning is required (Westpfahl, 1999).

For  $uv$ -plane based continuum subtraction, a low-order polynomial function is fitted to the line-free channels. Then the fitted function is subtracted from the visibility data containing the spectral line signal. Finally, the subtracted  $uv$  data is imaged and cleaned to reconstruct

cube (Westpfahl, 1999).

Although, we made use of other facilities in this PhD research (e.g. UT-MOST, LBA, ATCA, MeerKAT), our contributions focused primarily on MWA and ASKAP, and the data processing for these other facilities was done using standard procedures as detailed in the relevant research chapters.

## 2.5 Observing strategies for black hole X-ray binaries at radio frequencies

As described in Section 1.3, the all-sky monitors have increased our ability to detect outbursts from XRBs. Currently, we expect  $\sim 4 - 12$  outbursts (over the whole sky) per year with a mean duration of  $\approx 250$  days, out of which 50% will be bright (nearly 50 mJy at 5 GHz; Tetarenko et al. 2016). Taking the conservative estimate, we can expect a minimum of two BH-XRB outbursts every year visible to the SKA-precursors (MWA, ASKAP and MeerKAT). In the case of the MWA, its sensitivity plays an important role in detecting low-frequency ( $< 300$  MHz) emission from radio jets. In the extended configuration, we expect to reach noise levels of  $\sim 10$  mJy after stacking nearly 30 minutes ( $15 \times 2$ -min) of snapshots, which is necessary for detecting radio jets in XRBs (as demonstrated by our detections of the black hole XRBs MAXI J1535–571 (Chapter 5), MAXI J1348–630 (Chapter 6) and MAXI J1820+070 (Chapter 6) with the MWA). MeerKAT is regularly observing (every week) outbursting XRBs under the large survey project ThunderKAT (Fender et al., 2016). For ASKAP, there are no dedicated projects triggered on individual sources; it’s more of a survey facility. But we observed with single DDT snapshots to get the HI spectrum when the source was brightest.

XRB outbursts are characterized by a sudden and rapid increase in broadband intensity (reaching a maximum in about a week at GHz frequencies) with bright radio flaring at the peak followed by a gradual decline. The optimal strategy for

detecting XRB outbursts with MWA is to trigger on an outburst once reported by X-ray all-sky monitors such as *MAXI* or *Swift*/BAT. 30 min of triggered observations is typically sufficient to detect an XRB, preferably in the extended configuration (EC) for maximum sensitivity. At the peak of the BH-XRB X-ray outburst, the source undergoes a rapid flaring event (launching transient jets), displaying variability on 1-2 day timescales at low radio frequencies for up to two weeks (e.g. the 2015 V404 Cygni outburst; Tetarenko et al. 2017). Daily monitoring for a period of 2 weeks is typically sufficient to monitor the full hard-to-soft x-ray spectral state transition. The peak of the radio flaring event is also the best time for HI observations with ASKAP.

The compact jets are observed during the hard X-ray spectral state, which is observed in the beginning and the decaying phase of the outburst (typically before and after the peak of the outburst). The compact jets are characterised by slow variations on timescales of the order of a week. Therefore, to observe the compact jets at low radio frequencies with the MWA, the source can be monitored with weekly cadence in the hard X-ray spectral state. The low variability also makes them well suited to the weekly MeerKAT cadence.

To fully sample the broadband spectrum of both types of jets in the low-frequency regime ( $< 300$  MHz), we can observe the source at multiple different MWA frequency bands. At high-frequencies ( $> 300$  MHz), we can monitor the source with the Australian suite of radio telescopes, including UTMOST, ASKAP, ATCA and LBA. In the following Chapters 3, 4, 5 and 6, we present the results obtained from our observing strategy of BH-XRBs.

## Chapter 3

# An ASKAP distance constraint to MAXI J1535–571

This chapter is a reproduction of J. Chauhan, J. C. A. Miller-Jones, G. E. Anderson, W. Raja, A. Bahramian, A. Hotan, B. Indermuehle, M. Whiting, J. R. Allison, C. Anderson, J. Bunton, B. Koribalski, and E. Mahony (2019), “An HI absorption distance to the black hole candidate X-ray binary MAXI J1535–571”, *Monthly Notices of the Royal Astronomical Society*, Letters, Volume 488, Issue 1, page L129–L133,  
DOI: <https://doi.org/10.1093/mnrasl/slz113>.

The chapter is slightly different from the original journal article due to minor modifications, such as the exclusion of some introductory material (already discussed in Chapter 1), referencing to earlier chapters to maintain the consistency within this thesis. We also add some material that was not included in the original publication due to space constraints.

As discussed in Section 1.6.1, distance to an astrophysical object is an essential quantity to calculate physical quantities from observables. In this chapter, we measured the kinematic distance (discussed in Section 1.6.1) to MAXI J1535–571 using HI absorption spectra from ASKAP early science observations. ASKAP is a synthesis radio telescope located at MRO in Western Australia (Section 1.8.2), which has already established its ability to detect HI absorption from extra-

galactic sources (Allison et al., 2015, 2017). With the ASKAP we monitored the black hole candidate X-ray binary MAXI J1535–571 over seven epochs from 21 September to 2 October 2017. Using ASKAP observations, we studied the HI absorption spectrum from gas clouds along the line-of-sight and thereby constrained the distance to the source. By comparing the maximum negative radial velocities measured from the HI absorption spectra, we were able to place the source at the near kinematic distance, with a strong upper limit on the tangent point. This allowed us to determine the peak luminosity of the outburst, and showed that the soft-to-hard spectral state transition occurred at a much lower luminosity than is typical for BH-XRBs. Finally, the research conducted in this chapter highlights the capabilities of new wide-field radio telescopes to probe Galactic transient outbursts, by allowing us to observe both a target source and a background comparison source in a single telescope pointing.

### 3.1 MAXI J1535–571

On 2 September 2017, an uncatalogued XRB was co-discovered by the Monitor of All-sky X-ray Image<sup>1</sup> (*MAXI*; Matsuoka et al., 2009) and the Neil Gehrels Swift Observatory (*Swift*; Gehrels et al., 2004), and designated MAXI J1535–571 (Negoro et al., 2017a; Kennea et al., 2017a). In J2000.0 coordinates, the source is located at RA = 15:35:19.714±0.007, DEC = –57:13:47.583±0.024 (Galactic coordinates  $l = 323.72407^\circ$ ,  $b = -1.12887^\circ$ ; Russell et al. 2017b). Multi-wavelength studies of the system strongly suggest that the accreting compact object is a stellar-mass black hole (Dinçer, 2017; Kennea, 2017; Negoro et al., 2017b; Russell et al., 2017b,a). However, the physical parameters, including the black hole mass and distance, and the peak luminosity of the outburst are still uncertain.

---

<sup>1</sup><http://maxi.riken.jp/top/index.html>

Table 3.1: Details of our ASKAP observations of MAXI J1535–571.

| Observation ID | Observation Start date (DD-MM-YYYY) | Observation Start time (hh:mm:ss) | MJD <sup>b</sup> | Exposure time (hh:mm:ss) | Flux Density <sup>a</sup> $S_0$ (mJy) | rms noise (mJy beam <sup>-1</sup> ) |
|----------------|-------------------------------------|-----------------------------------|------------------|--------------------------|---------------------------------------|-------------------------------------|
| 4340           | 21-09-2017                          | 03:06:32                          | 58017.17         | 02:02:26                 | $579.6 \pm 2.1$                       | 0.74                                |
| 4364           | 22-09-2017                          | 01:30:02                          | 58018.12         | 02:51:50                 | $156.1 \pm 1.9$                       | 0.72                                |
| 4367           | 22-09-2017                          | 10:35:41                          | 58018.50         | 03:00:56                 | $306.1 \pm 1.3$                       | 0.54                                |
| 4374           | 23-09-2017                          | 13:23:39                          | 58019.58         | 01:00:52                 | $478.2 \pm 2.4$                       | 0.91                                |
| 4410           | 30-09-2017                          | 03:29:59                          | 58026.23         | 04:00:56                 | $39.8 \pm 0.8$                        | 0.53                                |
| 4414           | 01-10-2017                          | 03:35:00                          | 58027.23         | 04:01:01                 | $26.3 \pm 0.8$                        | 0.54                                |
| 4418           | 02-10-2017                          | 03:39:59                          | 58028.24         | 04:01:22                 | $21.4 \pm 0.7$                        | 0.52                                |

<sup>a</sup>  $1\sigma$  errors are quoted, calculated by adding in quadrature the  $1\sigma$  error on the Gaussian fit and the  $1\sigma$  rms noise in the image.

<sup>b</sup> Mid point of our observations.

## 3.2 Observations and Data reduction

During the 2017 outburst of MAXI J1535–571, ASKAP observed the source over seven epochs from 21 September to 2 October 2017. At the time of these early science observations, ASKAP was operated in a sub-array of twelve dishes, which provides an angular resolution of  $\sim 30$  arcsec. All observations were conducted at a central frequency of 1.34 GHz with a processed bandwidth of 192 MHz. The total bandwidth was further divided into 10368 fine channels, each with a frequency resolution of 18.519 kHz, with visibilities recorded every 10 s. Further details of the observations can be seen in Table 3.1.

We reduced our data using the standard ASKAP data analysis software, `ASKAPsoft`<sup>2</sup> (pipeline version 0.24.1). For continuum imaging, we performed dynamic flagging of faulty antennas, faulty channels, and baselines affected by radio frequency interference (RFI) during bandpass calibration. Bandpass and flux calibration were performed using the calibrator source PKS B1934–638, and the bandpass solution was interpolated across frequencies where data were flagged. The `IMFIT` task in the Common Astronomy Software Application (CASA v5.1.2-4; McMullin et al., 2007) package was used for measuring the flux densities and  $1\sigma$  uncertainties of MAXI J1535–571 from the continuum images, which are listed in Table 3.1.

With a flux density  $> 150$  mJy during the first four epochs, there was enough signal-to-noise to detect H I absorption towards MAXI J1535–571. We used the `SIMAGER` task to generate spectral-line cubes, and performed only stokes-V flagging to avoid removing the true absorption line in the H I region. We applied the bandpass solutions to the raw spectral data and extracted a sub-spectral cube with 1000 channels centered at 1.42 GHz and a velocity resolution of  $\sim 4$  km/s. Note that our conclusions should not be affected by the Galactic H I absorption towards PKS B1934–638, which is very narrow (FWHM  $< 6$  km/s; approximately

---

<sup>2</sup><http://www.atnf.csiro.au/computing/software/askapsoft/sdp/docs/current/index.html>

one channel wide) and therefore only affects the H I absorption line at local standard of rest (LSR) velocity = 0 km s<sup>-1</sup> (Dénes et al., 2018). We extracted the H I spectra corresponding to MAXI J1535–571 and a nearby extragalactic comparison source PMN J1533–5642 (= MGPS J153358–564218; Griffith & Wright, 1993; Murphy et al., 2007), located at RA = 15:33:57.439, DEC = –56:42:17.183 (uncertainty of 10 arcsec), and analysed the H I absorption complexes with significance exceeding 3 $\sigma$ .

### 3.3 Results

The continuum image of the region around MAXI J1535–571 for the 21 September 2017 observation is shown in Figure 3.1, where the source is detected at high significance ( $> 200\sigma$ ). Residual calibration, deconvolution and amplitude errors remain in our images due to these data being obtained during ASKAP’s early science phase with 12 of 36 active antennas, causing reduced UV coverage, the use of the rapidly evolving `ASKAPsoft` software, and the lack of complete instrumental characterisation that will only improve over time. Figure 3.1 also shows the extragalactic comparison source MGPS J153358–564218 with a measured flux density of  $340 \pm 2$  mJy on 21 September 2017, which remained stable to better than 10% between all the epochs.

In Figure 3.2, we present the 1.34 GHz light curve of MAXI J1535–571 from 21 September to 2 October 2017. During this period we observed two distinct peaks on 21 and 23 September, reaching flux densities  $> 450$  mJy, likely corresponding to separate flaring events. Subsequently, the radio flux density of MAXI J1535–571 gradually decreased, reaching a level of  $\sim 20$  mJy by 2 October.

We downloaded the on-demand X-ray light curves from *MAXI* in the energy range 2.0–20.0 keV to create a hardness-intensity diagram (HID) for MAXI J1535–571, presented in Figure 3.3. From the HID, all our radio observations were taken in the soft-intermediate spectral state (Tao et al., 2018). This confirms that MAXI J1535–571 underwent radio flaring behaviour during the hard-to-soft X-ray

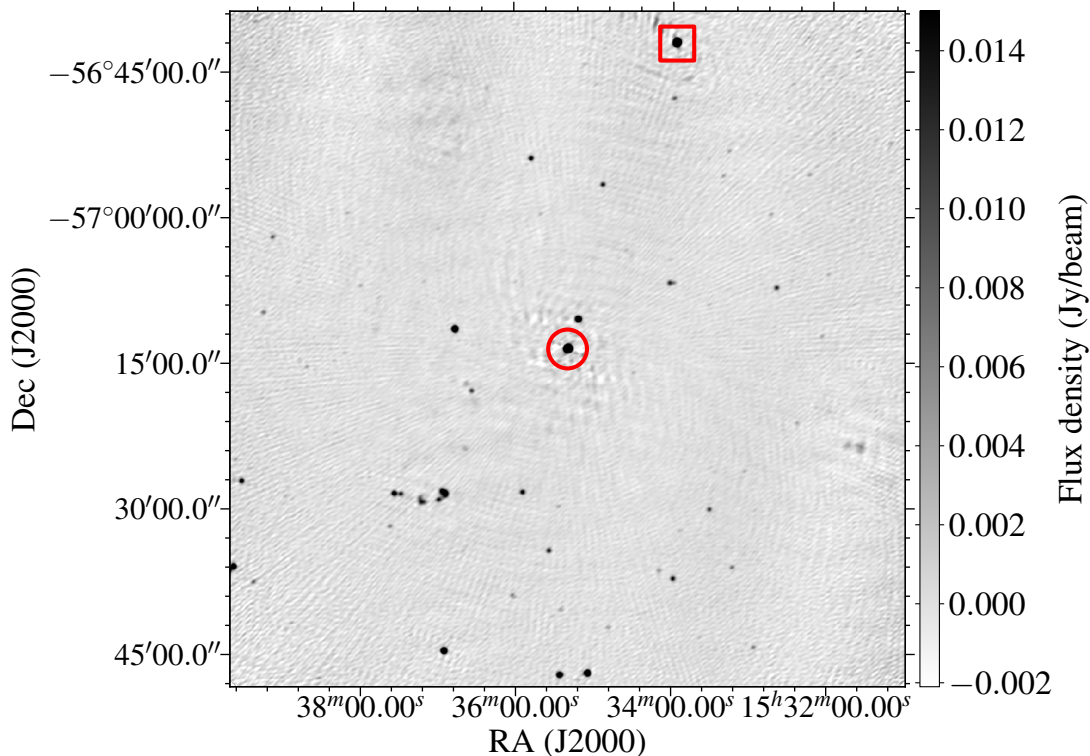


Figure 3.1: 1.34 GHz ASKAP continuum image of our 21 September 2017 observation centered at RA = 15:35:19.71, DEC =  $-57:13:47.58$  with a size of  $1.15^\circ \times 1.15^\circ$ . The positions of MAXI J1535-571 and the comparison extragalactic source MGPS J153358-564218 are indicated by the red circle and square, respectively.

spectral state transition, as is typical for XRBs (Fender et al., 2004).

### 3.3.1 H I absorption spectra

In Figure 3.4, we show the H I spectrum for MAXI J1535-571 for the first epoch (21 September 2017). In the same plot, we also display the spectrum for the extragalactic source MGPS J153358-564218, and the  $3\sigma$  rms noise levels for the spectra of both sources. For both sources, we measured the rms noise per channel from the spectral cube, taking the median noise value in each channel from a number of regions close to the source to mitigate against any faint Galactic H I emission in any given region. The rms noise level for both sources is shown as the dotted line (with their respective red and blue colours) in Figure 3.4, where  $S_\nu$  is the flux density measured from the data cube and  $S_0$  is that measured

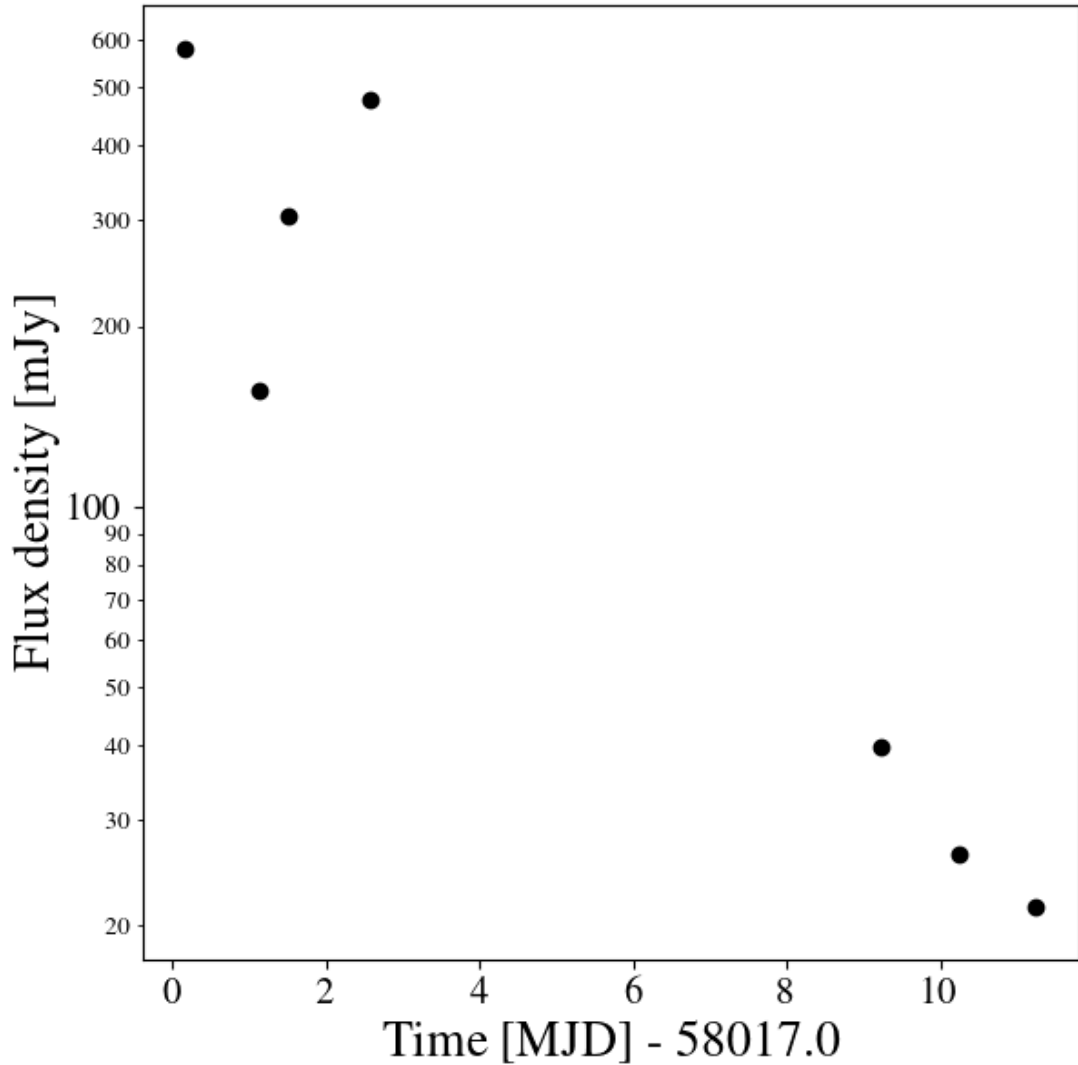


Figure 3.2: ASKAP light curve of MAXI J1535–571 at 1.34 GHz. The peak flux density of MAXI J1535–571 exceeded 500 mJy.

from the continuum image via the `IMFIT` task. In the case of MAXI J1535–571, we observed a significant ( $> 3\sigma$ ) H I absorption complex with a maximum negative velocity of  $-69 \pm 4 \text{ km s}^{-1}$ . In the second epoch, the H I absorption lines are weaker due to the lower flux density. Therefore, we have not used the second epoch because the sensitivity was not high enough to reliably determine

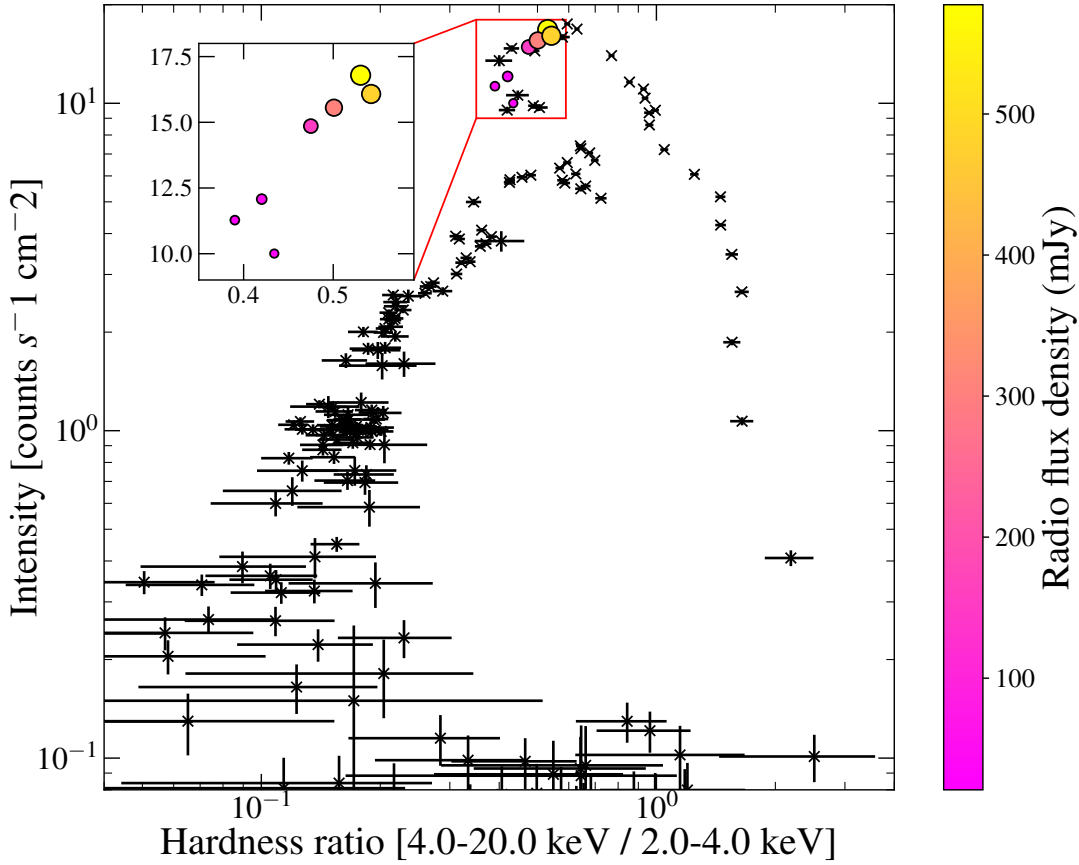


Figure 3.3: Hardness intensity diagram (HID) for the 2017 outburst of MAXI J1535–571. The HID is made from public *MAXI* data, where intensity is the count rate in the energy range 2.0–20.0 keV, and the hardness ratio is the ratio of count rates in the 4.0–20.0 keV and 2.0–4.0 keV energy bands (Tao et al., 2018). Those X-ray data-points with simultaneous radio detections are highlighted with circles, whose size and color correspond to the measured radio flux density (zoomed in the inset of the plot). The radio flare occurred during the hard-to-soft X-ray spectral state transition.

the maximum velocity out to which absorption could be observed. The third and fourth epochs are excluded from this analysis due to the presence of RFI in the HI spectrum.

For Galactic longitudes  $270^\circ \leq l \leq 360^\circ$ , the expected radial velocities from Galactic rotation are negative. Figure 3.5 shows the calculated variation of velocity of the local standard of rest ( $V_{\text{LSR}}$ ) with distance from the Sun ( $d$ ) in the direction of MAXI J1535–571. For the determination of  $V_{\text{LSR}}$ , we presumed the

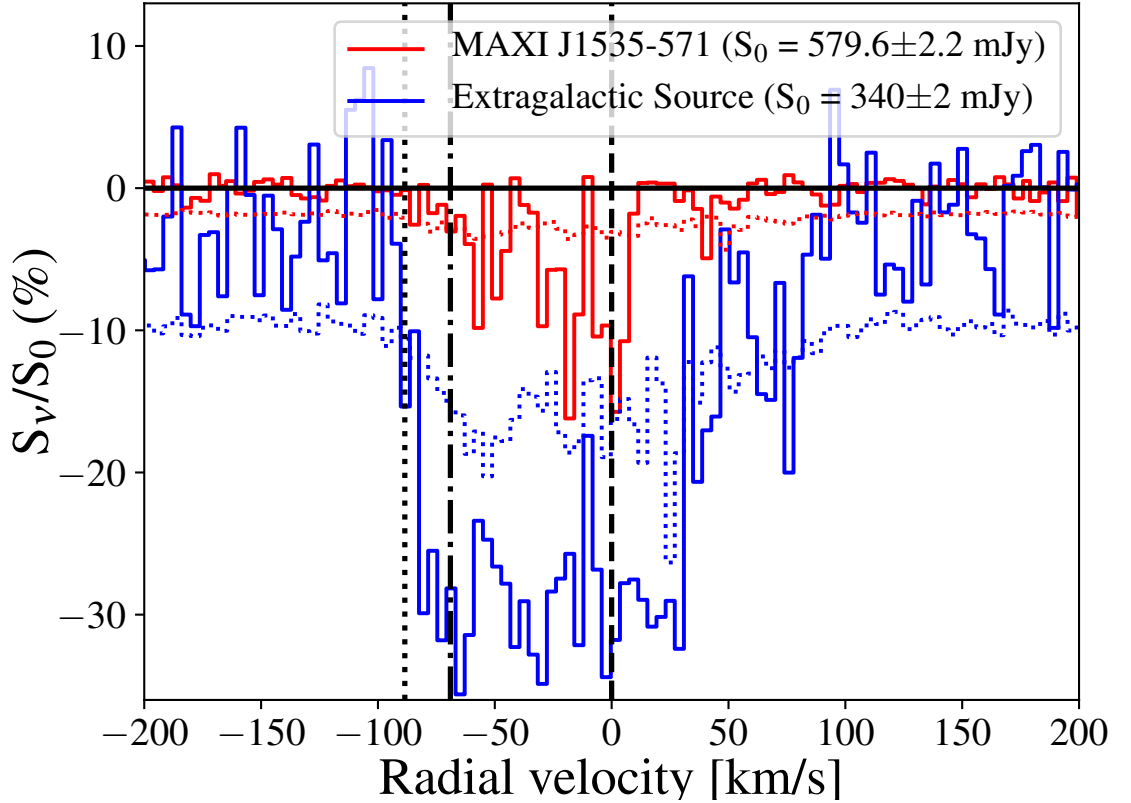


Figure 3.4: The H I absorption spectrum observed from MAXI J1535–571 on 21 September 2017, when the source was brightest ( $S_0 = 579.6 \pm 2.1$  mJy). Spectra of MAXI J1535–571 and the extragalactic source MGPS J153358–564218 (in the local standard of rest frame) are displayed in red and blue, respectively.  $S_\nu$  is measured from the data cube and  $S_0$  is determined from the continuum image. The solid black horizontal line shows the zero flux level. The red and blue dotted lines represent the  $3\sigma$  rms noise levels (calculated directly from individual channel image in the spectral cube) for MAXI J1535–571 and the extragalactic source, respectively. The latter is higher due to being located further out in the primary beam. The dashed vertical line shows the rest velocity. The maximum negative velocity of significant ( $> 3\sigma$ ) absorption in the MAXI J1535–571 spectrum (dash-dotted vertical line at  $-69$  km s $^{-1}$ ) places a lower limit on the source distance of  $4.1_{-0.5}^{+0.6}$  kpc. The maximum negative velocity derived from the extragalactic source spectrum (dotted vertical line at  $-89$  km s $^{-1}$ ) constrains the upper limit on the distance of MAXI J1535–571 to be that of the tangent point at  $6.7_{-0.2}^{+0.1}$  kpc.

Galactic rotation curve to be flat with a circular velocity ( $V_0$ ) and a Galactic centre distance ( $R_0$ ) of  $240 \pm 8$  km s $^{-1}$  and  $8.34 \pm 0.16$  kpc, respectively (Reid et al.,

2014).  $V_{\text{LSR}}$  is symmetric about the tangent point distance ( $R = R_0 \cos l \equiv 6.7_{-0.2}^{+0.1}$  kpc), and therefore provides two estimates of the distance, near and far, within the solar circle. Beyond  $d = 13.2$  kpc, where  $R > R_0$ ,  $V_{\text{LSR}}$  becomes positive. If MAXI J1535–571 is at or beyond the tangent point, velocities of its absorption spectrum are independent of its distance until  $R > R_0$ . Therefore, in that case we would not be able to place strong constraints on its distance, other than being located beyond the tangent point.

Furthermore, the gas clouds in the Milky Way may not all be following circular motions. Therefore, we have followed the prescription given by Wenger et al. (2018), who used the rotation curve given by Reid et al. (2014) with a Monte Carlo approach<sup>3</sup> to derive a more robust kinematic distance and uncertainty. Using the observed maximum negative absorption velocity and the methodology of Wenger et al. (2018), we constrain the near and far source distances to be  $4.1_{-0.5}^{+0.6}$  kpc and  $9.3_{-0.6}^{+0.5}$  kpc, respectively.

The HI absorption spectrum of the extragalactic source MGPS J153358–564218 (Figure 3.4) shows  $> 3\sigma$  significance absorption out to a maximum negative velocity of  $-89 \pm 4$  km s<sup>-1</sup>, which is due to more distant gas clouds, and consistent (within uncertainties) with the tangent point velocity of  $-92_{-9}^{+8}$  km s<sup>-1</sup> (obtained following Reid et al. 2014 and Wenger et al. 2018). Absorption at the tangent point velocity is not seen towards MAXI J1535–571, implying that MAXI J1535–571 should be located closer than the tangent point distance of  $6.7_{-0.2}^{+0.1}$  kpc (Figure 3.5) and must therefore be at (or slightly beyond) the near kinematic distance.

### 3.4 Discussion

As outlined in Section 3.3.1, we place a lower limit of  $4.1_{-0.5}^{+0.6}$  kpc on the distance to MAXI J1535–571. The more negative radial velocities detected towards the extragalactic source must therefore be coming from larger distances, out to at

---

<sup>3</sup><http://www.treywenger.com/kd/index.php>

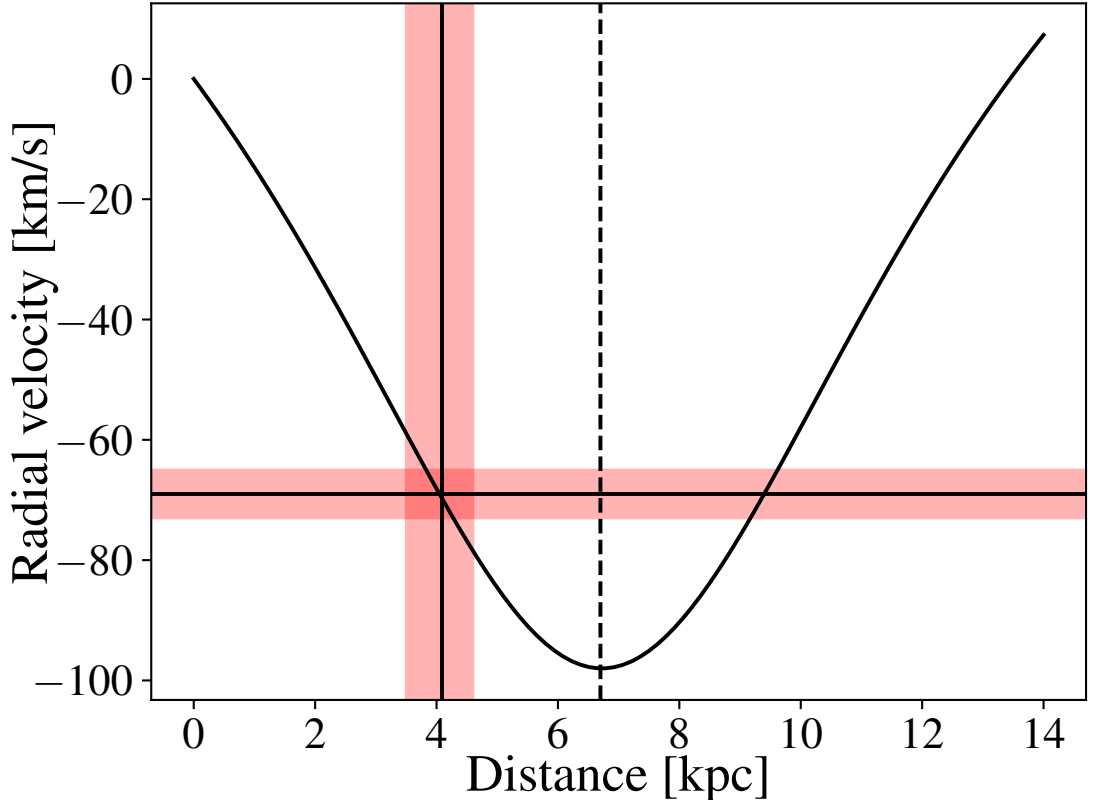


Figure 3.5: The variation of the predicted velocity (for circular rotation) of the local standard of rest ( $V_{\text{LSR}}$ ) as a function of distance from the Sun ( $d$ ), in the direction of MAXI J1535–571. The horizontal line shows the velocity of  $-69 \pm 4$  km s $^{-1}$ , measured from the HI absorption complex of the first epoch. The vertical line displays the most likely distance ( $4.1^{+0.6}_{-0.5}$  kpc) to MAXI J1535–571. The shaded region across both the lines highlight the respective error regions, as derived from the Monte Carlo approach of Wenger et al. (2018). The dashed line displays the position of the tangent point, which is our robust distance upper limit of  $6.7^{+0.1}_{-0.2}$  kpc.

least the tangent point at  $6.7^{+0.1}_{-0.2}$  kpc. If we discount the unlikely scenario that all absorption at intermediate velocities comes from gas clouds more distant than the tangent point, we find a most probable distance of  $4.1^{+0.6}_{-0.5}$  kpc for MAXI J1535–571. In the following subsections we discuss the implications of these distance constraints.

### 3.4.1 Spectral state transition luminosity

According to Kalemci et al. (2013), the soft-to-hard spectral state transition in black hole XRBs usually occurs between 0.3 and 3 per cent of the Eddington luminosity. A *Swift*/XRT observation on 29 April 2018 was identified as the point of the soft-to-hard spectral state transition (Tao et al., 2018), with an unabsorbed X-ray flux of  $\sim 6 \times 10^{-12} \text{ erg cm}^{-2} \text{ s}^{-1}$ . Using our distance estimates, and assuming a typical black hole mass of  $8 \pm 1 M_{\odot}$  (Kreidberg et al., 2012), we calculate a transition luminosity of  $1.2 - 3.4 \times 10^{-5}$  times the Eddington luminosity, which is much lower than is typical for black hole XRBs (Kalemci et al., 2013).

Such a peculiar behavior has been seen in a few other sources, and there are a few possible explanations. Vahdat Motlagh et al. (2019) hypothesised that a new episode of accretion during an outburst decay could launch a new soft state, with a lower transition luminosity than the normal 0.3 – 3 % of the Eddington luminosity. Alternatively, Petrucci et al. (2008) and Begelman & Armitage (2014) suggested that low viscosity or low magnetic fields in the accretion disk could also decrease the state transition luminosity.

### 3.4.2 Peak X-ray luminosity

Stiele & Kong (2018) observed a peak absorbed X-ray flux of  $\sim 3.7 \times 10^{-7} \text{ erg cm}^{-2} \text{ s}^{-1}$  from MAXI J1535–571 in the energy range 0.6–10 keV. Using our derived distance of  $4.1_{-0.5}^{+0.6} \text{ kpc}$ , this corresponds to an absorbed luminosity of  $7.5 - 19.9 \times 10^{38} \text{ erg s}^{-1}$ . For a compact object of typical black hole mass  $8 \pm 1 M_{\odot}$  (Kreidberg et al., 2012), this corresponds to  $> 78$  per cent of the Eddington luminosity. Tao et al. (2018) reported that over the peak of the outburst, the X-ray spectrum could be fit with a slim disk model, suggesting a luminosity close to the Eddington luminosity. Their conclusion is therefore consistent with our distance estimate.

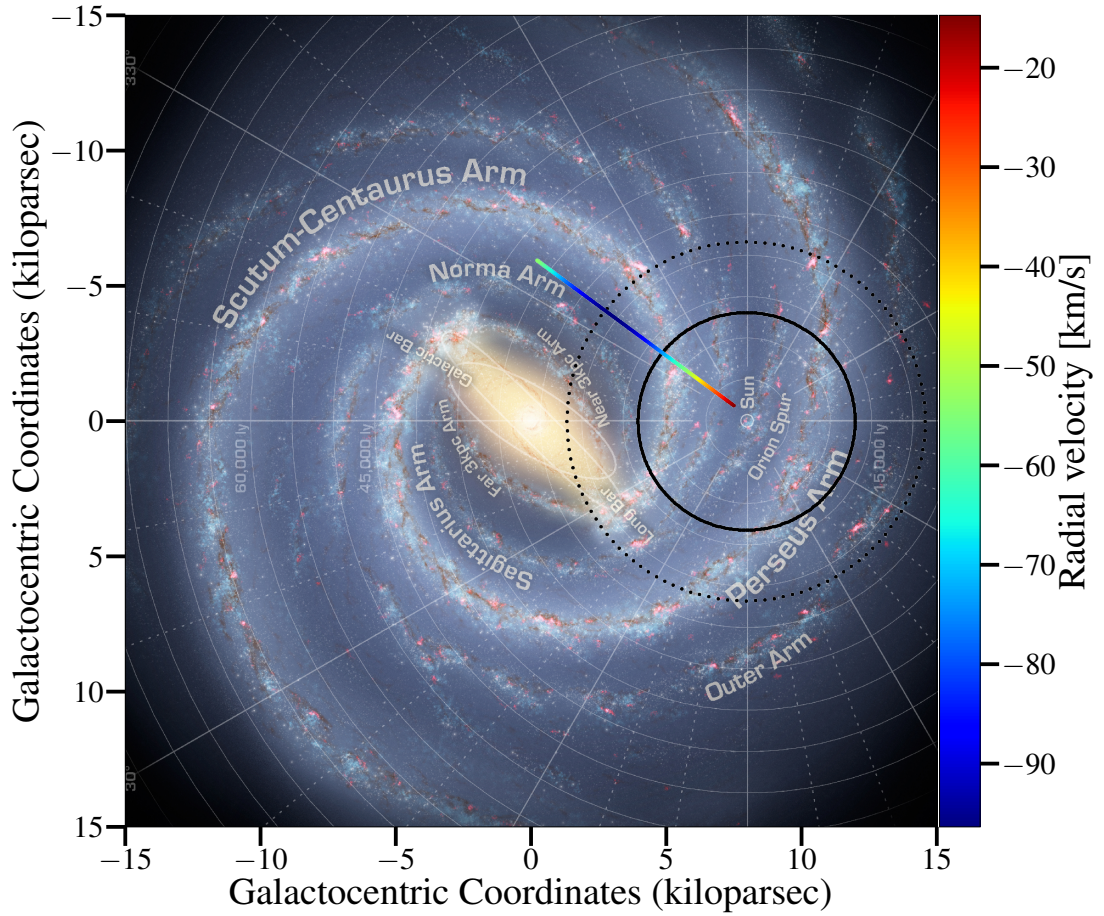


Figure 3.6: The variation of  $V_{\text{LSR}}$  with distance from the Sun along the line of sight to MAXI J1535–571, overlaid on a schematic of the Milky Way. The Scutum-Centaurus arm of the Milky Way lies in-between the Sun and MAXI J1535–571. The colour bar displays the variation of the predicted velocity (for circular rotation) of the local standard of rest ( $V_{\text{LSR}}$ ) as a function of distance from the Sun ( $d$ ), in the direction of MAXI J1535–571. The thick and the dashed circles correspond to the most likely distance ( $4.1^{+0.6}_{-0.5}$  kpc) and the robust upper limit ( $6.7^{+0.1}_{-0.2}$  kpc), respectively. We place MAXI J1535–571 beyond the Scutum-Centaurus arm but within  $6.7^{+0.1}_{-0.2}$  kpc.

### 3.4.3 Line-of-sight hydrogen column density

From our distance constraints and Galactic latitude ( $b$ ), we infer MAXI J1535–571 to lie 0.08–0.13 kpc below the Galactic plane, well within the scale height of

the Milky Way disk ( $\sim 0.3$  kpc; Mandel, 2016). Using X-ray spectroscopy, the absorption column density ( $n_{\text{H}}$ ) towards MAXI J1535–571 was found to be in the range  $2.8 - 5.6 \times 10^{22} \text{ cm}^{-2}$  (Miller et al., 2018; Stiele & Kong, 2018; Tao et al., 2018), which is consistent with the predicted Galactic absorption value of  $2.0 \pm 1.0 \times 10^{22} \text{ cm}^{-2}$  in the direction of MAXI J1535–571, calculated from the extinction maps and estimated correlation between  $n_{\text{H}}$  and  $A_{\text{V}}$  (Schlafly & Finkbeiner, 2011; Bahramian et al., 2015; Foight et al., 2016). The high value of  $n_{\text{H}}$  for MAXI J1535–571 is probably due to enhanced absorption in the Scutum-Centaurus arm of the Milky Way, through which we view MAXI J1535–571 (Figure 3.6).

#### 3.4.4 Radio/X-ray correlation and the source distance

The observed distance constraints will help in understanding the radio/X-ray correlation for MAXI J1535–571. Russell et al. (2017b) considered a distance of 6.5 kpc for MAXI J1535–571 and calculated the corresponding radio luminosity (at 5 GHz) and X-ray luminosity (in 2–10 keV). The authors have shown that MAXI J1535–571 is located near the radio-faint track of the black hole X-ray binaries in the radio/X-ray correlation diagram (magenta cross symbol in Figure 3.7). The limits determined on the distance in this study narrowed down the uncertainty in the position of MAXI J1535–571 on the radio/X-ray correlation diagram (cyan plus symbol in Figure 3.7). The source is located at the top of the radio-faint branch of the black hole X-ray binaries in the radio/X-ray correlation diagram.

#### 3.4.5 Natal kick and the source distance

In the absence of direct kick measurements, determining the distance of the source is important to understand the origin (direct-collapse or supernova explosion) of the compact object in the X-ray binary (Jonker & Nelemans, 2004). It is discovered that height of the X-ray binary above the Galactic plane provides us information on the velocity kick that the compact object receives at the time of birth (White & van Paradijs, 1996; Repetto et al., 2012, 2017). Using the current

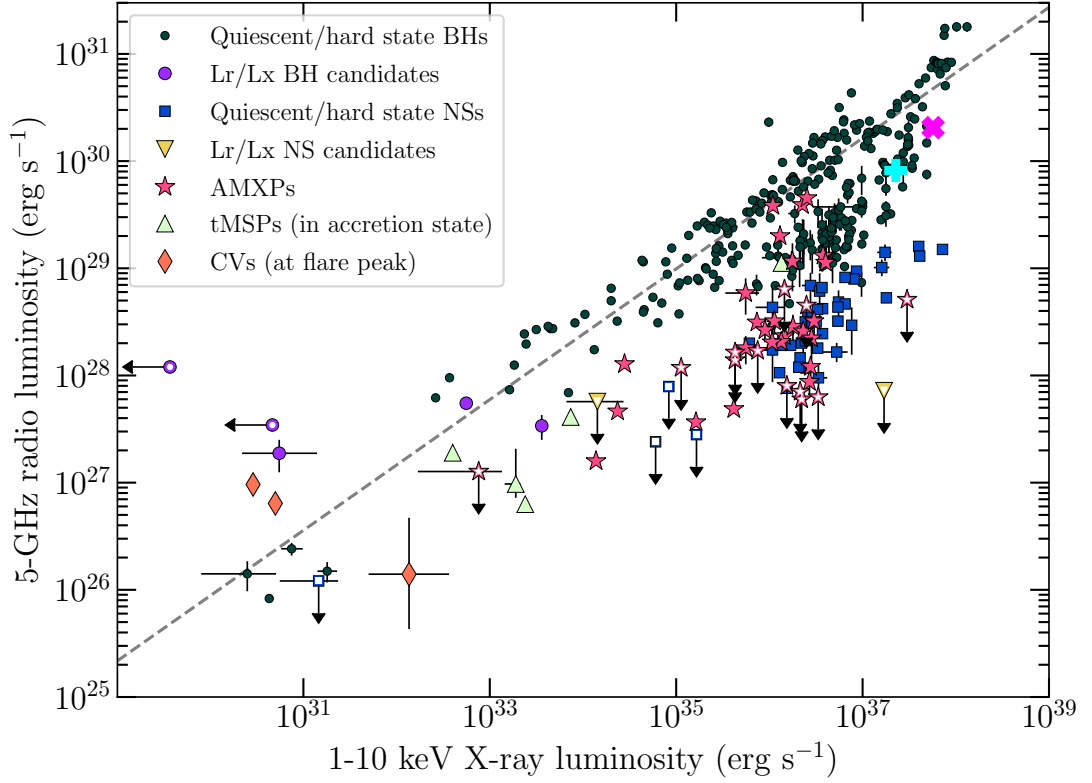


Figure 3.7: Radio–X-ray luminosity correlations for BH-XRBs and other classes of accreting compact objects including, neutron star XRBs and outbursting cataclysmic variables. The plot is adapted from Bahramian et al. (2018) and the best-fit correlation for black hole LMXBs is shown with the dashed line ( $\beta = 0.61$ ; Gallo et al., 2014). The radio/X-ray correlation for MAXI J1535–571 determined by Russell et al. (2017b) using a source distance of 6.5 kpc is shown with the magenta cross symbol. The radio/X-ray correlation obtained using our distance estimates is indicated by the cyan plus symbol. Our distance constraints help in understanding the nature of the compact object.

distance estimates, the height of MAXI J1535–571 (above the Galactic plane) is found to be in the range -0.08 to -0.13 kpc, whereas the scale height of the Milky Way disk is  $\sim 0.3$  kpc (Mandel, 2016). This suggests that the system received a kick that took it out of the Plane, but is now moving back through the Plane - we just happen to be observing it at the right moment in time.

## 3.5 Summary

In this chapter, we measured a kinematic distance to the black hole candidate XRB MAXI J1535–571 using an HI absorption spectrum obtained from ASKAP early science observations. A comparison extragalactic source in the same field shows HI absorption out to  $-89 \pm 4 \text{ km s}^{-1}$  (consistent with coming from the tangent point at  $6.7_{-0.2}^{+0.1} \text{ kpc}$ ), whereas MAXI J1535–571 shows no significant HI absorption beyond  $-69 \pm 4 \text{ km s}^{-1}$ . Therefore, the most probable distance to the source is  $4.1_{-0.5}^{+0.6} \text{ kpc}$ , with a robust upper limit of  $6.7_{-0.2}^{+0.1} \text{ kpc}$ .

Our distance constraints have confirmed that MAXI J1535–571 was accreting close to the Eddington rate at the peak of the outburst, in agreement with X-ray spectral fitting results by Tao et al. (2018). We also demonstrate that the soft-to-hard X-ray spectral state transition in MAXI J1535–571 occurred at a very low fraction ( $1.2 - 3.4 \times 10^{-5}$ ) of the Eddington luminosity, which could either be due to a second episode of accretion partway through the outburst decay, or to a low viscosity and magnetic field in the accretion disk.

This chapter also highlights the importance of modern radio telescopes such as ASKAP, which provide both high sensitivity and a wide field-of-view. In this project, the wide field-of-view of ASKAP afforded us the opportunity to study the HI absorption spectrum of both MAXI J1535–571 and a comparison extragalactic source within the same observation. The high sensitivity and high spectral resolution of ASKAP allowed us to extract the HI spectrum from just two hours of observation, placing stringent constraints on the distance to MAXI J1535–571.

In the next chapter, we refine the approach developed in this chapter, and determine the kinematic distance to black hole candidate XRB MAXI J1348–630 using further observations with the full ASKAP array. To check the robustness of our distance measurements, we also observed the source with MeerKAT, and compare the results from the two SKA precursor interferometers.

# Chapter 4

## Measuring a kinematic distance to MAXI J1348–630 using the SKA precursors ASKAP and MeerKAT

This chapter is adapted from J. Chauhan, J. C. A. Miller-Jones, W. Raja, J. R. Allison, P. F. L. Jacob, G. E. Anderson, F. Carotenuto, S. Corbel, R. Fender, A. Hotan, M. Whiting, P. A. Woudt, B. Koribalski, and E. Mahony (2021), “Measuring the distance to the black hole candidate X-ray binary MAXI J1348–630 using HI absorption”, *Monthly Notices of the Royal Astronomical Society*, Letters, Volume 501, Issue 1, page L60–L64, DOI: <https://doi.org/10.1093/mnrasl/slaa195>

The chapter is marginally different from the published article due to some minor changes, such as the omission of some introductory text (already discussed in Chapter 1), referencing to earlier chapters to maintain the consistency within this thesis.

Following the approach outlined in Section 1.6.1 and Chapter 3, we monitored a second BH-XRB MAXI J1348–630 in outburst with the full ASKAP array

to constrain the kinematic distance to this new source. MAXI J1348–630 was slightly fainter ( $\sim 155$  mJy) in comparison to MAXI J1535–571 (Chapter 3). In this chapter, We present H I absorption spectra of the black hole candidate X-ray binary MAXI J1348–630 using the ASKAP and MeerKAT. We monitored the source with MeerKAT also to demonstrate the same technique with MeerKAT, which does not have as large a field of view as ASKAP (about  $1 \text{ deg}^2$  rather than  $30 \text{ deg}^2$ ), but has higher sensitivity (albeit lower spectral resolution at the time of the observations). So, it’s rather a proof-of-concept observation with MeerKAT. We also refined our technique from Chapter 3 by building a stacked spectrum of several nearby extragalactic comparison sources rather than using a single comparison source. This allowed us to show that the XRB was at the near distance, and certainly this side of the tangent point. The MeerKAT H I spectrum of MAXI J1348–630 (obtained from the older, low-resolution 4k mode) is consistent with the re-binned ASKAP spectrum, highlighting the potential for MeerKAT to perform routine distance measurements for XRBs via H I absorption now that the higher-spectral resolution correlator mode is available. The distance measurement allowed us to quantify the peak luminosity of the outburst, and the luminosity of the spectral state transition, which were relatively typical for BH-XRB outbursts. In conjunction with existing X-ray data, this allowed us to refine the estimated BH mass.

## 4.1 MAXI J1348–630

On 2019 January 26, the Monitor of All-sky X-ray Image<sup>1</sup> (*MAXI*; Matsuoka et al., 2009) discovered an uncatalogued XRB at a position RA (J2000) =  $13^{\text{h}}48^{\text{m}}12.79^{\text{s}} \pm 0.03^{\text{s}}$  Dec (J2000) =  $-63^{\text{d}}16'28.48'' \pm 0.04''$  (Galactic coordinates:  $l = 309.26407$  deg,  $b = -1.10297$  deg; Russell et al. 2019b), referred to as MAXI J1348–630 (Yatabe et al., 2019). The optical counterpart of the source was detected by Denisenko et al. (2019), and the outburst was subsequently observed across the electromag-

---

<sup>1</sup><http://maxi.riken.jp/top/index.html>

netic spectrum (e.g. Carotenuto et al., 2019; Chauhan et al., 2019a; Kennea & Negoro, 2019). The system is believed to harbour a stellar-mass black hole (Russell et al., 2019b; Zhang et al., 2020a), although the key system parameters are poorly constrained.

## 4.2 Observations and Data reduction

### 4.2.1 ASKAP

ASKAP (Hotan et al., 2014) observed MAXI J1348–630 on 2019 February 13 for 9.91 hours (on source exposure 8.39 hours) from 13:22–23:16 UTC, using the full array of 36 dishes, with 36 overlapping beams. The large field of view ( $\approx 30 \text{ deg}^2$ ) and high angular resolution ( $\sim 25''$ ) of ASKAP allow us to simultaneously detect the HI absorption towards both MAXI J1348–630 and a set of nearby extragalactic sources (Table 4.1), enabling a discrimination between near and far kinematic distances. Our observation was performed at a central frequency of 1.34 GHz, with a total bandwidth of 288 MHz divided into 15368 fine channels, each of which has a frequency resolution of 18.519 kHz (velocity resolution  $3.9 \text{ km s}^{-1}$ ).

For reducing our multiple-beam full array data on MAXI J1348–630, we used the ASKAP data analysis software, `ASKAPsoft`<sup>2</sup>. Although our MAXI J1348–630 data have more antennas and beams, we follow a similar calibration procedure to that described in Chauhan et al. (2019b). However, for generating the spectral cube from the calibrated, continuum-subtracted measurement set created by `ASKAPsoft`, we used the `TCLEAN` task in the Common Astronomy Software Application (`CASA` v5.1.2-4; McMullin et al., 2007) to ensure we could use the same procedure to extract both MeerKAT and ASKAP spectra, and to allow quick optimisation of our imaging parameters (e.g. *uv*-range, deconvolution depth, deconvolver), given the demand on supercomputing time to run `ASKAPsoft`. We

---

<sup>2</sup><http://www.atnf.csiro.au/computing/software/askapsoft/sdp/docs/current/index.html>

Table 4.1: Co-ordinates and 1.42-GHz ASKAP flux densities of MAXI J1348–630 and our extragalactic comparison sources. Positions taken from [1] Russell et al. (2019b); [2] Murphy et al. (2007).

| Source Name             | RA (J2000)<br>(hh:mm:ss) | Dec (J2000)<br>(dd:mm:ss) | Flux Density <sup>a</sup><br>(mJy) |
|-------------------------|--------------------------|---------------------------|------------------------------------|
| MAXI J1348–630 [1]      | 13:48:12.79              | –63:16:28.48              | 155 ± 2                            |
| MGPS J134353–624941 [2] | 13:43:53.13              | –62:49:41.4               | 86 ± 1                             |
| MGPS J134551–634755 [2] | 13:45:51.50              | –63:47:55.7               | 104 ± 1                            |
| MGPS J134559–635023 [2] | 13:45:59.85              | –63:50:23.1               | 79 ± 1                             |
| MGPS J134625–632600 [2] | 13:46:25.73              | –63:26:00.7               | 71 ± 1                             |
| MGPS J135145–635836 [2] | 13:51:45.91              | –63:58:36.8               | 114 ± 1                            |
| MGPS J135236–631600 [2] | 13:52:36.51              | –63:16:00.0               | 141 ± 1                            |
| MGPS J135401–633032 [2] | 13:54:01.09              | –63:30:32.1               | 81 ± 1                             |
| MGPS J135546–632642 [2] | 13:55:46.25              | –63:26:42.5               | 1181 ± 2                           |

<sup>a</sup>  $1\sigma$  errors are quoted, calculated by adding in quadrature the error on the Gaussian fit and the rms noise in the image.

produced a spectral sub-cube of 378 channels centered at the rest frequency (1420.4 MHz) of the H I line using a Briggs weighting parameter (robustness) of 0.5, and adopting a minimum baseline length of 700 m.

From the ASKAP spectral cube, we extracted the H I absorption spectrum for MAXI J1348–630 and the eight extragalactic sources listed in Table 4.1, by measuring the brightness in each frequency channel at the position corresponding to the peak flux density (determined from the continuum image). We used the `IMFIT` task in `CASA` to measure source flux densities and  $1\sigma$  uncertainties from the continuum images.

## 4.2.2 MeerKAT

MAXI J1348–630 was monitored as part of the MeerKAT Large Survey Project for slow transients (ThunderKAT; Fender et al. 2016), the first results of which were recently published by Carotenuto et al. (2019). Here we use data from 2019

Table 4.2: Details of time-resolved analysis of our ASKAP observation of MAXI J1348–630 on 13 February 2019.

| Time Bin | Start time (hh:mm:ss) | MJD <sup>a</sup>  | Flux Density <sup>b</sup> (mJy) |
|----------|-----------------------|-------------------|---------------------------------|
| TW01     | 13:22:06.6            | 58527.578 ± 0.021 | 208.9 ± 10.5                    |
| TW02     | 14:22:29.6            | 58527.619 ± 0.020 | 231.2 ± 11.6                    |
| TW03     | 15:22:22.6            | 58527.661 ± 0.020 | 252.1 ± 12.6                    |
| TW04     | 16:29:53.7            | 58527.704 ± 0.016 | 242.4 ± 12.1                    |
| TW05     | 17:29:56.7            | 58527.745 ± 0.016 | 200.5 ± 10.1                    |
| TW06     | 18:29:49.8            | 58527.787 ± 0.016 | 170.9 ± 8.6                     |
| TW07     | 19:29:52.8            | 58527.829 ± 0.016 | 149.6 ± 7.5                     |
| TW08     | 20:29:55.8            | 58527.870 ± 0.016 | 133.3 ± 6.7                     |
| TW09     | 21:29:59.9            | 58527.912 ± 0.016 | 123.9 ± 6.2                     |
| TW10     | 22:29:52.9            | 58527.954 ± 0.016 | 110.5 ± 5.6                     |

<sup>a</sup> Mid point of our observations.

<sup>b</sup>  $1\sigma$  errors are quoted, calculated by adding in quadrature the  $1\sigma$  error on the Gaussian fit, 5 % systematics on the flux, and the  $1\sigma$  rms noise in the image.

February 09 between 05:08 and 05:23 (UTC), when the source was brightest in the radio ( $486 \pm 2$  mJy at 1.42 GHz; Carotenuto et al. 2021a) and therefore most sensitive to HI absorption. This is also the epoch closest to that observed with ASKAP. MeerKAT provides a field of view of  $0.86 \text{ deg}^2$ , and a spatial resolution of  $\sim 10''$  at 1.42 GHz. Our observations were carried out using 60 MeerKAT antennas, at a central frequency of 1284 MHz, with 860 MHz of bandwidth. Only the 4k correlator mode was available, which gave a spectral resolution of 209 kHz, equal to  $44 \text{ km s}^{-1}$  at 1420.4 MHz. A 2 min observation of PKS B1421–490 either side of the target scan, and a separate 10 min observation of PKS B1934–638, were carried out for reference calibration.

Spectral line data reduction was carried out using a standard procedure that implemented tasks from MIRIAD (Sault et al. 1995). The data were first converted to FITS format using CASA, selecting only channels in the range 10 MHz either side

of 1420.4 MHz (equivalent to radial velocities of  $\pm 2000 \text{ km s}^{-1}$ ). Calibration of the bandpass and flux scale was carried out using PKS B1934–638 (Reynolds 1994b), and the time varying antenna gains using PKS B1421–490. To avoid corrupting the calibration solutions with Galactic HI emission and absorption, the central 20 channels ( $\pm 400 \text{ km s}^{-1}$ ) were flagged and then interpolated from neighbouring channels. Further self-calibration of the MAXI J1348–630 data was carried out to correct the time-varying gain phase, where we have assumed that the effect of wide-field aberration due to sources at the edge of the field of view is negligible. Subtraction of the continuum flux density was carried out in two stages, first by subtracting a CLEAN model of the continuum from the visibilities using the UVMODEL task, and then using UVLIN to remove residual signal. After subtraction of the continuum flux density, a spectral cube was formed within 5 arcmin of MAXI J1348–630 from the continuum-subtracted and calibrated visibilities using a robustness of 0.5, and a minimum baseline length of 700 m. The final spectrum was extracted from the cube, adopting a similar procedure to that described for ASKAP in Section 4.2.1.

### 4.3 Results

In Figure 4.1 we present an ASKAP continuum image of the MAXI J1348–630 field created by mosaicing beams 14, 15, 20 and 21. Residual uncertainties remain around the bright ( $> 1 \text{ Jy}$ ) sources (e.g. extragalactic source MGPS J135546–632642 in Figure 4.1) at the level of 1–2%, due to remaining calibration and deconvolution errors.

We detected MAXI J1348–630 in our ASKAP data with a flux density of  $155 \pm 2 \text{ mJy}$  at 1.42 GHz. We also selected eight extragalactic comparison sources in the field, which are listed in Table 4.1, and also shown in Figure 4.1. At the time of the ASKAP observation, MAXI J1348–630 was transiting from the hard to the soft X-ray spectral state (Tominaga et al., 2020), where many black hole XRBs undergo transient jet ejection events (Fender et al., 2004).

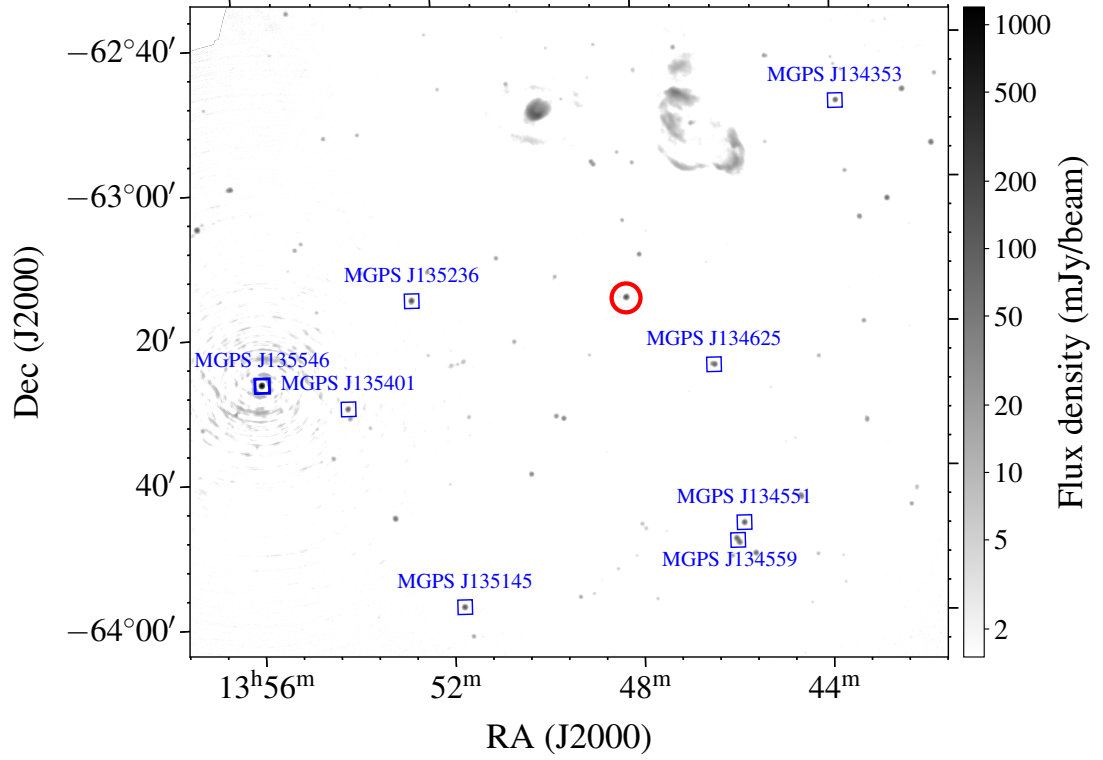


Figure 4.1: A continuum mosaic of the field surrounding MAXI J1348–630, from our 1.34-GHz ASKAP observation on 2019 February 13. The image has a size of  $1.7^\circ \times 1.5^\circ$ , centered at RA =  $13^{\text{h}}49^{\text{m}}19.78^{\text{s}}$ , DEC =  $-63^{\text{d}}20'23.93''$ . The location of MAXI J1348–630 is highlighted with the red circle, and the comparison extragalactic sources (listed in Table 4.1) are indicated by the blue squares.

To characterize the short-timescale variability in MAXI J1348–630 during our ASKAP observation, we generated a continuum image for each of ten hour-long time bins, which are presented in Table 4.2. We present the time-resolved 1.34-GHz light curve of MAXI J1348–630 for beam 20 (for which the source is closest to the centre of the beam) in Figure 4.2. This shows a short-duration flare, peaking at  $252 \pm 13$  mJy at 15:51:32 (UTC), and then gradually decreasing to  $111 \pm 6$  mJy by 22:53:16 (UTC). The radio flux density of the extragalactic sources in the same ASKAP beam remained constant during the observation, verifying that the variation seen from MAXI J1348–630 is intrinsic to the source.

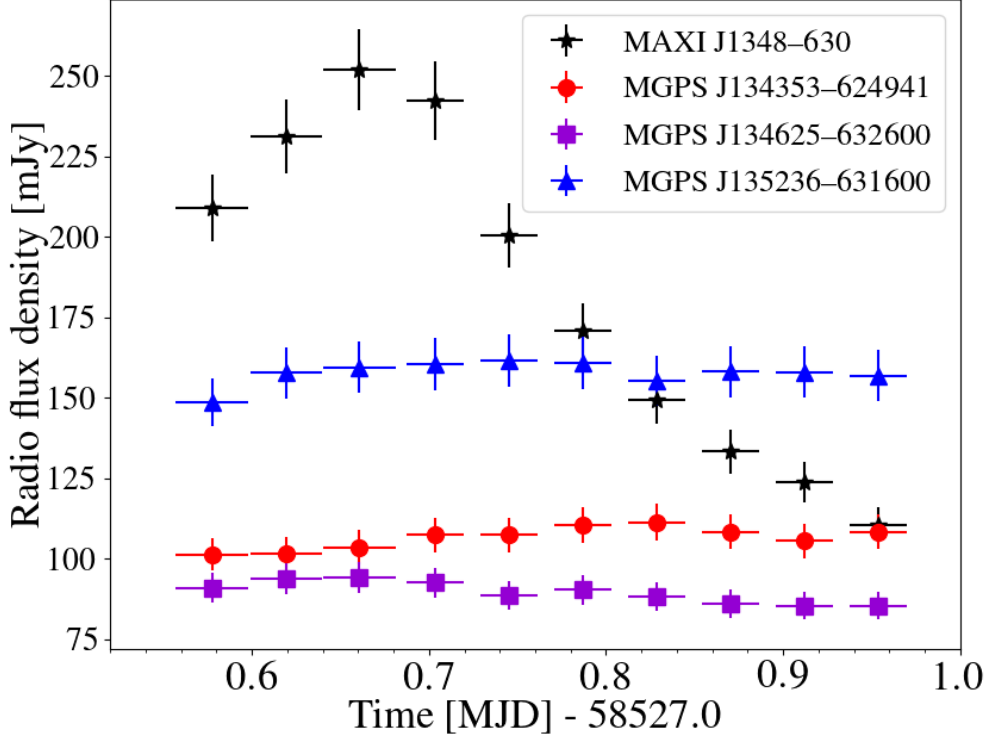


Figure 4.2: The time-resolved 1.34-GHz ASKAP light curve of MAXI J1348–630 (black stars) and the extragalactic sources, for beam 20 only. The flux density of MAXI J1348–630 varies on a  $\sim 1$ -hour time scale, whereas the extragalactic sources remain constant within error bars, demonstrating that the variability observed in MAXI J1348–630 is intrinsic to the source.

### 4.3.1 H I absorption spectra

In Figure 4.3, we show the spectrum for MAXI J1348–630, together with a stacked spectrum for all eight extragalactic sources, and the  $3\sigma$  noise levels measured from nearby regions. We detect significant ( $> 3\sigma$ ) H I absorption complexes out to maximum negative velocities (with respect to the local standard of rest, or LSR) of  $-31 \pm 4 \text{ km s}^{-1}$  and  $-50 \pm 4 \text{ km s}^{-1}$  for MAXI J1348–630 and the extragalactic sources, respectively.

To determine the distance to MAXI J1348–630, we computed the Galactic rotation curve for the Galactic longitude of MAXI J1348–630, and determined the variation of the radial velocity ( $V_{\text{LSR}}$ ) of the LSR with distance from the Sun

(d). For simplicity we assumed that the Galactic rotation curve is flat, that the Milky Way is rotating with a circular velocity ( $V_0$ ) of  $240 \pm 8 \text{ km s}^{-1}$  (Reid et al., 2014), and that the Sun is located at a distance  $R_0 = 8.34 \pm 0.16 \text{ kpc}$  from the Galactic centre (Reid et al., 2014). Figure 4.4 shows that the predicted LSR radial velocities are negative within a few kpc of the Sun, and by comparison with our observed H I spectrum allows us to determine the near distance, the far distance and the tangent point distance ( $R_T = R_0 \cos l \equiv 5.3 \pm 0.1 \text{ kpc}$ ) for this line of sight. If MAXI J1348-630 is at or beyond the tangent point, velocities of its absorption spectrum are independent of its distance until  $R > R_0$ . Therefore, if that were the case we would only be able to constrain it to being located beyond the tangent point.

To determine robust constraints on the kinematic distance, we adopted the recipes suggested by Wenger et al. (2018), who developed a Monte Carlo approach<sup>3</sup> for inferring kinematic distances and associated uncertainties, using the rotation curve provided by Reid et al. (2014). Using this approach, we determined the near and far distances of MAXI J1348-630 to be  $2.2_{-0.6}^{+0.5} \text{ kpc}$  and  $8.4_{-0.6}^{+0.6} \text{ kpc}$ , respectively. The maximum negative absorption velocity (with respect to the LSR) observed for the extragalactic sources ( $-50 \pm 4 \text{ km s}^{-1}$ ) is in good agreement with the tangent point velocity ( $-54 \pm 4 \text{ km s}^{-1}$ ) for this line of sight (within error bars, and calculated using Reid et al. 2014 and Wenger et al. 2018). H I absorption at the tangent point velocity is not observed towards MAXI J1348-630, implying that it must be closer than the tangent point distance of  $5.3 \pm 0.1 \text{ kpc}$ , and thereby most likely placing the source at the near kinematic distance of  $2.2_{-0.6}^{+0.5} \text{ kpc}$ .

#### 4.3.1.1 Comparison with the MeerKAT spectrum

MeerKAT detected MAXI J1348-630 as a bright point source, of flux density  $486 \pm 2 \text{ mJy}$  at  $1.42 \text{ GHz}$  (Carotenuto et al., 2021a). In the 4k correlator mode

---

<sup>3</sup><http://www.treywenger.com/kd/index.php>

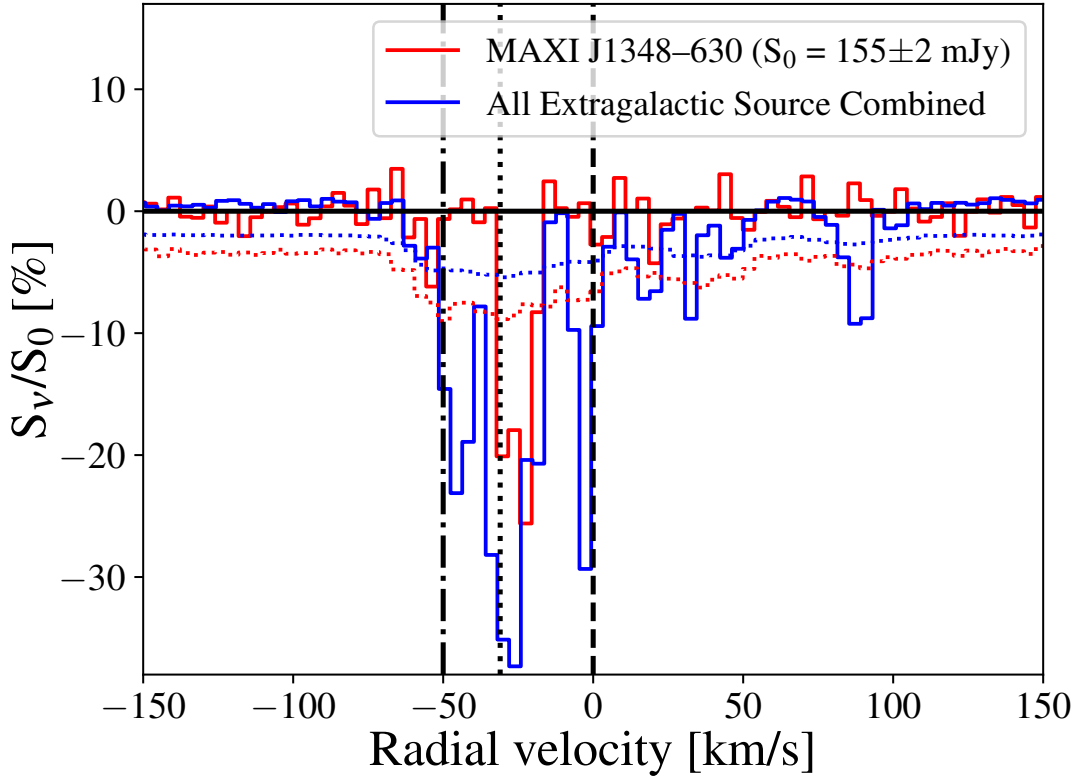


Figure 4.3: The H I absorption complex observed in the direction of MAXI J1348–630 using our ASKAP observation from 2019 February 13.  $S_\nu$  is calculated from the spectral cube, whereas  $S_0$  is measured from the continuum image. The red and blue curves show the H I absorption against MAXI J1348–630 and the stack of the eight extragalactic sources (Table 4.1), respectively. The corresponding dotted lines represent the respective per-channel  $3\sigma$  noise levels (normalized to the source continuum flux density), taken from nearby source-free regions. The black dashed vertical line represents the rest frequency of the H I line. The dotted ( $-31 \text{ km s}^{-1}$ ) and dot-dashed vertical ( $-50 \text{ km s}^{-1}$ ) lines highlight the ( $> 3\sigma$  significant) maximum negative radial velocities (with respect to the LSR) observed from the spectra of MAXI J1348–630, and the merged extragalactic sources, respectively. The maximum negative velocity of  $-31 \pm 4 \text{ km s}^{-1}$  towards MAXI J1348–630 determines the most probable distance as  $2.2_{-0.6}^{+0.5} \text{ kpc}$ , whereas the non-detection of more negative velocities sets a stringent upper limit of the tangent point at  $5.3 \pm 0.1 \text{ kpc}$ .

that was used, MeerKAT had a velocity resolution of  $44 \text{ km s}^{-1}$ , so we rebinned our ASKAP data (with velocity resolution  $3.9 \text{ km s}^{-1}$ ) to match the MeerKAT resolution. The uncertainties on the MeerKAT spectra are smaller, both because the instrument has a lower system temperature, and because MAXI J1348–630

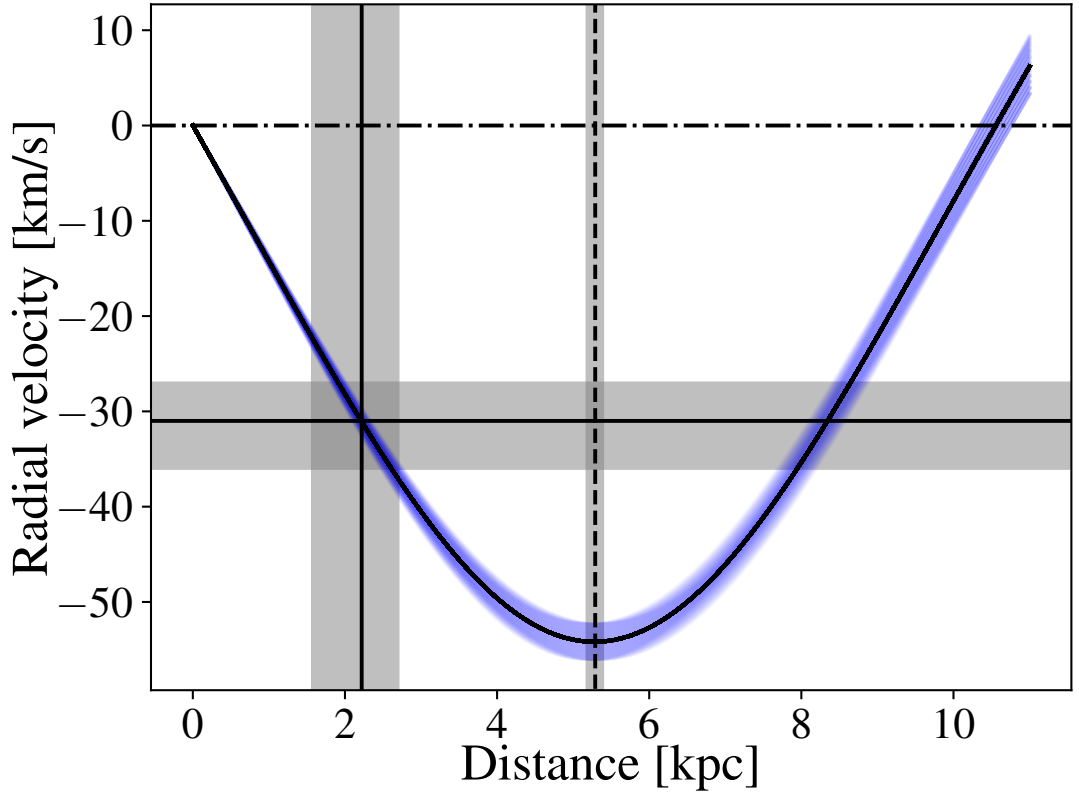


Figure 4.4: The expected variation of the radial velocity of the local standard of rest in the direction of MAXI J1348–630 with distance from the Sun, calculated using the Monte Carlo approach described by Wenger et al. (2018). The black line represents the expected curve, and the blue shaded region shows the effect of incorporating the  $1\sigma$  uncertainties on the Galactic rotation parameters from Reid et al. (2014). The horizontal solid line shows the maximum negative radial velocity (with respect to the LSR) measured from the H I absorption spectrum. The solid and dashed vertical lines show the most likely distance and the tangent point distance, respectively. The grey shaded regions show the  $1\sigma$  uncertainties. The most probable distance of MAXI J1348–630 is the near kinematic distance of  $2.2^{+0.5}_{-0.6}$  kpc.

was brighter at the time of the MeerKAT observations than it was during the ASKAP observations ( $155 \pm 2$  mJy at 1.42 GHz). Nonetheless, as shown in Figure 4.5, the two spectra are consistent within uncertainties.

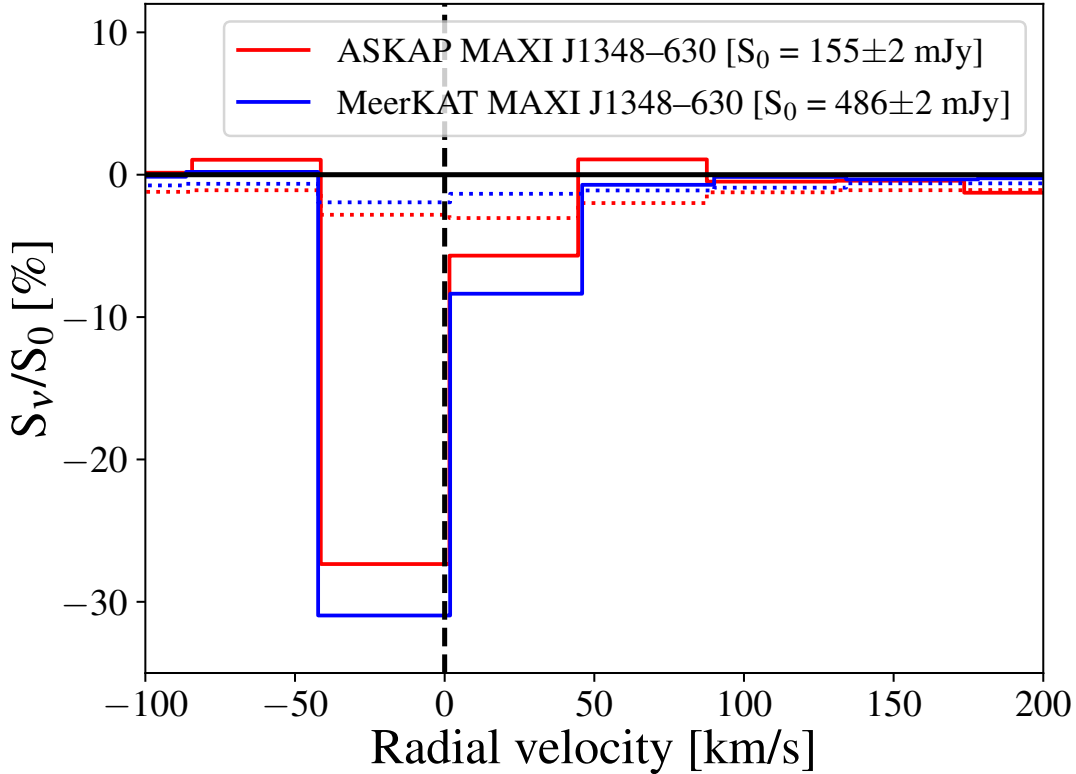


Figure 4.5: The MeerKAT (blue) and rebinned ASKAP (red) H I absorption spectra towards MAXI J1348–630. The  $3\sigma$  rms noise levels for both instruments are shown as dotted lines. The two spectra match well within uncertainties.

## 4.4 Discussion

### 4.4.1 Comparison with other distance constraints

Using the soft-to-hard X-ray spectral state transition luminosity and the measured column density towards the source, Tominaga et al. (2020) placed it in front of the Scutum-Centaurus arm, at  $< 4$  kpc. Our measured H I distance is consistent with (albeit more precise than) this estimate (can be seen in Figure 4.6), and implies a state transition luminosity towards the lower end of their assumed range. Tominaga et al. (2020) further used their measured inner disk radius in the soft X-ray spectral state to constrain the black hole mass as a function of distance, inclination angle and black hole spin. Fitting the X-ray data of Tominaga et al. (2020) with the same `kerrbb` model, and leaving the distance

free to vary within our  $1\sigma$  uncertainty range, we find that the lower limit on the inferred black hole mass (for the case of a non-rotating black hole with an inclination angle of  $0^\circ$ ) reduces to  $3.7M_\odot$ , rising to  $5.8M_\odot$  for an inclination angle of  $60^\circ$ . If the system is at low inclination and slowly rotating, this weakens the evidence for a particularly massive black hole in the system. Although, Tomimaga et al. (2020) also mentioned MAXI J1348–630 is located in front of the Galactic Scutum–Centaurus arm at a distance of  $\sim 3.8$  kpc (for a face-on disk). Their distance constraints are falling in line with our distance estimates of  $2.2_{-0.6}^{+0.5}$  kpc. Our distance constraints are more accurate because we used more direct approach.

Recently, Lamer et al. (2021) measured the geometric distance to MAXI J1348–630 using the dust scattering ring. The authors placed the source at 3.39 kpc with 1.1 % statistical uncertainty and 10 % systematic uncertainty, which is higher than our distance estimates ( $2.2_{-0.6}^{+0.5}$  kpc) but found to be within our robust upper limit of  $5.3 \pm 0.1$  kpc. It could be possible that systematics affecting our HI measurements and the possible reasons would be:

1. There is an absence of intervening HI gas between our distance ( $2.2_{-0.6}^{+0.5}$  kpc) and the X-ray binary, such that we don't see absorption at the corresponding velocities.
2. There are non-circular rotations of the gas clouds that we are not taking into account.
3. Given that both the methods are model dependent, there are unaccounted systematics in one, or both, distance determination methods (HI absorption and X-ray dust scattering).

We are adopting our HI distance for the remainder of the chapter, and that future work will help determine the cause of the discrepancy, particularly any systematics that could impact one technique or the other.

#### 4.4.2 Distance constraint and its implications

Tominaga et al. (2020) studied the complete outburst of MAXI J1348–630 using *MAXI*/GSC data in the 2–20 keV energy range. They found the peak of the outburst to have occurred on 2019 February 09, and the soft-to-hard spectral state transition to have occurred on 2019 April 27 (Tominaga et al., 2020). We used the High Energy Astrophysics Science Archive Research Center (HEASARC) tool WebPIMMS<sup>4</sup> to calculate the bolometric X-ray flux in the energy range 0.01–100 keV from the X-ray flux (2–20 keV) and spectral model determined by Tominaga et al. (2020). We derived a peak unabsorbed X-ray flux of  $2.8 \pm 0.2 \times 10^{-7}$  erg cm<sup>-2</sup> s<sup>-1</sup>, and an unabsorbed flux of  $4.2 \pm 0.5 \times 10^{-8}$  erg cm<sup>-2</sup> s<sup>-1</sup> for the soft-to-hard X-ray spectral state transition, corresponding to luminosities of  $1.6 \pm 0.9 \times 10^{38}$  and  $2.4 \pm 1.4 \times 10^{37}$  erg s<sup>-1</sup>, respectively, at our preferred distance.

If we consider the compact object to be a black hole (Russell et al., 2019b; Zhang et al., 2020a) of typical mass  $8 \pm 1 M_{\odot}$  (Kreidberg et al., 2012), the peak unabsorbed luminosity corresponds to  $0.17 \pm 0.10 L_{\text{Edd}}$ , where  $L_{\text{Edd}}$  is the Eddington luminosity. This is in reasonable agreement with the range of  $0.2\text{--}0.4 L_{\text{Edd}}$  found for canonical black hole XRBs (McClintock & Remillard, 2009). We further found that the system transitioned from the soft to the hard X-ray spectral state at  $0.025 \pm 0.015 L_{\text{Edd}}$ , consistent with the range of  $0.003\text{--}0.03 L_{\text{Edd}}$  determined by Maccarone (2003), Kalemci et al. (2013) and Vahdat Motlagh et al. (2019) for typical black hole XRBs.

#### 4.4.3 Future X-ray binary monitoring

Over the past year, MeerKAT has conducted weekly XRB monitoring (e.g. Bright et al., 2020; Tremou et al., 2020; Williams et al., 2020) under the large survey project ThunderKAT (Fender et al., 2016). However, the low spectral resolution limited the potential for HI studies. The recent correlator upgrade (providing 32K spectral channels with a velocity resolution of  $6.1$  km s<sup>-1</sup>) enables spectral

---

<sup>4</sup><https://heasarc.gsfc.nasa.gov/cgi-bin/Tools/w3pimms/w3pimms.pl>

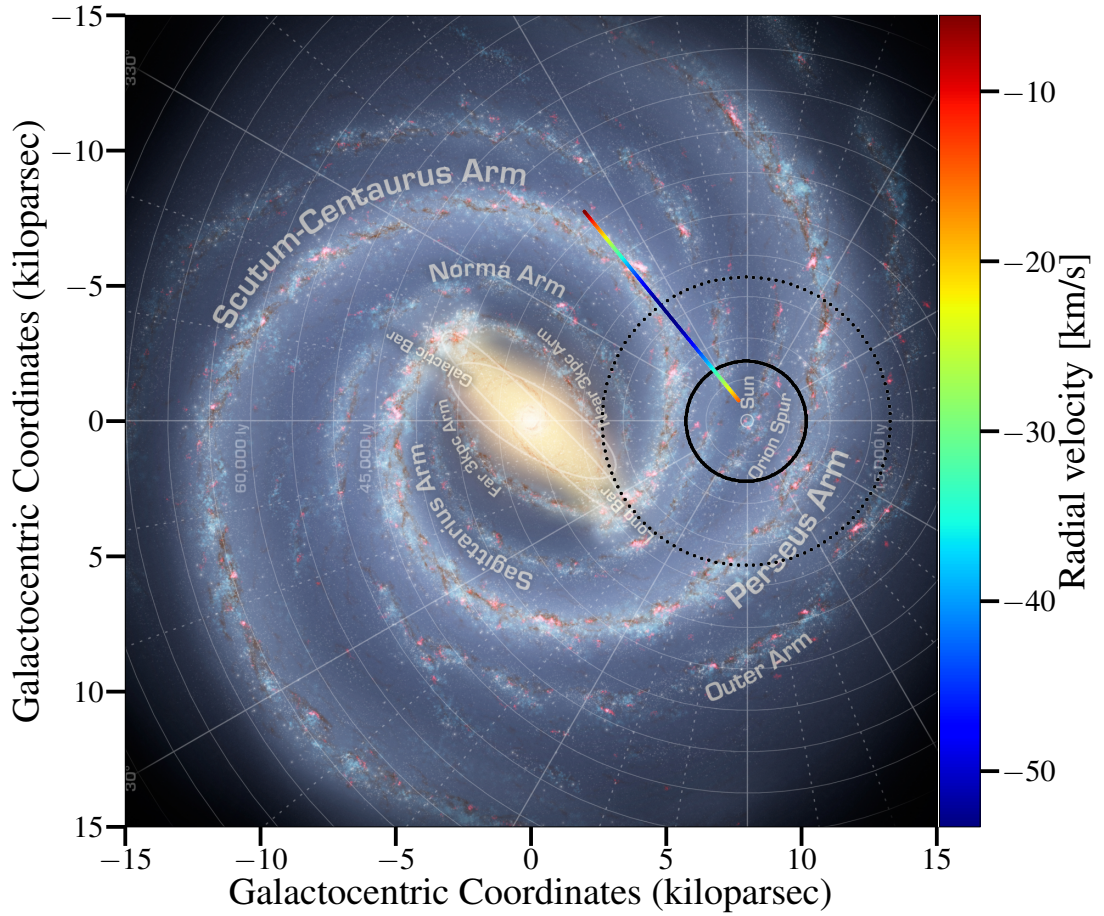


Figure 4.6: The variation of the theoretically predicted velocity (for circular motion) of the local standard of rest ( $V_{\text{LSR}}$ ) with distance from the Sun in the direction of MAXI J1348–630, overlaid on a cartoon diagram of the Milky Way. MAXI J1348–630 lies tangential to the Scutum-Centaurus arm of the Milky Way. The colour bar shows the predicted variation of the  $V_{\text{LSR}}$  as a function of distance from the Sun ( $d$ ), along the line of sight to MAXI J1348–630. The thick and the dashed circles represent the most likely distance ( $2.2^{+0.5}_{-0.6}$  kpc) and the robust upper limit ( $5.3 \pm 0.1$  kpc), respectively. Our distance constraints also place MAXI J1348–630 in front of the Scutum-Centaurus arm of the Milky Way, which is also consistent with the low  $n_{\text{H}}$  ( $0.64 \times 10^{22} \text{ cm}^{-3}$ ; Zhang et al. 2020a) determined from the X-ray studies.

resolution comparable to that of ASKAP. Our data demonstrate the future potential of MeerKAT, which with its high sensitivity will be well placed to routinely

provide H I distance estimates for all bright, outbursting XRBs.

The combined temporal coverage of our ASKAP and MeerKAT observations shows that the flare detected by ASKAP (Figure. 4.2) is a secondary re-brightening, following the peak detected during the MeerKAT observation (Carotenuto et al., 2019). This is not unusual, as multiple jet ejections have been observed in several previous black hole XRB outbursts (e.g. Mirabel & Rodríguez, 1994; Brocksopp et al., 2013). In future, the combination of MeerKAT and ASKAP observations, together with higher frequency facilities, will provide high-cadence light curves that can help constrain key parameters such as jet speed, energetics and geometry (Tetarenko et al., 2017).

## 4.5 Conclusions

We have used ASKAP to detect H I absorption towards MAXI J1348–630 out to a maximum negative radial velocity (with respect to the LSR) of  $-31 \pm 4 \text{ km s}^{-1}$ , implying a most probable kinematic distance of  $2.2^{+0.5}_{-0.6} \text{ kpc}$ . By comparison with the absorption towards a stack of the extragalactic sources in the field of view, we place a robust upper limit of  $5.3 \pm 0.1 \text{ kpc}$ , corresponding to the tangent point distance.

Using our preferred distance and assuming a canonical black hole mass of  $8 \pm 1 M_{\odot}$ , we found that MAXI J1348–630 was accreting at  $17 \pm 10 \%$  of the Eddington luminosity over the peak of the outburst, and the soft-to-hard X-ray spectral state transition happened at  $2.5 \pm 1.5 \%$  of the Eddington luminosity, consistent in both cases with what has been found for other black hole XRBs. Using our distance measurements, Carotenuto et al. (2021a,b) determine jet speed, jet inclination and radio/X-ray correlation for MAXI J1348–630.

Finally, our study highlights the synergies between ASKAP and MeerKAT, demonstrating the potential for routine H I distance measurements for future black hole X-ray binaries in outburst.

These distances are crucial to being able to derive physical quantities from

observables. In the next chapter, we use the distance determination to MAXI J1535–571 (Chapter 3) to inform a broadband radio study of the transient radio jets in that system. With observations from the MWA and a suite of Australian radio telescopes, we determine the jet opening angle, the magnetic field strength and the minimum energy of the transient jet in MAXI J1535–571.



## Chapter 5

# Using SKA precursors to study the transient jets in MAXI J1535–571

This chapter is a reproduction of J. Chauhan, J. C. A. Miller-Jones, G. E. Anderson, A. Paduano, M. Sokolowski, C. Flynn, P. J. Hancock, N. Hurley-Walker, D. L. Kaplan, T. D. Russell, A. Bahramian, S. W. Duchesne, D. Altamirano, S. Croft, H. A. Krimm, G. R. Sivakoff, R. Soria, C. M. Trott, R. B. Wayth, V. Gupta, M. Johnston-Hollitt, and S. J. Tingay. “A broadband radio view of transient jet ejecta in the black hole candidate X-ray binary MAXI J1535–571”, *Publications of the Astronomical Society of Australia*, Volume 38, eid e045, page e045, DOI: <https://doi.org/10.1017/pasa.2021.38>.

The chapter is slightly different from the submitted article due to minor changes, such as the exclusion of some introductory content (already discussed in Chapter 1), referencing to earlier chapters to maintain the coherence within this thesis.

As discussed in Chapter 1, close to the peak of a BH-XRB outburst, we observe transient jets when sources transit from the hard to the soft X-ray spectral state. By determining the physical properties of the jets, we can quantify their

contribution to the energy budget of the outburst and in combination with the X-ray studies provide information on the coupling between the ejection of jets and the accretion process that powers them. In this chapter, we present a broadband radio study of the transient jets ejected from the black hole candidate X-ray binary MAXI J1535–571, which underwent a prolonged outburst beginning on 2 September 2017. We monitored MAXI J1535–571 with the MWA at frequencies from 119 to 186 MHz over six epochs from 20 September to 14 October 2017. The source was quasi-simultaneously observed over the frequency range 0.84–19 GHz by the UTMOST, ASKAP, ATCA, and LBA. We detected a spectral turnover between 250 and 500 MHz during the brightest radio flare, which we ascribe to SSA. We measured the source size from the LBA data, which with the spectral turnover enabled us to determine the jet opening angle, the magnetic field strength and the minimum energy. Our fitted magnetic field is consistent with that inferred from the equipartition approach, suggesting the jet knot to be close to equipartition. Our study highlights the capabilities of the Australian suite of radio telescopes to jointly probe radio jets in black hole X-ray binaries via simultaneous observations over a broad frequency range, and with differing angular resolutions. This suite allows us to determine the physical properties of X-ray binary jets. Finally, our study emphasizes the potential contributions that can be made by SKA in the study of BH-XRBs.

## 5.1 MAXI J1535–571

MAXI J1535–571 underwent a prolonged outburst beginning on 2 September 2017 (Negoro et al., 2017a; Kennea et al., 2017b), which was first detected by the Monitor of All-sky X-ray Image<sup>1</sup> (*MAXI*; Matsuoka et al., 2009) and the Neil Gehrels Swift Observatory<sup>2</sup> (*Swift*/BAT; Gehrels et al., 2004; Barthelmy et al., 2005). The outburst discovery was followed by a multi-wavelength monitoring

---

<sup>1</sup><http://maxi.riken.jp/top/index.html>

<sup>2</sup><https://swift.gsfc.nasa.gov/>

campaign by the XRB community (e.g., Dingler, 2017; Russell et al., 2017b; Miller et al., 2018; Parikh et al., 2019; Russell et al., 2020). MAXI J1535–571 underwent a bright radio flaring event reaching  $\sim 590$  mJy at 1.34 GHz around 21 September 2017 (Chapter 3, Russell et al., 2019c).

Most of the physical parameters of MAXI J1535–571 are still uncertain. Recently, the H I absorption line was used to determine a source distance of  $4.1_{-0.5}^{+0.6}$  kpc (Chapter 3), implying that at the peak of its outburst MAXI J1535–571 was accreting near to the Eddington limit. Russell et al. (2019c) performed an extensive analysis of MAXI J1535–571 in the radio frequency band (5.5–19 GHz) and detected a discrete transient jet knot moving away from the compact object at a speed of  $\geq 0.69c$ . The authors also constrained the jet inclination angle (at the time of ejection) to be  $\leq 45^\circ$ .

## 5.2 Observations and Data reduction

### 5.2.1 MWA

During the 2017–2018 outburst of MAXI J1535–571, the MWA observed the source over six epochs from 20 September to 14 October 2017. In its Phase I, the MWA had an angular resolution of  $\sim 3$  arcmin at 154 MHz (Tingay et al., 2013). During the Phase II major upgrade in 2017, the angular resolution was increased by a factor of  $\sim 2$ , and the sensitivity by a factor of  $\sim 4$ , due to the associated reduction in the confusion noise (Wayth et al., 2018). At the time of our observations, the MWA was being upgraded from Phase I to Phase II, changing the resolution and sensitivity in each observation. The observations from the third, fourth and fifth epochs (26, 28 and 29 September 2017) have been excluded from this study due to the small number ( $< 64$ ) of available tiles, leading to poor data quality, and low resolution and sensitivity.

Our observations were carried out in three frequency bands centred at 119, 154 and 186 MHz, with 30.72 MHz of bandwidth at each frequency. We observed

MAXI J1535–571 for around 26 minutes in each frequency band, except on 14 October 2017 when we were restricted to 8 minutes per band (Table 5.1). Our observations comprised 13 individual 2-minute snapshots, followed by a 112-s observation of a bright, calibrator source Hercules A. Further details of the MWA observations can be found in Table 5.1.

We initially processed the raw visibility data with the `COTTER` software (Offringa et al., 2015), which also excises the channels contaminated by radio-frequency interference (RFI) using the in-built `AOFlogger` (Offringa et al., 2012) tool, and converts the data to measurement set format. We then calibrated the data with the Common Astronomy Software Application (`CASA` v5.1.2-4: McMullin et al., 2007), using a bright, persistent extragalactic calibrator source (Hercules A). We made images using `WSClean` (Offringa et al., 2014), employing Briggs weighting with a robust parameter of 0. We used the `flux_warp`<sup>3</sup> software package (Duchesne et al., 2020) to calibrate the flux density scale of each two-minute snapshot image using the persistent point sources from the Galactic and Extragalactic All-sky MWA (GLEAM) catalogue (Hurley-Walker et al., 2017) that could be identified in our image. The maximum correction found to be required to the absolute flux density scale was 10%. Finally, we used the `ROBBIE`<sup>4</sup> software package (Hancock et al., 2019), to correct the image for possible ionospheric distortions using the in-built `fits_warp`<sup>5</sup> software package (Hurley-Walker & Hancock, 2018), and then create a mean image at each frequency band after stacking the individual two-minute snapshot images.

## 5.2.2 UTMOST

The Molonglo Observatory Synthesis Telescope has been recently refurbished (Bailes et al., 2017) via the UTMOST project. The telescope now operates in a 31-MHz band centred at 835 MHz, although the sensitivity is not uniform

---

<sup>3</sup>[https://gitlab.com/Sunmish/flux\\_warp](https://gitlab.com/Sunmish/flux_warp)

<sup>4</sup><https://github.com/PaulHancock/Robbie>

<sup>5</sup>[https://github.com/nhurleywalker/fits\\_warp](https://github.com/nhurleywalker/fits_warp)

across the band. The effective centre (weighted mean) of the band is 843 MHz. The telescope observes in a single circular polarization. It synthesises 351 narrow ( $\approx 46$  arcsec) fanbeams with its East-West oriented arm, which tile out a wide ( $4^\circ$ ) field of view. Since June 2017 it has operated as a transit instrument, carrying out a Fast Radio Burst search and pulsar timing program.

Sources transit across the primary beam in 16 minutes on the equator, and in approximately 30 minutes at the declination of MAXI J1535–571, traversing the 351 fanbeams. The data processing backend writes these fanbeams as “filterbank” files to disk at  $327 \mu\text{sec}$  resolution for 320 frequency channels, at a resolution of 98 kHz. In normal operations, these are decimated to  $654 \mu\text{sec}$  and  $40 \times 0.7$  MHz channels.

Transit observations of MAXI J1535–571 were obtained on 21, 26 and 27 September 2017, and all resulted in clear detections. For each observation, we measured the S/N of the source from the decimated filterbanks as it transited the fanbeam pattern, referencing it to sources of known flux density from the Molonglo Galactic Plane Survey (undertaken at Molonglo prior to it becoming a transit instrument; Murphy et al., 2007). These sources (MGPS 1541–5645, MGPS 1525–5709, MGPS 1533–5642 and MGPS 1532–5556, whose known flux densities are 282, 226, 544 and 1092 mJy respectively) are at very similar declinations, both ahead of and behind the source in right ascension. A modest fraction of the data was affected by mobile handset traffic in small sub-sections of the observing band, and this was flagged and removed. Subtraction of the background was required as the source is in the Galactic plane and there are a number of weak sources around the target. These could be identified readily as they traverse the field of view at a declination-dependent rate. Analysis of the flux calibration sources showed that systematics dominated the error budget, and were of the order of 30 to 50% of the flux density.

### 5.2.3 LBA

We observed MAXI J1535–571 with LBA on 23–24 September 2017, from 22:26 to 05:30 UTC (MJD  $58020.08 \pm 0.14$ ) under project code V456. The array comprised seven stations (the phased-up ATCA, Ceduna, Hobart, Katherine, the Tidbinbilla 70-m dish DSS43, Warkworth and Yarragadee), although not all antennas were present at all times. We observed at a central frequency of 8.441 GHz, with the full 64 MHz of bandwidth split into four 16-MHz IF pairs. We used the bright extragalactic calibrator source PKS 0537-441 as a fringe finder and bandpass calibrator, and the closer source PMN J1515–5559 ( $3.03^\circ$  from MAXI J1535–571) as a phase reference calibrator. We used a 5-minute phase referencing cycle time, spending 3.5 min on the target and 1.5 min on the calibrator in each cycle. The data were correlated using the DiFX software correlator (Deller et al., 2007, 2011), and reduced according to standard procedures within the Astronomical Image Processing System (AIPS, version 31DEC17; Greisen, 2003).

Since we used the phased ATCA as one of our LBA stations, the observations also yielded a stand-alone ATCA data set. We reduced these data within *CASA* (version 5.6.2), using the standard calibrator PKS 1934–638 as a bandpass calibrator and to set the flux density scale. The array was in its compact H168 configuration<sup>6</sup>, with a maximum baseline of 192 m between the inner five antennas, and the sixth antenna located 4.4 km away. We imaged the stand-alone ATCA data using the inner five antennas only. MAXI J1535–571 was significantly detected, and its flux density derived by fitting a point source in the image plane using the *IMFIT* task in *CASA*.

### 5.2.4 ASKAP

ASKAP monitored the 2017–2018 outburst of MAXI J1535–571 over seven different epochs, from 21 September to 2 October 2017 (see Table 5.1). A de-

---

<sup>6</sup><https://www.narrabri.atnf.csiro.au/cgi-bin/obstools/baselines2.cgi?array=h168>

tailed description of the ASKAP observations and data reduction is presented in Chapter 3. All the early science observations were carried out with an ASKAP sub-array of twelve dishes at a central frequency of 1.34 GHz with a processed bandwidth of 192 MHz. In this sub-array, ASKAP has an angular resolution of  $\sim 30$  arcsec. We processed our early science data with the standard ASKAP data analysis software, `ASKAPsoft`<sup>7</sup> (pipeline version 0.24.1; Guzman et al., 2019). We estimated the flux densities (and  $1\sigma$  uncertainties) of the source from the continuum images by using the `IMFIT` task in `CASA` v5.1.2-4.

### 5.2.5 ATCA

ATCA densely monitored the complete 2017–2018 outburst of MAXI J1535–571 (Russell et al., 2019c; Parikh et al., 2019). The source was observed over thirty-seven epochs between 5 September 2017 and 11 May 2018. To complement our lower-frequency monitoring with ASKAP and MWA, we focus our analysis on those ATCA observations taken on 21, 23, 27 and 30 September 2017 (included in Table 5.1). For these four ATCA epochs, data were recorded at 5.5, 9.0, 17.0 and 19.0 GHz, with 2 GHz of bandwidth at each central frequency. To determine the overall behaviour of MAXI J1535–571 during the radio flaring event, we included all ATCA observations between 15 September and 25 October 2017 in our multi-frequency light curve presented in Section 5.3.4. For a detailed description of the full ATCA monitoring and data analysis, see Russell et al. (2019c).

---

<sup>7</sup><http://www.atnf.csiro.au/computing/software/askapsoft/sdp/docs/current/index.html>

Table 5.1: Details of the radio observations of MAXI  
J1535–571 used in this paper.

| Begin of Table                            |  |                  |                           |           |                               |   |            |
|---|--|------------------|---------------------------|-----------|-------------------------------|---|------------|
| Observation<br>Start date<br>(dd-mm-yyyy) | Observation<br>Start time<br>(hh:mm:ss)<br>(UTC) | MJD <sup>a</sup> | Exposure<br>time<br>(min) | Telescope | Central<br>frequency<br>(GHz) | Flux density <sup>b</sup><br>$S_0$<br>(mJy) | References |
| 20-09-2017<br>(MWA Epoch 1)               | 07:15:50   | 58016.31         | 28                        | MWA       | 0.119                         | < 201                                       | This work  |
|   | 07:17:50   | 58016.31         | 28                        | MWA       | 0.154                         | < 102                                       | This work  |
|   | 07:13:50   | 58016.31         | 28                        | MWA       | 0.186                         | < 84  | This work  |
| 21-09-2017<br>(MWA Epoch 2)               | 07:11:58   | 58017.31         | 26                        | MWA       | 0.119                         | $152 \pm 41$                                | This work  |
|   | 07:13:50   | 58017.31         | 26                        | MWA       | 0.154                         | $172 \pm 17$                                | This work  |
|   | 07:15:50   | 58017.31         | 26                        | MWA       | 0.186                         | $194 \pm 16$                                | This work  |
|   | 05:21:24   | 58017.31         | 30                        | UTMOST    | 0.840                         | $500 \pm 160$                               | This work  |
|   | 03:06:32   | 58017.17         | 122                       | ASKAP     | 1.34                          | $579.6 \pm 2.1$                             | [1]        |
|   | 09:01:30   | 58017.46         | 100                       | ATCA      | 5.5                           | $150.4 \pm 0.1$                             | [2]        |
|   | 09:01:30   | 58017.46         | 100                       | ATCA      | 9.0                           | $121.3 \pm 2.0$                             | [2]        |
| 08:33:50                                  | 58017.46   | 100              | ATCA                      | 17.0      | $91.8 \pm 0.1$                | [2]   |            |

| Continuation of Table 5.1                 |  |                  |                           |           |                               |   |            |
|---|--|------------------|---------------------------|-----------|-------------------------------|---|------------|
| Observation<br>Start date<br>(dd-mm-yyyy) | Observation<br>Start time<br>(hh:mm:ss)<br>(UTC) | MJD <sup>a</sup> | Exposure<br>time<br>(min) | Telescope | Central<br>frequency<br>(GHz) | Flux density <sup>b</sup><br>$S_0$<br>(mJy) | References |
|   | 08:33:50   | 58017.46         | 100                       | ATCA      | 19.0                          | $85.8 \pm 0.1$                              | [2]        |
| 22-09-2017                                | 01:30:02   | 58018.12         | 172                       | ASKAP     | 1.34                          | $156.1 \pm 1.9$                             | [1]        |
|   | 10:35:41   | 58018.50         | 181                       | ASKAP     | 1.34                          | $306.1 \pm 1.3$                             | [1]        |
| 23-09-2017                                | 13:23:39   | 58019.58         | 61                        | ASKAP     | 1.34                          | $478.2 \pm 2.4$                             | [1]        |
|   | 12:22:30   | 58019.52         | 20                        | ATCA      | 5.5                           | $377.2 \pm 1.2$                             | [2]        |
|   | 12:22:30   | 58019.52         | 20                        | ATCA      | 9.0                           | $324.2 \pm 0.3$                             | [2]        |
|   | 11:54:50   | 58019.52         | 30                        | ATCA      | 17.0                          | $240.2 \pm 0.4$                             | [2]        |
|   | 11:54:50   | 58019.52         | 30                        | ATCA      | 19.0                          | $223.2 \pm 0.5$                             | [2]        |
|   | 22:26:36   | 58020.08         | 212                       | ATCA      | 8.44                          | $333 \pm 1$                                 | This work  |
|   | 22:26:36   | 58020.08         | 212                       | LBA       | 8.44                          | $\lesssim 100^c$                            | This work  |
| 26-09-2017                                | 09:40:00   | 58022.41         | 30                        | UTMOST    | 0.840                         | $200 \pm 100$                               | This work  |
| 27-09-2017                                | 09:40:00   | 58023.41         | 30                        | UTMOST    | 0.840                         | $100 \pm 50$                                | This work  |
|   | 09:35:10   | 58023.42         | 30                        | ATCA      | 5.5                           | $127.5 \pm 0.3$                             | [2]        |
|   | 09:35:10   | 58023.42         | 30                        | ATCA      | 9.0                           | $114.3 \pm 0.2$                             | [2]        |

| Continuation of Table 5.1                 |  |                  |                           |           |                               |   |            |
|---|--|------------------|---------------------------|-----------|-------------------------------|---|------------|
| Observation<br>Start date<br>(dd-mm-yyyy) | Observation<br>Start time<br>(hh:mm:ss)<br>(UTC) | MJD <sup>a</sup> | Exposure<br>time<br>(min) | Telescope | Central<br>frequency<br>(GHz) | Flux density <sup>b</sup><br>$S_0$<br>(mJy) | References |
|   | 09:07:30   | 58023.41         | 38                        | ATCA      | 17.0                          | $95.2 \pm 0.2$                              | [2]        |
|   | 09:07:30   | 58023.41         | 38                        | ATCA      | 19.0                          | $90.6 \pm 0.3$                              | [2]        |
| 30-09-2017                                | 03:29:59   | 58026.23         | 241                       | ASKAP     | 1.34                          | $39.8 \pm 0.8$                              | [1]        |
|   | 06:45:20   | 58026.29         | 20                        | ATCA      | 5.5                           | $29.4 \pm 0.2$                              | [2]        |
|   | 06:45:20   | 58026.29         | 20                        | ATCA      | 9.0                           | $26.8 \pm 0.1$                              | [2]        |
|   | 06:17:40   | 58026.29         | 30                        | ATCA      | 17.0                          | $23.0 \pm 0.1$                              | [2]        |
|   | 06:17:40   | 58026.29         | 30                        | ATCA      | 19.0                          | $23.5 \pm 0.1$                              | [2]        |
| 01-10-2017                                | 03:35:00   | 58027.23         | 241                       | ASKAP     | 1.34                          | $26.3 \pm 0.8$                              | [1]        |
| 02-10-2017                                | 03:39:59   | 58028.24         | 241                       | ASKAP     | 1.34                          | $21.4 \pm 0.7$                              | [1]        |
| 14-10-2017                                | 05:29:26   | 58040.23         | 8                         | MWA       | 0.119                         | $< 117$                                     | This work  |
| (MWA Epoch 6)                             | 05:31:26   | 58040.23         | 8                         | MWA       | 0.154                         | $< 66$                                      | This work  |
|   | 05:33:26   | 58040.23         | 8                         | MWA       | 0.186                         | $82 \pm 17$                                 | This work  |
| End of Table                              |  |                  |                           |           |                               |   |            |

<sup>a</sup> Mid point of the observations.

<sup>b</sup>  $1\sigma$  errors are presented, calculated by adding in quadrature the  $1\sigma$  rms noise in the image and the  $1\sigma$  error on the Gaussian fit to the source. For MWA, we also add in quadrature a 10% uncertainty on the flux density scale.

<sup>c</sup> Source is significantly detected on short baselines, but measured flux density falls off with baseline length.

[1] Chapter 3; [2] Russell et al. (2019c).

Note: All upper limits are given at the  $3\sigma$  level.

## 5.3 Results

The 2017–2018 outburst of MAXI J1535–571 was detected across a broad radio frequency band by our set of complementary Australian telescopes. Our monitoring campaign allowed us to track the evolution of a transient jet knot (denoted as S2 by Russell et al., 2019c).

### 5.3.1 Outburst evolution

In Figure 5.1, we present the publicly-available one-day averaged X-ray light curves from *MAXI*, *Swift*/XRT, and *Swift*/BAT monitoring data of MAXI J1535–571, indicating the dates of the MWA, UTMOST, ASKAP, ATCA, and LBA observations. We have highlighted the X-ray spectral states from Tao et al. (2018) and Nakahira et al. (2018), as described in Russell et al. (2019c). As is typical for BH-XRBs (Fender et al., 2004), MAXI J1535–571 underwent a bright radio flaring event during its transition from the hard to the soft X-ray spectral state, peaking at  $\sim 590$  mJy at 1.34 GHz on 21 September 2017 (Chapter 3, Russell et al., 2019c). Figure 5.1 shows that most of our radio monitoring data were taken over the peak of the outburst, when the source was in the soft–intermediate X-ray spectral state (Chapter 3, Russell et al., 2019c).

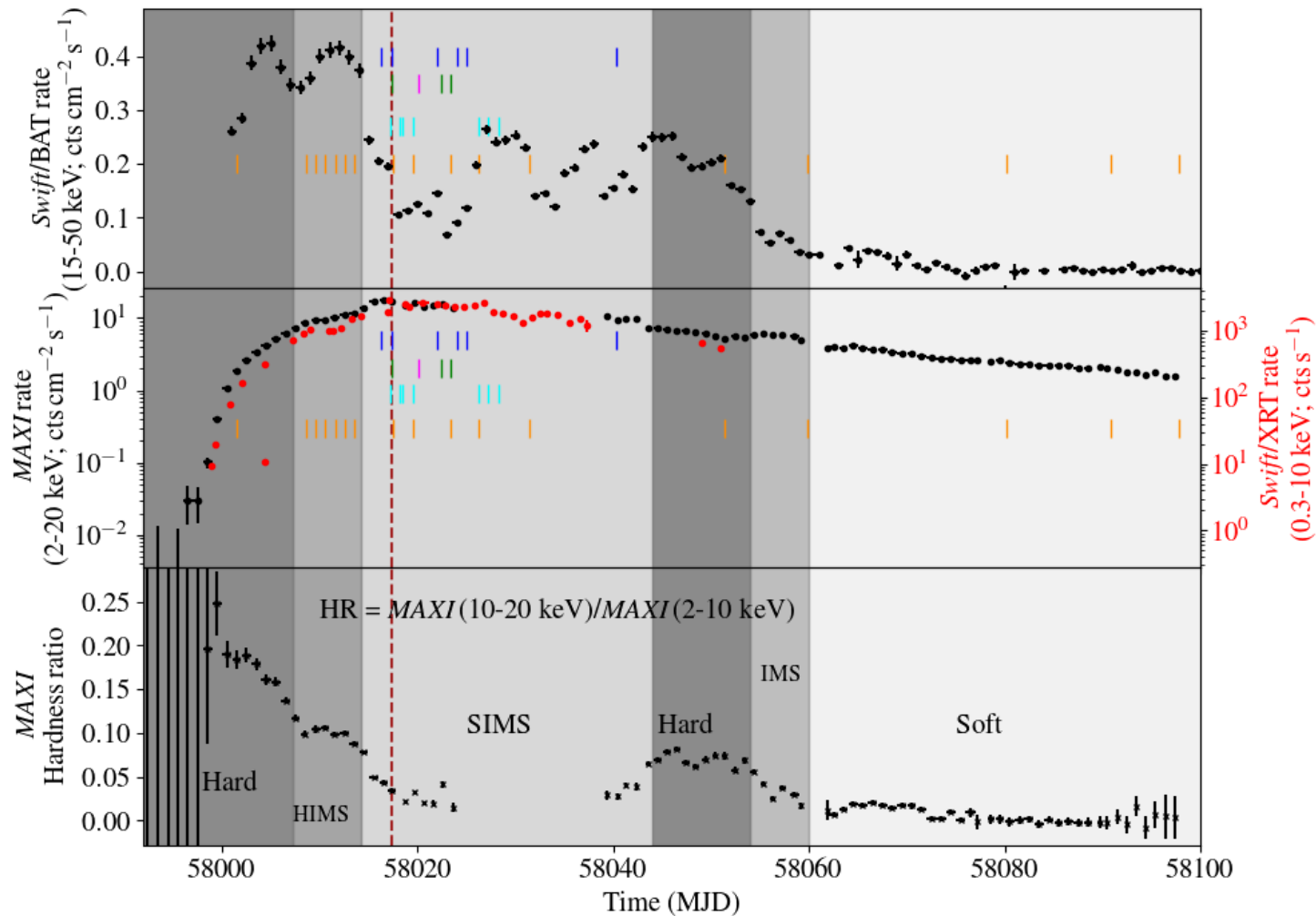


Figure 5.1: Top and Middle panels: One-day averaged *Swift*/BAT, *Swift*/XRT and *MAXI* light curves of MAXI J1535–571 in the energy ranges 15.0–50.0 keV, 0.3–10.0 keV and 2.0–20.0 keV, respectively. Blue vertical lines highlight the dates of the MWA observations, green vertical lines indicate the UTMOST observations, and the LBA observation is denoted by the magenta vertical line. We also plot the dates of the ASKAP and ATCA observations with cyan and orange vertical lines, respectively (Chapter 3, Russell et al., 2019c). The dashed brown vertical line indicates the 21 September 2017 observation when the source was brightest (reaching  $\sim 590$  mJy at 1.34 GHz in ASKAP observation), when we were able to measure a quasi-simultaneous broadband radio spectrum. Bottom panel: Variation of the hardness ratio (HR) calculated from *MAXI* on-demand public data. The HR is defined as the ratio of count rates in the 10.0–20.0 keV and 2.0–10.0 keV energy bands. Our observations were all taken during the soft–intermediate state.

### 5.3.2 Low-frequency radio detections of MAXI J1535–571

MAXI J1535–571 was detected at all three MWA frequencies (119, 154 and 186 MHz) on 21 September 2017 (our second MWA epoch), and this is the first transient BH-XRB detected by MWA (to our knowledge). The source was not detected at any of the three frequencies on 20 September (the first MWA epoch), whereas on 14 October (the sixth MWA epoch), MAXI J1535–571 was detected only at 186 MHz, with  $4.8\sigma$  significance (see Table 5.1).

In Figure 5.2, we show the 186-MHz MWA continuum image of MAXI J1535–571 and the surrounding region for the 21 September 2017 observation, where the source was detected at  $> 10\sigma$  significance. For comparison, we also show the ASKAP 1.34-GHz continuum image of the same region on the same day, highlighting the difference in resolution of the two instruments.

MAXI J1535–571 was also detected in all three of the UTMOST observations, taken on 21, 26 and 27 September 2017. We obtain 843-MHz flux density estimates of  $500 \pm 160$ ,  $200 \pm 100$  and  $100 \pm 50$  mJy (with the uncertainties dominated by systematics), respectively, indicating a clear fading of the source over the 6 day span of the observations (see Table 5.1).

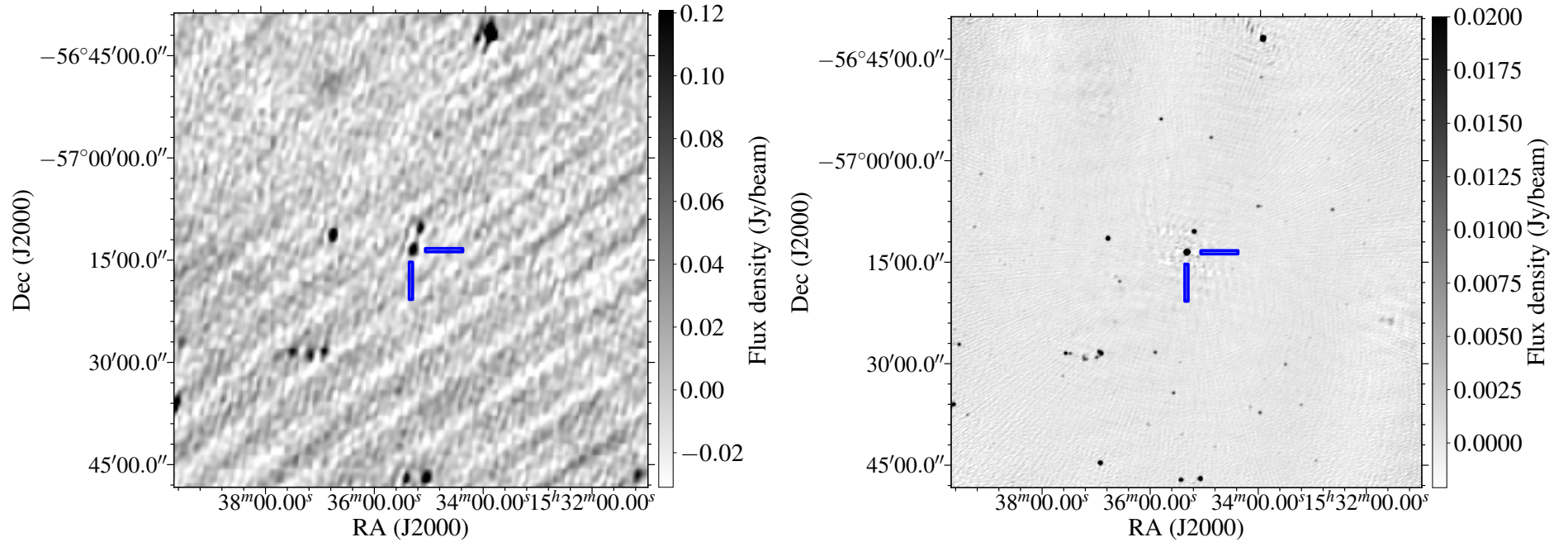


Figure 5.2: MWA (186 MHz; left panel) and ASKAP (1.34 GHz; right panel) continuum images of MAXI J1535–571 taken during the bright radio flare on 21 September 2017. The image is centred at the position of MAXI J1535–571 (RA = 15:35:19.71, DEC =  $-57:13:47.58$ ; Russell et al., 2019c) with a size of  $1.16^\circ \times 1.16^\circ$ . In the MWA image, the diagonal stripes are sidelobes associated with PKS 1610–60 that is present to the south-east of MAXI J1535–571. These deconvolution artefacts are due to imperfect calibration resulting from the MWA’s ongoing configuration change. MAXI J1535–571 is significantly detected in both images, and is indicated by the cross-hairs.

### 5.3.3 Source size

The stand-alone ATCA data observed as part of our LBA run on 23 September 2017 measured a flux density of  $333 \pm 1$  mJy at 8.44 GHz (statistical errors only; to this should be added an additional systematic uncertainty on the flux density scale of 1–2%). By contrast, the LBA data indicated a much lower level of emission, suggesting that a significant fraction of the ATCA emission was resolved out on the longer LBA baselines. Clear fringes were only seen on the two shortest baselines (ATCA–Tidbinbilla, and Tidbinbilla–Hobart, respectively), with the flux density being  $< 100$  mJy in both cases, and higher on the shorter baseline. Since both baselines have almost the same orientation, this difference is a function only of baseline length, and hence places constraints on the source size scale.

The measured flux densities on these short baselines were seen to vary smoothly by up to a factor of 2 over the course of the observing run. The simultaneous stand-alone ATCA data rule out this being due to intrinsic source variability, demonstrating that these baselines are probing the source structure. We used Difmap (Shepherd, 1997) to project the visibilities along a range of different position angles, and found that when projected along a position angle of  $125^\circ$  East of North (the position angle of the moving jet knot S2 detected by Russell et al., 2019c), they could be fit by a Gaussian of amplitude 333 mJy (fixed to the measured ATCA flux density), with a width (standard deviation) of  $6.1 \pm 0.1$  M $\lambda$  (where M $\lambda$  = million wavelengths). Assuming that the jet knot brightness profile can be well approximated by a Gaussian, this corresponds to a size scale of  $34 \pm 1$  mas. Our *uv*-coverage from these two baselines alone does not permit us to constrain the size scale in the perpendicular direction, so we assume that the knot can be modelled as a circular Gaussian of width  $\theta_s = 34 \pm 1$  mas (corresponding to a physical size of  $139_{-17}^{+21}$  AU, calculated using the source distance of  $4.1_{-0.5}^{+0.6}$  kpc from Chapter 3).

This size constraint can be used to determine parameters including the magnetic field strength, the opening angle of the jet, and the synchrotron minimum

energy, improving our understanding of the energetics of the transient jet ejection.

### 5.3.4 Multi-frequency radio light curve

MAXI J1535–571 was observed by the Australian suite of radio telescopes during its radio flaring event in September 2017. The 0.12 – 19 GHz radio light curve spanning from 15 September (MJD 58011) to 26 October (MJD 58052) is shown in Figure 5.3. Russell et al. (2019c, 2020) observed the compact jets beginning to quench around 17 September (MJD 58013.6), at the end of the HIMS, and just before the radio flaring event. In the light curve, we observed two clear peaks on 21 and 23 September 2017, in each of which the 1.34 GHz radio flux density exceeded 450 mJy. The two peaks could arise from two separate ejection events. However, with no direct evidence for a second component from imaging studies (our LBA data or the ATCA data of Russell et al. 2019c), it is also possible that the second peak in the light curve is due to re-brightening of the original synchrotron-emitting jet knot as it interacts with the surrounding medium. In order to differentiate between these two scenarios, of multiple ejections and the interaction of the transient jet with the surroundings, in future outbursts we would need high cadence monitoring of the radio flaring event with VLBI, because VLBI will help in imaging the transient jet ejections. A high-cadence X-ray monitoring will also be important to see if a second hard-to-soft state transition was made. After the second peak, the radio flux density of the source gradually decayed at all frequencies, reaching  $\sim 13$  mJy in the 5.5–19.0 GHz frequency band on 5 October 2017 (Russell et al., 2019c).

The MWA detection on 21 September 2017 (MJD 58017.31) coincides with the first radio flaring event observed from MAXI J1535–571 (see Figure 5.3), in which the maximum flux density reached  $580 \pm 2$  mJy at 1.34 GHz. However, the interpretation of the 186-MHz MWA detection on 14 October 2017 (MJD 58040.23) is less clear. It either corresponds to the fading tail of the bright ejecta, or to low-frequency emission from the re-formed compact jets. Both interpretations

are plausible. The transient ejecta would have a steep, optically thin spectrum, making them brightest at low radio frequencies. However, the MWA detection occurred in the SIMS (see Figure 5.3), and the compact jets should already have reformed at GHz frequencies by the time of the subsequent HIMS, as seen in MAXI J1836–194 (Russell et al., 2014). Furthermore, the MWA detection was at a similar flux density to the 5–19 GHz ATCA detection of the re-formed compact jets on 25 October 2017 (Russell et al., 2019c).

### 5.3.5 Radio spectrum

On 21 September 2017, the MWA spectrum was rising with frequency, whereas above 1 GHz, it was falling with frequency. This implies a spectral turnover. However, the observations from MWA, ASKAP and ATCA were not strictly simultaneous. Given the rapid flux density variations during the flaring events, this non-simultaneity could bias our broadband radio spectrum. We therefore broke the ASKAP and ATCA data into short time chunks of  $\sim 20$  minutes each and fit them with a power law (Figure 5.4), which we extrapolated back to the time of the MWA observations to reconstruct a simultaneous broadband radio spectrum. We also tried to fit the light curves with an exponential decay, but the  $\chi^2$  values of the fits were lower for the power law fits, particularly at the higher frequencies of 17 and 19 GHz. Our reconstructed simultaneous 0.12–19.0 GHz spectrum (Figure 5.5) shows a clear turnover between 250 and 500 MHz, with a low-frequency spectral index of  $\alpha_l = 0.91 \pm 0.60$  between 119 and 186 MHz, and a high-frequency spectral index of  $\alpha_h = -0.44 \pm 0.01$  above 1 GHz.

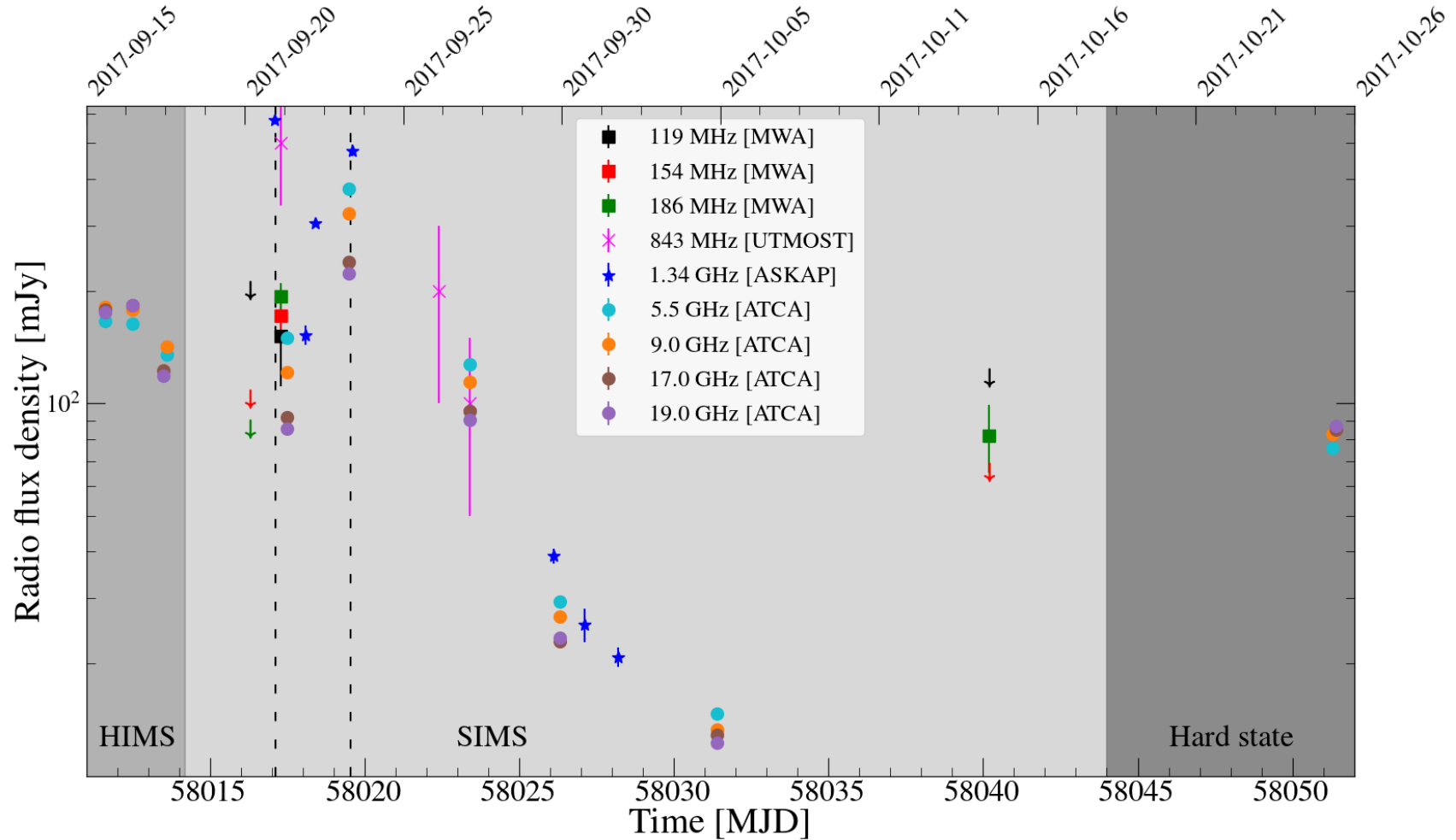


Figure 5.3: Multi-frequency radio light curve of MAXI J1535-571. Solid squares, crosses, stars and circles correspond to MWA, UTMOST, ASKAP and ATCA observations, respectively. Different colours indicate different observing frequencies, as indicated by the plot legend. In the case of MWA non-detections, downward-pointing arrows represent  $3\sigma$  upper limits on the radio flux density. The medium-dark shaded region highlights the HIMS, the SIMS is represented by the light shaded region, and the dark shaded region highlights the hard X-ray spectral state. At the start and end of the light curve, ATCA points indicate the quenching and reappearance of the compact jets (Russell et al., 2019c, 2020). The two peaks are highlighted with the vertical dashed lines. The best-sampled date was 21 September (MJD 58017), during the first peak in the light curve.

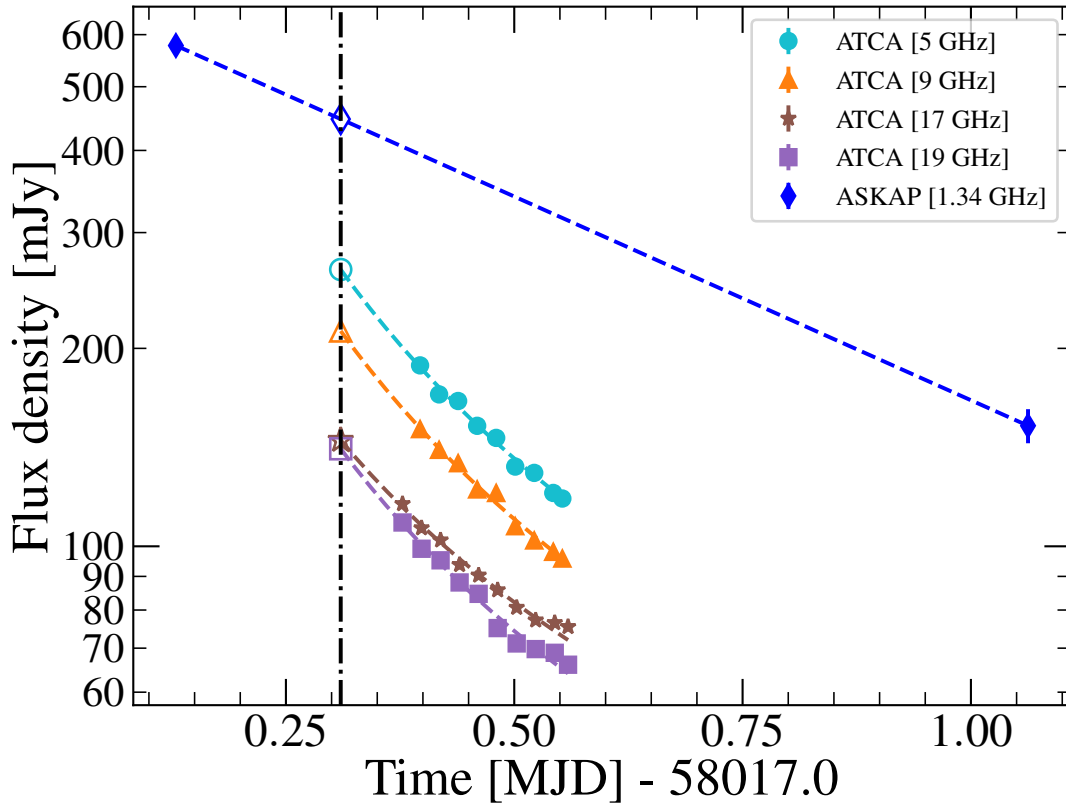


Figure 5.4: Short time-scale light curves of the ATCA observations on 21 September 2017. The vertical dash-dotted line indicates the time of the MWA observation. ASKAP/ATCA flux densities are interpolated/extrapolated to the time of the MWA observations, and shown with hollow markers. Each plotted symbol and its colour represents a different observing frequency, as indicated in the legend. The dashed lines represent the fitted power law models for the respective light curves (as described in Section 5.3.5). By extrapolating/interpolating the flux density decays seen with ATCA and ASKAP, we reconstructed a strictly simultaneous radio spectrum at the time of the MWA observation.

## 5.4 Radio spectral analysis

To understand the physical scenario behind the observed low-frequency spectral turnover in our 21 September observation, we considered the R-T effect, FFA by thermal plasma and SSA, all of which can produce a low-frequency turnover in the radio spectrum (e.g., Gregory & Seaquist, 1974; Miller-Jones et al., 2004).

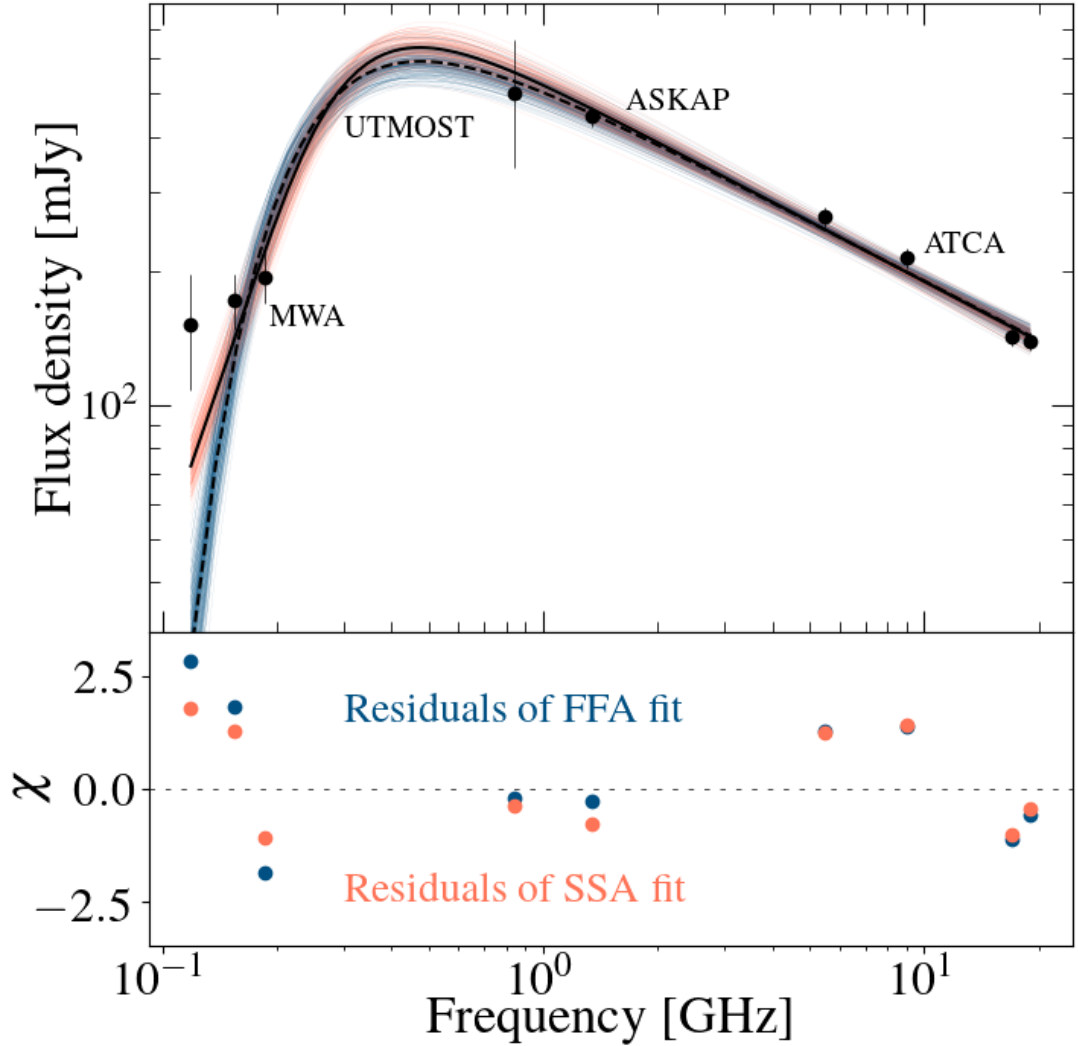


Figure 5.5: Top panel: Broadband radio spectrum of MAXI J1535–571 on 21 September 2017. The flux densities are from MWA (this work), UTMOST (this work), ASKAP (Chapter 3) and ATCA (Russell et al., 2019c), as indicated. The black solid line highlights the median of the posterior distribution for the SSA model (discussed in Section 5.4.3), whereas the black dashed line shows the median of the posterior distribution for the FFA model (described in Section 5.4.2). We have added systematic uncertainties on the flux densities measured by MWA (10%), ASKAP (5%) and ATCA (a conservative 5%, as appropriate for the higher frequencies; Partridge et al., 2016), to incorporate the cross-telescope uncertainties. The orange and blue traces show random draws from the posterior distributions of the best fits for the SSA and FFA models, respectively. Bottom panel: Residuals relative to the median of the posterior distributions for both the SSA and FFA models. The low-frequency residuals are lower for the SSA model. The low-frequency turnover allows us to estimate several of the physical parameters of the jet.

### 5.4.1 The Tsytovitch-Razin Effect

The T–R effect is dominant when synchrotron radiation passes through cold plasma, where the refractive index of the ambient medium is  $< 1$ . In such a condition, the beaming from the relativistic electrons can be reduced, which can make synchrotron radiation less potent, and results in a sharp cutoff at low-frequencies (Tsytovich, 1951; Razin, 1960; Miller-Jones et al., 2004).

The frequency  $\nu$  (GHz) at which the T–R effect becomes important is given by

$$\nu \approx 2 \times 10^{-14} \left( \frac{n_{the}}{B} \right),$$

where  $n_{the}$  ( $m^{-3}$ ) is the density of the surrounding thermal matter and  $B$  (G) is the magnetic field strength of the jet knot (Miller-Jones et al., 2004). Using equipartition arguments, Russell et al. (2019c) placed limits on  $B \approx 10$ –500 mG. Hence, if the T–R effect was the phenomenon responsible for the spectral turnover between 0.24 and 0.45 GHz,  $n_{the}$  would be unphysically high, at  $\gtrsim 1.2 \times 10^{11} m^{-3}$ . Hence, we can rule out the possibility of the T–R effect.

### 5.4.2 Free-Free Absorption

In the case of FFA, free electrons either in an external screen, or from thermal material mixed with synchrotron-emitting plasma, absorb the synchrotron photons in the presence of massive ions (Kellermann, 1966). For an ionised hydrogen cloud of length  $l$  (in parsec; Mezger & Henderson, 1967), temperature  $T_{eq}$  ( $\times 10^4$  K), and electron number density  $n_e$  (in  $cm^{-3}$ ), the optical depth ( $\tau_\nu$ ) to FFA at frequency  $\nu_{GHz}$  (in GHz) can be expressed as (Tingay & de Kool, 2003)

$$\tau_\nu \approx 3.2 \times 10^{-7} T_{eq}^{-1.35} \nu_{GHz}^{-2.1} \int n_e^2 dl. \quad (5.1)$$

To investigate the possibility of free-free absorption in our source, we con-

sidered the simplest scenario of a single homogeneous absorbing screen of free electrons and scattering ions. This predicts a flux density and optical depth that scale with frequency as

$$S_\nu = S_0 \nu^\alpha e^{-\tau_\nu}, \quad (5.2)$$

$$\tau_\nu = \left( \frac{\nu}{\nu_p} \right)^{-2.1}, \quad (5.3)$$

where  $\nu_p$  is the frequency at which the optical depth becomes unity,  $S_0$  is the flux density of the source at frequency  $\nu_p$ , and  $\alpha$  is the spectral index of the synchrotron spectrum (Callingham et al., 2015).

We tried to fit our observed broad-band radio spectrum (Figure 5.5) with this FFA model (highlighted with the dashed line, blue traces, and blue residuals in Figure 5.5), using a Bayesian approach, which provided best-fit estimates and parameter uncertainties. We created a Markov Chain Monte Carlo (MCMC) simulation, incorporated uniform priors of  $\alpha = -10 - 0$ ,  $S_0 = 1 - 1000$  mJy, and  $\nu_p = 0.05 - 10$  GHz, and used the PyMC3<sup>8</sup> package developed by Salvatier et al. (2016). The model estimated values and  $1\sigma$  uncertainties of  $\alpha = -0.44 \pm 0.02$ ,  $S_0 = 526 \pm 28$  mJy and  $\nu_p = 0.23 \pm 0.01$  GHz. The slope predicted by the model in the low-frequency regime is  $2.96 \pm 0.16$ , which is inconsistent with the measured slope of  $\alpha_l = 0.91 \pm 0.60$  (Section 5.3.5) at a high significance ( $\lesssim 3\sigma$ ). We therefore do not favour FFA as an explanation for the low-frequency turnover.

We also explored whether FFA from an external ionized gas region can be physically supported as a reasonable interpretation for the low-frequency turn over observed in the radio spectrum of MAXI J1535–571. We focused on H II regions because heavy ions and free electrons are in abundance in these regions. We used  $S_0$  and  $\nu_p$  estimated from the FFA model because the fitted turnover ( $\nu_p = 0.23 \pm 0.01$  GHz) is broadly consistent with the observed low-frequency turnover between 250 and 500 MHz (Figure 5.5). Since  $\tau_\nu \approx 1$  at  $\nu_p$ , then using Equation (5.1) we calculate acceptable combinations of the electron number den-

---

<sup>8</sup><https://docs.pymc.io/>

sity ( $n_e$ ) and size of the H II region ( $l$ ) for the typical temperature ( $T_{\text{eq}}$ ) range of 7000 to 50,000 K for canonical H II regions (Dopita et al., 2006). We found  $n_e$  in the range 4 to 18,000  $\text{cm}^{-3}$  for an H II region of size 0.004 to 4,100 pc (Dopita et al., 2006). For our interpretation, we focus only on the classical H II regions, since compact and ultra-compact H II regions are only present in extreme conditions close to Sgr A\* (e.g. G-0.02-0.07, Mills et al., 2011; Lau et al., 2014, 2016). Using the relationship between the absorption column density  $n_{\text{H}}$  and  $l$  derived by Hunt & Hirashita (2009), then for the line of sight towards MAXI J1535-571 ( $n_{\text{H}} \approx (4 - 7) \times 10^{22} \text{ cm}^{-3}$ , Miller et al. 2018; Xu et al. 2018), we infer  $l = 3$  to 10 pc, implying  $n_e = 80$  to 300  $\text{cm}^{-3}$  (see Hunt & Hirashita, 2009).

We consider a hypothetical H II region along the line of sight to MAXI J1535-571, and calculate various  $H_\alpha$  quantities using the calculated range of  $n_e$  and  $l$ . Following the prescription given in the Osterbrock & Ferland (2006), we find the total  $H_\alpha$  luminosity of a hypothetical H II region in the range  $\sim 10^{36}$  to  $10^{39} \text{ erg s}^{-1}$ , which is typical for the Milky Way and other elliptical galaxies (Smith & Kennicutt, 1989; Bradley et al., 2006; Lee et al., 2011). The  $H_\alpha$  flux for a hypothetical H II region located at a distance of  $\sim 4.1 \text{ kpc}$  ( $\approx$  distance to MAXI J1535-571, Chapter 3) is  $\approx 4 \times 10^{-9}$  to  $2 \times 10^{-6} \text{ erg cm}^{-2} \text{ s}^{-1}$ , and the corresponding surface brightness is  $\approx 5 \times 10^{-15}$  to  $3 \times 10^{-11} \text{ erg cm}^{-2} \text{ s}^{-1} \text{ arcsec}^{-2}$ .

We analysed the data from the Southern H-Alpha Sky Survey Atlas<sup>9</sup> (SHASSA, Gaustad et al. 2001; Finkbeiner 2003) to search for such  $H_\alpha$  emission, but did not find any evidence of an H II region along the line of sight to MAXI J1535-571. The  $3\sigma$  upper limit on the mean surface brightness for a circular region of radius  $0.35^\circ$  centered on MAXI J1535-571 is  $\sim 2 \times 10^{-15} \text{ erg cm}^{-2} \text{ s}^{-1} \text{ arcsec}^{-2}$ , which is lower than the predicted surface brightness from an H II region with the characteristics derived above.

We also calculated the total radio flux density at 5 GHz (the frequency used for most H-alpha surveys) of the above hypothesized H II region using the prescrip-

---

<sup>9</sup><http://amundsen.swarthmore.edu/SHASSA>

tion given by Caplan & Deharveng (1986), which is estimated to be 4 to 2000 Jy. The corresponding radio surface brightness is  $\approx 5 \times 10^{-6}$  to  $3 \times 10^{-2}$  Jy arcsec $^{-2}$ . From the ATCA observation of MAXI J1535–571 on 22 February 2018, Russell et al. (2019c) measured a deep  $3\sigma$  upper limit on the 5.5-GHz radio flux density of 0.1 mJy. The corresponding  $3\sigma$  upper limit on the radio surface brightness is  $3.4 \times 10^{-7}$  Jy arcsec $^{-2}$ , which is well below the estimated surface brightness for the hypothesized H II region. Both radio and H $\alpha$  observational constraints therefore argue against the presence of an H II region along the line of sight towards MAXI J1535–571, making it unlikely that FFA is the main cause of the observed low-frequency turnover.

### 5.4.3 Synchrotron Self-Absorption

SSA is often suggested to be responsible for the low-frequency turnover in the radio spectrum of X-ray binaries (Gregory & Seaquist, 1974; Seaquist, 1976). SSA is an internal property of the source, and the turnover arises because below a certain frequency the electrons become optically thick to their own synchrotron radiation. In the case of SSA, at frequencies below the turnover ( $< \nu_p$ ), where  $\tau_\nu \gg 1$  (in the optically thick region), the synchrotron self-absorbed spectrum varies as  $S_\nu \propto \nu^{5/2}$  (e.g., Rybicki & Lightman, 1979). At frequencies above the turnover ( $> \nu_p$ ), in the optically thin region ( $\tau_\nu \ll 1$ ), the spectrum scales as  $S_\nu \propto \nu^\alpha$  ( $\alpha < 0$ ) (e.g. van der Laan, 1966a; Rybicki & Lightman, 1979). Finally, the structure of the source defines the width of the turnover region. A synchrotron self-absorbed spectrum can be parametrised as

$$S_\nu = S_0 \left( \frac{\nu}{\nu_p} \right)^{-(\beta-1)/2} \left[ \frac{1 - e^{-\tau'_\nu}}{\tau'_\nu} \right], \quad (5.4)$$

$$\tau'_\nu = \left( \frac{\nu}{\nu_p} \right)^{-(\beta+4)/2}, \quad (5.5)$$

where  $\beta$  is the power-law index of the electron energy distribution, and  $\nu_p$  represents the frequency where the source becomes optically thick (Tingay & de Kool, 2003; Callingham et al., 2015). At  $\nu_p$ , the mean free path of the synchrotron photons that scatter off the non-thermal electrons becomes comparable to the geometrical size of the synchrotron source (the jet knot).

The SSA model provides a better fit in the low-frequency band as compared to the FFA model, as highlighted by the black solid line, orange traces and orange residuals in Figure 5.5. After fitting the spectrum of MAXI J1535–571 with the SSA model in Equation (5.4) and using uniform priors  $\beta = 0 - 10$ ,  $S_0 = 1 - 1000$  mJy, and  $\nu_p = 0.05 - 10$  GHz, we estimated (with  $1\sigma$  uncertainties)  $S_0 = 882 \pm 56$  mJy,  $\beta = 1.90 \pm 0.04$  and  $\nu_p = 0.32 \pm 0.01$  GHz.

Using the aforementioned values together with our direct LBA size measurement, we can derive the minimum energy parameters without having to rely on the rise time of the radio flare to constrain the source size, or minimising the energy with respect to the source expansion rate, as recently proposed by Fender & Bright (2019). We follow Fender (2006), who give an expression for the synchrotron minimum energy as

$$E_{\min} \sim 3 \times 10^8 \eta^{4/7} \left( \frac{fV}{\text{cm}^3} \right)^{3/7} \left( \frac{\nu_p}{\text{Hz}} \right)^{2/7} \left( \frac{L_{\nu_p}}{\text{erg s}^{-1} \text{Hz}^{-1}} \right)^{4/7}, \quad (5.6)$$

where  $V$  is the volume of the synchrotron emitting plasma,  $f$  is the filling factor of the jet knot (assumed to be 1),  $\nu_p$  is the turnover frequency, and  $L_{\nu_p}$  is the luminosity of the jet knot at the turnover frequency.  $\eta = (1 + \beta_{pe})$ , where  $\beta_{pe}$  is the ratio of energy in protons to that in electrons, which we assume to be 0, such that  $\eta = 1$  (Fender, 2006).

The LBA observed MAXI J1535–571 on 23–24 September 2017 (MJD 58020.082 $\pm$ 0.147),  $\sim 3$  days after the peak of the radio outburst. Assuming a constant expansion speed, and an ejection date of MJD 58010.8 $^{+2.7}_{-2.5}$  (Russell et al., 2019c), we estimate the source size on 21 September to be 23.8 $^{+3.0}_{-2.8}$  mas. To calculate  $V$ , we assume the jet knot to be spherical of the measured size. From Equation 5.6,

we find a minimum energy value of  $E_{\min} = 6.5 \pm 2.5 \times 10^{41}$  erg, which is at the high end of the range  $10^{38} - 10^{42}$  erg reported from other XRBs such as V404 Cygni, Cygnus X-3, and GRS 1915+105 (e.g. Chandra & Kanekar, 2017; Fender & Bright, 2019).

We also follow Fender (2006) to calculate the minimum energy magnetic field strength, expressed as

$$B_{\text{eq}} \sim 1.6 \times 10^4 \eta^{2/7} \left( \frac{fV}{\text{cm}^3} \right)^{-2/7} \left( \frac{\nu_p}{\text{Hz}} \right)^{1/7} \left( \frac{L_{\nu_p}}{\text{erg s}^{-1} \text{Hz}^{-1}} \right)^{2/7}, \quad (5.7)$$

The minimum-energy magnetic field strength is found to be  $B_{\text{eq}} = 40 \pm 5$  mG, which is in line with the limits (10–500 mG) defined by Russell et al. (2019c), and comparable to canonical values for XRBs (Fender & Bright, 2019).

## 5.5 Discussion

Our study demonstrates the capabilities of the Australian suite of radio telescopes. As outlined in Section 5.3.5, we detected a low-frequency turnover in the broad-band radio spectrum of MAXI J1535–571. Due to limited high-cadence monitoring at low-frequencies, the low-frequency turnovers have previously been detected in just five BH-XRBs; SS 433, Cygnus X-3, V404 Cygni, GRS 1915+105 and MAXI J1348–630 (Seaquist et al., 1980, 1982; Miller-Jones et al., 2004; Chandra & Kanekar, 2017; Fender & Bright, 2019; Chauhan et al., 2019a) out of  $\sim 60$  black hole candidate XRBs (Corral-Santana et al., 2016; Tetarenko et al., 2016). In Section 5.4, we found that the low-frequency turnover is most likely due to SSA. In the following subsections, we discuss the implications of our derived SSA model parameters.

### 5.5.1 Magnetic field strength

Under the assumption that the low-frequency turnover is due to synchrotron self absorption, we can use our LBA measurement of the size of the jet knot to constrain the magnetic field strength  $B_s$  of the knot, as has often been done for the extragalactic jets. This can be determined (Marscher, 1983) as

$$B_s = 10^{-5} b(\alpha) \theta_s^4 \nu_p^5 S_0^{-2} \left[ \frac{\delta_{\text{bp}}}{1+z} \right] \text{ G}, \quad (5.8)$$

where  $\theta_s$  is the angular size of the synchrotron emitting region in mas,  $S_0$  is the radio flux density in Jy at the self-absorption turnover frequency  $\nu_p$  (measured in GHz), and  $\delta_{\text{bp}} = [\Gamma(1 - \beta \cos i)]^{-1}$  is the Doppler factor of the jet, with  $i$  being the inclination angle of the jet axis to the line of sight,  $\beta (= v/c)$  the jet speed, and  $\Gamma = [1 - \beta^2]^{-1/2}$  the bulk Lorentz factor of the jet. The quantity  $b(\alpha)$  is a slowly varying function of the high-frequency spectral index  $\alpha$ , which has a value of  $\approx 3.4$  for  $\alpha = -0.6$ . For a Galactic object the redshift  $z$  can be set to 0.

From the proper motion of the approaching jet knot, Russell et al. (2019c) constrained the product  $\beta \cos i \geq 0.49$ , implying that the jet speed  $\beta \geq 0.69$ , and  $i \leq 45^\circ$ . Using the aforementioned constraints, we defined a uniform distribution of  $0.69 \leq \beta \leq 1.0$  and  $1/\sqrt{2} \leq \cos i \leq 1$ , which corresponds to a distribution of  $i$  in the range  $0^\circ \leq i \leq 45^\circ$ . We calculated the probability density function for  $\delta_{\text{bp}}$ , finding that the 5–95% likelihood range for  $\delta_{\text{bp}}$  is 1.0–3.4. We used our fitted self-absorption turnover frequency and the radio flux density at that frequency (from Section 5.4.3) to determine the magnetic field strength as a function of source size, as shown in Figure 5.6. In Section 5.4.3, we calculate the source size on 21 September to be  $23.8_{-2.8}^{+3.0}$  mas, which corresponds to a jet expansion speed ( $\beta_m$ , in units of  $c$ ) of  $0.09 \pm 0.04$ . From equation (5.8), this implies a magnetic field strength of  $104_{-78}^{+80}$  mG,<sup>10</sup> which is consistent with the limits of

---

<sup>10</sup>The uncertainty on the magnetic field strength ( $B_s$ ) is dominated by the error on the ejection date, which dominates the uncertainty on the source size on 21 September 2017. To reduce the uncertainty on the ejection time in future outbursts, we would need to perform high-cadence VLBI monitoring of the source near the peak of the outburst.

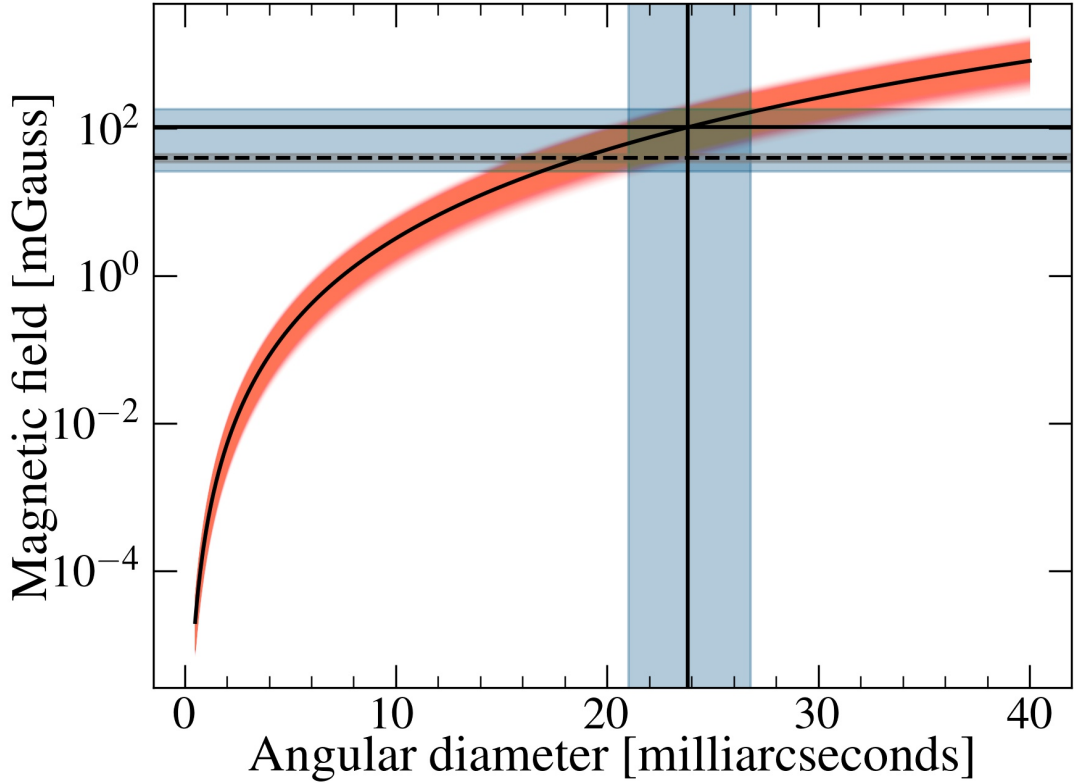


Figure 5.6: Variation of the magnetic field strength ( $B_s$ ) with angular size ( $\theta_s$ ) of the jet knot, according to Equation (5.8). The red shaded region around the main curve highlights the  $1\sigma$  uncertainties on the self-absorption turnover frequency  $\nu_p$ , the corresponding radio flux density  $S_0$ , and our calculated range for the Doppler factor  $\delta_{bp}$ . The vertical line at 23.8 mas indicates the estimated source size on 21 September 2017 (derived from our LBA observation on 23–24 September 2017, assuming constant expansion speed). The solid horizontal line shows the magnetic field strength ( $104^{+80}_{-78}$  mG) corresponding to the inferred source size. The shaded regions across all the horizontal and vertical lines indicate the  $1\sigma$  uncertainties. The dashed black horizontal line at 40 mG corresponds to the minimum energy field strength  $B_{eq}$ . Our SSA modelling and LBA size constraint suggest that the jet knot is close to equipartition.

10–500 mG derived from equipartition arguments by Russell et al. (2019c). Our derived magnetic field strength for MAXI J1535–571 is roughly consistent with the values reported for other X-ray binary jets (10 mG in SS 433; Seaquist et al. 1982, 250 mG in V404 Cygni; Chandra & Kanekar 2017).

The minimum energy magnetic field strength ( $B_{eq} \approx 40 \pm 5$  mG) estimated in Section 5.4.3 via the formalism of Fender (2006) is consistent (within uncertain-

ties) with the magnetic field strength ( $B_s$ ) determined from the LBA size measurement and synchrotron self-absorption theory. This suggests that the transient jet in MAXI J1535–571 is likely to be close to equipartition.

### 5.5.2 Jet opening angle

Russell et al. (2019c) analysed and fit the proper motion of the discrete jet knot with three different models; ballistic motion, constant deceleration, and ballistic motion plus late-time deceleration. They found that the proper motion of the transient ejecta could be best described by ballistic motion for the first  $\sim 260$  days, followed by late-time deceleration. In this model, the ejection event occurred on MJD  $58010.8^{+2.7}_{-2.5}$ . The opening angle  $\phi_{\text{op}}$  can be calculated as (Miller-Jones et al., 2006)

$$\tan \phi_{\text{op}} \approx \frac{\theta_s}{\mu_{\text{app}}(t_{\text{obs}} - t_{\text{ej}})}, \quad (5.9)$$

where  $\theta_s$  is the size of the jet knot,  $\mu_{\text{app}}$  is the proper motion of the approaching jet knot, and  $(t_{\text{obs}} - t_{\text{ej}})$  is the time between the ejection event and the observation.

With the measured proper motion of the jet component,  $\mu_{\text{app}} = 47.2 \pm 1.5$  mas day $^{-1}$  (Russell et al., 2019c), our LBA size measurement ( $\theta_s = 34 \pm 1$  mas) implies an opening angle of  $\phi_{\text{op}} = 4.5 \pm 1.2^\circ$  (independent of the inclination angle of the jet axis). The opening angle is consistent with the upper limit of  $\leq 10^\circ$  determined by Russell et al. (2019c).

Constraints on the jet opening angle  $\phi_{\text{op}}$  have only been determined for a small sample of BH-XRBs (Miller-Jones et al., 2006; Rushton et al., 2017; Tetarenko et al., 2018a), with all except three of these measurements being upper limits. The upper limits of Miller-Jones et al. (2006) range from  $< 2^\circ$  (for the steady hard-state jets in Cygnus X–1) to  $\leq 25.1^\circ$  (for V4641 Sgr). The measured values are for Cygnus X–3 ( $5 \pm 0.5^\circ$ ; Miller-Jones et al. 2006), XTE J1908+094 ( $\sim 58^\circ$ ; Rushton et al. 2017) and V404 Cygni ( $4^\circ - 10^\circ$ ; Tetarenko et al. 2017). Thus, our opening angle measurement is also in agreement with the typical constraints available for other BH-XRBs.

### 5.5.2.1 Lorentz factor

If the jet is not confined, we can use our measurement of the opening angle to constrain the bulk jet Lorentz factor via the formalism given by Miller-Jones et al. (2006) as

$$\Gamma = \left[ 1 + \frac{\beta_{\text{exp}}^2}{\tan^2 \phi_{\text{op}} \sin^2 i} \right]^{1/2}, \quad (5.10)$$

where  $\beta_{\text{exp}}$  is the expansion velocity of the plasma cloud and  $i$  is the inclination angle. We assume two different scenarios for the expansion of the jet knot. In one case, we assume the knot is expanding at the relativistic sound speed,  $c/\sqrt{3}$ . Alternatively, we assume the plasma knot is expanding freely with speed  $c$  (Miller-Jones et al., 2006). We determine  $\Gamma$  for all permissible values of  $i$  ( $\leq 45^\circ$ ; Russell et al. 2019c) as shown in Figure 5.7. For all allowed values of  $i$ ,  $\Gamma > 10$  (Figure 5.7).

The commonly-assumed range for the Lorentz factor in transient XRB jets is  $2 < \Gamma < 5$  (Miller-Jones et al., 2006); significantly lower than that inferred for MAXI J1535–571 assuming free expansion. But some recent studies (e.g., Casella et al., 2010; Tetarenko et al., 2019, 2021) have suggested that the Lorentz factors may be significantly higher. However, XRB jet Lorentz factors are typically poorly constrained; Fender (2003) demonstrated that for any significantly relativistic jet, we can only determine a lower limit on  $\Gamma$  (if the distance to the source is poorly constrained) using the proper motions of the bipolar ejecta. From the constraints on  $\beta \cos i$  derived by Russell et al. (2019c), high Lorentz factors would imply a very low inclination angle, which is relatively improbable, and inconsistent with the disk inclination angles determined from X-ray spectral fitting of the Fe  $K\alpha$  line (Miller et al., 2018; Xu et al., 2018). We therefore suggest that the jet knot in MAXI J1535–571 is not freely expanding, and is instead externally confined. This is in agreement with the relatively low expansion speed of  $\beta_{\text{m}} = 0.09 \pm 0.04$  derived from the measured source size in Section 5.5.1. Our calculated  $\beta_{\text{m}}$  is consistent with the limit ( $< 0.18 c$ ) determined by Russell et al.

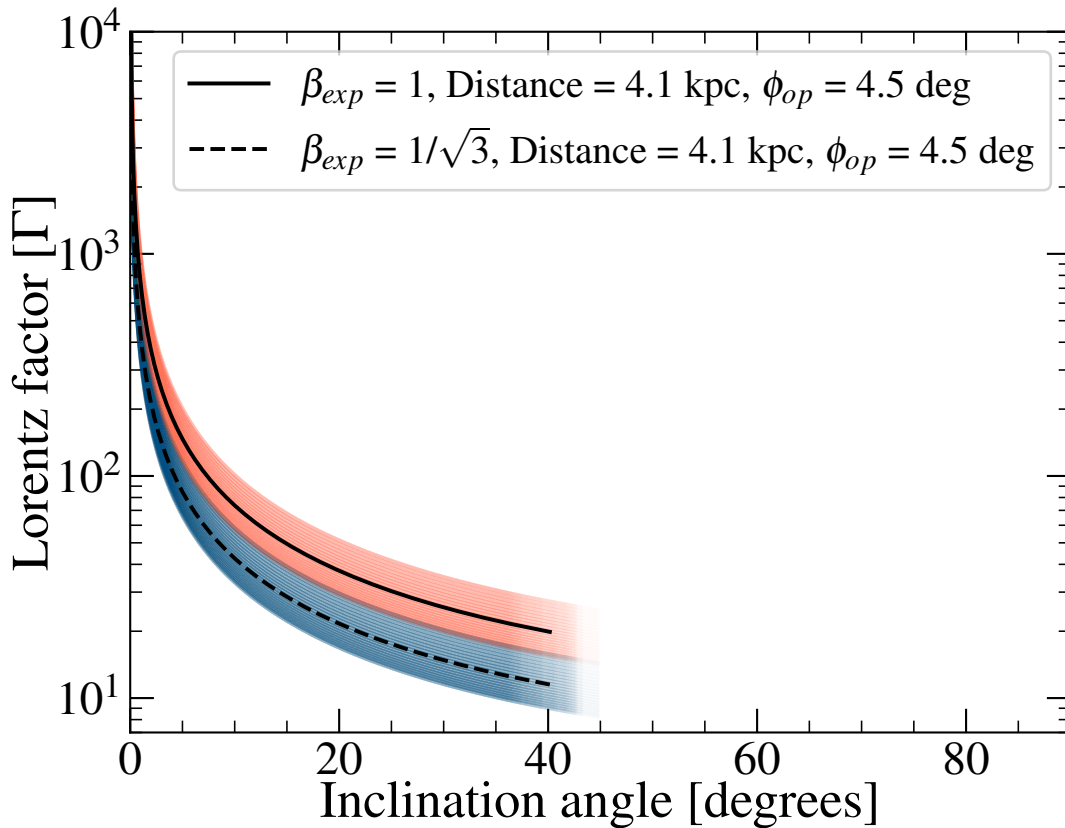


Figure 5.7: The variation of the bulk Lorentz factor with the inclination angle. The solid and the dashed black lines highlight the expected curves for expansion speeds of  $c$  and  $c/\sqrt{3}$ , respectively. The orange (expansion speed  $c$ ) and the blue (expansion speed  $c/\sqrt{3}$ ) shaded regions show the effect of incorporating the  $1\sigma$  uncertainty on the opening angle and the distance to the source ( $4.1^{+0.6}_{-0.5}$  kpc; Chapter 3). If the jet is freely expanding, we would predict a bulk Lorentz factor  $\Gamma > 10$ .

(2019c) for the expansion speed. Additionally, Tetarenko et al. (2017) estimated similarly low expansion speeds of  $0.01$ – $0.1c$  for the transient jet knots in V404 Cygni, and found that the jet knot was externally confined. Potential confinement mechanisms could include the disc magnetic field, the thermal gas pressure from the surrounding medium, or inertial confinement by an outflowing wind (see, e.g., Begelman et al., 1984; Ferrari, 1998; Miller-Jones et al., 2006). With the available results, we cannot discriminate between the above-mentioned confinement mechanisms. Confinement due to the thermal gas pressure from the surrounding medium is certainly plausible, because the jet knot would have travelled a signif-

icant distance from the black hole between the time of ejection and the time of our observations.

### 5.5.3 Future studies with the SKA-Low

Our study showcases the potential contributions that SKA-Low (frequency range 50–350 MHz) could make to the study of radio jets from black hole X-ray binaries. MAXI J1535–571 was relatively bright, and hence accessible to the current SKA precursor facilities. Most BH XRB jets are somewhat fainter [e.g., EXO 1846–031 (Williams et al., 2019), MAXI J1820+070 (Bright et al., 2020), and MAXI J1803–298 (Espinasse et al., 2021)], peaking at a few tens of mJy at GHz frequencies. Such faint systems would require (sub-)mJy-level sensitivity for us to detect them at low radio frequencies, and could not be effectively probed by MWA. While lower-power transient jets may initially be smaller, and hence would evolve more rapidly, their spectra should nonetheless evolve to lower frequencies with time (van der Laan, 1966a), albeit with fainter peak flux densities. Provided they are observed sufficiently early in their evolution, the higher expected sensitivity of SKA-Low ( $14\text{--}26 \mu\text{Jy beam}^{-1} \text{hr}^{-1/211}$ ) should therefore allow us to study the transient jets from faint BH XRBs, as well as neutron star XRBs, whose faintness has to date precluded the kinds of detailed studies performed on black holes. The SKA-Low will therefore enable the detailed exploration of accretion-ejection coupling across a broader range of stellar-mass compact objects (see, e.g., Corbel et al., 2015, for further details).

## 5.6 Conclusions

In this work, we have conducted a multi-wavelength study of the transient jet from the black hole candidate XRB MAXI J1535–571. We presented new results from MWA, UTMOST and LBA, and included previously-published results from

---

<sup>11</sup><https://www.astron.nl/telescopes/square-kilometre-array/>

ASKAP and ATCA, collectively providing spectral coverage from 0.12–19 GHz. During our campaign, we made the first MWA detection of a transient radio jet from a black hole XRB, detecting MAXI J1535–571 at a significance  $> 10\sigma$ . Using our LBA observation on 23 September 2017, we constrained the source size to  $34 \pm 1$  mas, which corresponds to a physical size of  $139_{-17}^{+21}$  AU, calculated using a source distance of  $4.1_{-0.5}^{+0.6}$  from Chapter 3. The size constraints allowed us to calculate the jet opening angle to be  $4.5 \pm 1.2^\circ$ . Given the large bulk Lorentz factor that would be implied in the case of a freely-expanding jet, we infer that the jet knot is likely to be externally confined.

Our broad-band spectrum on 21 September 2017 indicates the presence of a low-frequency spectral turnover, whose peak frequency is strongly constrained by the MWA observations. The detected low-frequency turnover is likely due to synchrotron self-absorption. We fitted the broadband spectrum with a self-absorption model, and calculated the power-law index of the energy distribution for the relativistic electrons of the source ( $\beta = 1.90 \pm 0.04$ ), the turnover frequency ( $\nu_p = 0.32 \pm 0.01$  GHz), and the corresponding peak flux density ( $S_0 = 882 \pm 56$  mJy).

We further used our LBA size constraint along with the turnover frequency and the peak flux density obtained from the SSA model fitting to calculate the magnetic field strength ( $104_{-78}^{+80}$  mG) and the minimum energy ( $6.5 \pm 2.5 \times 10^{41}$  erg) of the jet knot. These estimates are consistent with the values estimated for MAXI J1535–571 by Russell et al. (2019c), and with canonical XRB values.

Finally, our study highlights the combined capabilities of the Australian suite of radio telescopes including MWA, UTMOST, ASKAP, ATCA and LBA, which can provide sensitive and simultaneous broadband coverage of radio jets in XRBs. This will be significantly augmented over the coming years as we move into the era of the SKA.

Having demonstrated that low-frequency telescopes such as the MWA can be used to study the transient jets in BH-XRBs, we now turn our attention to the

compact jets. In the next chapter, we present the first detection of compact jets at frequencies below 300 MHz, detailing our MWA observations of two BH-XRBs, namely MAXI J1820+070 and MAXI J1348–630. We also present a qualitative comparison of our results with the physical jet models for the compact jets.



## Chapter 6

# Low-frequency MWA detections of compact jets in two black hole XRBs

In this chapter, we present a broadband radio study of the compact jets from two black hole XRBs; MAXI J1820+070 and MAXI J1348–630, which underwent outbursts in March 2018 and January 2019, respectively. We monitored both the sources with the MWA during the compact jet phases of their outbursts, and combined the MWA data with quasi-simultaneous higher-frequency data from other facilities. This is the first time that compact jets have been detected from black hole XRBs at low radio frequencies ( $< 300$  MHz). The broadband spectra of the compact jets in both the sources were found to be comparatively flat, with no indications of any low-frequency turnover. We interpret these unbroken spectra in light of prevailing theoretical models for compact jets. Finally, this chapter emphasizes the importance of the SKA precursor telescope MWA for the monitoring of compact jets in BH-XRBs. Note that the processing of MWA data sets for MAXI J1820+070 and MAXI J1348–630 finished in December 2020. We, therefore, present a qualitative comparison of our results with the physical models for the compact jets.

## 6.1 Introduction

### 6.1.1 MAXI J1820+070

In early March 2018, ASAS-SN discovered an optical transient, ASASSN-18ey (Denisenko, 2018; Tucker et al., 2018), which was detected by *MAXI* on 11 March 2018 as an X-ray transient and designated MAXI J1820+070 (Kawamuro et al., 2018; Shidatsu et al., 2018). The system is a low-mass X-ray binary, and harbours a dynamically confirmed black hole of mass  $8.48^{+0.79}_{-0.72} M_{\odot}$ , with a K-type dwarf companion star (Torres et al., 2019, 2020). Using radio parallax measurements for MAXI J1820+070 from VLBI observations, Atri et al. (2020) constrained the distance to the source to be  $2.96 \pm 0.33$  kpc. In the *Gaia* EDR3 data release (Gaia Collaboration et al., 2020), the source distance was found to be  $2.66^{+0.85}_{-0.52}$  kpc, which is consistent with the distance measurements of Atri et al. (2020). The authors also found that the radio jets were at an angle of  $63 \pm 3$  degrees to the line of sight (Atri et al., 2020).

During its 2018–2019 outburst, MAXI J1820+070 was bright across the electromagnetic spectrum from radio through to X-rays (e.g., Bright et al., 2018; Trushkin et al., 2018; Gandhi et al., 2018; Paice et al., 2019; Stiele & Kong, 2020; Buisson et al., 2021). From initial X-ray monitoring (early March 2018), the source was found to be in the hard X-ray spectral state (Bozzo et al., 2018; Del Santo & Segreto, 2018; Uttley et al., 2018), during which the compact jets were detected (e.g., Tetarenko et al., 2018b; Trushkin et al., 2018). MAXI J1820+070 continued to be in a prolonged hard X-ray spectral state until early July 2018, when it transitioned to the soft X-ray spectral state (Homan et al., 2020). During the course of this X-ray spectral state transition, the compact jets were quenched (Tetarenko et al., 2018b), and the source underwent a radio flaring event, with apparently superluminal discrete transient jet ejections (Bright et al., 2020; Espinasse et al., 2020).

On 12 April 2018, Rodi et al. (2021) generated a spectral energy distribution

(SED) spanning from the radio (meter-wavelength frequencies; 339 MHz from VLITE) to the high energy X-rays ( $\approx 400$  keV from *INTEGRAL*/IBIS/ISGRI) for MAXI J1820+070. The authors performed a broadband fit to the SED using a model that includes a leptonic jet with an acceleration region, a synchrotron-dominated cooling region and an irradiated disk consisting of a Compton hump. Through this modelling, Rodi et al. (2021) found that the jet emission governed the spectrum up to  $\sim 10^{14}$  Hz, after which coronal and disk emission dominated. The flat radio spectrum was due to synchrotron cooling of the accelerated electrons, and the magnetic field and cross-section of the acceleration region were found to be  $\approx 2 \times 10^4$  G and  $\approx 3 \times 10^9$  cm, respectively (Rodi et al., 2021). In radio, the authors mostly concentrated on the high-frequency part to study the high-frequency turnover (Rodi et al., 2021), which is thought to be the jet base (Russell et al., 2013).

Recently, Tetarenko et al. (2021) performed a fast timing study of MAXI J1820+070 during its hard X-ray spectral state observation on 12 April 2018. Using the multi-wavelength data spanning from radio to X-ray band, the authors have found that the emission was highly variable, and also show multiple rapid flaring events (Tetarenko et al., 2021). From the modelling of variability, Tetarenko et al. (2021) found the compact jets in MAXI J1820+070 to be highly relativistic ( $\Gamma = 6.81_{-1.15}^{+1.06}$ ), and confined to a small region, with an opening angle of  $0.45_{-0.11}^{+0.13}$  degrees. The authors further reported that the jets extracted a significant amount of power ( $\approx 0.6L_{1-100\text{ keV}}$ ) from the system (Tetarenko et al., 2021). Using the jet power and bulk jet speed, Tetarenko et al. (2021) found that protons cannot be in majority in the jet of MAXI J1820+070. The authors finally reported that in the jet base region the magnetic field strength is  $> 6 \times 10^3$  G. Tetarenko et al. (2021) also focused on the high-frequency part ( $> 5$  GHz) of the compact jet.

### 6.1.2 MAXI J1348–630

We have already provided an introduction to MAXI J1348–630 in Chapter 4. Using the HI absorption measurements from the ASKAP and MeerKAT observations, we constrained the distance to the source to  $2.2_{-0.6}^{+0.5}$  kpc in Chapter 4 of this thesis (Chauhan et al., 2021). Using our preferred distance constraints we found that the source reached  $17 \pm 10\%$  of the Eddington luminosity at the peak of its outburst. MAXI J1348–630 transited from the soft to the hard X-ray spectral state at  $2.5 \pm 1.5\%$  of the Eddington luminosity.

Carotenuto et al. (2021a) have presented the results from radio (using the MeerKAT and ATCA) and X-ray monitoring (using *MAXI* and *Swift*/XRT) of MAXI J1348–630. The authors detected and studied the evolution of both types of jets; the compact and the transient jets. MAXI J1348–630 underwent two independent discrete ejections separated by a period of  $\sim 2$  months, one of which had a measured proper motion of  $\gtrsim 100$  mas day $^{-1}$  (Carotenuto et al., 2021a). The authors constrained the jet speed ( $\geq 0.69c$ ) and the jet inclination angle ( $\leq 46^\circ$ ) with the help of measured proper motion and our distance estimates (Chapter 4). The authors further found that MAXI J1348–630 could be residing within a low-density cavity (Carotenuto et al., 2021a).

Recently, Carotenuto et al. (2021b) studied the spectra of compact jets in MAXI J1348–630 in the GHz-frequency band over the course of the outburst. The authors detected a peculiar behaviour in MAXI J1348–630, where the source displayed a hybrid radio/X-ray correlation. In this case, MAXI J1348–630 started out on the “radio-quiet track” and then transitioned to the “standard track” (Corbel et al., 2013; Bright et al., 2020; Shaw et al., 2021). Such behaviour had previously been observed in only a few other sources (Carotenuto et al., 2021b).

In this chapter, we report our MWA observations of the compact radio jets from two black hole XRBs; MAXI J1820+070 and MAXI J1348–630. To study the multi-frequency spectra of the compact jets, we combine previously-published high-frequency ( $> 1$  GHz) data from Tetarenko et al. 2021 [MAXI J1820+070;

from Karl G. Jansky Very Large Array (VLA) and Atacama Large Millimeter/Sub-Millimeter Array (ALMA) observations] and Carotenuto et al. 2021a (MAXI J1348–630; from MeerKAT and ATCA observations). In the case of MAXI J1820+070, we also include a VLITE observation on 12 April 2018 at 339 MHz (Polisensky et al., 2018). We provide a comprehensive description of our monitoring campaign and data reduction methodology in Section 6.2. In Section 6.3, we present our results, including an analysis of the broadband spectrum. Section 6.4 discusses the importance of our results, and finally, Section 6.5 provides the conclusions from our work.

## 6.2 Observations and Data reduction

### 6.2.1 MAXI J1820+070

#### 6.2.1.1 MWA

During the 2018–2019 outburst of MAXI J1820+070, the MWA observed the source with a daily cadence from 19 March to 26 March 2018 under the project code D0014. The MWA further observed MAXI J1820+070 on 01 April, 12 April and 21 April 2018. During our monitoring campaign MWA was in its extended configuration (discussed in Section 1.8.1), which is most suitable for observing BH-XRBs due to higher sensitivity (due to the reduced confusion noise) afforded by improved angular resolution (Wayth et al., 2018).

Our observations were performed in three different frequency bands centred at 154, 186, and 216 MHz, each having a processed bandwidth of 30.72 MHz. We monitored MAXI J1820+070 for 14 to 30 min (given in Table 6.1) in each frequency band on all dates except for 12 April 2018, when we observed the source for 60 min as we were participating in a multi-wavelength monitoring campaign (Tetarenko et al., 2021) and 21 April 2018, when we observed for 40 min due to the source being in the declining phase of its outburst. Our observations included 7 to 15 independent 2-min snapshots, accompanied by a 120-s observation of the

standard, bright calibrator source Hydra A. Further information on the MWA monitoring can be seen in Table 6.1.

For processing the MWA data, we primarily depend on the `MWA-fast-image-transients` pipeline<sup>1</sup>. Additionally, we applied the `fits_warp` tool for correcting ionospheric distortions (Hurley-Walker & Hancock, 2018), and the `flux_warp` and `ROBBIE` software packages to correct for the absolute flux density calibration and to perform image stacking, respectively (Duchesne et al., 2020; Hancock et al., 2019). A complete guide for the MWA data reduction has already been presented in Section 2.3.

In our observations, the source significance is  $< 5\sigma$ . Therefore, after initial flux density scale calibration, we tested the accuracy of the flux densities of the sources ( $> 5\sigma$ ). We compared the MWA observation at 154 MHz with the Tata Institute for Fundamental Research GMRT Sky Survey Alternative Data Release catalogue<sup>2</sup> (TGSS ADR; Intema et al., 2017) at 150 MHz. We observed that the measured MWA flux densities are higher by 20 to 30 %, and the discrepancy increased when the flux density of the sources was  $< 100$  mJy ( $< 5\sigma$ ). Similarly, we also checked the flux density scales of the 186 and 216 MHz MWA observations and found that they were also higher. Hurley-Walker et al. (2019) already observed some fluctuations in the flux densities of Galactic sources at low frequencies (Figure 8 of Hurley-Walker et al. 2019).

The reason behind such a discrepancy could be that MWA had limited resolution in Phase I when the Galactic and Extragalactic All-sky MWA (GLEAM) survey (Hurley-Walker et al., 2017) was conducted. During our compact jet observations, MWA was in its Phase II extended configuration, which has a higher resolution by nearly a factor of 2 as compared to Phase I (Wayth et al., 2018). Therefore, diffuse emission in the Galactic Plane could have been resolved out during our observations, resulting in lower flux density as compared to the Phase I GLEAM data. Hence, the calibration of the flux density scales with the

---

<sup>1</sup><https://github.com/PaulHancock/MWA-fast-image-transients>

<sup>2</sup><http://tgssadr.strw.leidenuniv.nl/doku.php>

`flux_warp` tool using the GLEAM catalogue could have biased the measured flux densities high.

To remove the offset in the MWA flux density scales, we took additional steps along with the `flux_warp` tool. We calibrated our 154-MHz MWA observations with the TGSS-ADR1 catalogue. In the case of our 186 and 216 MHz observations, we first applied the `flux_warp` tool, then to remove any local effect we used calibrator sources within a  $3^\circ$  region around our target sources and corrected the flux density offsets. Finally, we cross matched the calibrator sources in the  $3^\circ$  region around MAXI J1820+070 and MAXI J1348–630, with the VLA Low-Frequency Sky Survey (VLSS at 74 MHz; Cohen et al., 2007), TGSS-ADR1, the NRAO VLA Sky Survey (NVSS at 1.4 GHz Condon et al., 1998) and the Very Large Array Sky Survey (VLASS at 3 GHz Lacy et al., 2020). We generated a radio spectrum from 74 MHz to 3 GHz and modelled it with a power-law using a Bayesian approach. We overlaid MWA data points on the fitted spectrum and checked the consistency of the flux density scales. If required, we bootstrapped the flux density calibration depending on this analysis.

#### **6.2.1.2 VLITE**

MAXI J1820+070 was observed at 339 MHz with VLITE on 12 April 2018 (MJD 58220.428) from 07:25 to 13:07 UTC, where the on-source exposure was 53 min (Polisensky et al., 2018). The authors calculated the radio flux density of the source to be  $33 \pm 5.3$  mJy. The VLITE observation complimentary to the VLA observations, using the simultaneously-mounted P-band system on the VLA (Polisensky et al., 2018). For more information on the VLITE observation see Polisensky et al. (2018).

#### **6.2.1.3 High-frequency ( $> 5$ GHz) observations**

Tetarenko et al. (2021) monitored MAXI J1820+070 over a broad frequency band from 5.5 GHz to 343.5 GHz with observations from VLA and ALMA. To comple-

ment our MWA low-frequency observations on 12 April 2018, we incorporate these monitoring results from Tetarenko et al. (2021) into our study (included in Table 6.1). For a comprehensive description of the full multi-wavelength coverage and data reduction, see Tetarenko et al. (2021).

Table 6.1: Details of the observations of MAXI J1820+070 used in this Chapter.

| Observation<br>Start date<br>(dd-mm-yyyy) | Observation<br>Start time<br>(hh:mm:ss)<br>(UTC) | MJD <sup>a</sup> | Exposure<br>time<br>(min) | Telescope | Central<br>frequency<br>(GHz) | Flux density <sup>b</sup><br>$S_0$<br>(mJy) | References |
|---|--|------------------|---------------------------|-----------|-------------------------------|---|------------|
| 19-03-2018                                | 21:10:38   | 58196.89         | 18                        | MWA       | 0.154                         | $49 \pm 16$                                 | This work  |
|   | 21:12:38   | 58196.89         | 18                        | MWA       | 0.186                         | $42 \pm 11$                                 | This work  |
|   | 22:05:42   | 58196.93         | 30                        | MWA       | 0.216                         | $27 \pm 6$                                  | This work  |
| 20-03-2018                                | 21:06:46   | 58197.89         | 18                        | MWA       | 0.154                         | $60 \pm 15$                                 | This work  |
|   | 21:08:46   | 58197.22         | 18                        | MWA       | 0.186                         | $36 \pm 11$                                 | This work  |
|   | 22:05:50   | 58197.93         | 26                        | MWA       | 0.216                         | $33 \pm 8$                                  | This work  |
| 21-03-2018                                | 21:02:46   | 58198.89         | 18                        | MWA       | 0.154                         | $< 43$                                      | This work  |
|   | 21:04:46   | 58198.89         | 18                        | MWA       | 0.186                         | $57 \pm 13$                                 | This work  |
|   | 22:07:50   | 58198.93         | 20                        | MWA       | 0.216                         | $31 \pm 9$                                  | This work  |
| 22-03-2018                                | 20:58:54   | 58199.89         | 18                        | MWA       | 0.154                         | $50 \pm 15$                                 | This work  |
|   | 22:07:58   | 58199.93         | 16                        | MWA       | 0.216                         | $41 \pm 11$                                 | This work  |

| Continuation of Table 6.1                 |  |                  |                           |           |                               |   |            |
|---|--|------------------|---------------------------|-----------|-------------------------------|---|------------|
| Observation<br>Start date<br>(dd-mm-yyyy) | Observation<br>Start time<br>(hh:mm:ss)<br>(UTC) | MJD <sup>a</sup> | Exposure<br>time<br>(min) | Telescope | Central<br>frequency<br>(GHz) | Flux density <sup>b</sup><br>$S_0$<br>(mJy) | References |
| 23-03-2018                                | 22:07:58   | 58200.94         | 18                        | MWA       | 0.154                         | $48 \pm 14$                                 | This work  |
|   | 22:09:58   | 58200.94         | 18                        | MWA       | 0.186                         | $34 \pm 9$                                  | This work  |
|   | 22:11:58   | 58200.94         | 16                        | MWA       | 0.216                         | $< 27$                                      | This work  |
| 24-03-2018                                | 22:10:06   | 58201.94         | 16                        | MWA       | 0.154                         | $46 \pm 14$                                 | This work  |
|   | 22:12:06   | 58201.94         | 14                        | MWA       | 0.186                         | $49 \pm 11$                                 | This work  |
|   | 22:14:06   | 58201.94         | 16                        | MWA       | 0.216                         | $39 \pm 10$                                 | This work  |
| 25-03-2018                                | 22:12:06   | 58202.94         | 16                        | MWA       | 0.154                         | $47 \pm 15$                                 | This work  |
|   | 22:10:06   | 58202.94         | 16                        | MWA       | 0.216                         | $< 36$                                      | This work  |
| 26-03-2018                                | 21:31:10   | 58203.90         | 18                        | MWA       | 0.154                         | $< 42$                                      | This work  |
|   | 22:10:14   | 58203.93         | 14                        | MWA       | 0.186                         | $54 \pm 11$                                 | This work  |
|   | 22:12:14   | 58203.93         | 14                        | MWA       | 0.216                         | $< 25$                                      | This work  |
| 01-04-2018                                | 20:32:46   | 58209.87         | 20                        | MWA       | 0.154                         | $< 37$                                      | This work  |
|   | 20:34:46   | 58209.88         | 20                        | MWA       | 0.186                         | $39 \pm 10$                                 | This work  |

| Continuation of Table 6.1                 |  |                  |                           |           |                               |   |            |
|---|--|------------------|---------------------------|-----------|-------------------------------|---|------------|
| Observation<br>Start date<br>(dd-mm-yyyy) | Observation<br>Start time<br>(hh:mm:ss)<br>(UTC) | MJD <sup>a</sup> | Exposure<br>time<br>(min) | Telescope | Central<br>frequency<br>(GHz) | Flux density <sup>b</sup><br>$S_0$<br>(mJy) | References |
|   | 20:36:46   | 58209.88         | 20                        | MWA       | 0.216                         | $33 \pm 9$                                  | This work  |
| 12-04-2018                                | 19:13:36   | 58220.87         | 60                        | MWA       | 0.154                         | $34 \pm 7$                                  | This work  |
|   | 19:15:36   | 58220.87         | 60                        | MWA       | 0.186                         | $36 \pm 6$                                  | This work  |
|   | 19:17:36   | 58220.87         | 60                        | MWA       | 0.216                         | $33 \pm 5$                                  | This work  |
|   | 07:23:00   | 58220.43         | 53                        | VLITE     | 0.339                         | $33 \pm 5.3$                                | [1]        |
|   | ~07:25:58  | ~58220.31        | 360                       | VLA       | 5.25                          | $46 \pm 3.25$                               | [2]        |
|   | ~07:25:58  | ~58220.31        | 360                       | VLA       | 7.45                          | $48.1 \pm 3.41$                             | [2]        |
|   | ~07:25:58  | ~58220.31        | 360                       | VLA       | 8.5                           | $48.3 \pm 3.42$                             | [2]        |
|   | ~07:25:58  | ~58220.31        | 360                       | VLA       | 11.0                          | $49.2 \pm 3.49$                             | [2]        |
|   | ~07:25:58  | ~58220.31        | 360                       | VLA       | 20.9                          | $58.7 \pm 6.65$                             | [2]        |
|   | ~07:25:58  | ~58220.31        | 360                       | VLA       | 25.9                          | $60.5 \pm 6.85$                             | [2]        |
|   | ~08:20:58  | ~58220.35        | 120                       | ALMA      | 343.5                         | $125.3 \pm 8.86$                            | [2]        |
| 21-04-2018                                | 20:02:00   | 58229.87         | 40                        | MWA       | 0.154                         | $50 \pm 10$                                 | This work  |
|   | 20:04:00   | 58229.88         | 40                        | MWA       | 0.186                         | $39 \pm 8$                                  | This work  |

| Continuation of Table 6.1                 |  |                  |                           |           |                               |   |            |
|---|--|------------------|---------------------------|-----------|-------------------------------|---|------------|
| Observation<br>Start date<br>(dd-mm-yyyy) | Observation<br>Start time<br>(hh:mm:ss)<br>(UTC) | MJD <sup>a</sup> | Exposure<br>time<br>(min) | Telescope | Central<br>frequency<br>(GHz) | Flux density <sup>b</sup><br>$S_0$<br>(mJy) | References |
|   | 20:06:00   | 58229.88         | 40                        | MWA       | 0.216                         | $33 \pm 7$                                  | This work  |
| End of Table                              |  |                  |                           |           |                               |   |            |

<sup>a</sup> Mid point of the observations.

<sup>b</sup> We quote  $1\sigma$  errors on the flux density, which are calculated by adding the  $1\sigma$  RMS noise in the continuum image and the  $1\sigma$  uncertainty on the Gaussian fit to the source in quadrature. For MWA, we also incorporate an absolute flux density calibration error of 10% (again, added in quadrature).

[1] Polisensky et al. (2018); [2] Tetarenko et al. (2021).

Note: All upper limits are quoted at the  $3\sigma$  level.

## 6.2.2 MAXI J1348–630

### 6.2.2.1 MWA

MAXI J1348–630 was observed as part of the MWA monitoring project for XRB transient outbursts (G0052). Here we include data from 6 to 16 February 2019, when the source was in outburst and bright ( $> 50$  mJy) at low radio frequencies ( $< 300$  MHz). Our observations were carried out using 128 MWA tiles in the extended configuration (Section 1.8.1), in two separate frequency bands centred at 154 and 216 MHz, with 30.72 MHz of bandwidth at each frequency. MAXI J1348–630 was monitored for 60 min at each frequency, where each observation comprised of 30 individual 2-min snapshots (Table 6.2). To calibrate our MAXI J1348–630 observations, we used the standard calibrator source Centaurus A, observed for 176 s following the MAXI J1348–630 observations. We analysed our MAXI J1348–630 data using the procedure described in detail in Section 2.3.

### 6.2.2.2 MeerKAT

Carotenuto et al. (2021a) monitored MAXI J1348–630 with MeerKAT under the umbrella of the large survey project; ThunderKAT (Fender et al., 2016). The source was observed with nearly weekly cadence for 15-min from 29 January 2019 (MJD 58512) to 3 March 2020 (58910) for a total of 48 epochs. The observation on 29 January 2019 (MJD 58512) was the only instance when the on-source exposure was 20-min (two separate 10-min scans). All observations were carried out at a central frequency 1.28 GHz, with a total bandwidth of 860 MHz. To complement our MWA observations, we include MeerKAT observations between 6 February (MJD 58520) and 16 February 2019 (MJD 58530) in our analysis, which are also listed in Table 6.2. To put our MWA observations of MAXI J1348–630 during the radio flaring episode in context, we incorporate all MeerKAT observations between 27 January 2019 (MJD 58510) and 01 March 2019 (MJD 58543) in our multi-radio frequency light curve displayed in Section 6.3.2.2. For more details on MeerKAT monitoring and data processing see Carotenuto et al. (2021a).

### 6.2.2.3 ATCA

ATCA monitored the 2019–2020 outburst of MAXI J1348–630 over thirty-one epochs between 26 January and 14 December 2019 (Carotenuto et al., 2021a). To complement our low-frequency ( $< 300$  MHz) monitoring with MWA, our analysis only includes those ATCA observations taken between 6 February (MJD 58520) and 16 February 2019 (MJD 58530). Over this period, ATCA observed MAXI J1348–630 in four main frequency bands centred at 5.5, 9, 16.7 and 21.2 GHz, with 2 GHz of bandwidth at each frequency (included in Table 6.2). To study the overall behaviour of the source at high frequencies ( $> 5$  GHz) during the radio flaring event, we combine all ATCA observations between 27 January 2019 (MJD 58510) and 4 March 2019 (58546) in our multi-frequency light curve presented in Section 6.3.2.2.

Table 6.2: Summary of the MAXI J1348–630 observations used in this study.

| Observation<br>Start date<br>(dd-mm-yyyy) | MJD                 | Telescope | Central<br>frequency<br>(GHz) | Flux density <sup>a</sup><br>$S_0$<br>(mJy) | References |
|---|---------------------|-----------|-------------------------------|---|------------|
| 06-02-2019                                | $58520.84 \pm 0.02$ | MWA       | 0.154                         | $68 \pm 13$                                 | This work  |
|   | $58520.86 \pm 0.02$ | MWA       | 0.216                         | $79 \pm 9$                                  | This work  |
| 07-02-2019                                | $58521.84 \pm 0.02$ | MWA       | 0.154                         | $92 \pm 14$                                 | This work  |
|   | $58521.86 \pm 0.02$ | MWA       | 0.216                         | $82 \pm 9$                                  | This work  |
|   | $58521.97 \pm 0.09$ | ATCA      | 5.5                           | $52.3 \pm 0.1$                              | [1]        |
|   | $58521.97 \pm 0.09$ | ATCA      | 9.0                           | $52.1 \pm 0.1$                              | [1]        |
|   | $58521.99 \pm 0.07$ | ATCA      | 16.7                          | $52.8 \pm 0.6$                              | [1]        |
|   | $58521.99 \pm 0.07$ | ATCA      | 21.2                          | $51.7 \pm 0.6$                              | [1]        |

| Continuation of Table 6.2                 |                     |           |                               |   |            |
|---|---------------------|-----------|-------------------------------|---|------------|
| Observation<br>Start date<br>(dd-mm-yyyy) | MJD                 | Telescope | Central<br>frequency<br>(GHz) | Flux density <sup>a</sup><br>$S_0$<br>(mJy) | References |
| 08-02-2019                                | $58522.84 \pm 0.02$ | MWA       | 0.154                         | $103 \pm 16$                                | This work  |
|   | $58522.86 \pm 0.02$ | MWA       | 0.216                         | $98 \pm 11$                                 | This work  |
| 09-02-2019                                | $58523.84 \pm 0.02$ | MWA       | 0.154                         | $429 \pm 44$                                | This work  |
|   | $58523.86 \pm 0.02$ | MWA       | 0.216                         | $450 \pm 45$                                | This work  |
|   | $58523.22 \pm 0.01$ | MeerKAT   | 1.3                           | $485.6 \pm 1.6$                             | [1]        |
|   | $58523.93 \pm 0.06$ | ATCA      | 5.5                           | $129.8 \pm 1.5$                             | [1]        |
|   | $58523.93 \pm 0.06$ | ATCA      | 9.0                           | $105 \pm 1$                                 | [1]        |
|   | $58523.94 \pm 0.03$ | ATCA      | 16.7                          | $74.5 \pm 0.4$                              | [1]        |
|   | $58523.94 \pm 0.03$ | ATCA      | 21.2                          | $66.7 \pm 0.5$                              | [1]        |
| 10-02-2019                                | $58524.84 \pm 0.02$ | MWA       | 0.154                         | $463 \pm 47$                                | This work  |
|   | $58524.86 \pm 0.02$ | MWA       | 0.216                         | $504 \pm 51$                                | This work  |
| 11-02-2019                                | $58525.84 \pm 0.02$ | MWA       | 0.154                         | $295 \pm 31$                                | This work  |
|   | $58525.86 \pm 0.02$ | MWA       | 0.216                         | $280 \pm 28$                                | This work  |
|   | $58525.86 \pm 0.01$ | ATCA      | 5.5                           | $223.0 \pm 0.7$                             | [1]        |
|   | $58525.86 \pm 0.01$ | ATCA      | 9.0                           | $191.5 \pm 0.5$                             | [1]        |
|   | $58525.87 \pm 0.01$ | ATCA      | 16.7                          | $146.3 \pm 0.3$                             | [1]        |
|   | $58525.87 \pm 0.01$ | ATCA      | 21.2                          | $140.0 \pm 0.5$                             | [1]        |
| 12-02-2019                                | $58526.84 \pm 0.02$ | MWA       | 0.154                         | $402 \pm 41$                                | This work  |
|   | $58526.86 \pm 0.02$ | MWA       | 0.216                         | $334 \pm 34$                                | This work  |
| 13-02-2019                                | $58527.84 \pm 0.02$ | MWA       | 0.154                         | $214 \pm 23$                                | This work  |
|   | $58527.86 \pm 0.02$ | MWA       | 0.216                         | $180 \pm 18$                                | This work  |
|   | $58527.76 \pm 0.21$ | ASKAP     | 1.42                          | $155 \pm 2$                                 | [2]        |
|   | $58527.91 \pm 0.11$ | ATCA      | 5.5                           | $60.0 \pm 0.5$                              | [1]        |
|   | $58527.91 \pm 0.11$ | ATCA      | 9.0                           | $45.2 \pm 1.4$                              | [1]        |

| Continuation of Table 6.2                 |                     |           |                               |   |            |
|---|---------------------|-----------|-------------------------------|---|------------|
| Observation<br>Start date<br>(dd-mm-yyyy) | MJD                 | Telescope | Central<br>frequency<br>(GHz) | Flux density <sup>a</sup><br>$S_0$<br>(mJy) | References |
|   | $58527.96 \pm 0.07$ | ATCA      | 16.7                          | $36.7 \pm 0.4$                              | [1]        |
|   | $58527.96 \pm 0.07$ | ATCA      | 21.2                          | $31.5 \pm 0.5$                              | [1]        |
| 14-02-2019                                | $58528.84 \pm 0.02$ | MWA       | 0.154                         | $54 \pm 9$                                  | This work  |
|   | $58528.86 \pm 0.02$ | MWA       | 0.216                         | $57 \pm 7$                                  | This work  |
| 16-02-2019                                | $58530.84 \pm 0.02$ | MWA       | 0.154                         | $< 40$                                      | This work  |
|   | $58530.86 \pm 0.02$ | MWA       | 0.216                         | $< 23$                                      | This work  |
| End of Table                              |                     |           |                               |   |            |

<sup>a</sup> We quote  $1\sigma$  errors on the flux density, which are calculated by adding the  $1\sigma$  RMS noise in the continuum image and the  $1\sigma$  uncertainty on the Gaussian fit to the source in quadrature. For MWA, we also incorporate an absolute flux density calibration error of 10% (again, added in quadrature).

[1] Carotenuto et al. (2021a); [2] Chapter 4

Note: All upper limits are quoted at the  $3\sigma$  level.

## 6.3 Results

Both BH-XRBs MAXI J1820+070 and MAXI J348–630 were studied across a broad electromagnetic spectrum during their outbursts (e.g., Chapter 4; Bright et al., 2018; Kennea & Negoro, 2019; Paice et al., 2019; Stiele & Kong, 2020; Tominaga et al., 2020; Zhang et al., 2020a; Buisson et al., 2021), with multiple detections at radio frequencies (e.g., Chapter 4; Bright et al., 2018; Atri et al., 2020; Tetarenko et al., 2021; Carotenuto et al., 2021a). During our MWA monitoring campaign MAXI J1820+070 was in the hard X-ray spectral state (Homan et al., 2020; Tetarenko et al., 2021), whereas MAXI J1348–630 was observed in

the intermediate X-ray spectral state, making a transition from the hard to the soft X-ray spectral state (Zhang et al., 2020a). MAXI J1348–630 was also detected at radio frequencies (MHz to GHz) while it was in the soft X-ray spectral state (Zhang et al., 2020a; Carotenuto et al., 2021a).

### 6.3.1 MAXI J1820+070

#### 6.3.1.1 Low-frequency radio detections of MAXI J1820+070

The MWA observations of MAXI J1820+070 took place while the source was in its hard state so our low frequency ( $< 300$  MHz) detections were of the compact jet. This is the first compact jet detection by MWA, and likely to first ever low frequency ( $< 300$  MHz) detection of a compact jet from a BH-XRB.

In Figure 6.1, we show the 186 MHz detection of MAXI J1820+070 during our 12 April 2018 observation, where the source was detected at  $> 4\sigma$  significance. MAXI J1820+070 was detected in all three frequency bands centered at 154, 186 and 216 MHz. The source was also detected on other occasions during our low-frequency ( $< 300$  MHz) monitoring campaign (see Table 6.1).

#### 6.3.1.2 Radio and X-ray light curve

We first compared the X-ray and low-frequency radio light curve of MAXI J1820+070 in order to understand the radio emission in-comparison to the X-ray behaviour. This involved downloading the publicly available one-day averaged *Swift*/BAT<sup>3</sup> X-ray light curve of MAXI J1820+070 monitoring, which has been presented in the top panel of Figure 6.2. The dates of the MWA observations have been indicated by red vertical lines. In the bottom panel of Figure 6.2, we have shown the low-frequency radio light curve at all three MWA frequencies (154, 186 and 216 MHz). The light curve shows no prominent peak, and MAXI J1820+070 remains nearly constant in flux density throughout our observing campaign. There are a few points when the source flux density increases, but these variations are

---

<sup>3</sup><https://swift.gsfc.nasa.gov/results/transients/weak/MAXIJ1820p070/>

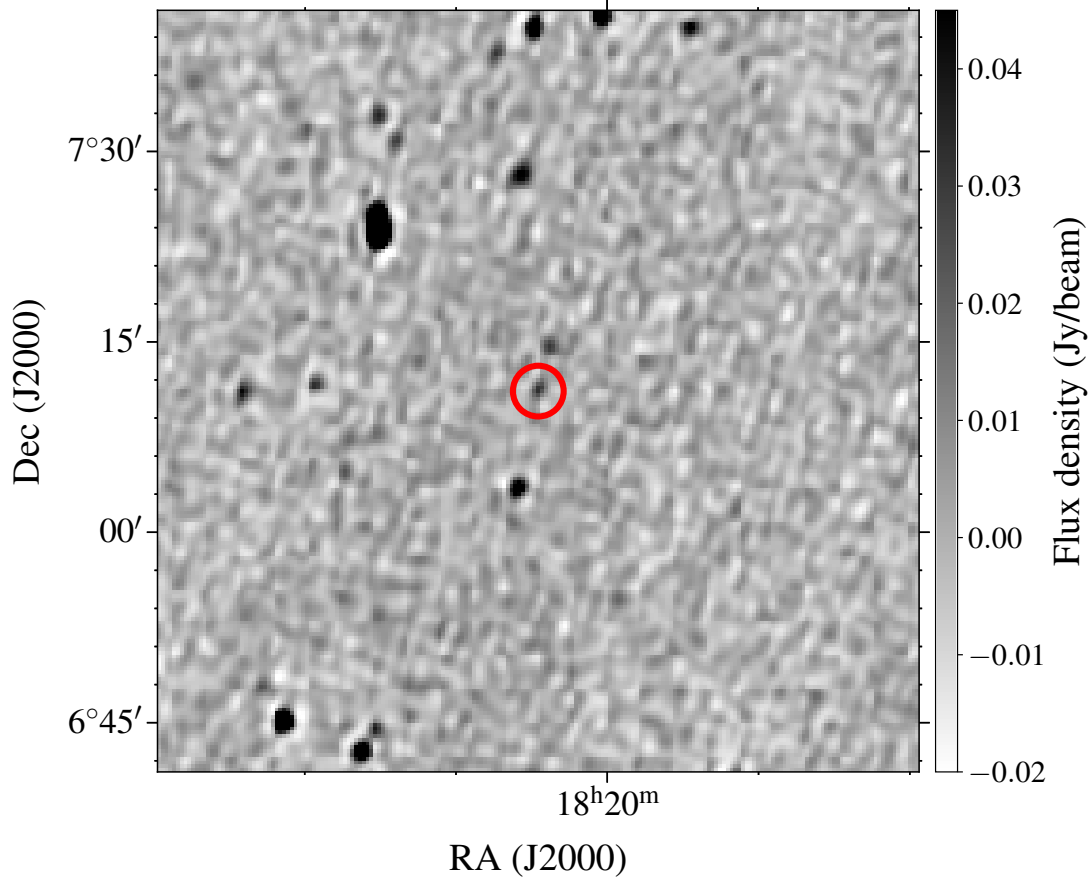


Figure 6.1: The MWA continuum image of MAXI J1820+070 at 186 MHz observed on 12 April 2018, centered at RA = 18:20:21.94, DEC = 07:11:07.16 with a size of  $1.5^\circ \times 1.5^\circ$ . The location of the source is indicated by the red circle, and was detected with at a significance  $> 4\sigma$ .

within the  $1\sigma$  uncertainties. This radio light curve is consistent with the canonical behaviour of compact jets (Fender et al., 2004). On a few occasions, MAXI J1820+070 was not detected at one or more frequencies during our MWA observations. This could be due to ionospheric distortions or a loss in sensitivity from some local instrumental effects (such as broken dipoles or even complete broken tiles), which result in poorer data quality. The MWA flux density values have large uncertainties as the flux density calibration methodology described in Section 2.3 has limitations when the significance of the source is  $< 10\sigma$ . The 12 April 2018 observation (indicated with the dashed magenta vertical line in the bottom panel of Figure 6.2) coincided with a multi-wavelength observing campaign (Tetarenko et al., 2021), which has allowed us to study the broadband radio spectrum of the compact jet down to 154 MHz (see Section 6.3.1.3).

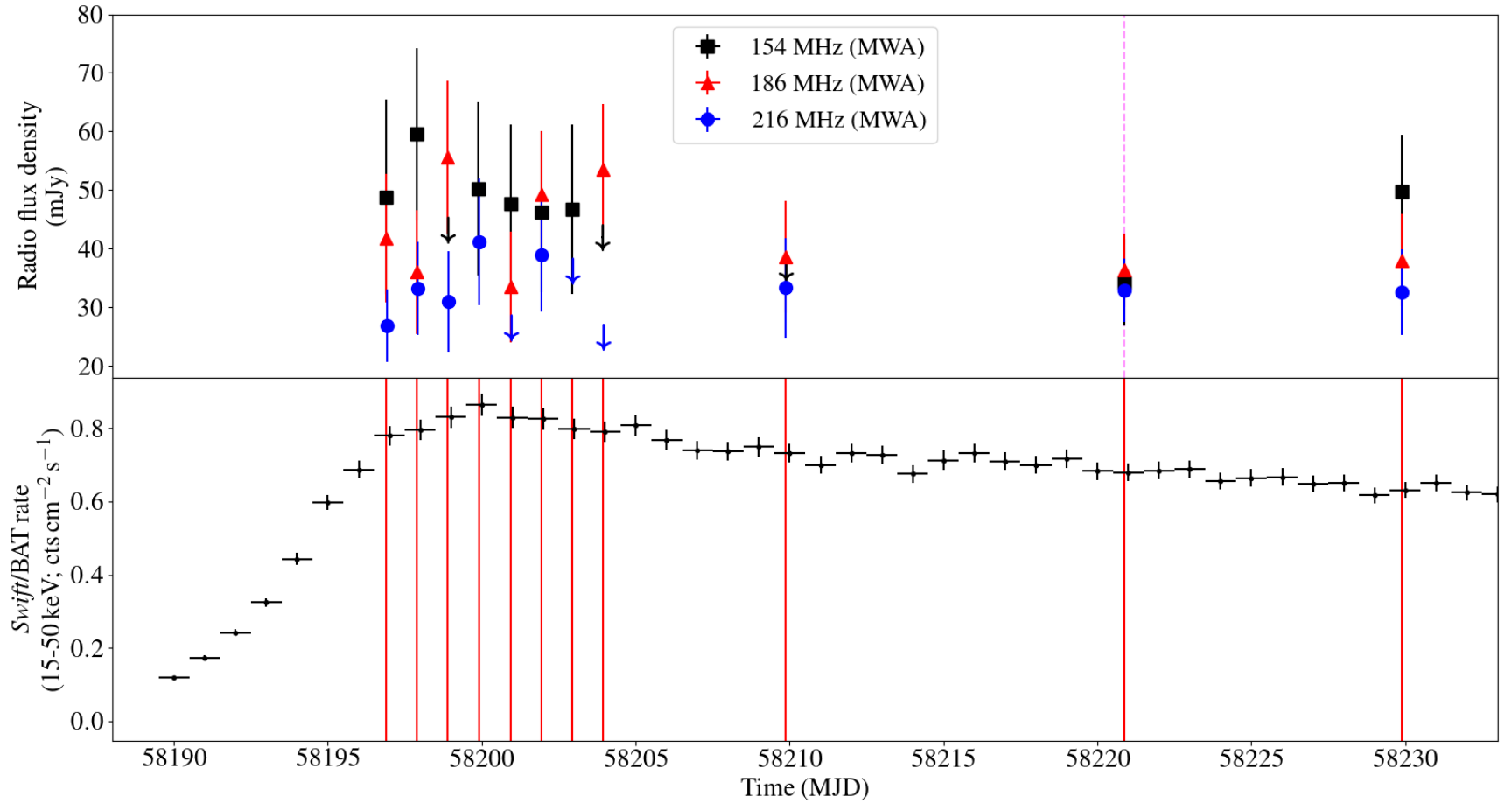


Figure 6.2: Top panel: One-day average *Swift*/BAT light curve for MAXI J1820+070 in the energy range 15–50 keV. Red vertical lines highlight the epochs of the MWA observations. MAXI J1820+070 was in the hard X-ray spectral state during the MWA monitoring. Bottom panel: The low-frequency MWA light curve of MAXI J1820+070. Throughout the MWA monitoring, the flux density of the source remains constant within the  $1\sigma$  uncertainties. The MWA observation on 12 April 2018 indicated with the dashed magenta line was part of a large multi-wavelength monitoring campaign from radio, through optical to X-rays.

### 6.3.1.3 Broadband spectrum

As we are trying to understand the nature of the compact jet spectrum at low radio frequencies ( $< 300$  MHz), we only consider the data up to sub-mm wavelengths from Tetarenko et al. (2021). Using time-averaged radio ( $> 300$  MHz) and sub-mm flux density measurements of MAXI J1820+070 taken on 12 April 2018 from Polisensky et al. (2018) and Tetarenko et al. (2021) combined with our MWA low-frequency ( $< 300$  MHz) detections for the same epoch, we generated a broadband spectrum of the compact jets in the frequency range 0.154 to 343.5 GHz, as shown in Figure 6.3. We note that the MWA observations were not strictly simultaneous with the high-frequency observations. Given that the radio flux density of the source is almost constant in the low-frequency regime (Figure 6.2), this non-simultaneity should not significantly influence our interpretation of the broadband compact jet spectrum.

The compact jet spectrum is slightly inverted up to the sub-mm band, consistent with this being the optically thick part of the jet spectrum (Chapter 1). For spectral fitting we used a Bayesian approach, because it provides robust estimates and uncertainties to the model parameters. We created a Markov Chain Monte Carlo (MCMC) simulation to completely sample the parameter space. We fit our observed broadband spectrum (Figure 6.3) with a power-law;  $S_\nu = S_0 \nu^\alpha$ , where  $\alpha$  (spectral-index) and  $S_0$  (amplitude at reference frequency 186 MHz) are our sampled parameters, assuming uniform priors of  $-10 < \alpha < 2$  and  $1 < S_0 < 100$  mJy. To perform this analysis, we used the PyMC3<sup>4</sup> package developed by Salvatier et al. (2016), which explores the complete parameter space through a specified set of walkers. On every step, the choice of the next set of model parameters as evaluated from the likelihood of the previous parameters. We ran our model with 20 chains and 1000 steps per walker. The best fit is plotted as the black solid line (median of the posterior distribution of power-law) with red traces (these are random draws from the posterior probability distribution)

---

<sup>4</sup><https://docs.pymc.io/>

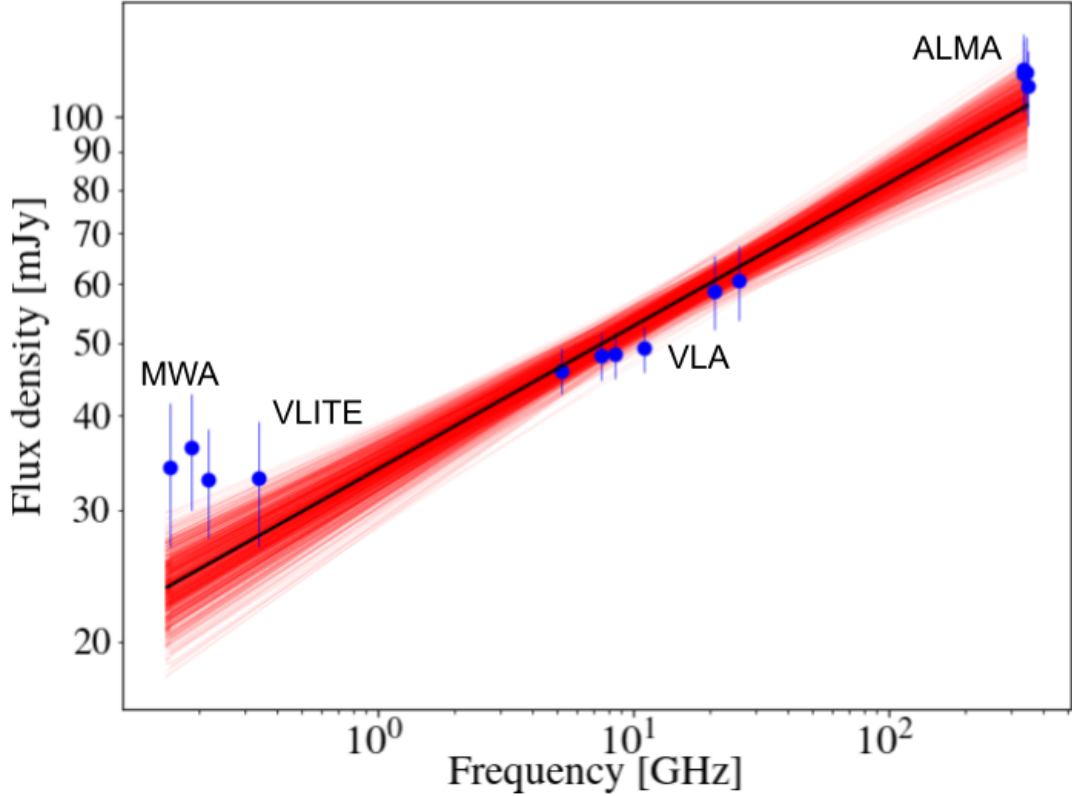


Figure 6.3: Broadband spectrum of MAXI J1820+070 on 12 April 2018. The flux densities are from MWA (this work), VLITE (Polisensky et al., 2018), VLA (Tetarenko et al., 2021), and ALMA (Tetarenko et al., 2021), as indicated. The black line highlights the best-fit power-law. We also add extra uncertainty on the radio flux densities of MWA (10%), VLITE (5%), VLA (5%) and ALMA (a conservative 5%, as appropriate for the higher frequencies; Partridge et al., 2016), to account for the non-simultaneity and cross-telescope uncertainties. The red traces show 1000 random draws from the posterior distributions of the best fit for the power-law. The spectrum shows no evidence of a low-frequency turnover.

to indicate the range in possible solutions in Figure 6.3.

Our Bayesian analysis derived parameter values and  $1\sigma$  uncertainties are  $\alpha = 0.19 \pm 0.02$  and  $S_0 = 26 \pm 2$  mJy. In Figure 6.4 we show the corresponding corner plot that illustrate the best fit parameter values and the correlation between them. The spectral index calculated in this study is close to that reported at frequencies  $> 5$  GHz by Tetarenko et al. (2021). Our results show we have not detected a low-frequency turnover as predicted by various theoretical models (e.g., Jamil et al., 2010; Malzac, 2014).

At MWA frequencies, we observed a slight increase in the radio flux density (relative to the best-fitting power law) that could be due to the limitations in the absolute flux calibration. Alternatively, this could be due to a slightly older transient jet knot that had expanded. The probability of such an event is fairly low because there was no previous hard-to-soft X-ray state transition (as monitored by X-ray facilities), so this seems unlikely. Additionally, it could also be possible that over time, MAXI J1820+070 had inflated large-scale synchrotron-emitting radio structures around itself, which could be visible in the low frequency band (e.g., Kaiser et al., 2004). To test for the presence of a plasma bubble around MAXI J1820+070, we analysed MWA data of the MAXI J1820+070 region monitored under the project code G0004 from 2016 to 2018 ( $\sim 5$  hours). We did not detect any signature of a large-scale synchrotron-emitting radio bubble at the location of MAXI J1820+070 and our best  $3\sigma$  upper limits are 13 mJy at 186 MHz. Although, we have not detected any large scale structure with the MWA. we can not discard the possibility of such a plasma bubble with high confidence. It could be possible such a structure is present at lower radio flux density, and sufficient to explain the 5-10 mJy MWA excess that we observed.

### **6.3.2 MAXI J1348–630**

#### **6.3.2.1 Low-frequency radio detections of MAXI J1348–630**

The continuum image of the MAXI J1348–630 field at 216 MHz for the 7 February 2019 observation is shown in Figure 6.5, where MAXI J1348–630 is detected at a significance  $> 6\sigma$ . The source was detected at both the MWA frequencies (154 and 216 MHz) on 7 February 2019, and is therefore the third transient XRB detection with the MWA [the other two being MAXI J1535–571 (Chapter 5) and MAXI J1820+070 (Section 6)]. The source was detected at both frequencies throughout our MWA observing campaign with the exception of 16 February 2019, for which we quote  $3\sigma$  upper limits (see Table 6.2).

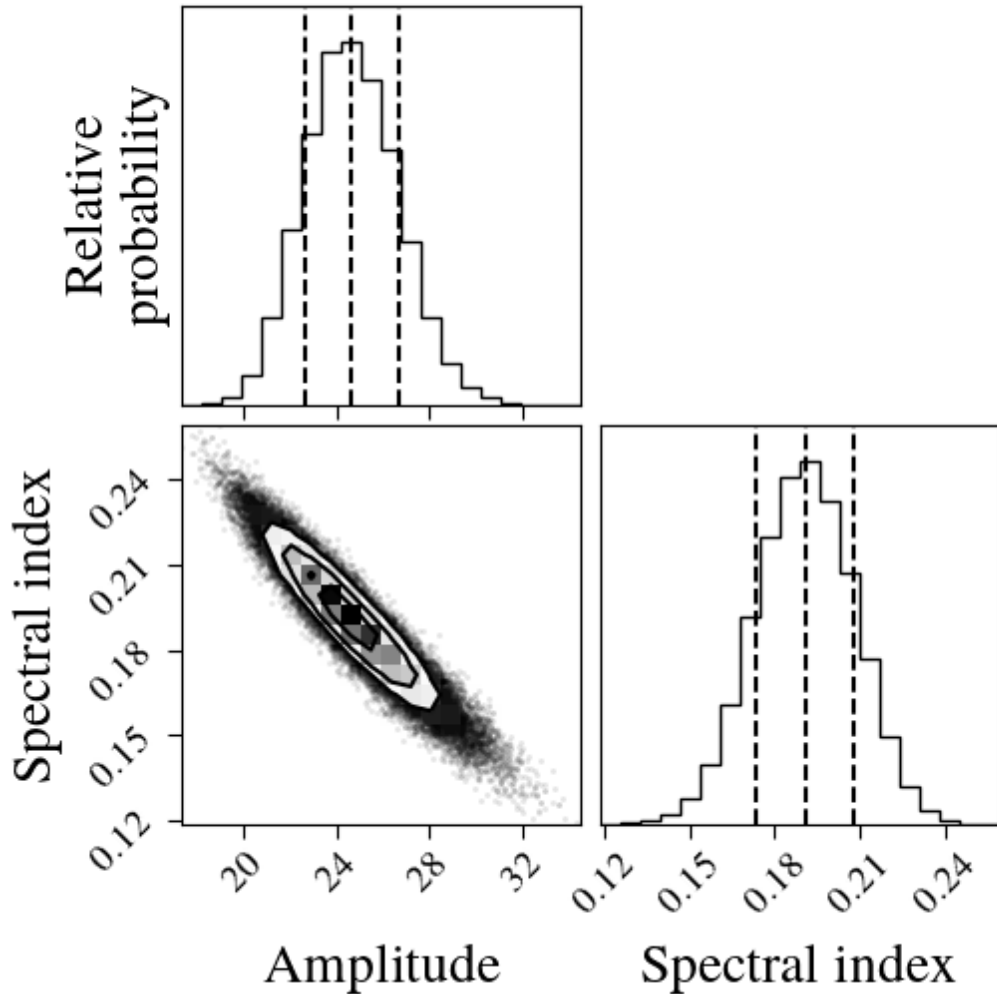


Figure 6.4: A corner plot displaying the posterior distribution of parameters derived from our spectral modelling. The dashed vertical lines and the contours show the 16<sup>th</sup>, 50<sup>th</sup> and 84<sup>th</sup> percentiles of the probability distribution. A correlation between the power-law spectral index and the amplitude is observed, which suggests that for less steep spectrum the amplitude is larger.

### 6.3.2.2 Multi-frequency radio light curve

During our low-frequency MWA observing program, MAXI J1348–630 was also monitored by ASKAP (Chapter 4), MeerKAT and ATCA (Carotenuto et al., 2021a). The 0.15 — 21.2 GHz radio light curves span from 27 January 2019 (MJD 58510) to 1 March 2019 (MJD 58543), and are shown in Figure 6.6.

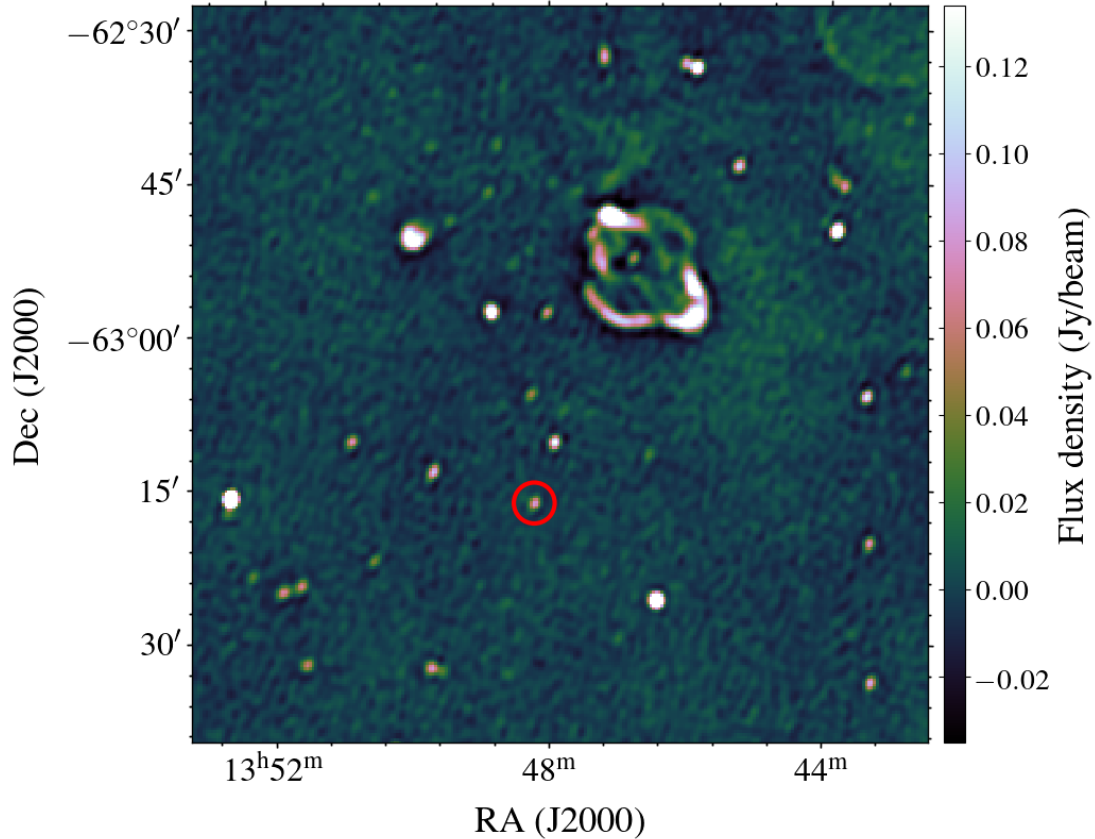


Figure 6.5: The MWA continuum image of MAXI J1348–630 field at 216 MHz observed on 7 February 2019, centered at RA = 13:47:50.33, DEC = -63:03:54.73 with a size of  $1.5^\circ \times 1.5^\circ$ . The source was significantly detected ( $> 6\sigma$ ), and is indicated by the red circle.

Carotenuto et al. (2021a) observed the compact jets peak on 05 February 2019 (MJD 58519.86) in the frequency band 5–20 GHz, which then started to decay on 7 February 2019 (MJD 58521.97), one day before MAXI J1348–630 entered the soft X-ray spectral state (Zhang et al., 2020a; Carotenuto et al., 2021a). In the light curve, we detected two clear peaks on 10 and 12 February 2019 (MJDs 58524.84 and 58526.84) with the MWA, where the 154 MHz radio flux density exceeded 400 mJy on each occasion. After the second peak, the radio flux density of the synchrotron source gradually declined at all frequencies, reaching  $\sim 1.5$  mJy at 1.3 GHz on 1 March 2019 (MJD 58543.08, Carotenuto et al., 2021a).

Using the MeerKAT and ATCA observations, (Carotenuto et al., 2021a) found

that the compact jets faded after 7 February 2019 (MJD 58521.97), with the transient jets first being detected on 9 February 2019 (MJD 58523.22). The authors have not been able to precisely determine when the compact jets switched off. Carotenuto et al. (2021a) further suggested that the compact jets could have switch off either before or during the launching of the transient jet knot.

The MWA observation on 7 February 2019 (MJD 58521.97) was close in time to the multi-frequency coverage of the fading compact jets observed with ATCA. The MWA detection on 9 February 2019 (MJD 58523.22) coincides with the earliest detection of the transient jets from MAXI J1348–630 (see Figure 6.6), where it reached a maximum radio flux density of  $\sim 486$  mJy at 1.3 GHz (Carotenuto et al., 2021a). Note that while this multi-frequency light curve covers the complete radio flaring event associated with the outburst, detecting both the compact and the transient jets, the focus of this chapter is on the compact jets only. For the rest of this chapter, we therefore focus our analysis on the multi-frequency radio spectrum obtained on 7 February 2019 (see Section 6.3.2.3 for details).

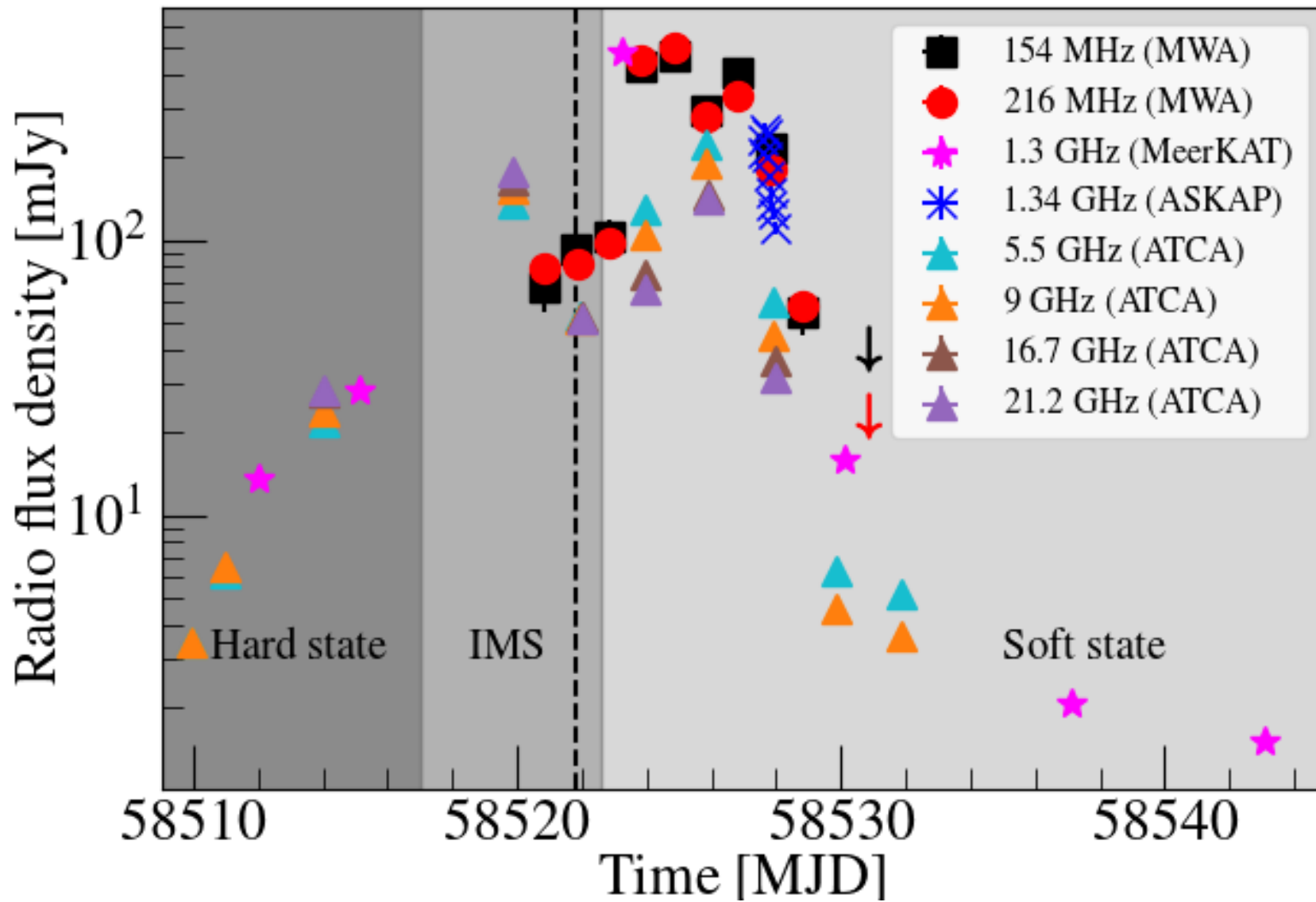


Figure 6.6: Multi-frequency radio light curve of MAXI J1348–630. Different symbols and colours indicate different instruments and observing frequencies, as shown in the plot legend. The MWA non-detections are indicated with the downward-pointing arrows, which represent  $3\sigma$  upper limits on the radio flux density. The dark shaded region highlights the hard X-ray spectral state, the medium-dark shaded region indicates the IMS, with the soft X-ray spectral state represented by the light shaded region. The dashed vertical line highlight the broadband coverage of the compact jets on or around 7 February 2019.

### 6.3.2.3 Radio spectrum

When the compact jet emission was in its decaying phase on 7 February 2019, MWA detected the source in the low-frequency band ( $< 300$  MHz), which was quasi-simultaneously observed with the ATCA (Carotenuto et al., 2021a). We used these data to create a 0.15 — 21.2 GHz broadband radio spectrum of the compact jet, which is displayed in Figure 6.7, assuming the time difference the MWA and ATCA observations is small enough to not impact our broadband radio spectral analysis.

The spectrum in the frequency range 0.15 — 21.2 GHz covers the optically thick part of the compact jet spectrum (Chapter 1). We model our observed broadband compact jet spectrum with a power law using the same technique as described for MAXI J1820+070 in Section 6.3.1.3, where the best fit is plotted as black line, with the red traces showing the range of possible solutions (see Figure 6.7). We assumed uniform priors of  $-2.5 < \alpha < 2.5$  and  $1 < S_0 < 500$  mJy, result in best-fit parameter values and  $1\sigma$  uncertainties of  $\alpha = -0.17 \pm 0.02$  and  $S_0 = 93 \pm 7$  mJy at a reference frequency of 186 MHz. The corner plot presentation of the best-fit results of the Bayesian fitting, which highlight the best-fit values and the correlation between modelling parameters is shown in Figure 6.8. The spectral index determined through modelling suggests a comparatively flat or slightly steep radio spectrum down to 154 MHz, with no indication of any low-frequency spectral turnover.

## 6.4 Discussion

Our study demonstrates the potential of the MWA in detecting the compact jets from BH-XRBs in the low-frequency band. As outlined in Sections 6.3.1.3 and 6.3.2.3, we present the first broadband spectrum of compact jets extended down to 154 MHz. The absence of detections of compact jets at frequencies  $< 300$  MHz could be due to the lack of sensitive low-frequency ( $< 300$  MHz) monitoring cam-

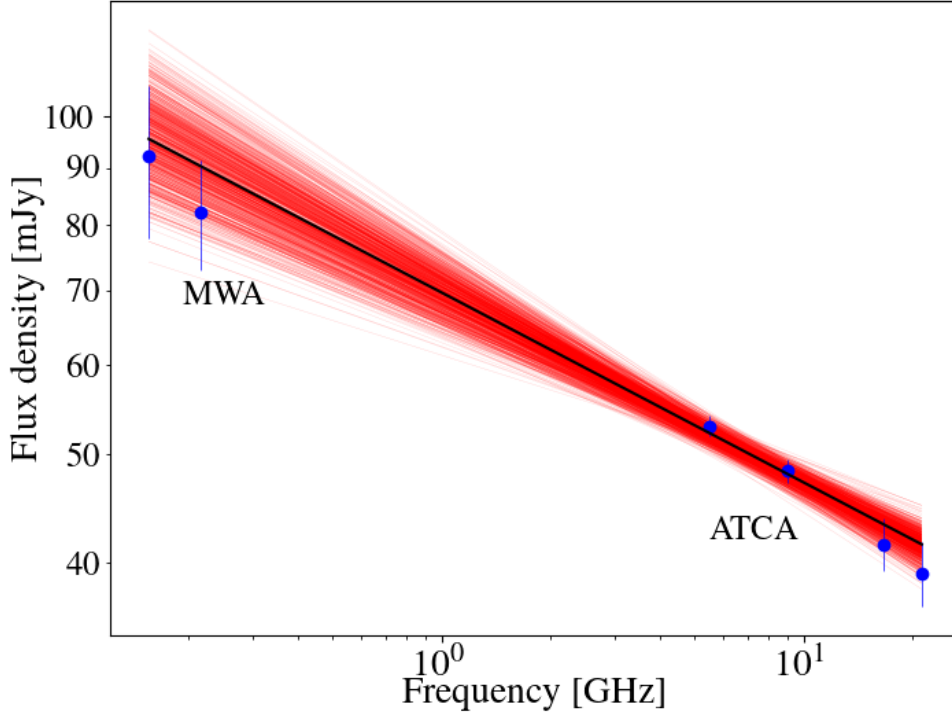


Figure 6.7: Broadband radio spectrum of MAXI J1348–630 on 07 February 2019. The flux densities are from MWA (this work) and ATCA (Carotenuto et al., 2021a), as indicated. We interpolated ATCA flux densities for the MWA time. The black line indicates the best-fit power-law. We also add extra uncertainty on the radio flux densities of MWA (10%) and ATCA (a conservative 5%, as appropriate for the higher frequencies; Partridge et al., 2016), to incorporate the quasi-simultaneity and cross-telescope uncertainties. The red traces show 1000 random draws from the posterior distributions of the best fit for the power-law. In the broadband compact jet spectrum we have not observed any signature of a low-frequency turnover.

paigns using the telescopes such as MWA, LOFAR and uGMRT. The other reason could be that both MAXI J1820+070 and MAXI J1348–630 were relatively bright during their hard X-ray spectral state as compared to canonical BH-XRBs (Remillard & McClintock, 2006). The bright hard X-ray spectral states could be inherent to both sources, or it could be due to, the two systems are located close to us with distances  $< 3$  kpc (Chapter 4; Atri et al., 2020). We reported in Sections 6.3.1.3 and 6.3.2.3 that there was no evidence for a low-frequency

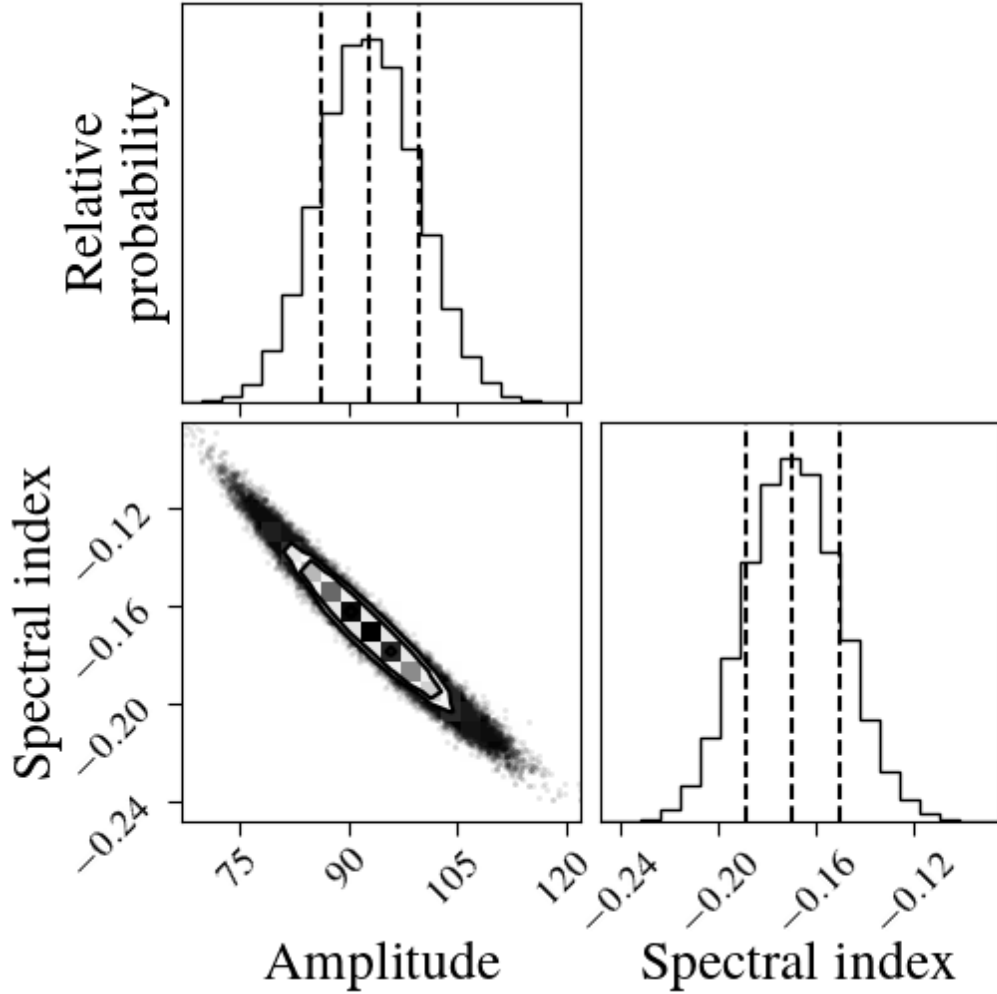


Figure 6.8: Corner plots showing the results of the MCMC power-law spectral fit. The panels display the histograms of the posterior distribution (one-dimensional) for the free model parameters. The contours and the vertical lines represent the 16<sup>th</sup>, 50<sup>th</sup> and 84<sup>th</sup> percentiles of the probability distribution. We observed a correlation between the fitted power-law spectral index and the amplitude.

turnover in the broadband compact jet spectrum of either MAXI J1820+070 or MAXI J1348–630. In the following subsections, we will discuss the implications of our study.

#### 6.4.1 MAXI J1820+070

During its 2018 outburst, MAXI J1820+070 displayed a peculiar behaviour as it was in the prolonged hard X-ray spectral state for more than four months (from March 2018 to early July 2018; Homan et al. 2020), whereas canonical BH-XRBs

spend just a few weeks in the initial hard X-ray spectral state (e.g., Remillard & McClintock, 2006; Belloni, 2010). MAXI J1820+070 was bright across the electromagnetic spectrum during its outburst, which provided opportunities for studies from radio through optical, UV to high energy X-rays, allowing for the study of multi-frequency correlations (e.g.; Bright et al., 2018; Paice et al., 2019; Zhang et al., 2020b). Muñoz-Darias et al. (2019) detected disk wind signatures in the hard X-ray spectral state in optical studies, which were later found to be simultaneous with the radio jet. Using X-ray timing studies, Wang et al. (2021) suggested that vertical expansion in the corona launched a transient jet knot during the hard to the soft X-ray spectral state transition.

In Section 6.3.1.2, we observed that the compact jets were detected from day one of our monitoring without any delay at lower frequencies. If there was no delay in the rise of the MHz emission, then it would suggest that there was no time delay between the compact jets switching on at GHz and MHz frequencies. This contradicts the assumption that the radio jet becomes progressively optically thin, allowing it to be successively detected at lower radio frequencies with increasing distance from the compact object. As radio jets have already been detected from quiescent BH-XRBs (Plotkin et al., 2021), it could be possible that a radio jet already existed in MAXI J1820+070 during the quiescent state but was not detected by existing radio telescopes due to sensitivity limits (if this sky position was ever observed). Then during the outburst phase when the inner accretion rate increased, it provided more power to the radio jets and made them detectable (e.g., Fender, 2010).

Rodi et al. (2021) modelled the complete SED of MAXI J1820+070 on 12 April 2018, and mostly target the high-frequency turnover connected to the acceleration region of the compact jet. The authors studied the compact jet spectrum down to 339 MHz with their modelling focuses on the optically thin part of the compact jet spectrum. In our study of MAXI J1820+070, we extended the spectral analysis of the compact jet spectrum down to 154 MHz. The main aim of

our broadband spectrum presented in Section 6.3.1.3 is to understand how low in frequency the compact jet spectrum extends and whether there is a low-frequency spectral turnover above 150 MHz. We focused on the optically thick part of the compact jet spectrum, and made efforts to detect the low-frequency turnover that is postulated by various theoretical studies (e.g.; Jamil et al., 2010; Malzac, 2014) yet we do not observe this signature (see details in Section 6.4.3)

## 6.4.2 MAXI J1348–630

During its 2019/2020 outburst, MAXI J1348–630 displayed relatively canonical behaviour, where the source underwent a complete HID cycle. The source was bright from radio through optical to X-rays wavelengths (e.g., Chapter 4; Russell et al., 2019a; Carotenuto et al., 2021a,b).

During our low-frequency MWA monitoring, we observed two distinct peaks on 10 and 12 February 2019 (MJDs 58524.84 and 58526.84) in the multi-frequency radio light curve (Figure 6.6). Apart from these aforementioned peaks, we also detected another peak on 13 February 2019 at 1.42 GHz in our ASKAP time-resolved study (Chapter 4; note that this peak was not detected in our MWA observations, which could indicate a signal delay in time with decreasing frequency, a lack of sensitivity or a lack of low frequency emission). These three flaring events could have arisen from three separate ejections events as multiple ejections have already been observed on short timescales from V404 Cygni (Tetarenko et al., 2017; Miller-Jones et al., 2019). However, Carotenuto et al. (2021a) did not detect any second and third component close to the MWA (12 February 2019) and ASKAP (13 February 2019) peaks in the MeerKAT and ATCA data. Although, Carotenuto et al. (2021a) have observed a second component on 15 April 2019, which was nearly two months later than the third peak detected with ASKAP. It is also possible that the multiple peaks in the light curve of MAXI J1348–630 could be due to re-brightening of the primary synchrotron-emitting source/transient jet knot when it interacted with the ambient medium. It is also possible that

these flares were generated by different shells colliding with one another creating internal shocks rather than external.

Carotenuto et al. (2021a,b) studied the compact jet spectrum in the frequency band 1.3 to 20 GHz, and mainly target the optically thick part of the compact jet spectrum, which is usually flat (Fender et al., 2000). In this research, we extended the compact jet spectrum in MAXI J1348–630 down to 154 MHz. Our observed broadband compact jet spectrum extends from 0.15 — 21.2 GHz as shown in Figure 6.7, and was found to be relatively flat with a power law spectral index of  $\alpha = -0.096 \pm 0.024$ . The compact jet spectrum of MAXI J1348–630 also shows no indication of a low-frequency turnover, hypothesised by various theoretical compact jet models (e.g.; Jamil et al., 2010; Malzac, 2014).

### 6.4.3 Compact jet spectrum

In Sections 6.3.1.3 and 6.3.2.3, we presented broadband compact jet spectra of MAXI J1820+070 and MAXI J1348–630. We found that the two spectra were relatively flat from 0.15 MHz to  $> 20$  GHz, with no signs of any low-frequency turnover. In this section, we qualitatively compare our results with two theoretical compact jet models; the single acceleration model (Pe’er & Casella, 2009) and the internal shock model (Jamil et al., 2010; Malzac, 2014).

As discussed in Section 1.5.1, in the case of the single acceleration model, Pe’er & Casella (2009) considered a single event of particle acceleration due to a shock at the base of the jet. The authors suggested that the toroidal component of the magnetic field decays along the axis of the jet to maintain the electron temperature (Pe’er & Casella, 2009). The authors changed various physical parameters, including the magnetic field strength, electron energy distribution and the energy losses to recover the observed compact jet spectrum from the astrophysical sources. The single acceleration model given by Pe’er & Casella (2009) ignored the spectrum beyond  $\sim 500$  MHz. We qualitatively compared our observed broadband spectra (radio flux density and extent in the low-frequency

regime) from MAXI J1820+070 and MAXI J1348–630 with simulated spectra corresponding to different physical parameters from Pe’er & Casella (2009). In order to push the low frequency turnover below 150 MHz, the magnetic field strength at the jet base would need be weak  $\lesssim 3 \times 10^4$  G combined with a jet that has a relatively narrow geometry. This magnetic field strength is consistent with that calculated by Shidatsu et al. (2018), Rodi et al. (2021) and Tetarenko et al. (2021) for MAXI J1820+070. For consistency with their calculated spectra, the electron energy distribution has power-law index of  $p = 2.5$ , and the accelerated electrons generally lose energy through synchrotron radiation with a small contribution from adiabatic losses. The radio flux density ( $\sim 10$  mJy) in the simulated spectra is significantly lower than observed in our broadband spectra (50 – 100 mJy) for both MAXI J1820+070 and MAXI J1348–630.

The internal shock model (Jamil et al., 2010; Malzac, 2014) provides a more realistic explanation of the compact jets, because this models suggests that the fluctuations in the accretion flow drive the Lorentz factor fluctuations in the radio jet, discussed in Section 1.5.1. The model predicts a low-frequency turnover around 1 GHz, which is directly related to the distance from the black hole (between  $10^7 R_g$  and  $10^8 R_g$ ; where  $R_g$  is the gravitational radii) where the jets dissipate all their energy through internal shocks as calculated by the fluctuations observed in the Lorentz factors injected into the model (Malzac, 2014). The non-detection of any low-frequency turnover down to 154 MHz in our spectra of BH-XRBs suggests that the compact jets are dissipating their energy at larger distances from the black hole ( $> 10^8 R_g$ ). For a  $10 M_\odot$  black hole, a distance of  $10^8 R_g \approx 3 \times 10^{12}$  m. This corresponds to around 3 light hours. Therefore, we might not expect to see a delay of more than a few hours between the GHz and MHz emission ramping up, discussed in Section 6.3.1.2. Finally, the time scale of the Lorentz factor fluctuations should be large enough such that shock dissipation can power the compact jet emission to a greater distance from the black hole (Malzac, 2014).

## 6.5 Conclusions

In this chapter, we have conducted a multi-wavelength study of the compact jets from the BH-XRBs MAXI J1820+070 and MAXI J1348–630. We presented new results from MWA, and included previously-published high-frequency results from VLA and ALMA for MAXI J1820+070. In the case of MAXI J1348–630, we incorporated already-published high-frequency results from MeerKAT and ATCA. We generated broadband spectra extending from 0.15–343.5 and 0.15–21.2 GHz for MAXI J1820+070 and MAXI J1348–630, respectively. During our low-frequency observing campaign, we detected compact radio jets for the first time from a BH-XRB using the MWA.

In the low-frequency radio light curve of MAXI J1820+070, we detected compact jets from the beginning of our monitoring campaign, suggesting that there was little to no delay between the GHz and MHz jet emission ramping up. In the broadband spectra of the compact jets in both the XRBs, we have not detected any signatures of low-frequency turnover down to 154 MHz. This demonstrates that the Lorentz factor fluctuations used by (Malzac, 2014) in the inter shock model for compact jets should be larger.

Finally, our study highlights the capabilities of the MWA in detecting the compact jets from BH-XRBs.

# Chapter 7

## Discussion, Conclusions and Future work

As described in Section 1.7, few previous studies have investigated the low-frequency behaviour of the radio jets in black hole X-ray binaries. Low-frequency monitoring together with high-frequency studies of black hole XRBs promises to provide important insights into the outflow of matter from these systems, which is necessary for addressing some of the fundamental open questions related to the ejection of matter such as

- How are the jets launched into space?
- How is the environment of the source influenced by the jets?

This PhD research was aimed at exploiting the capabilities of the SKA precursors in exploring the low-frequency behaviour of the radio jets in black hole X-ray binaries.

### 7.1 Discussion

#### 7.1.1 HI absorption distances to black hole XRBs

We described the importance of the distance to an astrophysical source in Section 1.6.1, and in Chapters 3 and 4. Where available, a high-precision parallax

is the most precise model-independent method for measuring the distance to an XRB. But as described in Section 1.6.1, and Chapter 3, parallax measurements are not available for many systems. When distance can not be determined using other approaches, an alternative technique, for sufficiently radio-bright systems, is to use the Doppler-shifted H I absorption line. Wenger et al. (2018) found that the mean difference between the kinematic distance and the parallax distance is around 21% (median difference 17%), which is significantly smaller than the uncertainties ( $\sim 50\%$ ) reported on the XRB distances by Jonker & Nelemans (2004), where various methods discussed in Section 1.6.1 have been used to determine the source distances. Therefore, kinematic distances typically improve XRB distance estimates.

From as early as 1976, the Doppler-shifted H I absorption line proved to be an important tool to constrain the distance to pulsars and XRBs (e.g.; Ables & Manchester, 1976; Goss & Mebold, 1977). The approach was applied to the black hole XRBs GRS 1915+105 and SS 433 by Dhawan et al. (2000) and Lockman et al. (2007), respectively. Between 2007 and 2017,  $\sim 50$  XRB outbursts have been reported (e.g.; Negoro et al., 2011; Barthelmy et al., 2015; Negoro et al., 2016a,b; Tetarenko et al., 2016), but there is no published study reporting H I absorption distances to any of these XRBs. One of the reasons behind such a paucity of H I absorption studies of XRBs could be the lack of sensitive instruments combined with the fact that most XRB outbursts are quite faint ( $\lesssim 100$  mJy; Fender et al. 2009). H I absorption measurements are only possible for sufficient bright systems, such that the signal-to-noise ratio is high enough to significantly detect ( $> 3\sigma$ ) an H I absorption complex. Therefore, this technique is typically limited to bright black hole XRBs, either persistent (e.g. SS 433), or close to the peak of an outburst as most neutron star XRBs don't get bright enough ( $\lesssim 10$  mJy; Migliari & Fender 2006) for an H I absorption complex to be significantly detected. The other reason could be that researchers working on XRBs might not have been motivated to undertake H I studies; telescopes such

as VLA, ATCA, the Westerbork Synthesis Radio Telescope (WSRT), Parkes and the Green Bank Telescope (GBT) have had the capability to perform H I studies for the past few decades.

The advent of new, sensitive SKA precursor telescopes operating in the 1-2 GHz band, including ASKAP and MeerKAT, have provided new opportunities for H I studies. Moreover, their wide fields of view allow us to observe comparison background extragalactic sources in the same observation, which are used as a comparison source in order to discriminate between near and far distances. This PhD research has therefore rejuvenated the technique of kinematic distance determinations for BH-XRBs as it uses both ASKAP and MeerKAT to constrain the distances to two radio-bright systems; MAXI J1535–571 (Chapter 3) and MAXI J1348–630 (Chapter 4). In the following, we discuss the advantages afforded by the wide field-of-views and spectral resolution of the SKA precursor instruments for this work.

Distance constraints can be placed on Galactic systems via parallax measurements. For such measurements to be possible, it is necessary to observe the source over the course of at least 1 year, either in the radio or optical band. While radio parallax measurements using very long baseline interferometry has been performed using the Australian LBA for nearby systems such as pulsars (e.g., Deller et al., 2008, 2009; Miller-Jones et al., 2018) and star formation regions (Krishnan et al., 2015, 2017), outside of outbursts, BH-XRBs are not typically bright enough to be detectable at radio wavelengths (note that the LBA is only able to measure parallaxes out to a few kpc ). For a radio parallax measurement to be possible, the BH-XRB needs to be a recurrent system, persistent or sufficiently radio-bright in quiescence (e.g., Miller-Jones et al., 2009). It is also only possible for *Gaia* to obtain optical parallax measurements for BH-XRBs if the donor star is bright, which is often too extinguished and/or faint outside of outburst, particularly as XRBs are often at low Galactic latitudes. Therefore the Doppler-shifted H I absorption approach is extremely useful for distance estimates, especially for

those XRBs located in or close to the Galactic plane, where optical and radio parallax methods are not applicable, yet LSR velocities are well defined as stars and gas tend to follow Galactic rotation.

In this PhD research, we demonstrated the advantages of the wide field of view of the SKA precursor telescopes. When measuring distances based on the HI absorption method, we obtain two distance constraints (near and far, Section 1.6.1) for a single radial velocity measurement. The wide field of view of the SKA precursors allow us to overcome this degeneracy by providing us with an opportunity to study a set of comparison extragalactic sources in the same observation. The emission from the extragalactic sources passes through a significantly large number of hydrogen clouds as compared to our XRBs so the HI absorption complex in the direction of the extragalactic sources extends out to the tangent point velocity. Comparing the HI absorption complex towards our XRB source and the comparison extragalactic source thereby helps us distinguish between near and far kinematic distances.

This PhD work also suggested that going forward, the SKA precursor facilities including ASKAP and MeerKAT, which operate around 1 GHz, will be able to routinely measure distances to bright ( $> 50$  mJy) XRBs using the HI absorption line approach. For this research, we performed HI measurements for both MAXI J1535–571 (Chapter 3) and MAXI J1348–630 (Chapter 4) with ASKAP, which provides nearly 16k channels, corresponding to a velocity resolution of  $3.9 \text{ km s}^{-1}$ . We also obtained MeerKAT observations of MAXI J1348–630, which at the time was running in a low-resolution 4k mode, providing a velocity resolution of  $44 \text{ km s}^{-1}$ . Note that MeerKAT has recently undergone a correlator upgrade and has now started observing with a higher resolution 32k mode, corresponding to an increased velocity resolution of  $6.1 \text{ km s}^{-1}$ , which is nearly comparable to ASKAP. However, owing to its lower system temperature, MeerKAT can get reasonable HI absorption measurements towards slightly fainter XRBs ( $> 20$  mJy), allowing us to constrain their distances. Additionally, MeerKAT can

also operate in a zoom mode to further improve its velocity resolution but request a special setup. However, the 32k mode is the standard continuum observing mode for MeerKAT, enabling distance measurements for all routine continuum observations. For the last two years, MeerKAT has been performing weekly observations of all bright, outbursting XRBs (e.g. Bright et al., 2020; Tremou et al., 2020; Williams et al., 2020) under the auspices of the large survey project ThunderKAT (Fender et al., 2016). Hence, following the recent correlator upgrade, H I absorption studies of XRBs can now become a routine practice.

Furthermore, our distance estimates have been used to calculate the physical properties of both systems MAXI J1535–571 (Chapter 3) and MAXI J1348–630 (Chapter 4), including the peak X-ray luminosity, the soft-to-hard X-ray spectral state transition luminosity, and the black hole mass (Chapter 4). From our distance measurements, we found that at the peak of its outburst, MAXI J1535–571 reached  $> 78\%$  of its Eddington luminosity, and therefore belongs to a relatively small group of BH-XRBs that undergo outbursts and reach  $> 75\%$  of Eddington luminosity at the peak of their outburst, out of  $\sim 60$  BH-XRBs  $< 10$  Galactic BH-XRBs are known to show such peak X-ray luminosity (Corral-Santana et al., 2016; Tetarenko et al., 2016). By contrast, MAXI J1348–630 only reached 17% of its Eddington luminosity, which is a typical level for canonical BH-XRBs (Tetarenko et al., 2016). Using the prescription described by Tetarenko et al. (2016), the peak X-ray luminosities of BH-XRBs help in determining the total energy budget of an outburst.

As a result of our distance estimates, we demonstrated that the transition of MAXI J1535–571 between its soft and hard X-ray spectral states occurred at an X-ray luminosity 1000 times lower than seen from canonical black hole XRBs (Kalemci et al., 2013; Vahdat Motlagh et al., 2019). This atypical behaviour of MAXI J1535–571 could be due to the low magnetic fields or low viscosity in the accretion disk (Petrucci et al., 2008; Begelman & Armitage, 2014). The other explanation could be there was another accretion event during the outburst decay,

which could trigger a new soft state (Vahdat Motlagh et al., 2019). On the other hand, MAXI J1348–630 transitioned from the soft to the hard X-ray spectral at  $2.5 \pm 1.5\%$  of the Eddington luminosity, which is canonical for Galactic BH-XRBs (Kalemci et al., 2013; Vahdat Motlagh et al., 2019).

Using our distance constraints, Russell et al. 2019c (observations from ATCA) and Carotenuto et al. 2021a (observations from MeerKAT and ATCA) constrained the jet velocity and the jet inclination angle for MAXI J1535–571 and MAXI J1348–630, respectively. Jet speeds are required to determine the relativistic nature of the outflow, and the amount of energy jets extract from the system and deposit into the surroundings (e.g., Rodi et al., 2021; Tetarenko et al., 2021). Finally, the correlation study of jet energy with X-ray luminosity can help us in addressing one of the fundamental questions; how inflow and outflow are coupled (e.g., Corbel et al., 2013; Gallo et al., 2014; Russell et al., 2015, 2019b; Carotenuto et al., 2021b). This demonstrates the importance of obtaining precise distance measurements to new X-ray binary transients.

### 7.1.2 Low-frequency studies of transient jets

Transient jets from black hole XRBs are adiabatically expanding, relativistically moving plasma clouds, which are launched into space from the inner part of the system (Section 1.5.2). Transient jets have previously been observed in many XRB outbursts (e.g., Motch, 1998; Miller-Jones et al., 2011; Baglio et al., 2016; Bright et al., 2020; Espinasse et al., 2020), and resolved in several cases with VLBI (e.g., Yang et al., 2011; Brocksopp et al., 2013; Rushton et al., 2017; Miller-Jones et al., 2019). However, the majority of previous monitoring with connected-element interferometers has focused on frequencies  $> 1$  GHz (e.g., Branson et al., 1972; Hjellming & Balick, 1972; Fender et al., 1995, 1997, 1999, 2000; Waltman et al., 1994, 1995, 1996; Tetarenko et al., 2017; Russell et al., 2019c; Carotenuto et al., 2021a), which predominantly sample the optically-thin part of the spectrum. Furthermore, most recent BH-XRB studies have focused on higher radio

frequencies, where instruments were more sensitive, and sources showed more marked brightness variations.

Up until now, low-frequency transient jet monitoring has only been done for a handful of BH-XRBs (e.g., Gregory & Seaquist, 1974; Miller-Jones et al., 2004; Broderick et al., 2018b; Chandra & Kanekar, 2017). One of the reasons behind such a sparse monitoring at low-frequencies was the lack of sensitive low-frequency instruments combined with the majority of outbursts being too faint (reaching  $< 100$  mJy at 1 GHz and therefore necessarily much fainter at MHz frequencies; e.g., Fender et al. 2000; Miller-Jones et al. 2004). The development of modern radio telescopes such as the SKA precursors (MWA, ASKAP and MeerKAT) and other instruments including the Low-Frequency Array (LOFAR; van Haarlem et al., 2013), the VLA Low Band Ionospheric, Transient Experiment (VLITE; Clarke et al., 2016), the upgraded Giant Metrewave Radio Telescope (uGMRT; Ananthakrishnan, 1995) and UTMOST, have increased our ability to detect XRBs at low radio frequencies ( $< 1$  GHz).

Another challenge to low frequency monitoring of outbursting BH-XRBs has been the lack of accessibility to appropriate imaging algorithms and the computational power necessary to deconvolve wide fields of view of bright sources in order to detect faint XRB outbursts. However, there has been a huge amount of progress over the past few years with new software developments (e.g., WSCLEAN; Offringa et al., 2014) enabling more routine imaging of the large fields of view of low-frequency instruments.

Obtaining a broad band radio spectrum of transient jets is important for locating the low frequency spectral turn-over. The turnover frequency, together with source size constraints obtained using VLBI can be used to constrain the physical properties of the jets, including the magnetic field strength, the jet opening angle, the jet power, and the minimum energy of the transient jet knot, which eventually helps us in understanding the energetics of the jet and its impact on the surrounding environment (e.g.; Begelman et al., 1984; Ferrari, 1998; Miller-

Jones et al., 2006; Russell et al., 2019c). As mentioned in Section 5.5, till now, the low-frequency spectral turnover has only been detected in a handful of BH-XRBs due to limited low-frequency monitoring with the sensitive instruments.

In this PhD research, we have shown that coupling GHz-frequency radio telescopes with new, sensitive lower-frequency ( $< 500$  MHz) telescopes can fully sample the radio spectrum of the transient jets. We have made the first transient jet detection of a BH-XRB with the MWA; MAXI J1535–571 (Chapter 5). The MWA measurements constrained the broadband radio spectrum in the low-frequency regime, which demonstrated the existence of a low-frequency turnover in the radio spectrum of MAXI J1535–571 (Section 5.3.5). This displayed the capabilities of the SKA precursor MWA in detecting transient jets at low radio frequencies ( $< 300$  MHz). When we fitted the observed broadband spectrum with a physical model (FFA or SSA; Section 5.4), we found that the quality of the fit significantly improved after creating a simultaneous broadband spectrum (Sections 5.3.5 and 5.4), and the uncertainties on the model parameters also reduced. Therefore, our research work also displayed the importance of simultaneity (or at least being able to interpolate/extrapolate to produce a simultaneous spectrum; Sections 5.3.5 and 5.4). This PhD research also displayed that when we combined our radio information with existing constraints from optical H- $\alpha$  surveys, we can convincingly ascertain the physical absorption mechanism responsible for the turnover (Section 5.4.2).

Further, when we coupled the turnover frequency with the source size constraints from LBA, we obtained all the necessary information to directly determine the magnetic field strength of the source, rather than having to assume equipartition (Section 5.5.1). This magnetic field strength field measurement from synchrotron theory was consistent with that derived assuming equipartition (Section 5.4.3), which suggest that the transient jet knot (or plasma cloud) in MAXI J1535–571 was close to equipartition (Section 5.5.1). While calculating the synchrotron minimum energy, we found that with accurate source volumes (from

the LBA size measurements), we were able to provide more accurate energetics than are usually possible from flare rise times alone (Section 5.4.3). The LBA size constraints helped us in calculating the jet opening angle (Section 5.5.2), which was further used to put constraints on the jet Lorentz factor in MAXI J1535–571 (Section 5.5.2.1). By constraining the physical parameters of the jet, we were able to place a lower limit on its energy, which provides important constraints on the power extracted by the transient jets from the accretion process. Hence, we can get a better understanding of the accretion and ejection coupling and further determine the overall energy budget of the system. Finally, we can compare the energy carried away by the radio ejection with the peak X-ray luminosity. The peak X-ray luminosity was observed to be  $7.5 - 19.9 \times 10^{38} \text{ erg s}^{-1}$ , and by dividing the minimum energy by the rise time of the radio flare (the time since the ATCA upper limits from the previous day), we find a lower limit on the jet power of  $7.5 \times 10^{36} \text{ erg s}^{-1}$ . Hence, placing a lower limit of 1% of the accretion power flowing outwards in the jets (note there is an upper limit on the rise time and a lower limit on the energy, since this is the minimum energy required to generate the observed synchrotron emission). Determining the fraction of the accretion power carried away by the jets is important in determining the connection between accretion and ejection, and also helps to quantify the impact of X-ray binary feedback on the surroundings. This demonstrates the importance of observations by sensitive low-frequency ( $< 300 \text{ MHz}$ ) telescopes (such as MWA) for investigating jet physics in XRBs.

Transient jets show variability on 1-2 day timescales in the low-frequencies regime ( $< 300 \text{ MHz}$ ) for up to two weeks (Section 2.5). From the multi-frequency observing campaign on MAXI J1535–571 (Chapter 5), we learned that to precisely probe the evolution of the turnover frequency in the transient jets, we need to simultaneously monitor the source with high cadence (daily) over the peak of the outburst for nearly two weeks from a few MHz to GHz frequencies and couple these monitoring with VLBI observations. The VLBI observations are necessary

to accurately evaluate the ejection time, which is ultimately important to precisely constrain the physical parameters related to the jet energetics, such as the source size, the magnetic field strength, the minimum energy, and the jet opening angle. Therefore, this PhD demonstrates the necessary framework required for regular monitoring of the XRB outbursts with the SKA precursor telescopes, which will help us in understanding the evolution of the transient jet over a complete Bh-XRB outburst.

### 7.1.3 Detection of the compact jets at low-frequency

The properties of compact jets are discussed in detail in Section 1.5.1. These jets are known to have flat to inverted radio spectra over a broad frequency range above 1 GHz (Fender et al., 2000). Various theoretical models predict the presence of a low-frequency turnover in the radio spectrum (Pe'er & Casella, 2009; Jamil et al., 2010; Malzac, 2014). The predicted low-frequency turnover is thought to be connected to the physical properties of the compact jets, such as the extent of the compact jets into its surrounding environment, and the energy distribution of the particles (Pe'er & Casella, 2009; Jamil et al., 2010; Malzac, 2014). The low-frequency turnover or break could also be due to self-absorption, or a low-frequency cutoff in the electron energy distribution (Fender et al., 2000).

The physics of compact jets have been well-studied at GHz-frequencies (e.g., Fender et al., 2000; Markoff, 2007; Russell et al., 2015, 2019c; Carotenuto et al., 2021a), with extensive investigations into the radio/X-ray correlation (e.g., Corbel et al., 2013; Gallo et al., 2014; Russell et al., 2014, 2015), and their broadband spectra (e.g., Fender et al., 2000; Markoff, 2007), including the high-frequency spectral break arising from the point at which the jet becomes optically thin (Russell et al., 2014). Compact jets have previously not been studied in the low-frequency regime ( $< 1$  GHz), as they are usually far less luminous than transient jets. As a result, until now the low-frequency extent of these jets has been unknown. Detections of the low-frequency component of the compact jets are

strongly motivated as they carry information about the downstream distance at which shocks and energy dissipation occur (Malzac, 2014), and the magnetic field strength (Pe’er & Casella, 2009). The detailed modelling of the broadband jet spectrum will eventually help constrain physical parameters of the jets such as the magnetic field strength, the energy distribution of the particles.

The development of the modern, sensitive low-frequency interferometers, including the SKA precursor telescope MWA, LOFAR, and uGMRT, operating at frequencies  $< 1$  GHz, have provided new possibilities for detecting and monitor compact jets at low radio frequencies. Using the SKA precursor telescope MWA, this PhD research reported the first-time detection of compact jets in the low-frequency band ( $< 500$  MHz), and also measured the radio spectrum in the low-frequency regime to constrain the low-frequency turn-over or break (see Chapter 6). MWA detected compact jets from two black hole XRBs; MAXI J1820+070 and MAXI J1348–630, which showed no signature of a low-frequency turnover or break in the radio spectrum up to 154 MHz. The non-detection of the low-frequency turnover predicted by Malzac (2014) indicated that compact jets are dissipating their energy out to larger distances from the central engine (black hole). This result can provide a piece of crucial information, which will help in improving our understanding of the accretion/ejection coupling. As discussed in Section 6.4.3, the absence of a low-frequency turnover means that the Lorentz factor fluctuations should extend out to long timescales. According to Malzac (2014), the Lorentz factor fluctuations being injected at the jet base are governed by the variations in the X-ray emission (the X-ray power spectrum is assumed to map into the Lorentz factor power spectrum). So, observational constraints on the internal shock model can provide another direct link between accretion inflow and jet outflow.

We have not found evidence for long-lasting, diffuse, jet-blown bubbles in MAXI J1820+070. The discovery of such bubbles would constrain the ambient density and the jet power. However, higher sensitivity (and possibly resolution)

would likely be needed to make progress in this area, and that may require the SKA. Finally, with MWA observations obtaining the first low frequency detections of compact jets, this PhD research demonstrates the potential of the more sensitive SKA-Low to probe the physical properties of compact jets from a much larger and fainter population of XRBs.

#### 7.1.4 Strategies for SKA

The lessons we have learned in this PhD research can help inform the future framework necessary for observing the radio jets from black hole X-ray binaries with the future Square Kilometre Array<sup>1</sup> (Phase 1), which will comprises two components; SKA1-Low (50 to 350 MHz) and SKA1-Mid (350 MHz to 13.5 GHz). In addition, it also demonstrates the type of science we expect to extract about XRBs and their jets through future SKA observations.

From experience gained from the H I absorption studies of MAXI J1535–571 and MAXI J1348–630, we would propose a single observation of around 15 min (decided from our MAXI J1535–571 observations with ASKAP) of a bright XRB ( $\sim 500$  mJy) with the SKA1-Mid, which will provide a significant ( $> 3\sigma$ ) H I absorption complex to constrain the kinematic distance. For a faint ( $\sim 20$  mJy) XRB, we might need to integrate for longer time (around 30-min, as was necessary for the ASKAP monitoring of MAXI J1348–630). It will be beneficial to observe the source close to the peak of the X-ray outburst because, at that point, the source flux density will be highest.

The lessons learned from the broadband observations of the transient jets in MAXI J1535–571 will allow us to develop a monitoring strategy of transient jets with the SKA. As soon as an XRB outburst is detected by an all sky X-ray monitor, we would continuously observe its behaviour in X-rays, and accordingly plan our radio observations. To study the evolution of the low-frequency turnover, close to the peak of the X-ray outburst, we would observe the source daily for

---

<sup>1</sup><https://www.astron.nl/telescopes/square-kilometre-array/>

two week (discussed in Section 2.5) with the SKA. It's beneficial to monitor the source simultaneously from low to high frequencies (MHz to GHz) as these jets do vary on day-length timescales at low frequencies ( $< 300$  MHz) but show high-variability at frequencies  $> 1$  GHz. So, multi-frequency observations that are not (quasi-) simultaneous will not provide an accurate represent the activity and therefore simultaneous observations will help in reducing the uncertainties on the physical parameters, including the magnetic field strength and the minimum energy. If this is not possible then quasi-simultaneously, so that we would interpolate/extrapolate to produce a simultaneous spectrum. VLBI observations are important to constrain the source size, which helps us with the physical parameters described above. The correlation study between X-ray luminosity and jet energy will help us in determining the correlation between accretion and ejection.

Finally, due to its large collecting area of around  $419,000 \text{ m}^2$ , SKA1-Low will provide very high sensitivity in the low-frequency regime, which will help us to detect compact jets from the faintest XRBs. Our MWA detections of compact jets from MAXI J1820+070 and MAXI J1348–630 demonstrates that dedicated monitoring of XRBs with SKA1-Low while these systems are in the hard X-ray spectral state with a weekly cadence, stopping when the high-frequency radio flux densities drop below a critical level (nearly  $100 \mu\text{Jy}$  for 1 hour observation; calculated from sensitivity) will be effective for deriving important jet physics. One of the main goals for SKA1-Low compact jet monitoring would be to try to detect the signature of any low frequency spectral turnover. If such a turnover exists, we can study how the break varies with luminosity and hardness/spectral state. The turnover frequency conveys information about the downstream extent of the jet from the compact jets (Malzac, 2014). Hence, its detection will provide insight into how far from the black hole compact jets impart their energy in the surrounding medium, and modulate their surrounding environment. Further, the higher sensitivity of SKA1-Low would help us in extending these studies to a broader range of systems, including neutron star XRBs and black hole XRBs in

quiescence.

## 7.2 Conclusions

This thesis has presented low-frequency studies of the radio jets in black hole X-ray binaries. We have observed three black hole XRBs; MAXI J1535–571, MAXI J1348–630 and MAXI J1820+070, with the SKA precursor arrays. This PhD research has rejuvenated the use of the Doppler-shifted H I absorption line to estimate the kinematic distance to black hole XRBs, where we used ASKAP to constrain the kinematic distance to MAXI J1535–571 and MAXI J1348–630 (Chapters 3 and 4). This thesis also highlighted the capabilities of the Australian suite of radio telescopes for studying the transient radio jets from the black hole XRBs, as demonstrated by the broadband study of MAXI J1535–571 (Chapter 5). Further precursor observations presented in this thesis also provide new information on the low-frequency behaviour of compact radio jets in BH-XRBs (Chapter 6). The main conclusions from this thesis are summarised below:

### 7.2.1 Kinematic distances to black hole XRBs

In Chapter 3, we constrained the kinematic distance to MAXI J1535–571. We studied the H I absorption complex in the direction of the source and detected a significant ( $> 3\sigma$ ) H I absorption line with a maximum negative radial velocity of  $-69 \pm 4 \text{ km s}^{-1}$ . After solving the Galactic rotation curve for the MAXI J1535–571 position, the near and the far kinematic distances corresponding to the observed radial velocity were found to be  $4.1_{-0.5}^{+0.6} \text{ kpc}$  and  $9.3_{-0.6}^{+0.5} \text{ kpc}$ , respectively. To break the degeneracy of the near and the far distances, we observed an extragalactic source in the field of view. We detected a significant ( $> 3\sigma$ ) H I absorption complex with a maximum negative radial velocity of  $-89 \pm 4 \text{ km s}^{-1}$ , which was consistent with the tangent velocity. The non-detection of absorption at the tangent point velocity for MAXI J1535–571 signifies that the source is located at

the near point distance of  $4.1_{-0.5}^{+0.6}$  kpc.

Using our distance constraints, we found that at the peak of the outburst the unabsorbed X-ray luminosity of MAXI J1535–571 was  $> 78\%$  of the Eddington luminosity ( $L_{\text{Edd}}$ ). We also discovered that during the decay phase of the outburst, the source transited from the soft to the hard X-ray spectral state at a lower-than-expected luminosity of  $1.2 - 3.4 \times 10^{-5}$  times the Eddington luminosity, whereas the standard range is  $0.3 - 3\%$  of the Eddington luminosity. Our distance constraints have demonstrated that MAXI J1535–571 is a non-standard black hole XRB (Tetarenko et al., 2016).

After following a similar strategy, we estimated the distance to the black hole X-ray binary MAXI J1348–630 in Chapter 4. Towards MAXI J1348–630, we measured an appreciable ( $> 3\sigma$ ) H I absorption complex with a maximum negative radial velocity of  $-31 \pm 4 \text{ km s}^{-1}$ . After correlating the observed radial velocity with the Galactic rotation curve for the MAXI J1348–630 location, we found a near kinematic distance of  $2.2_{-0.6}^{+0.5}$  kpc, and a far kinematic distance of  $8.4 \pm 0.6$  kpc. We selected eight extragalactic sources in the field of view of MAXI J1348–630 and stacked their H I spectra to generate a robust comparison H I spectrum. The stacked spectrum showed a maximum negative radial velocity of  $-50 \pm 4 \text{ km s}^{-1}$ , which was congruent (within uncertainties) with the tangent point velocity of  $-54 \pm 4 \text{ km s}^{-1}$ . Absorption at the tangent point velocity was not observed for MAXI J1348–630, which positioned the source at the near distance of  $2.2_{-0.6}^{+0.5}$  kpc. The resulting distance constraint suggested that the peak X-ray luminosity of MAXI J1348–630 was  $17 \pm 10\%$  of the Eddington luminosity, and the soft-to-hard spectral state transition occurred at  $2.5 \pm 1.5\%$  of the Eddington luminosity. The physical characteristics determined using our obtained distance constraints suggested that MAXI J1348–630 is a canonical black hole XRB (Tetarenko et al., 2016).

## 7.2.2 Physical properties of the transient jets in MAXI J1535–571

The broadband study of the transient jets in MAXI J1535–571 was presented in Chapter 5. For the first time we detected transient jets with the SKA precursor telescope MWA. We also quasi-simultaneously monitored MAXI J1535–571 in the frequency range 0.84 to 19 GHz with the Australian suite of radio telescopes including UTMOST, ASKAP, ATCA and LBA. With the LBA observation on 23 September 2017, we measured the source size to be  $34 \pm 1$  mas, which further helped us in constraining the opening angle of the jet to be  $4.5 \pm 1.2^\circ$ . From the calculations of the Lorentz factor we found that the jet knot was externally confined.

We detected a low-frequency turnover in the broadband radio spectrum, whose frequency ( $0.32 \pm 0.01$  GHz) was strongly constrained by the MWA detection. We found that the turnover was likely to be due to synchrotron self-absorption. The turnover frequency, determined after fitting the spectrum with a SSA model, along with the LBA size constraints helped us in determining various physical parameters of the transient jet including the magnetic field strength ( $104_{-78}^{+80}$  mG) and the minimum energy ( $6.5 \pm 2.5 \times 10^{41}$  erg) of the jet knot. We also discovered that the plasma cloud in MAXI J1535–571 was close to equipartition as the magnetic field strength calculated using synchrotron self-absorption theory was consistent with the minimum energy magnetic field strength. We found that the magnetic field strength obtained for the transient jet in MAXI J1535–571 is close to the values reported for canonical XRBs (e.g., Fender & Bright, 2019). However, the minimum energy calculated for the jet knot in MAXI J1535–571 was at the high end of the range  $10^{38} - 10^{42}$  erg obtained from other canonical XRBs (e.g., Fender & Bright, 2019).

This study marked the beginning of XRB monitoring with the SKA precursors and demonstrates the strength of simultaneous observing campaigns with the full Australian suite of radio telescopes.

### **7.2.3 Low-frequency study of compact jets in black hole XRBs**

One of the most important outcomes of this PhD research is the detection of compact jets at low radio frequencies. In Chapter 6 we report the study of compact jets in the black hole XRBs MAXI J1820+070 and MAXI J1348–630. In the broadband spectrum of both the sources, we have not observed any signs of a low-frequency turnover, which was postulated by various theoretical models (Pe’er & Casella, 2009; Jamil et al., 2010; Malzac, 2014). The non-detection of the low-frequency turnover suggested that the compact jets are continuing to dissipate their energy in the surrounding environment at a larger distance from the compact object, that has been previously predicted by the theoretical models.

## **7.3 Future work**

### **7.3.1 Small scale structures in neutral hydrogen**

In the case of black hole XRBs, the transient jet knots have been observed to be moving with a proper motion of more than tens of mas/day (Russell et al., 2019c), even close to hundreds of mas/day in a few cases (Carotenuto et al., 2021a). For a source distance of few kpc (Chapters 3 and 4), this proper motion corresponds to tens or even hundreds of AU/day. Therefore, every monitoring corresponds to a different line-of-sight. By studying the HI absorption complex for every observation and comparing them we would be able to probe small scale variations in the neutral hydrogen (e.g., Liu et al., 2021). The aforementioned approach will provide details on the structure function of the small-scale fluctuations in the neutral hydrogen of the Milky Way (e.g., Dhawan et al., 2000).

### 7.3.2 High cadence monitoring of transient jets

In Chapter 5, using the Australian suite of radio telescopes, we presented a broadband study of transient jets from MAXI J1535–571 and determined the transient jet parameters. Multiple broadband observations of transient jets over the course of a full BH-XRB outburst, coupled to VLBI monitoring to determine the source expansion, would allow us to characterise the evolution (or decay) of the magnetic field strength as the jets evolved and expanded. This study has previously not been done but would provide important constraints on how the magnetic field strength, the minimum energy and the structure of the transient jet knot evolve as it propagates downstream. Furthermore, denser high-frequency coverage together with higher-significance low-frequency detections could help definitively discriminate between the FFA and SSA explanations for the turnover.

Additionally, denser low-frequency monitoring during super-Eddington flaring events, coupled with higher-frequency light curves, could help in modelling the key jet properties the jet geometry, speed and energetics (augmenting studies such as Tetarenko et al. 2017).

High cadence (e.g. every 1–2 days) deep imaging of the transient jets from BH-XRBs could also provide information on the surrounding environment of the system, which could perhaps help us in identifying the jet-blown bubbles (e.g., Heinz, 2002).

### 7.3.3 Fitting the compact jet spectrum with physical models

In Chapter 6, we presented the detection of compact jets in two BH-XRBs at frequencies  $< 300$  MHz with the MWA. We created broadband compact jet spectra down to 154 MHz and fitted them with a power-law (Sections 6.3.1.3 and 6.3.2.3). Finally, in Section 6.4.3 we presented a qualitative comparison of our results with the physical compact jet models such as the single acceleration model (Pe’er &

Casella, 2009) and the internal shock model (Pe'er & Markoff, 2012; Malzac, 2014).

To understand the behaviour of compact jets at low radio frequencies in detail, we would seek to fit the broadband spectra of both the sources with the internal shock model, which is the most widely-accepted physical model for compact jets. From the modelling parameters, we could then determine the physical properties of the compact jets, such as the magnetic field strength, the electron energy distribution and downstream distance at which energy is dissipated through shocks.

### 7.3.4 Monitoring with the SKA

In Chapters 5 and 6, we report out detection of transient and compact jets with the MWA, respectively. The MWA observations constrained the radio spectra of the jets in the low-frequency regime, but due to limited sensitivity, we were unable to precisely measure the low-frequency spectral index. For transient jets (Chapter 5), higher signal-to-noise low-frequency measurements will help us put tighter constraints on the turnover frequency, which will significantly reduce the uncertainties on the physical parameters derived from this value. In the case of compact jets (Chapter 6), more accurate low frequency measurements through higher signal-to-noise detections will ensure that any signature of a low-frequency turnover will not be washed out by large error bars, which would consequently contaminate the information on the extent of the compact jets from the black hole.

In the coming years, when SKA will be up and running, there will be a revolution in the study and understanding of radio jets, their impact on the surrounding medium, and the coupling between inflow and outflow. The large collecting area of the SKA will provide unprecedented high sensitivity, which will help us in monitoring the ejection of matter during all accretion states in black hole XRBs. High cadence monitoring during bright outbursting states and low-luminosity quiescent states will provide us with an opportunity to study

the jet acceleration at all accretion rates. SKA will also allow us to monitor neutron star XRBs, where the ejection of the matter is less well explored owing to their comparative radio faintness. Finally, SKA will help us in determining how accretion powered radio jets are launched into space at all size scales, and what their feedback is on the surrounding environment.

## 7.4 Contribution of this thesis

This PhD thesis stressed the importance of low-frequency observations of the radio jets in XRBs, and the contributions low-frequency observations can make to the fundamental open questions on jet launching, jet energetics and hence feedback to the surroundings.

In Chapters 3 and 4, we constrained the distance to two XRBs. The distance is important to constrain physical parameters like peak X-ray luminosity, and state transition luminosity. Peak luminosity is important to understand the accretion energy budget. Our distance constraints were further used by Russell et al. (2019c) and Carotenuto et al. (2021a) to calculate the jet velocity, the inclination angle, the magnetic field strength, the equipartition energy, the jet radius. These physical parameters are important to understand the energetics of the jets. Using these parameters we can further determine the amount of energy extracted by the jets from the system, and compare it with the accretion power (as calculated from X-ray observations), thereby probing the link between accretion and jet ejection.

In Chapter 5, our MWA detections of the transient jet we found to be important to constrain the broadband spectrum in the low-frequency regime and helped in detecting the spectral turnover, which we attributed to synchrotron self-absorption. The turnover frequency together with the source size and the distance constrained in Chapter 3 have thereby helped us in determining the magnetic field strength, the equipartition energy, and the jet opening angle. These physical parameters eventually helped us in understanding the energetics of the

jet, which is important to understand the energy budget of the jets and hence the jet launching mechanism.

Finally, in Chapter 6, we made a first-time low-frequency detections of the compact jet. Using our low-frequency observations we constrained the compact jet spectrum down to 150 MHz, and found no signatures of the low-frequency turnover predicted by various theoretical models. This suggests that the compact jets dissipate their energy via internal shocks (according to the internal shock model given by Malzac 2014) out to larger distances than previously believed, implying that Lorentz factor fluctuations at the jet base extend to longer timescales. This study thereby gives important information on the interaction of compact jets with their surroundings.

While our low-frequency observations have provided some new insights into the jet energetics, and hence their launching mechanism and interaction with the surroundings, they have also paved the way for further studies, in particular with SKA. And they have given us other critical information on the properties of the XRBs themselves (distance, peak luminosity, state transition luminosity) and also their jets (magnetic field strengths, dissipation radius for shocks, opening angles). In summary, this work has helped demonstrate the potential of low-frequency observations for furthering X-ray binary and jet science, and motivates future studies with a more comprehensive suite of facilities, a higher cadence, and more sensitive instruments.



# Appendices



# Appendix A

## Synchrotron radiation

Synchrotron radiation is non-thermal radiation, which is produced when relativistic electrons gyrate around magnetic field lines (Frank et al., 2002). The synchrotron emission can be highly polarised (fractional polarisation  $\sim 75\%$ ), and the spectrum can be well described by a power-law in frequency over a broad frequency range. Synchrotron radiation is one of the main sources of diffuse background radiation in our Milky Way (Haslam et al., 1981, 1982)

Following Rybicki & Lightman (1979) and Longair (2011), in a stationary observer's frame, the power emitted by a relativistic particle has a strongly bounded narrow conical angular distribution about the direction of the particle motion, which is mainly due to relativistic aberration (Fig. A.1). Such an effect is known as relativistic beaming. The half opening angle of the emission cone is  $1/\gamma$  in the stationary observer's frame, where  $\gamma$  is the Lorentz factor of the relativistic electron. Therefore, the stationary observer only detects the radiation when the motion of the electron is within an angle  $1/\gamma$  of the line of sight. This happens only for a short period during the orbit of the relativistic particle, and the stationary observer only observes a small pulse of radiation in every orbit. The frequency spectrum of the detected emission is then the Fourier transform of this narrow pulse after considering the relativistic effects including, the Doppler-shift, and the time dilation. The synchrotron radiation is broad-band in nature be-

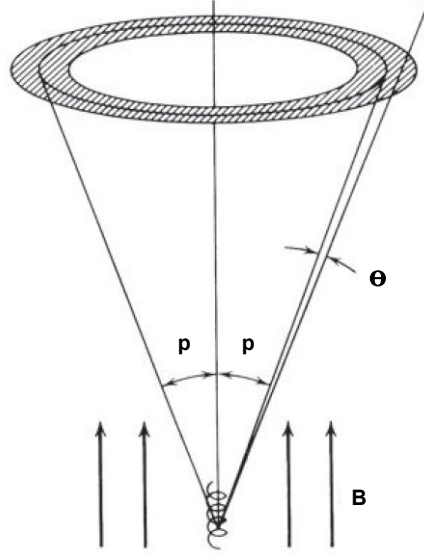


Figure A.1: Synchrotron emission from a relativistic electron.  $p$  is the pitch angle of the electron, and  $B$  is the magnetic field strength. The synchrotron emission is restricted to the shaded region, and  $\theta = 1/\gamma$ . The figure is taken from Rybicki & Lightman (1979).

cause the Fourier transform of the narrow pulse gives a broad spectrum. The spectrum of the radiation from a single electron has its maximum value at the critical angular frequency ( $\omega_{\text{crt}}$ ) defined as

$$\omega_{\text{crt}} = \frac{3}{2} \frac{c}{v} (\gamma^3 \omega_g \sin p), \quad (\text{A.1})$$

where  $v$  is the speed of the electron,  $c$  is the speed of light,  $p$  is the pitch angle of the electron, and  $\omega_g$  is the gyrofrequency of the electron defined as

$$\omega_g = \left( \frac{eB}{\gamma m_e} \right), \quad (\text{A.2})$$

where  $m_e$  and  $e$  are the mass and the charge of an electron, respectively.  $B$  is the magnetic field strength.

If we consider a single electron, the total synchrotron emissivity is expressed

(e.g. Longair 2011, eq. 8.58) by

$$j(\omega) = \frac{\sqrt{3} e^3 B \sin p}{8 \pi^2 \epsilon_0 c m_e} F\left(x = \frac{\omega}{\omega_{\text{crt}}}\right), \quad (\text{A.3})$$

where  $\omega$  is the frequency of emission, and  $F(x)$  is defined as

$$F(x) = x \int_x^\infty K_{5/3}(z) dz, \quad (\text{A.4})$$

where  $\omega/\omega_{\text{crt}} = \nu/\nu_{\text{crt}}$ , and  $\nu_{\text{crt}} = \omega_{\text{crt}}/2\pi$ .  $K_{5/3}(z)$  is a modified Bessel function of order  $5/3$ ,  $\epsilon_0$  is the permittivity of the free space.

In the case of the low and high frequency limits,  $F(x)$  can be defined as (e.g. Rybicki & Lightman 1979, eg. 6.34a and b)

$$F(x) = \frac{4\pi}{\sqrt{3}\Gamma_f(1/3)} \left(\frac{x}{2}\right)^{1/3} \quad \text{when } x \ll 1, \quad (\text{A.5})$$

$$F(x) = \left(\frac{\pi}{2}\right)^{1/2} x^{1/2} \exp(-x) \quad \text{when } x \gg 1, \quad (\text{A.6})$$

where  $\Gamma_f$  is the Gamma function. After substituting eq. A.5 in eq. A.3, we found that

$$j(\nu) = \frac{\sqrt{3} e^3 B \sin p}{8 \pi^2 \epsilon_0 c m_e} \frac{4\pi}{\sqrt{3}\Gamma_f(1/3)} \left(\frac{\nu}{2\nu_{\text{crt}}}\right)^{1/3}. \quad (\text{A.7})$$

The above equation highlights that at frequencies  $\nu \ll \nu_{\text{crt}}$ , the synchrotron emissivity becomes proportional to  $\nu^{1/3}$  (Fig. A.2).

When we substitute the value of  $F(x)$  from eq. A.6 in eq. A.3, we observed that

$$j(\nu) \propto \nu^{1/2} \exp(-\nu/\nu_{\text{crt}}). \quad (\text{A.8})$$

From the above solution we found that at  $\nu \gg \nu_{\text{crt}}$ , the synchrotron spectrum is governed by the exponential cutoff (Fig. A.2).

For a synchrotron emitting astrophysical object, the energy of the particles follow a power-law distribution. The energy spectrum of electrons having number density  $N(E)dE$  (per unit volume) in the energy interval  $E$  to  $E + dE$  is given

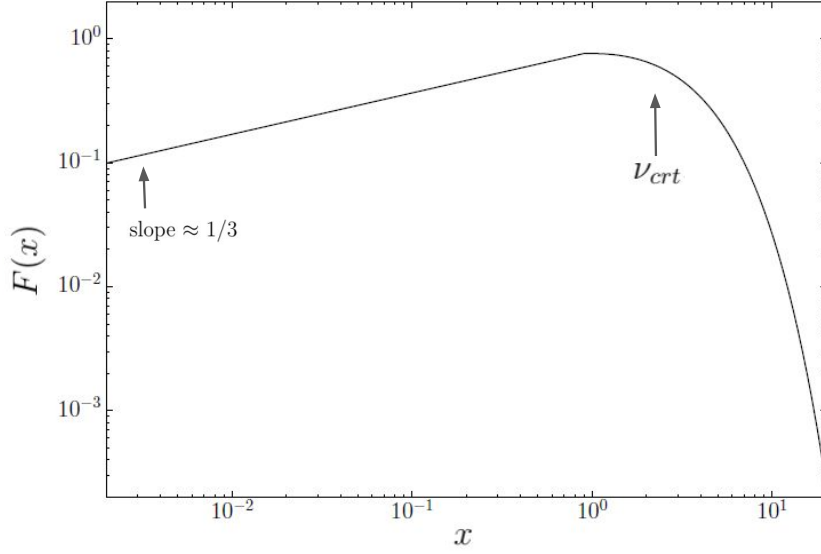


Figure A.2: The plot showing the synchrotron spectrum of a relativistic electron, which is proportional to  $F(x)$ . We defined frequency in terms of the critical frequency ( $\nu_{crit}$ ), where  $x = \omega/\omega_{crit} = \nu/\nu_{crit}$ .  $F(x)$  is given by eq. A.5 and A.6.

by

$$N(E)dE = \kappa E^{-a}dE, \quad (\text{A.9})$$

where  $a$  is the power-law index, and  $\kappa$  is the normalisation factor for the spectrum.

The total emissivity (per unit volume) of a synchrotron-emitting source is calculated by integrating over the complete energy spectrum of the electrons, which is defined (Longair 2011, eq. 8.83) as

$$J(\omega) = \int_0^\infty j(\omega) \kappa E^{-a}dE. \quad (\text{A.10})$$

After evaluating the integral, we find

$$J(\omega) = \frac{\sqrt{3} e^3 B \kappa \sin p}{8 \pi^2 \epsilon_0 c m_e (a+1)} \left( \frac{\omega m_e^3 c^4}{3 e B \sin p} \right)^{-(a-1)/2} \Gamma_f \left( \frac{a}{4} + \frac{19}{12} \right) \Gamma_f \left( \frac{a}{4} - \frac{1}{12} \right). \quad (\text{A.11})$$

The emissivity of an electron at a specific angular frequency,  $\omega$ , relies firmly

on the pitch angle,  $p$ . If we consider that the pitch angles follow an isotropic distribution, then the probability distribution for a pitch angle in the interval  $p$  to  $p + dp$  is given by

$$P(p) = \frac{1}{2} \sin p dp. \quad (\text{A.12})$$

Therefore, the total emissivity (per unit volume) becomes

$$J(\omega) = \frac{\sqrt{3} e^3 B \kappa}{16 \pi^2 \epsilon_0 c m_e (a + 1)} \left( \frac{\omega m_e^3 c^4}{3 e B} \right)^{\frac{-(a-1)}{2}} \sqrt{\pi} \frac{\Gamma_f\left(\frac{a}{4} + \frac{19}{12}\right) \Gamma_f\left(\frac{a}{4} - \frac{1}{12}\right) \Gamma_f\left(\frac{a}{4} + \frac{5}{4}\right)}{\Gamma_f\left(\frac{a}{4} + \frac{7}{4}\right)}. \quad (\text{A.13})$$

Finally, in terms of  $\nu$ ,  $B$  and  $\kappa$ , the expression for total emissivity can be expressed as

$$J(\nu) \propto \kappa B^{(a+1)/2} \nu^{-(a-1)/2}, \quad (\text{A.14})$$

The emitted synchrotron spectrum can be best described with a power-law in frequency ( $J(\nu) \propto \nu^{-(a-1)/2}$ ), with power-law index  $(a-1)/2$ . This highlights that the shape of the total observed spectrum is dominated by the electron energy distribution, not by the single electron emission spectrum.



# Appendix B

## COTTER

The COTTER (Offringa et al., 2015) software is a pre-processing pipeline specifically written for the MWA data processing. The various steps included in the COTTER software are summarised below (Offringa et al., 2015).

1. COTTER uses the AOFLAGGER (Offringa et al., 2012) tool for detecting and flagging RFI in cross-correlations.
2. creates CASA measurements sets or UV-FITS files from the raw files from correlator.
3. implement bandpass gain corrections and then calibrate the phases for changing cable lengths.
4. apply phase tracking to the preferred sky location.
5. flags incorrect or missing data samples from the correlator.
6. Finally, average the visibilities in time or in frequency or in both the domains to reduce the data volume.



# Appendix C

## Publications

### C.1 Publications included in this thesis

1. **J. Chauhan**, J. C. A. Miller-Jones, G. E. Anderson, W. Raja, A. Bahramian, A. Hotan, B. Indermuehle, M. Whiting, J. R. Allison, C. Anderson, J. Bunton, B. Koribalski, and E. Mahony (2019), “An H I absorption distance to the black hole candidate X-ray binary MAXI J1535–571”, *Monthly Notices of the Royal Astronomical Society*, Letters, Volume 488, Issue 1, page L129–L133, DOI: <https://doi.org/10.1093/mnrasl/slz113>.

This work is reproduced in Chapter 3.

2. **J. Chauhan**, J. C. A. Miller-Jones, W. Raja, J. R. Allison, P. F. L. Jacob, G. E. Anderson, F. Carotenuto, S. Corbel, R. Fender, A. Hotan, M. Whiting, P. A. Woudt, B. Koribalski, and E. Mahony (2021), “Measuring the distance to the black hole candidate X-ray binary MAXI J1348–630 using H I absorption”, *Monthly Notices of the Royal Astronomical Society*, Letters, Volume 501, Issue 1, page L60–L64, DOI: <https://doi.org/10.1093/mnrasl/slaa195>.

This work is reproduced in Chapter 4.

3. **J. Chauhan**, J. C. A. Miller-Jones, G. E. Anderson, A. Paduano, M.

Sokolowski, C. Flynn, P. J. Hancock, N. Hurley-Walker, D. L. Kaplan, T. D. Russell, A. Bahramian, S. W. Duchesne, D. Altamirano, S. Croft, H. A. Krimm, G. R. Sivakoff, R. Soria, C. M. Trott, R. B. Wayth, V. Gupta, M. Johnston-Hollitt, and S. J. Tingay. “A broadband radio view of transient jet ejecta in the black hole candidate X-ray binary MAXI J1535–571”, *Publications of the Astronomical Society of Australia*, Volume 38, eid e045, page e045, DOI: <https://doi.org/10.1017/pasa.2021.38>.

This work is reproduced in Chapter 5.

## C.2 Publications not included in this thesis

1. F. Carotenuto, S. Corbel, E. Tremou, T. D. Russell, A. Tzioumis, R. P. Fender, P. A. Woudt, S. E. Motta, J. C. A. Miller-Jones, **J. Chauhan**, A. J. Tetarenko, G. R. Sivakoff, I. Heywood, A. Horesh, A. J. van der Horst, E. Koerding, and K. P. Mooley (2021), “The black hole transient MAXI J1348-630: evolution of the compact and transient jets during its 2019/2020 outburst”, *Monthly Notices of the Royal Astronomical Society*, Volume 504, Issue 1, page 444–468, DOI: <https://doi.org/10.1093/mnras/stab864>.

This work presents broadband monitoring of the compact and transient jets in MAXI J1348-630 during its 2019/2020 outburst with MeerKAT and ATCA. I provided kinematic distance measurements to the source. I also gave radio flux density of the source for ASKAP observation on 13 February 2019.

2. J. W. Broderick, T. D. Russell, R. P. Fender, S. A Trushkin, D. A. Green, **J. Chauhan**, N. A. Nizhelskij, P. G. Tsybulev, N. N. Bursov, A. V. Shevchenko, G. G. Pooley, D. R. A. Williams, J. S. Bright, A. Rowlinson, and S. Corbel (2021), “Strong low-frequency radio flaring from Cygnus X-3 observed with LOFAR”, *Monthly Notices of the Royal Astronomical Society*, Volume 504, Issue 1, page 1482–1494, DOI: <https://doi.org/10.1093/mnras/stab864>.

[1093/mnras/stab708](https://doi.org/10.1093/mnras/stab708).

This work presents a low-frequency monitoring of Cygnus X-3 during the radio flaring event with LOFAR. I helped in the initial spectral modelling and interpretation of the obtained results.

3. P. Bharali, **J. Chauhan** and K. Boruah (2019), “Broad-band spectral study of X-ray transient MAXI J1820+070 using Swift/XRT and NuSTAR”, *Monthly Notices of the Royal Astronomical Society*, Volume 487, Issue 4, page 5946–5951, DOI: <https://doi.org/10.1093/mnras/stz1686>.

This work presents a broadband X-ray study of MAXI J1820+070 in the hard X-ray spectral state. I helped in the spectral modelling and interpretation of the obtained results.

4. P. Bharali, S. Chandra, **J. Chauhan**, J. A. García, J. Roy, M. Boettcher and K. Boruah (2019), “Re-awakening of GRS 1716-249 after 23 yr, observed by Swift/XRT and NuSTAR”, *Monthly Notices of the Royal Astronomical Society*, Volume 487, Issue 3, page 3150–3161, DOI: <https://doi.org/10.1093/mnras/stz1492>.

This work presents a timing and spectral study of GRS 1716–249 in the intermediate X-ray spectral state. I helped in the temporal and spectral modelling and interpretation of the obtained results.



# Appendix D

## Acknowledgement of facilities and funding

This scientific work makes use of the Murchison Radio-astronomy Observatory, operated by CSIRO. We acknowledge the Wajarri Yamatji people as the traditional owners of the Observatory site. Support for the operation of the MWA is provided by the Australian Government (NCRIS), under a contract to Curtin University administered by Astronomy Australia Limited.

The Australian SKA Pathfinder is part of the Australia Telescope National Facility which is managed by CSIRO. Operation of ASKAP is funded by the Australian Government with support from the National Collaborative Research Infrastructure Strategy. ASKAP uses the resources of the Pawsey Supercomputing Centre. Establishment of ASKAP, the Murchison Radio-astronomy Observatory and the Pawsey Supercomputing Centre are initiatives of the Australian Government, with support from the Government of Western Australia and the Science and Industry Endowment Fund.

The MeerKAT telescope is operated by the South African Radio Astronomy Observatory, which is a facility of the National Research Foundation, an agency of the Department of Science and Innovation.

The Australia Telescope Compact Array and Long Baseline Array are both

part of the Australia Telescope National Facility, which is funded by the Australian Government for operation as a National Facility managed by CSIRO. We acknowledge the Pawsey Supercomputing Centre which is supported by the Western Australian and Australian Governments.

JCAM-J is the recipient of Australian Research Council Future Fellowship (project number FT140101082) and GEA is the recipient of an Australian Research Council Discovery Early Career Researcher Award (project number DE180100346) funded by the Australian Government. NHW is the recipient of Australian Research Council Future Fellowship (project number FT190100231). DLK was supported by NSF grant AST-1816492. SWD acknowledges an Australian Government Research Training Program scholarship administered through Curtin University. DA acknowledges support from the Royal Society. SC and DLK were supported by NSF grant AST-1412421. GRS acknowledges support from Natural Sciences and Engineering Research Council of Canada (NSERC) Discovery Grant (RGPIN-06569-2016).

# Appendix E

## Statement of contribution by Co-authors

## To Whom It May Concern

I, Jaiverdhan Chauhan, have outlined my contributions and the contributions of the Co-Authors to the chapters in this thesis that have been adapted from published papers (Chapter 3, “An ASKAP distance constraint to MAXI J1535–571”, Chapter 4, “Measuring a kinematic distance to MAXI J1348–630 using the SKA precursors ASKAP and MeerKAT” and Chapter 5, “Using SKA precursors to study the transient jets in MAXI J1535–571”) and to Chapter 6, “Low-frequency MWA detections of compact jets in two black hole XRBs”.



**(Signature of candidate)**

I, as a Co-Author, endorse that the level of contribution indicated by the candidate at in ‘Statement of contribution by co-authors’ at the beginning of this thesis is appropriate.

**Prof. James C.A. Miller-Jones**



**(Full name of Co-Author)**

**(Signature of Co-Author)**

## To Whom It May Concern

I, Jaiverdhan Chauhan, have outlined my contributions and the contributions of the Co-Authors to the chapters in this thesis that have been adapted from published papers (Chapter 3, “An ASKAP distance constraint to MAXI J1535–571”, Chapter 4, “Measuring a kinematic distance to MAXI J1348–630 using the SKA precursors ASKAP and MeerKAT” and Chapter 5, “Using SKA precursors to study the transient jets in MAXI J1535–571”) and to Chapter 6, “Low-frequency MWA detections of compact jets in two black hole XRBs”.



(Signature of candidate)

I, as a Co-Author, endorse that the level of contribution indicated by the candidate at in ‘Statement of contribution by co-authors’ at the beginning of this thesis is appropriate.

Gemma Anderson

(Full name of Co-Author)



(Signature of Co-Author)

## To Whom It May Concern

I, Jaiverdhan Chauhan, have outlined my contributions and the contributions of the Co-Authors to the chapters in this thesis that have been adapted from published papers (Chapter 3, “An ASKAP distance constraint to MAXI J1535–571”, Chapter 4, “Measuring a kinematic distance to MAXI J1348–630 using the SKA precursors ASKAP and MeerKAT” and Chapter 5, “Using SKA precursors to study the transient jets in MAXI J1535–571”) and to Chapter 6, “Low-frequency MWA detections of compact jets in two black hole XRBs”.



**(Signature of candidate)**

I, as a Co-Author, endorse that the level of contribution indicated by the candidate at in ‘Statement of contribution by co-authors’ at the beginning of this thesis is appropriate.

Arash Bahramian

**(Full name of Co-Author)**



**(Signature of Co-Author)**

## To Whom It May Concern

I, Jaiverdhan Chauhan, have outlined my contributions and the contributions of the Co-Authors to the chapters in this thesis that have been adapted from published papers (Chapter 3, “An ASKAP distance constraint to MAXI J1535–571”, Chapter 4, “Measuring a kinematic distance to MAXI J1348–630 using the SKA precursors ASKAP and MeerKAT” and Chapter 5, “Using SKA precursors to study the transient jets in MAXI J1535–571”) and to Chapter 6, “Low-frequency MWA detections of compact jets in two black hole XRBs”.



**(Signature of candidate)**

I, as a Co-Author, endorse that the level of contribution indicated by the candidate at in ‘Statement of contribution by co-authors’ at the beginning of this thesis is appropriate.

Thomas D Russell

**(Full name of Co-Author)**



**(Signature of Co-Author)**

## To Whom It May Concern

I, Jaiverdhan Chauhan, have outlined my contributions and the contributions of the Co-Authors to the chapters in this thesis that have been adapted from published papers (Chapter 3, “An ASKAP distance constraint to MAXI J1535–571”, Chapter 4, “Measuring a kinematic distance to MAXI J1348–630 using the SKA precursors ASKAP and MeerKAT” and Chapter 5, “Using SKA precursors to study the transient jets in MAXI J1535–571”) and to Chapter 6, “Low-frequency MWA detections of compact jets in two black hole XRBs”.



**(Signature of candidate)**

I, as a Co-Author, endorse that the level of contribution indicated by the candidate at in ‘Statement of contribution by co-authors’ at the beginning of this thesis is appropriate.

**Wasim Raja**

**(Full name of Co-Author)**



**(Signature of Co-Author)**

**Signed on 28 April 2021**

## To Whom It May Concern

I, Jaiverdhan Chauhan, have outlined my contributions and the contributions of the Co-Authors to the chapters in this thesis that have been adapted from published papers (Chapter 3, “An ASKAP distance constraint to MAXI J1535–571”, Chapter 4, “Measuring a kinematic distance to MAXI J1348–630 using the SKA precursors ASKAP and MeerKAT” and Chapter 5, “Using SKA precursors to study the transient jets in MAXI J1535–571”) and to Chapter 6, “Low-frequency MWA detections of compact jets in two black hole XRBs”.



**(Signature of candidate)**

I, as a Co-Author, endorse that the level of contribution indicated by the candidate at in ‘Statement of contribution by co-authors’ at the beginning of this thesis is appropriate.

James Richard Allison

**(Full name of Co-Author)**



**(Signature of Co-Author)**

## To Whom It May Concern

I, Jaiverdhan Chauhan, have outlined my contributions and the contributions of the Co-Authors to the chapters in this thesis that have been adapted from published papers (Chapter 3, “An ASKAP distance constraint to MAXI J1535–571”, Chapter 4, “Measuring a kinematic distance to MAXI J1348–630 using the SKA precursors ASKAP and MeerKAT” and Chapter 5, “Using SKA precursors to study the transient jets in MAXI J1535–571”) and to Chapter 6, “Low-frequency MWA detections of compact jets in two black hole XRBs”.



**(Signature of candidate)**

I, as a Co-Author, endorse that the level of contribution indicated by the candidate at in ‘Statement of contribution by co-authors’ at the beginning of this thesis is appropriate.

Aidan W. Hotan

**(Full name of Co-Author)**



**(Signature of Co-Author)**

### To Whom It May Concern

I, Jaiverdhan Chauhan, have outlined my contributions and the contributions of the Co-Authors to the chapters in this thesis that have been adapted from published papers (Chapter 3, "An ASKAP distance constraint to MAXI J1535-571", Chapter 4, "Measuring a kinematic distance to MAXI J1348-630 using the SKA precursors ASKAP and MeerKAT" and Chapter 5, "Using SKA precursors to study the transient jets in MAXI J1535-571") and to Chapter 6, "Low-frequency MWA detections of compact jets in two black hole XRBs".



(Signature of candidate)

I, as a Co-Author, endorse that the level of contribution indicated by the candidate at in 'Statement of contribution by co-authors' at the beginning of this thesis is appropriate.

MARCIN SOKOLOWSKI  
(Full name of Co-Author)



(Signature of Co-Author)

c

## To Whom It May Concern

I, Jaiverdhan Chauhan, have outlined my contributions and the contributions of the Co-Authors to the chapters in this thesis that have been adapted from published papers (Chapter 3, “An ASKAP distance constraint to MAXI J1535–571”, Chapter 4, “Measuring a kinematic distance to MAXI J1348–630 using the SKA precursors ASKAP and MeerKAT” and Chapter 5, “Using SKA precursors to study the transient jets in MAXI J1535–571”) and to Chapter 6, “Low-frequency MWA detections of compact jets in two black hole XRBs”.

**(Signature of candidate)**

I, as a Co-Author, endorse that the level of contribution indicated by the candidate at in ‘Statement of contribution by co-authors’ at the beginning of this thesis is appropriate.

**Prof. Roberto Soria**

**(Full name of Co-Author)**

**(Signature of Co-Author)**

## To Whom It May Concern

I, Jaiverdhan Chauhan, have outlined my contributions and the contributions of the Co-Authors to the chapters in this thesis that have been adapted from published papers (Chapter 3, “An ASKAP distance constraint to MAXI J1535–571”, Chapter 4, “Measuring a kinematic distance to MAXI J1348–630 using the SKA precursors ASKAP and MeerKAT” and Chapter 5, “Using SKA precursors to study the transient jets in MAXI J1535–571”) and to Chapter 6, “Low-frequency MWA detections of compact jets in two black hole XRBs”.



**(Signature of candidate)**

I, as a Co-Author, endorse that the level of contribution indicated by the candidate at in ‘Statement of contribution by co-authors’ at the beginning of this thesis is appropriate.

Matthew T. Whiting

**(Full name of Co-Author)**



**(Signature of Co-Author)**

## To Whom It May Concern

I, Jaiverdhan Chauhan, have outlined my contributions and the contributions of the Co-Authors to the chapters in this thesis that have been adapted from published papers (Chapter 3, “An ASKAP distance constraint to MAXI J1535–571”, Chapter 4, “Measuring a kinematic distance to MAXI J1348–630 using the SKA precursors ASKAP and MeerKAT” and Chapter 5, “Using SKA precursors to study the transient jets in MAXI J1535–571”) and to Chapter 6, “Low-frequency MWA detections of compact jets in two black hole XRBs”.



(Signature of candidate)

I, as a Co-Author, endorse that the level of contribution indicated by the candidate at in ‘Statement of contribution by co-authors’ at the beginning of this thesis is appropriate.

Alessandro Paduano

(Full name of Co-Author)



(Signature of Co-Author)

## To Whom It May Concern

I, Jaiverdhan Chauhan, have outlined my contributions and the contributions of the Co-Authors to the chapters in this thesis that have been adapted from published papers (Chapter 3, “An ASKAP distance constraint to MAXI J1535–571”, Chapter 4, “Measuring a kinematic distance to MAXI J1348–630 using the SKA precursors ASKAP and MeerKAT” and Chapter 5, “Using SKA precursors to study the transient jets in MAXI J1535–571”) and to Chapter 6, “Low-frequency MWA detections of compact jets in two black hole XRBs”.



(Signature of candidate)

I, as a Co-Author, endorse that the level of contribution indicated by the candidate at in ‘Statement of contribution by co-authors’ at the beginning of this thesis is appropriate.

Elizabeth Mahony

(Full name of Co-Author)



(Signature of Co-Author)

## To Whom It May Concern

I, Jaiverdhan Chauhan, have outlined my contributions and the contributions of the Co-Authors to the chapters in this thesis that have been adapted from published papers (Chapter 3, “An ASKAP distance constraint to MAXI J1535–571”, Chapter 4, “Measuring a kinematic distance to MAXI J1348–630 using the SKA precursors ASKAP and MeerKAT” and Chapter 5, “Using SKA precursors to study the transient jets in MAXI J1535–571”) and to Chapter 6, “Low-frequency MWA detections of compact jets in two black hole XRBs”.



**(Signature of candidate)**

I, as a Co-Author, endorse that the level of contribution indicated by the candidate at in ‘Statement of contribution by co-authors’ at the beginning of this thesis is appropriate.

Prof. Baerbel S. Koribalski



**(Full name of Co-Author)**

**(Signature of Co-Author)**

## To Whom It May Concern

I, Jaiverdhan Chauhan, have outlined my contributions and the contributions of the Co-Authors to the chapters in this thesis that have been adapted from published papers (Chapter 3, “An ASKAP distance constraint to MAXI J1535–571”, Chapter 4, “Measuring a kinematic distance to MAXI J1348–630 using the SKA precursors ASKAP and MeerKAT” and Chapter 5, “Using SKA precursors to study the transient jets in MAXI J1535–571”) and to Chapter 6, “Low-frequency MWA detections of compact jets in two black hole XRBs”.



**(Signature of candidate)**

I, as a Co-Author, endorse that the level of contribution indicated by the candidate at in ‘Statement of contribution by co-authors’ at the beginning of this thesis is appropriate.

**Craig Stuart Anderson**

**(Full name of Co-Author)**



**(Signature of Co-Author)**

## To Whom It May Concern

I, Jaiverdhan Chauhan, have outlined my contributions and the contributions of the Co-Authors to the chapters in this thesis that have been adapted from published papers (Chapter 3, “An ASKAP distance constraint to MAXI J1535–571”, Chapter 4, “Measuring a kinematic distance to MAXI J1348–630 using the SKA precursors ASKAP and MeerKAT” and Chapter 5, “Using SKA precursors to study the transient jets in MAXI J1535–571”) and to Chapter 6, “Low-frequency MWA detections of compact jets in two black hole XRBs”.



**(Signature of candidate)**

I, as a Co-Author, endorse that the level of contribution indicated by the candidate at in ‘Statement of contribution by co-authors’ at the beginning of this thesis is appropriate.

**Balthasar Indermuehle**

**(Full name of Co-Author)**



**(Signature of Co-Author)**

## To Whom It May Concern

I, Jaiverdhan Chauhan, have outlined my contributions and the contributions of the Co-Authors to the chapters in this thesis that have been adapted from published papers (Chapter 3, “An ASKAP distance constraint to MAXI J1535–571”, Chapter 4, “Measuring a kinematic distance to MAXI J1348–630 using the SKA precursors ASKAP and MeerKAT” and Chapter 5, “Using SKA precursors to study the transient jets in MAXI J1535–571”) and to Chapter 6, “Low-frequency MWA detections of compact jets in two black hole XRBs”.



(Signature of candidate)

I, as a Co-Author, endorse that the level of contribution indicated by the candidate at in ‘Statement of contribution by co-authors’ at the beginning of this thesis is appropriate.

John David Bunton

(Full name of Co-Author)



(Signature of Co-Author)

**To Whom It May Concern**

I, Jaiverdhan Chauhan, have outlined my contributions and the contributions of the Co-Authors to the chapters in this thesis that have been adapted from published papers (Chapter 3, "An ASKAP distance constraint to MAXI J1535-571", Chapter 4, "Measuring a kinematic distance to MAXI J1348-630 using the SKA precursors ASKAP and MeerKAT" and Chapter 5, "Using SKA precursors to study the transient jets in MAXI J1535-571") and to Chapter 6, "Low-frequency MWA detections of compact jets in two black hole XRBs".



(Signature of candidate)

I, as a Co-Author, endorse that the level of contribution indicated by the candidate at in 'Statement of contribution by co-authors' at the beginning of this thesis is appropriate.

Paul Hancock  
(Full name of Co-Author)



(Signature of Co-Author)

## To Whom It May Concern

I, Jaiverdhan Chauhan, have outlined my contributions and the contributions of the Co-Authors to the chapters in this thesis that have been adapted from published papers (Chapter 3, “An ASKAP distance constraint to MAXI J1535–571”, Chapter 4, “Measuring a kinematic distance to MAXI J1348–630 using the SKA precursors ASKAP and MeerKAT” and Chapter 5, “Using SKA precursors to study the transient jets in MAXI J1535–571”) and to Chapter 6, “Low-frequency MWA detections of compact jets in two black hole XRBs”.



(Signature of candidate)

I, as a Co-Author, endorse that the level of contribution indicated by the candidate at in ‘Statement of contribution by co-authors’ at the beginning of this thesis is appropriate.

**Natasha Hurley-Walker**

(Full name of Co-Author)



(Signature of Co-Author)

## To Whom It May Concern

I, Jaiverdhan Chauhan, have outlined my contributions and the contributions of the Co-Authors to the chapters in this thesis that have been adapted from published papers (Chapter 3, “An ASKAP distance constraint to MAXI J1535–571”, Chapter 4, “Measuring a kinematic distance to MAXI J1348–630 using the SKA precursors ASKAP and MeerKAT” and Chapter 5, “Using SKA precursors to study the transient jets in MAXI J1535–571”) and to Chapter 6, “Low-frequency MWA detections of compact jets in two black hole XRBs”.



**(Signature of candidate)**

I, as a Co-Author, endorse that the level of contribution indicated by the candidate at in ‘Statement of contribution by co-authors’ at the beginning of this thesis is appropriate.

Chris Flynn

**(Full name of Co-Author)**



**(Signature of Co-Author)**

## To Whom It May Concern

I, Jaiverdhan Chauhan, have outlined my contributions and the contributions of the Co-Authors to the chapters in this thesis that have been adapted from published papers (Chapter 3, “An ASKAP distance constraint to MAXI J1535–571”, Chapter 4, “Measuring a kinematic distance to MAXI J1348–630 using the SKA precursors ASKAP and MeerKAT” and Chapter 5, “Using SKA precursors to study the transient jets in MAXI J1535–571”) and to Chapter 6, “Low-frequency MWA detections of compact jets in two black hole XRBs”.



(Signature of candidate)

I, as a Co-Author, endorse that the level of contribution indicated by the candidate at in ‘Statement of contribution by co-authors’ at the beginning of this thesis is appropriate.

PATRICIA F. L. JACOB  
(Full name of Co-Author)



(Signature of Co-Author)

## To Whom It May Concern

I, Jaiverdhan Chauhan, have outlined my contributions and the contributions of the Co-Authors to the chapters in this thesis that have been adapted from published papers (Chapter 3, “An ASKAP distance constraint to MAXI J1535–571”, Chapter 4, “Measuring a kinematic distance to MAXI J1348–630 using the SKA precursors ASKAP and MeerKAT” and Chapter 5, “Using SKA precursors to study the transient jets in MAXI J1535–571”) and to Chapter 6, “Low-frequency MWA detections of compact jets in two black hole XRBs”.



**(Signature of candidate)**

I, as a Co-Author, endorse that the level of contribution indicated by the candidate at in ‘Statement of contribution by co-authors’ at the beginning of this thesis is appropriate.

Rob Fender.

•



**(Full name of Co-Author)**

**(Signature of Co-Author)**

## To Whom It May Concern

I, Jaiverdhan Chauhan, have outlined my contributions and the contributions of the Co-Authors to the chapters in this thesis that have been adapted from published papers (Chapter 3, “An ASKAP distance constraint to MAXI J1535–571”, Chapter 4, “Measuring a kinematic distance to MAXI J1348–630 using the SKA precursors ASKAP and MeerKAT” and Chapter 5, “Using SKA precursors to study the transient jets in MAXI J1535–571”) and to Chapter 6, “Low-frequency MWA detections of compact jets in two black hole XRBs”.



(Signature of candidate)

I, as a Co-Author, endorse that the level of contribution indicated by the candidate at in ‘Statement of contribution by co-authors’ at the beginning of this thesis is appropriate.

S. Corbel

(Full name of Co-Author)



(Signature of Co-Author)

## To Whom It May Concern

I, Jaiverdhan Chauhan, have outlined my contributions and the contributions of the Co-Authors to the chapters in this thesis that have been adapted from published papers (Chapter 3, “An ASKAP distance constraint to MAXI J1535–571”, Chapter 4, “Measuring a kinematic distance to MAXI J1348–630 using the SKA precursors ASKAP and MeerKAT” and Chapter 5, “Using SKA precursors to study the transient jets in MAXI J1535–571”) and to Chapter 6, “Low-frequency MWA detections of compact jets in two black hole XRBs”.

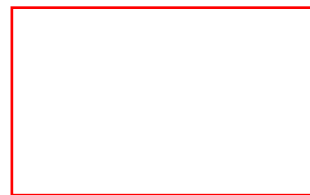


(Signature of candidate)

I, as a Co-Author, endorse that the level of contribution indicated by the candidate at in ‘Statement of contribution by co-authors’ at the beginning of this thesis is appropriate.

*PATRICK ALAN WOODS*

(Full name of Co-Author)



(Signature of Co-Author)

## To Whom It May Concern

I, Jaiverdhan Chauhan, have outlined my contributions and the contributions of the Co-Authors to the chapters in this thesis that have been adapted from published papers (Chapter 3, “An ASKAP distance constraint to MAXI J1535–571”, Chapter 4, “Measuring a kinematic distance to MAXI J1348–630 using the SKA precursors ASKAP and MeerKAT” and Chapter 5, “Using SKA precursors to study the transient jets in MAXI J1535–571”) and to Chapter 6, “Low-frequency MWA detections of compact jets in two black hole XRBs”.

**(Signature of candidate)**

I, as a Co-Author, endorse that the level of contribution indicated by the candidate at in ‘Statement of contribution by co-authors’ at the beginning of this thesis is appropriate.

**(Full name of Co-Author)**

Francesco Carotenuto

**(Signature of Co-Author)**

## To Whom It May Concern

I, Jaiverdhan Chauhan, have outlined my contributions and the contributions of the Co-Authors to the chapters in this thesis that have been adapted from published papers (Chapter 3, “An ASKAP distance constraint to MAXI J1535–571”, Chapter 4, “Measuring a kinematic distance to MAXI J1348–630 using the SKA precursors ASKAP and MeerKAT” and Chapter 5, “Using SKA precursors to study the transient jets in MAXI J1535–571”) and to Chapter 6, “Low-frequency MWA detections of compact jets in two black hole XRBs”.



**(Signature of candidate)**

I, as a Co-Author, endorse that the level of contribution indicated by the candidate at in ‘Statement of contribution by co-authors’ at the beginning of this thesis is appropriate.

David Kaplan

**(Full name of Co-Author)**



**(Signature of Co-Author)**

**To Whom It May Concern**

I, Jaiverdhan Chauhan, have outlined my contributions and the contributions of the Co-Authors to the chapters in this thesis that have been adapted from published papers (Chapter 3, "An ASKAP distance constraint to MAXI J1535-571", Chapter 4, "Measuring a kinematic distance to MAXI J1348-630 using the SKA precursors ASKAP and MeerKAT" and Chapter 5, "Using SKA precursors to study the transient jets in MAXI J1535-571") and to Chapter 6, "Low-frequency MWA detections of compact jets in two black hole XRBs".



(Signature of candidate)

I, as a Co-Author, endorse that the level of contribution indicated by the candidate at in 'Statement of contribution by co-authors' at the beginning of this thesis is appropriate.

HANS A. KRIMM

(Full name of Co-Author)



(Signature of Co-Author)

## To Whom It May Concern

I, Jaiverdhan Chauhan, have outlined my contributions and the contributions of the Co-Authors to the chapters in this thesis that have been adapted from published papers (Chapter 3, "An ASKAP distance constraint to MAXI J1535-571", Chapter 4, "Measuring a kinematic distance to MAXI J1348-630 using the SKA precursors ASKAP and MeerKAT" and Chapter 5, "Using SKA precursors to study the transient jets in MAXI J1535-571") and to Chapter 6, "Low-frequency MWA detections of compact jets in two black hole XRBs".



**(Signature of candidate)**

I, as a Co-Author, endorse that the level of contribution indicated by the candidate at in 'Statement of contribution by co-authors' at the beginning of this thesis is appropriate.

**Diego Altamirano**

**(Full name of Co-Author)**



**(Signature of Co-Author)**

## To Whom It May Concern

I, Jaiverdhan Chauhan, have outlined my contributions and the contributions of the Co-Authors to the chapters in this thesis that have been adapted from published papers (Chapter 3, “An ASKAP distance constraint to MAXI J1535–571”, Chapter 4, “Measuring a kinematic distance to MAXI J1348–630 using the SKA precursors ASKAP and MeerKAT” and Chapter 5, “Using SKA precursors to study the transient jets in MAXI J1535–571”) and to Chapter 6, “Low-frequency MWA detections of compact jets in two black hole XRBs”.



**(Signature of candidate)**

I, as a Co-Author, endorse that the level of contribution indicated by the candidate at in ‘Statement of contribution by co-authors’ at the beginning of this thesis is appropriate.

**Gregory R. Sivakoff**

**(Full name of Co-Author)**



**(Signature of Co-Author)**

## To Whom It May Concern

I, Jaiverdhan Chauhan, have outlined my contributions and the contributions of the Co-Authors to the chapters in this thesis that have been adapted from published papers (Chapter 3, “An ASKAP distance constraint to MAXI J1535–571”, Chapter 4, “Measuring a kinematic distance to MAXI J1348–630 using the SKA precursors ASKAP and MeerKAT” and Chapter 5, “Using SKA precursors to study the transient jets in MAXI J1535–571”) and to Chapter 6, “Low-frequency MWA detections of compact jets in two black hole XRBs”.



**(Signature of candidate)**

I, as a Co-Author, endorse that the level of contribution indicated by the candidate at in ‘Statement of contribution by co-authors’ at the beginning of this thesis is appropriate.

**Stefan William Duchesne**

**(Full name of Co-Author)**



**(Signature of Co-Author)**

## To Whom It May Concern

I, Jaiverdhan Chauhan, have outlined my contributions and the contributions of the Co-Authors to the chapters in this thesis that have been adapted from published papers (Chapter 3, “An ASKAP distance constraint to MAXI J1535–571”, Chapter 4, “Measuring a kinematic distance to MAXI J1348–630 using the SKA precursors ASKAP and MeerKAT” and Chapter 5, “Using SKA precursors to study the transient jets in MAXI J1535–571”) and to Chapter 6, “Low-frequency MWA detections of compact jets in two black hole XRBs”.



**(Signature of candidate)**

I, as a Co-Author, endorse that the level of contribution indicated by the candidate at in ‘Statement of contribution by co-authors’ at the beginning of this thesis is appropriate.

Randall Wayth

**(Full name of Co-Author)**



**(Signature of Co-Author)**

## To Whom It May Concern

I, Jaiverdhan Chauhan, have outlined my contributions and the contributions of the Co-Authors to the chapters in this thesis that have been adapted from published papers (Chapter 3, “An ASKAP distance constraint to MAXI J1535–571”, Chapter 4, “Measuring a kinematic distance to MAXI J1348–630 using the SKA precursors ASKAP and MeerKAT” and Chapter 5, “Using SKA precursors to study the transient jets in MAXI J1535–571”) and to Chapter 6, “Low-frequency MWA detections of compact jets in two black hole XRBs”.



**(Signature of candidate)**

I, as a Co-Author, endorse that the level of contribution indicated by the candidate at in ‘Statement of contribution by co-authors’ at the beginning of this thesis is appropriate.

**Cathryn Margaret Trott**

**(Full name of Co-Author)**



**(Signature of Co-Author)**

## To Whom It May Concern

I, Jaiverdhan Chauhan, have outlined my contributions and the contributions of the Co-Authors to the chapters in this thesis that have been adapted from published papers (Chapter 3, “An ASKAP distance constraint to MAXI J1535–571”, Chapter 4, “Measuring a kinematic distance to MAXI J1348–630 using the SKA precursors ASKAP and MeerKAT” and Chapter 5, “Using SKA precursors to study the transient jets in MAXI J1535–571”) and to Chapter 6, “Low-frequency MWA detections of compact jets in two black hole XRBs”.



(Signature of candidate)

I, as a Co-Author, endorse that the level of contribution indicated by the candidate at in ‘Statement of contribution by co-authors’ at the beginning of this thesis is appropriate.

Steve Croft

(Full name of Co-Author)



(Signature of Co-Author)

## To Whom It May Concern

I, Jaiverdhan Chauhan, have outlined my contributions and the contributions of the Co-Authors to the chapters in this thesis that have been adapted from published papers (Chapter 3, “An ASKAP distance constraint to MAXI J1535–571”, Chapter 4, “Measuring a kinematic distance to MAXI J1348–630 using the SKA precursors ASKAP and MeerKAT” and Chapter 5, “Using SKA precursors to study the transient jets in MAXI J1535–571”) and to Chapter 6, “Low-frequency MWA detections of compact jets in two black hole XRBs”.



**(Signature of candidate)**

I, as a Co-Author, endorse that the level of contribution indicated by the candidate at in ‘Statement of contribution by co-authors’ at the beginning of this thesis is appropriate.

**Vivek Gupta**

**(Full name of Co-Author)**



**(Signature of Co-Author)**

## To Whom It May Concern

I, Jaiverdhan Chauhan, have outlined my contributions and the contributions of the Co-Authors to the chapters in this thesis that have been adapted from published papers (Chapter 3, “An ASKAP distance constraint to MAXI J1535–571”, Chapter 4, “Measuring a kinematic distance to MAXI J1348–630 using the SKA precursors ASKAP and MeerKAT” and Chapter 5, “Using SKA precursors to study the transient jets in MAXI J1535–571”) and to Chapter 6, “Low-frequency MWA detections of compact jets in two black hole XRBs”.



**(Signature of candidate)**

I, as a Co-Author, endorse that the level of contribution indicated by the candidate at in ‘Statement of contribution by co-authors’ at the beginning of this thesis is appropriate.

Alexandra Tetarenko

**(Full name of Co-Author)**



**(Signature of Co-Author)**

## To Whom It May Concern

I, Jaiverdhan Chauhan, have outlined my contributions and the contributions of the Co-Authors to the chapters in this thesis that have been adapted from published papers (Chapter 3, “An ASKAP distance constraint to MAXI J1535–571”, Chapter 4, “Measuring a kinematic distance to MAXI J1348–630 using the SKA precursors ASKAP and MeerKAT” and Chapter 5, “Using SKA precursors to study the transient jets in MAXI J1535–571”) and to Chapter 6, “Low-frequency MWA detections of compact jets in two black hole XRBs”.



(Signature of candidate)

I, as a Co-Author, endorse that the level of contribution indicated by the candidate at in ‘Statement of contribution by co-authors’ at the beginning of this thesis is appropriate.

*Prof Melanie Johnston-Hollitt*

(Full name of Co-Author)



(Signature of Co-Author)

## To Whom It May Concern

I, Jaiverdhan Chauhan, have outlined my contributions and the contributions of the Co-Authors to the chapters in this thesis that have been adapted from published papers (Chapter 3, “An ASKAP distance constraint to MAXI J1535–571”, Chapter 4, “Measuring a kinematic distance to MAXI J1348–630 using the SKA precursors ASKAP and MeerKAT” and Chapter 5, “Using SKA precursors to study the transient jets in MAXI J1535–571”) and to Chapter 6, “Low-frequency MWA detections of compact jets in two black hole XRBs”.



**(Signature of candidate)**

I, as a Co-Author, endorse that the level of contribution indicated by the candidate at in ‘Statement of contribution by co-authors’ at the beginning of this thesis is appropriate.

**Prof. Steven Tingay**

**(Full name of Co-Author)**



**(Signature of Co-Author)**



# Bibliography

- B. P. Abbott, et al. (2016). ‘Observation of Gravitational Waves from a Binary Black Hole Merger’. **116**(6):061102.
- J. G. Ables & R. N. Manchester (1976). ‘Hydrogen-line absorption observations of distant pulsars.’. *Astronomy and Astrophysics* **50**:177–184.
- M. A. Abramowicz, et al. (1995). ‘Thermal Equilibria of Accretion Disks’. *The Astrophysical Journal Letters* **438**:L37.
- J. R. Allison, et al. (2017). ‘Illuminating the past 8 billion years of cold gas towards two gravitationally lensed quasars’. *Monthly Notices of the Royal Astronomical Society* **465**(4):4450–4467.
- J. R. Allison, et al. (2015). ‘Discovery of H I gas in a young radio galaxy at  $z = 0.44$  using the Australian Square Kilometre Array Pathfinder’. *Monthly Notices of the Royal Astronomical Society* **453**(2):1249–1267.
- S. Ananthakrishnan (1995). ‘The Giant Meterwave Radio Telescope / GMRT’. *Journal of Astrophysics and Astronomy Supplement* **16**:427.
- B. Anderson, et al. (1972). ‘Observations at 408 MHz of the Cyg X-3 Radio Outburst’. *Nature Physical Science* **239**(95):117–118.
- G. E. Anderson, et al. (2017). ‘The peculiar mass-loss history of SN 2014C as revealed through AMI radio observations’. *Monthly Notices of the Royal Astronomical Society* **466**(3):3648–3662.

- G. E. Anderson, et al. (2019a). ‘Discovery of a radio transient in M81’. *Monthly Notices of the Royal Astronomical Society* **489**(1):1181–1196.
- M. M. Anderson, et al. (2019b). ‘New Limits on the Low-frequency Radio Transient Sky Using 31 hr of All-sky Data with the OVRO-LWA’. *The Astrophysical Journal* **886**(2):123.
- R. Athreya (2009). ‘A New Approach to Mitigation of Radio Frequency Interference in Interferometric Data’. *The Astrophysical Journal* **696**(1):885–890.
- P. Atri, et al. (2020). ‘A radio parallax to the black hole X-ray binary MAXI J1820+070’. *Monthly Notices of the Royal Astronomical Society* **493**(1):L81–L86.
- J. W. M. Baars, et al. (2009). ‘Radio Astronomy in the Early Twenty-First Century (Invited Paper)’. *IEEE Proceedings* **97**(8):1377–1381.
- J. W. M. Baars, et al. (1977). ‘Reprint of 1977A&A....61...99B. The absolute spectrum of Cas A; an accurate flux density scale and a set of secondary calibrators.’. *Astronomy and Astrophysics* **500**:135–142.
- M. C. Baglio, et al. (2016). ‘1RXS J180408.9-342058: An ultra compact X-ray binary candidate with a transient jet’. *Astronomy and Astrophysics* **587**:A102.
- A. Bahramian, et al. (2015). ‘Limits on thermal variations in a dozen quiescent neutron stars over a decade’. *Monthly Notices of the Royal Astronomical Society* **452**(4):3475–3488.
- A. Bahramian, et al. (2018). ‘Radio/X-ray correlation database for X-ray binaries’.
- M. Bailes, et al. (2017). ‘The UTMOST: A Hybrid Digital Signal Processor Transforms the Molonglo Observatory Synthesis Telescope’. *Publications of the Astronomical Society of Australia* **34**:e045.

- C. Barnbaum & R. F. Bradley (1998). ‘A New Approach to Interference Excision in Radio Astronomy: Real-Time Adaptive Cancellation’. *The Astronomical Journal* **116**(5):2598–2614.
- S. D. Barthelmy, et al. (2005). ‘The Burst Alert Telescope (BAT) on the SWIFT Midex Mission’. *Space Science Reviews* **120**(3-4):143–164.
- S. D. Barthelmy, et al. (2015). ‘Swift trigger 643949 is V404 Cyg.’. *GRB Coordinates Network* **17929**:1.
- F. N. Bash & F. D. Ghigo (1973). ‘Recent Observations of Cyg X-3 at 365 MHz’. *Nature Physical Science* **241**(109):93–94.
- M. C. Begelman & P. J. Armitage (2014). ‘A Mechanism for Hysteresis in Black Hole Binary State Transitions’. *The Astrophysical Journal Letters* **782**(2):L18.
- M. C. Begelman, et al. (1984). ‘Theory of extragalactic radio sources’. *Reviews of Modern Physics* **56**(2):255–351.
- A. R. Bell (1978). ‘The acceleration of cosmic rays in shock fronts - I.’. *Monthly Notices of the Royal Astronomical Society* **182**:147–156.
- M. E. Bell, et al. (2019). ‘The Murchison Widefield Array Transients Survey (MWATS). A search for low-frequency variability in a bright Southern hemisphere sample’. *Monthly Notices of the Royal Astronomical Society* **482**(2):2484–2501.
- M. E. Bell, et al. (2014). ‘A survey for transients and variables with the Murchison Widefield Array 32-tile prototype at 154 MHz’. *Monthly Notices of the Royal Astronomical Society* **438**(1):352–367.
- E. C. Bellm, et al. (2019). ‘The Zwicky Transient Facility: System Overview, Performance, and First Results’. **131**(995):018002.

- T. Belloni, et al. (2005). ‘The evolution of the timing properties of the black-hole transient GX 339-4 during its 2002/2003 outburst’. *Astronomy and Astrophysics* **440**(1):207–222.
- T. M. Belloni (2010). *States and Transitions in Black Hole Binaries*, vol. 794, p. 53.
- R. D. Blandford & M. C. Begelman (1999). ‘On the fate of gas accreting at a low rate on to a black hole’. *Monthly Notices of the Royal Astronomical Society* **303**(1):L1–L5.
- R. D. Blandford & D. G. Payne (1982). ‘Hydromagnetic flows from accretion disks and the production of radio jets.’. *Monthly Notices of the Royal Astronomical Society* **199**:883–903.
- R. D. Blandford & R. L. Znajek (1977). ‘Electromagnetic extraction of energy from Kerr black holes.’. *Monthly Notices of the Royal Astronomical Society* **179**:433–456.
- G. C. Bower, et al. (2007). ‘Submillijansky Transients in Archival Radio Observations’. *The Astrophysical Journal* **666**(1):346–360.
- E. Bozzo, et al. (2018). ‘INTEGRAL observations of MAXI J1820+070’. *The Astronomer’s Telegram* **11478**:1.
- T. R. Bradley, et al. (2006). ‘A composite H ii region luminosity function in H $\alpha$  of unprecedented statistical weight’. *Astronomy and Astrophysics* **459**(1):L13–L16.
- N. J. B. A. Branson, et al. (1972). ‘Observations of Cygnus X-3 at the Mullard Radio Astronomy Observatory’. *Nature Physical Science* **239**(95):133–134.
- D. S. Briggs (1995). ‘High Fidelity Interferometric Imaging: Robust Weighting and NNLS Deconvolution’. In *American Astronomical Society Meeting*

*Abstracts*, vol. 187 of *American Astronomical Society Meeting Abstracts*, p. 112.02.

- F. H. Briggs, et al. (2000). ‘Removing Radio Interference from Contaminated Astronomical Spectra Using an Independent Reference Signal and Closure Relations’. *The Astronomical Journal* **120**(6):3351–3361.
- J. Bright, et al. (2018). ‘AMI radio observations of the black hole candidate MAXI J1820+070’. *The Astronomer’s Telegram* **11420**:1.
- J. S. Bright, et al. (2020). ‘An extremely powerful long-lived superluminal ejection from the black hole MAXI J1820+070’. *Nature Astronomy* **4**:697–703.
- C. Brocksopp, et al. (2013). ‘XTE J1752-223 in outburst: a persistent radio jet, dramatic flaring, multiple ejections and linear polarization’. *Monthly Notices of the Royal Astronomical Society* **432**(2):931–943.
- J. Broderick, et al. (2018a). ‘Simultaneous LOFAR and AMI-LA observations of MAXI J1820+070’. *The Astronomer’s Telegram* **11609**:1.
- J. Broderick, et al. (2015). ‘LOFAR detection of V404 Cyg at 150 MHz’. *The Astronomer’s Telegram* **7720**:1.
- J. W. Broderick, et al. (2018b). ‘LOFAR 150-MHz observations of SS 433 and W 50’. *Monthly Notices of the Royal Astronomical Society* **475**(4):5360–5377.
- D. J. K. Buisson, et al. (2021). ‘MAXI J1820+070 with NuSTAR - II. Flaring during the hard to soft state transition with a long soft lag’. *Monthly Notices of the Royal Astronomical Society* **500**(3):3976–3986.
- J. R. Callingham, et al. (2015). ‘Broadband Spectral Modeling of the Extreme Gigahertz-peaked Spectrum Radio Source PKS B0008-421’. *The Astrophysical Journal* **809**(2):168.

- F. Camilo, et al. (2018). ‘Revival of the Magnetar PSR J1622-4950: Observations with MeerKAT, Parkes, XMM-Newton, Swift, Chandra, and NuSTAR’. *The Astrophysical Journal* **856**(2):180.
- J. Caplan & L. Deharveng (1986). ‘Extinction and reddening of H II regions in the Large Magellanic Cloud.’. *Astronomy and Astrophysics* **155**:297–313.
- F. Carotenuto, et al. (2021a). ‘The black hole transient MAXI J1348-630: evolution of the compact and transient jets during its 2019/2020 outburst’. *Monthly Notices of the Royal Astronomical Society* .
- F. Carotenuto, et al. (2021b). ‘The hybrid radio/X-ray correlation of the black hole transient MAXI J1348-630’. *arXiv e-prints* .
- F. Carotenuto, et al. (2019). ‘MeerKAT follow-up observations of MAXI J1348-630 reveal bright radio flare at state transition’. *ATel* **12497**:1.
- B. W. Carroll & D. A. Ostlie (2017). *An introduction to modern astrophysics*. Cambridge University Press.
- P. Casella, et al. (2010). ‘Fast infrared variability from a relativistic jet in GX 339-4’. *Monthly Notices of the Royal Astronomical Society* **404**(1):L21–L25.
- P. Chandra & D. A. Frail (2012). ‘A Radio-selected Sample of Gamma-Ray Burst Afterglows’. *The Astrophysical Journal* **746**(2):156.
- P. Chandra & N. Kanekar (2017). ‘Giant Metrewave Radio Telescope Monitoring of the Black Hole X-Ray Binary, V404 Cygni during Its 2015 June Outburst’. *The Astrophysical Journal* **846**(2):111.
- J. Chauhan, et al. (2019a). ‘Low-frequency radio detection of MAXI J1348-630 with the MWA’. *The Astronomer’s Telegram* **12520**:1.
- J. Chauhan, et al. (2019b). ‘An H I absorption distance to the black hole candidate X-ray binary MAXI J1535-571’. *Monthly Notices of the Royal Astronomical Society* p. L116.

- J. Chauhan, et al. (2021). ‘Measuring the distance to the black hole candidate X-ray binary MAXI J1348-630 using H I absorption’. *Monthly Notices of the Royal Astronomical Society* **501**(1):L60–L64.
- B. G. Clark (1980). ‘An efficient implementation of the algorithm ‘CLEAN’’. *Astronomy and Astrophysics* **89**(3):377.
- B. G. Clark (1999). ‘Coherence in Radio Astronomy’. In G. B. Taylor, C. L. Carilli, & R. A. Perley (eds.), *Synthesis Imaging in Radio Astronomy II*, vol. 180 of *Astronomical Society of the Pacific Conference Series*, p. 1.
- T. E. Clarke, et al. (2016). ‘Commensal low frequency observing on the NRAO VLA: VLITE status and future plans’. In H. J. Hall, R. Gilmozzi, & H. K. Marshall (eds.), *Ground-based and Airborne Telescopes VI*, vol. 9906 of *Society of Photo-Optical Instrumentation Engineers (SPIE) Conference Series*, p. 99065B.
- A. S. Cohen, et al. (2007). ‘The VLA Low-Frequency Sky Survey’. *The Astronomical Journal* **134**(3):1245–1262.
- J. J. Condon, et al. (1998). ‘The NRAO VLA Sky Survey’. *The Astronomical Journal* **115**(5):1693–1716.
- S. Corbel, et al. (2013). ‘The ‘universal’ radio/X-ray flux correlation: the case study of the black hole GX 339-4’. *Monthly Notices of the Royal Astronomical Society* **428**(3):2500–2515.
- S. Corbel & R. P. Fender (2002). ‘Near-Infrared Synchrotron Emission from the Compact Jet of GX 339-4’. *The Astrophysical Journal Letters* **573**(1):L35–L39.
- S. Corbel, et al. (2000). ‘Coupling of the X-ray and radio emission in the black hole candidate and compact jet source GX 339-4’. *Astronomy and Astrophysics* **359**:251–268.

- S. Corbel, et al. (2015). ‘Incoherent transient radio emission from stellar-mass compact objects in the SKA era’. In *Advancing Astrophysics with the Square Kilometre Array (AASKA14)*, p. 53.
- S. Corbel, et al. (2003). ‘Radio/X-ray correlation in the low/hard state of GX 339-4’. *Astronomy and Astrophysics* **400**:1007–1012.
- J. M. Cordes, et al. (2004). ‘The Brightest Pulses in the Universe: Multifrequency Observations of the Crab Pulsar’s Giant Pulses’. *The Astrophysical Journal* **612**(1):375–388.
- T. Cornwell & E. B. Fomalont (1999). ‘Self-Calibration’. In G. B. Taylor, C. L. Carilli, & R. A. Perley (eds.), *Synthesis Imaging in Radio Astronomy II*, vol. 180 of *Astronomical Society of the Pacific Conference Series*, p. 187.
- T. Cornwell, et al. (2003). ‘EVLA Memo# 67 W Projection: A New Algorithm for Non-Coplanar Baselines’ .
- T. J. Cornwell, et al. (2005). ‘W Projection: A New Algorithm for Wide Field Imaging with Radio Synthesis Arrays’. In P. Shopbell, M. Britton, & R. Ebert (eds.), *Astronomical Data Analysis Software and Systems XIV*, vol. 347 of *Astronomical Society of the Pacific Conference Series*, p. 86.
- T. J. Cornwell, et al. (2008). ‘The Noncoplanar Baselines Effect in Radio Interferometry: The W-Projection Algorithm’. *IEEE Journal of Selected Topics in Signal Processing* **2**(5):647–657.
- T. J. Cornwell, et al. (2012). ‘Wide field imaging for the square kilometre array’. In P. J. Bones, M. A. Fiddy, & R. P. Millane (eds.), *Image Reconstruction from Incomplete Data VII*, vol. 8500 of *Society of Photo-Optical Instrumentation Engineers (SPIE) Conference Series*, p. 85000L.
- J. M. Corral-Santana, et al. (2016). ‘BlackCAT: A catalogue of stellar-mass black holes in X-ray transients’. *Astronomy and Astrophysics* **587**:A61.

- F. Coti Zelati, et al. (2021). ‘The New Magnetar SGR J1830-0645 in Outburst’. *The Astrophysical Journal Letters* **907**(2):L34.
- J. H. Croston, et al. (2018). ‘Particle content, radio-galaxy morphology, and jet power: all radio-loud AGN are not equal’. *Monthly Notices of the Royal Astronomical Society* **476**(2):1614–1623.
- P. Curran, et al. (2010). ‘Swift observations of black hole candidate, XTE J1752-223, during outburst’. In *Eighth Integral Workshop. The Restless Gamma-ray Universe (INTEGRAL 2010)*, p. 146.
- W. W. Dalton & C. L. Sarazin (1995). ‘High-Mass X-Ray Binary Populations. I. Galactic Modeling’. *The Astrophysical Journal* **440**:280.
- E. W. J. G. de Blok, et al. (2010). ‘An update on MeerKAT developments’. In J. van Leeuwen (ed.), *ISKAF2010 Science Meeting*, p. 5.
- M. Del Santo & A. Segreto (2018). ‘The hard X-ray spectrum of MAXI J1820+070 observed by Swift/BAT’. *The Astronomer’s Telegram* **11427**:1.
- A. T. Deller, et al. (2011). ‘DiFX-2: A More Flexible, Efficient, Robust, and Powerful Software Correlator’. **123**(901):275.
- A. T. Deller, et al. (2009). ‘Precision Southern Hemisphere VLBI Pulsar Astrometry. II. Measurement of Seven Parallaxes’. *The Astrophysical Journal* **701**(2):1243–1257.
- A. T. Deller, et al. (2007). ‘DiFX: A Software Correlator for Very Long Baseline Interferometry Using Multiprocessor Computing Environments’. **119**(853):318–336.
- A. T. Deller, et al. (2008). ‘Extremely High Precision VLBI Astrometry of PSR J0437-4715 and Implications for Theories of Gravity’. *The Astrophysical Journal Letters* **685**(1):L67.

- H. Dénes, et al. (2018). ‘Calibrating the HISA temperature: Measuring the temperature of the Riegel-Crutcher cloud’. *Monthly Notices of the Royal Astronomical Society* **479**(2):1465–1490.
- D. Denisenko (2018). ‘Optical follow-up of MAXI J1820+070 and possible identity with ASASSN-18ey’. *The Astronomer’s Telegram* **11400**:1.
- D. Denisenko, et al. (2019). ‘Optical counterpart of MAXI J1348-630’. *ATel* **12430**:1.
- V. Dhawan, et al. (2000). ‘AU-Scale Synchrotron Jets and Superluminal Ejecta in GRS 1915+105’. *The Astrophysical Journal* **543**(1):373–385.
- J. M. Dickey (1983). ‘A new distance to Cygnus X-3.’. *The Astrophysical Journal Letters* **273**:L71–L73.
- T. Dinçer (2017). ‘The near-infrared counterpart of X-ray transient MAXI J1535-571’. *The Astronomer’s Telegram* **10716**:1.
- M. A. Dopita, et al. (2006). ‘Compact H II Regions: What Lies Within?’. *The Astrophysical Journal* **639**(2):788–802.
- L. O. Drury (1983). ‘REVIEW ARTICLE: An introduction to the theory of diffusive shock acceleration of energetic particles in tenuous plasmas’. *Reports on Progress in Physics* **46**(8):973–1027.
- G. Dubus, et al. (2001). ‘The disc instability model for X-ray transients: Evidence for truncation and irradiation’. *Astronomy and Astrophysics* **373**:251–271.
- S. W. Duchesne, et al. (2020). ‘Murchison Widefield Array detection of steep-spectrum, diffuse, non-thermal radio emission within Abell 1127’. *Publications of the Astronomical Society of Australia* **37**:e037.
- P. Edwards (2012). ‘Fifty Years in Fifteen Minutes: The Impact of the Parkes Observatory’. *arXiv e-prints* p. arXiv:1210.2138.

- EHT MWL Science Working Group, et al. (2021). ‘Broadband Multi-wavelength Properties of M87 during the 2017 Event Horizon Telescope Campaign’. *The Astrophysical Journal Letters* **911**(1):L11.
- S. W. Ellingson, et al. (2009). ‘The Long Wavelength Array’. *IEEE Proceedings* **97**(8):1421–1430.
- A. A. Esin, et al. (1997). ‘Advection-Dominated Accretion and the Spectral States of Black Hole X-Ray Binaries: Application to Nova Muscae 1991’. *The Astrophysical Journal* **489**(2):865–889.
- M. Espinasse, et al. (2021). ‘MeerKAT radio detection of MAXI J1803-298’. *The Astronomer’s Telegram* **14607**:1.
- M. Espinasse, et al. (2020). ‘Relativistic X-Ray Jets from the Black Hole X-Ray Binary MAXI J1820+070’. *The Astrophysical Journal Letters* **895**(2):L31.
- Event Horizon Telescope Collaboration, et al. (2019a). ‘First M87 Event Horizon Telescope Results. VI. The Shadow and Mass of the Central Black Hole’. *The Astrophysical Journal Letters* **875**(1):L6.
- Event Horizon Telescope Collaboration, et al. (2019b). ‘First M87 Event Horizon Telescope Results. V. Physical Origin of the Asymmetric Ring’. *The Astrophysical Journal Letters* **875**(1):L5.
- Event Horizon Telescope Collaboration, et al. (2019c). ‘First M87 Event Horizon Telescope Results. IV. Imaging the Central Supermassive Black Hole’. *The Astrophysical Journal Letters* **875**(1):L4.
- Event Horizon Telescope Collaboration, et al. (2019d). ‘First M87 Event Horizon Telescope Results. III. Data Processing and Calibration’. *The Astrophysical Journal Letters* **875**(1):L3.

- Event Horizon Telescope Collaboration, et al. (2019e). ‘First M87 Event Horizon Telescope Results. II. Array and Instrumentation’. *The Astrophysical Journal Letters* **875**(1):L2.
- Event Horizon Telescope Collaboration, et al. (2019f). ‘First M87 Event Horizon Telescope Results. I. The Shadow of the Supermassive Black Hole’. *The Astrophysical Journal Letters* **875**(1):L1.
- H. Falcke & P. L. Biermann (1995). ‘The jet-disk symbiosis. I. Radio to X-ray emission models for quasars.’. *Astronomy and Astrophysics* **293**:665–682.
- H. Falcke, et al. (2004). ‘A scheme to unify low-power accreting black holes. Jet-dominated accretion flows and the radio/X-ray correlation’. *Astronomy and Astrophysics* **414**:895–903.
- R. Fender (2006). *Jets from X-ray binaries*, vol. 39, pp. 381–419.
- R. Fender (2010). ‘Disc-Jet’ Coupling in Black Hole X-Ray Binaries and Active Galactic Nuclei, vol. 794, p. 115.
- R. Fender & J. Bright (2019). ‘Synchrotron self-absorption and the minimum energy of optically thick radio flares from stellar mass black holes’. *Monthly Notices of the Royal Astronomical Society* **489**(4):4836–4846.
- R. Fender & E. Gallo (2014). ‘An Overview of Jets and Outflows in Stellar Mass Black Holes’. *Space Science Reviews* **183**(1-4):323–337.
- R. Fender, et al. (2016). ‘ThunderKAT: The MeerKAT Large Survey Project for Image-Plane Radio Transients’. In *MeerKAT Science: On the Pathway to the SKA*, p. 13.
- R. P. Fender (2001). ‘Powerful jets from black hole X-ray binaries in low/hard X-ray states’. *Monthly Notices of the Royal Astronomical Society* **322**(1):31–42.

- R. P. Fender (2003). ‘Uses and limitations of relativistic jet proper motions: lessons from Galactic microquasars’. *Monthly Notices of the Royal Astronomical Society* **340**(4):1353–1358.
- R. P. Fender, et al. (1995). ‘Simultaneous millimetre and radio observations of Cygnus X-3 in a quiescent radio state’. *Monthly Notices of the Royal Astronomical Society* **274**(2):633–638.
- R. P. Fender, et al. (2004). ‘Towards a unified model for black hole X-ray binary jets’. *Monthly Notices of the Royal Astronomical Society* **355**(4):1105–1118.
- R. P. Fender, et al. (1999). ‘MERLIN observations of relativistic ejections from GRS 1915+105’. *Monthly Notices of the Royal Astronomical Society* **304**(4):865–876.
- R. P. Fender, et al. (2009). ‘Jets from black hole X-ray binaries: testing, refining and extending empirical models for the coupling to X-rays’. *Monthly Notices of the Royal Astronomical Society* **396**(3):1370–1382.
- R. P. Fender, et al. (1997). ‘Rapid infrared flares in GRS 1915+105: evidence for infrared synchrotron emission’. *Monthly Notices of the Royal Astronomical Society* **290**(4):L65–L69.
- R. P. Fender, et al. (2000). ‘The very flat radio-millimetre spectrum of Cygnus X-1’. *Monthly Notices of the Royal Astronomical Society* **312**(4):853–858.
- C. Fendt & S. Sheikhnezami (2013). ‘Bipolar Jets Launched from Accretion Disks. II. The Formation of Asymmetric Jets and Counter Jets’. *The Astrophysical Journal* **774**(1):12.
- A. Ferrari (1998). ‘Modeling Extragalactic Jets’. *Annual Review of Astronomy and Astrophysics* **36**:539–598.
- D. P. Finkbeiner (2003). ‘A Full-Sky H $\alpha$  Template for Microwave Foreground Prediction’. *The Astrophysical Journal Supplement Series* **146**(2):407–415.

- D. R. Foight, et al. (2016). ‘Probing X-Ray Absorption and Optical Extinction in the Interstellar Medium Using Chandra Observations of Supernova Remnants’. *The Astrophysical Journal* **826**(1):66.
- E. B. Fomalont & R. A. Perley (1999). ‘Calibration and Editing’. In G. B. Taylor, C. L. Carilli, & R. A. Perley (eds.), *Synthesis Imaging in Radio Astronomy II*, vol. 180 of *Astronomical Society of the Pacific Conference Series*, p. 79.
- J. Frank, et al. (2002). *Accretion Power in Astrophysics: Third Edition*.
- R. H. Frater, et al. (1992). ‘The Australia Telescope - Overview’. *Journal of Electrical and Electronics Engineering Australia* **12**(2):103–112.
- P. A. Fridman & W. A. Baan (2001). ‘RFI mitigation methods in radio astronomy’. *Astronomy and Astrophysics* **378**:327–344.
- J. Fukue (2004). ‘Critical Accretion Disk’. **56**:569–580.
- Gaia Collaboration, et al. (2018). ‘Gaia Data Release 2. Summary of the contents and survey properties’. *Astronomy and Astrophysics* **616**:A1.
- Gaia Collaboration, et al. (2020). ‘Gaia Early Data Release 3: Summary of the contents and survey properties’. *arXiv e-prints* p. arXiv:2012.01533.
- E. Gallo, et al. (2005). ‘A dark jet dominates the power output of the stellar black hole Cygnus X-1’. *Nature* **436**(7052):819–821.
- E. Gallo, et al. (2003). ‘A universal radio-X-ray correlation in low/hard state black hole binaries’. *Monthly Notices of the Royal Astronomical Society* **344**(1):60–72.
- E. Gallo, et al. (2007). ‘The Spectral Energy Distribution of Quiescent Black Hole X-Ray Binaries: New Constraints from Spitzer’. *The Astrophysical Journal* **670**(1):600–609.

- E. Gallo, et al. (2012). ‘Assessing luminosity correlations via cluster analysis: evidence for dual tracks in the radio/X-ray domain of black hole X-ray binaries’. *Monthly Notices of the Royal Astronomical Society* **423**(1):590–599.
- E. Gallo, et al. (2014). ‘The radio/X-ray domain of black hole X-ray binaries at the lowest radio luminosities’. *Monthly Notices of the Royal Astronomical Society* **445**(1):290–300.
- P. Gandhi, et al. (2011). ‘A Variable Mid-infrared Synchrotron Break Associated with the Compact Jet in GX 339-4’. *The Astrophysical Journal Letters* **740**(1):L13.
- P. Gandhi, et al. (2018). ‘Red sub-second optical flaring in MAXI J1820+070 observed by ULTRACAM/NTT’. *The Astronomer’s Telegram* **11437**:1.
- P. Gandhi, et al. (2019). ‘Gaia Data Release 2 distances and peculiar velocities for Galactic black hole transients’. *Monthly Notices of the Royal Astronomical Society* **485**(2):2642–2655.
- R. Gathier, et al. (1986). ‘Distances to planetary nebulae. II. HI absorption observations.’. *Astronomy and Astrophysics* **157**:191–203.
- J. E. Gaustad, et al. (2001). ‘A Robotic Wide-Angle H $\alpha$  Survey of the Southern Sky’. **113**(789):1326–1348.
- N. Gehrels, et al. (2004). ‘The Swift Gamma-Ray Burst Mission’. *The Astrophysical Journal* **611**(2):1005–1020.
- K. Golap, et al. (2005). ‘Post Correlation RFI Excision’. In N. Kassim, M. Perez, W. Junor, & P. Henning (eds.), *From Clark Lake to the Long Wavelength Array: Bill Erickson’s Radio Science*, vol. 345 of *Astronomical Society of the Pacific Conference Series*, p. 366.
- W. M. Goss & U. Mebold (1977). ‘The distance of Cir X-1.’. *Monthly Notices of the Royal Astronomical Society* **181**:255–258.

- P. C. Gregory & E. R. Seaquist (1974). ‘The nature of Cygnus X-3 radio outbursts from an analysis of radiofrequency spectra.’ *The Astrophysical Journal* **194**:715–723.
- E. W. Greisen (2003). *AIPS, the VLA, and the VLBA*, vol. 285 of *Astrophysics and Space Science Library*, p. 109.
- M. R. Griffith & A. E. Wright (1993). ‘The Parkes-MIT-NRAO (PMN) Survey. I. The 1450 MHz Surveys and Data Reduction’. *The Astronomical Journal* **105**:1666.
- N. Gupta, et al. (2021). ‘Blind H I and OH Absorption Line Search: First Results with MALS and uGMRT Processed Using ARTIP’. *The Astrophysical Journal* **907**(1):11.
- Y. Gupta, et al. (2017). ‘The upgraded GMRT: opening new windows on the radio Universe’. *Current Science* **113**(4):707–714.
- J. Guzman, et al. (2019). ‘ASKAPsoft: ASKAP science data processor software’.
- F. Haardt & L. Maraschi (1991). ‘A Two-Phase Model for the X-Ray Emission from Seyfert Galaxies’. *The Astrophysical Journal Letters* **380**:L51.
- F. Haardt & L. Maraschi (1993). ‘X-Ray Spectra from Two-Phase Accretion Disks’. *The Astrophysical Journal* **413**:507.
- A. Hajela, et al. (2019). ‘A GMRT 150 MHz search for variables and transients in Stripe 82’. *Monthly Notices of the Royal Astronomical Society* **490**(4):4898–4906.
- G. Hallinan, et al. (2017). ‘A radio counterpart to a neutron star merger’. *Science* **358**(6370):1579–1583.
- G. Hampson, et al. (2012). ‘ASKAP PAF ADE — Advancing an L-band PAF design towards SKA’. In *2012 International Conference on Electromagnetics in Advanced Applications*, pp. 807–809.

- X. Han & R. M. Hjellming (1992). ‘Radio Observations of the 1989 Transient Event in V404 Cygni (= GS 2023+338)’. *The Astrophysical Journal* **400**:304.
- P. J. Hancock, et al. (2019). ‘ROBBIE: A batch processing work-flow for the detection of radio transients and variables’. *Astronomy and Computing* **27**:23.
- C. G. T. Haslam, et al. (1981). ‘A 408 MHz all-sky continuum survey. I - Observations at southern declinations and for the North Polar region.’. *Astronomy and Astrophysics* **100**:209–219.
- C. G. T. Haslam, et al. (1982). ‘A 408 MHz all-sky continuum survey. II. The atlas of contour maps.’. *Astronomy and Astrophysics Supplement Series* **47**:1–143.
- S. Heinz (2002). ‘Radio lobe dynamics and the environment of microquasars’. *Astronomy and Astrophysics* **388**:L40–L43.
- S. Heinz (2006). ‘Composition, Collimation, Contamination: The Jet of Cygnus X-1’. *The Astrophysical Journal* **636**(1):316–322.
- S. Heinz (2008). ‘Clues for the Composition of Relativistic Microquasar Jets’. *International Journal of Modern Physics D* **17**(10):1947–1952.
- S. Heinz & R. A. Sunyaev (2003). ‘The non-linear dependence of flux on black hole mass and accretion rate in core-dominated jets’. *Monthly Notices of the Royal Astronomical Society* **343**(3):L59–L64.
- G. Hellborg, et al. (2014). ‘Reference antenna-based subspace tracking for RFI mitigation in radio astronomy’. In *Signal and Information Processing (Global-SIP)*, pp. 1286–1290.
- R. M. Hjellming & B. Balick (1972). ‘More Unusual Radio Events in Cygnus X-3’. *Nature Physical Science* **239**(95):135–136.
- R. M. Hjellming & K. J. Johnston (1988). ‘Radio Emission from Conical Jets Associated with X-Ray Binaries’. *The Astrophysical Journal* **328**:600.

- R. M. Hjellming & M. P. Rupen (1995). ‘Episodic ejection of relativistic jets by the X-ray transient GRO J1655 - 40’. *Nature* **375**(6531):464–468.
- L. C. Ho (1999). ‘The Spectral Energy Distributions of Low-Luminosity Active Galactic Nuclei’. *The Astrophysical Journal* **516**(2):672–682.
- G. Hobbs, et al. (2020). ‘An ultra-wide bandwidth (704 to 4 032 MHz) receiver for the Parkes radio telescope’. *Publications of the Astronomical Society of Australia* **37**:e012.
- J. A. Högbom (1974). ‘Aperture Synthesis with a Non-Regular Distribution of Interferometer Baselines’. *Astronomy and Astrophysics Supplement Series* **15**:417.
- J. Homan, et al. (2020). ‘A Rapid Change in X-Ray Variability and a Jet Ejection in the Black Hole Transient MAXI J1820+070’. *The Astrophysical Journal Letters* **891**(2):L29.
- A. W. Hotan, et al. (2021). ‘Australian square kilometre array pathfinder: I. system description’. *Publications of the Astronomical Society of Australia* **38**:e009.
- A. W. Hotan, et al. (2014). ‘The Australian Square Kilometre Array Pathfinder: System Architecture and Specifications of the Boolardy Engineering Test Array’. *Publications of the Astronomical Society of Australia* **31**:e041.
- B. Humphreys & T. Cornwell (2011). ‘Analysis of convolutional resampling algorithm performance’. *SKA Memo* **132**.
- L. K. Hunt & H. Hirashita (2009). ‘The size-density relation of extragalactic H II regions’. *Astronomy and Astrophysics* **507**(3):1327–1343.
- N. Hurley-Walker, et al. (2017). ‘GaLactic and Extragalactic All-sky Murchison Widefield Array (GLEAM) survey - I. A low-frequency extragalactic catalogue’. *Monthly Notices of the Royal Astronomical Society* **464**(1):1146–1167.

- N. Hurley-Walker & P. J. Hancock (2018). ‘De-distorting ionospheric effects in the image plane’. *Astronomy and Computing* **25**:94–102.
- N. Hurley-Walker, et al. (2019). ‘GaLactic and Extragalactic All-sky Murchison Widefield Array (GLEAM) survey II: Galactic plane  $345^\circ \leq l \leq 67^\circ$ ,  $180^\circ \leq b \leq 240^\circ$ ’. *Publications of the Astronomical Society of Australia* **36**:e047.
- S. D. Hyman, et al. (2005). ‘A powerful bursting radio source towards the Galactic Centre’. *Nature* **434**(7029):50–52.
- J. Iben, Icko, et al. (1995a). ‘A Model of the Galactic X-Ray Binary Population. I. High-Mass X-Ray Binaries’. *The Astrophysical Journal Supplement Series* **100**:217.
- J. Iben, Icko, et al. (1995b). ‘A Model of the Galactic X-Ray Binary Population. II. Low-Mass X-Ray Binaries in the Galactic Disk’. *The Astrophysical Journal Supplement Series* **100**:233.
- S. Ichimaru (1977). ‘Bimodal behavior of accretion disks: theory and application to Cygnus X-1 transitions.’. *The Astrophysical Journal* **214**:840–855.
- A. F. Illarionov & R. A. Sunyaev (1975). ‘Why the Number of Galactic X-ray Stars Is so Small?’. *Astronomy and Astrophysics* **39**:185.
- H. T. Intema, et al. (2017). ‘The GMRT 150 MHz all-sky radio survey. First alternative data release TGSS ADR1’. *Astronomy and Astrophysics* **598**:A78.
- T. R. Jaeger, et al. (2012). ‘Discovery of a Meter-wavelength Radio Transient in the SWIRE Deep Field: 1046+59’. *The Astronomical Journal* **143**(4):96.
- O. Jamil, et al. (2010). ‘iShocks: X-ray binary jets with an internal shocks model’. *Monthly Notices of the Royal Astronomical Society* **401**(1):394–404.
- M. Janssen, et al. (2021). ‘Event Horizon Telescope observations of the jet launching and collimation in Centaurus A’. *Nature Astronomy* **5**:1017–1028.

- D. L. Jauncey, et al. (1994). ‘The Southern Hemisphere VLBI Experiment program, SHEVE’. In J. G. Robertson & W. J. Tango (eds.), *Very High Angular Resolution Imaging*, vol. 158 of *IAU Symposium 158*, pp. 131–134.
- S. Johnston, et al. (2007). ‘Science with the Australian Square Kilometre Array Pathfinder’. *Publications of the Astronomical Society of Australia* **24**(4):174–188.
- J. Jonas & MeerKAT Team (2016). ‘The MeerKAT Radio Telescope’. In *MeerKAT Science: On the Pathway to the SKA*, p. 1.
- P. G. Jonker & G. Nelemans (2004). ‘The distances to Galactic low-mass X-ray binaries: consequences for black hole luminosities and kicks’. *Monthly Notices of the Royal Astronomical Society* **354**(2):355–366.
- C. R. Kaiser, et al. (2004). ‘Revision of the Properties of the GRS 1915+105 Jets: Clues from the Large-Scale Structure’. *The Astrophysical Journal* **612**(1):332–341.
- E. Kalemci, et al. (2013). ‘Complete Multiwavelength Evolution of Galactic Black Hole Transients during Outburst Decay. I. Conditions for “Compact” Jet Formation’. *The Astrophysical Journal* **779**(2):95.
- G. Kanbach, et al. (2001). ‘Correlated fast X-ray and optical variability in the black-hole candidate XTE J1118+480’. *Nature* **414**(6860):180–182.
- T. Kawamuro, et al. (2018). ‘MAXI/GSC detection of a probable new X-ray transient MAXI J1820+070’. *The Astronomer’s Telegram* **11399**:1.
- K. I. Kellermann (1966). ‘Measurements of the flux density of discrete radio sources at 6 cm wavelength’. *Australian Journal of Physics* **19**:577.
- J. A. Kennea (2017). ‘Swift/XRT sees MAXI J1535-571 brightening and softening’. *The Astronomer’s Telegram* **10731**:1.

- J. A. Kennea, et al. (2017a). ‘MAXI J1535-571: Swift detection and localization’. *The Astronomer’s Telegram* **10700**:1.
- J. A. Kennea, et al. (2017b). ‘MAXI J1535-571: Swift detection and localization’. *The Astronomer’s Telegram* **10700**:1.
- J. A. Kennea & H. Negoro (2019). ‘MAXI J1348-630: Swift XRT localization, possible periodicity’. *ATel* **12434**:1.
- C. S. Kochanek, et al. (2017). ‘The All-Sky Automated Survey for Supernovae (ASAS-SN) Light Curve Server v1.0’. **129**(980):104502.
- J. Kocz, et al. (2010). ‘Radio Frequency Interference Removal through the Application of Spatial Filtering Techniques on the Parkes Multibeam Receiver’. *The Astronomical Journal* **140**(6):2086–2094.
- L. Kreidberg, et al. (2012). ‘Mass Measurements of Black Holes in X-Ray Transients: Is There a Mass Gap?’. *The Astrophysical Journal* **757**(1):36.
- V. Krishnan, et al. (2017). ‘Parallaxes of 6.7-GHz methanol masers towards the G 305.2 high-mass star formation region’. *Monthly Notices of the Royal Astronomical Society* **465**(1):1095–1105.
- V. Krishnan, et al. (2015). ‘First Parallax Measurements Towards a 6.7 GHz Methanol Maser with the Australian Long Baseline Array - Distance to G 339.884-1.259.’. *The Astrophysical Journal* **805**(2):129.
- T. A. Kuchar & T. M. Bania (1990). ‘H i Emission-Absorption Experiments toward Galactic H II Regions’. *The Astrophysical Journal* **352**:192.
- M. Lacy, et al. (2020). ‘The Karl G. Jansky Very Large Array Sky Survey (VLASS). Science Case and Survey Design’. **132**(1009):035001.
- G. Lamer, et al. (2021). ‘A giant X-ray dust scattering ring discovered with SRG/eROSITA around the black hole transient MAXI J1348-630’. *Astronomy and Astrophysics* **647**:A7.

- R. M. Lau, et al. (2016). ‘An Apparent Precessing Helical Outflow from a Massive Evolved Star: Evidence for Binary Interaction’. *The Astrophysical Journal* **818**(2):117.
- R. M. Lau, et al. (2014). ‘Dusty Cradles in a Turbulent Nursery: The Sgr A East H II Region Complex at the Galactic Center’. *The Astrophysical Journal* **794**(2):108.
- N. M. Law, et al. (2009). ‘The Palomar Transient Factory: System Overview, Performance, and First Results’. **121**(886):1395.
- T. J. W. Lazio, et al. (2010). ‘Surveying the Dynamic Radio Sky with the Long Wavelength Demonstrator Array’. *The Astronomical Journal* **140**(6):1995–2006.
- J. H. Lee, et al. (2011). ‘H II Region Luminosity Function of the Interacting Galaxy M51’. *The Astrophysical Journal* **735**(2):75.
- J. K. Leung, et al. (2021). ‘A search for radio afterglows from gamma-ray bursts with the Australian Square Kilometre Array Pathfinder’. *Monthly Notices of the Royal Astronomical Society* **503**(2):1847–1863.
- X. J. Li, et al. (2021). ‘Temporal Properties of Precursors, Main Peaks, and Extended Emissions of Short GRBs in the Third Swift/BAT GRB Catalog’. *The Astrophysical Journal Supplement Series* **252**(2):16.
- M. Liu, et al. (2021). ‘Tiny-scale Structure Discovered toward PSR B1557-50’. *The Astrophysical Journal Letters* **911**(1):L13.
- M. Livio, et al. (1999). ‘Extracting Energy from Black Holes: The Relative Importance of the Blandford-Znajek Mechanism’. *The Astrophysical Journal* **512**(1):100–104.

- F. J. Lockman, et al. (2007). ‘The distance to SS433/W50 and its interaction with the interstellar medium’. *Monthly Notices of the Royal Astronomical Society* **381**(3):881–893.
- M. S. Longair (2011). *High Energy Astrophysics*.
- C. R. Lynch, et al. (2017). ‘154 MHz Detection of Faint, Polarized Flares from UV Ceti’. *The Astrophysical Journal Letters* **836**(2):L30.
- T. J. Maccarone (2003). ‘Do X-ray binary spectral state transition luminosities vary?’. *Astronomy and Astrophysics* **409**:697–706.
- D. Maitra, et al. (2009). ‘Constraining jet/disc geometry and radiative processes in stellar black holes XTE J1118+480 and GX 339-4’. *Monthly Notices of the Royal Astronomical Society* **398**(4):1638–1650.
- C. Malacaria, et al. (2021). ‘GRB 210318B: Fermi GBM detection’. *GRB Coordinates Network* **29668**:1.
- J. Malzac (2014). ‘The spectral energy distribution of compact jets powered by internal shocks’. *Monthly Notices of the Royal Astronomical Society* **443**(1):299–317.
- I. Mandel (2016). ‘Estimates of black hole natal kick velocities from observations of low-mass X-ray binaries’. *Monthly Notices of the Royal Astronomical Society* **456**(1):578–581.
- S. Markoff (2007). ‘Constraining jet physics in weakly accreting black holes’. In V. Karas & G. Matt (eds.), *Black Holes from Stars to Galaxies – Across the Range of Masses*, vol. 238, pp. 145–149.
- S. Markoff, et al. (2001). ‘A jet model for the broadband spectrum of XTE J1118+480. Synchrotron emission from radio to X-rays in the Low/Hard spectral state’. *Astronomy and Astrophysics* **372**:L25–L28.

- S. Markoff, et al. (2003). ‘Exploring the role of jets in the radio/X-ray correlations of GX 339-4’. *Astronomy and Astrophysics* **397**:645–658.
- S. Markoff, et al. (2008). ‘Results from an Extensive Simultaneous Broadband Campaign on the Underluminous Active Nucleus M81\*: Further Evidence for Mass-scaling Accretion in Black Holes’. *The Astrophysical Journal* **681**(2):905–924.
- S. Markoff, et al. (2005). ‘Going with the Flow: Can the Base of Jets Subsume the Role of Compact Accretion Disk Coronae?’. *The Astrophysical Journal* **635**(2):1203–1216.
- A. P. Marscher (1983). ‘Accurate formula for the self-Compton X-ray flux density from a uniform, spherical, compact radio source.’. *The Astrophysical Journal* **264**:296–297.
- J. Marti, et al. (1992). ‘Modelling Cygnus X-3 radio outbursts : particle injection into twin jets.’. *Astronomy and Astrophysics* **258**:309.
- M. Matsuoka, et al. (2009). ‘The MAXI Mission on the ISS: Science and Instruments for Monitoring All-Sky X-Ray Images’. **61**:999.
- J. E. McClintock & R. A. Remillard (2009). ‘Black hole binaries’. In W. Lewin & M. van der Klis (eds.), *Compact Stellar X-ray Sources*, pp. 157–214. Cambridge Univ. Press.
- M. M. McGilchrist & J. M. Riley (1990). ‘The 7C survey of radio sources at 151 MHz : a search for low-frequency variability.’. *Monthly Notices of the Royal Astronomical Society* **246**:123.
- J. P. McMullin, et al. (2007). ‘CASA Architecture and Applications’. In R. A. Shaw, F. Hill, & D. J. Bell (eds.), *Astronomical Data Analysis Software and Systems XVI*, vol. 376 of *Astronomical Society of the Pacific Conference Series*, p. 127.

- D. L. Meier (2005). ‘Magnetically Dominated Accretion Flows (MDAFS) and Jet Production in the Lowhard State’. *Astrophysics and Space Science* **300**(1-3):55–65.
- K. Menou, et al. (1999). ‘Structure and properties of transition fronts in accretion discs’. *Monthly Notices of the Royal Astronomical Society* **305**(1):79–89.
- E. Meyer-Hofmeister, et al. (2009). ‘The hard to soft spectral transition in LMXBs-affected by recondensation of gas into an inner disk’. *Astronomy and Astrophysics* **508**(1):329–337.
- P. G. Mezger & A. P. Henderson (1967). ‘Galactic H II Regions. I. Observations of Their Continuum Radiation at the Frequency 5 GHz’. *The Astrophysical Journal* **147**:471.
- M. J. Middleton, et al. (2013). ‘Bright radio emission from an ultraluminous stellar-mass microquasar in M 31’. *Nature* **493**(7431):187–190.
- S. Migliari & R. P. Fender (2006). ‘Jets in neutron star X-ray binaries: a comparison with black holes’. *Monthly Notices of the Royal Astronomical Society* **366**(1):79–91.
- S. Migliari, et al. (2007). ‘Tracing the Jet Contribution to the Mid-IR over the 2005 Outburst of GRO J1655-40 via Broadband Spectral Modeling’. *The Astrophysical Journal* **670**(1):610–623.
- T. Mihara, et al. (2020). ‘MAXI/GSC detection of the magnetar AX J1846.4-0258’. *The Astronomer’s Telegram* **13922**:1.
- J. M. Miller, et al. (2018). ‘A NICER Spectrum of MAXI J1535-571: Near-maximal Black Hole Spin and Potential Disk Warping’. *The Astrophysical Journal Letters* **860**(2):L28.
- J. C. A. Miller-Jones, et al. (2021). ‘Cygnus X-1 contains a 21-solar mass black hole—Implications for massive star winds’. *Science* **371**(6533):1046–1049.

- J. C. A. Miller-Jones, et al. (2004). ‘Time-sequenced Multi-Radio Frequency Observations of Cygnus X-3 in Flare’. *The Astrophysical Journal* **600**(1):368–389.
- J. C. A. Miller-Jones, et al. (2018). ‘The geometric distance and binary orbit of PSR B1259-63’. *Monthly Notices of the Royal Astronomical Society* **479**(4):4849–4860.
- J. C. A. Miller-Jones, et al. (2006). ‘Opening angles, Lorentz factors and confinement of X-ray binary jets’. *Monthly Notices of the Royal Astronomical Society* **367**(4):1432–1440.
- J. C. A. Miller-Jones, et al. (2009). ‘The First Accurate Parallax Distance to a Black Hole’. *The Astrophysical Journal Letters* **706**(2):L230–L234.
- J. C. A. Miller-Jones, et al. (2011). ‘An accurate position for the black hole candidate XTE J1752-223: re-interpretation of the VLBI data’. *Monthly Notices of the Royal Astronomical Society* **415**(1):306–312.
- J. C. A. Miller-Jones, et al. (2012). ‘The first resolved imaging of milliarcsecond-scale jets in Circinus X-1’. *Monthly Notices of the Royal Astronomical Society* **419**(1):L49–L53.
- J. C. A. Miller-Jones, et al. (2019). ‘A rapidly changing jet orientation in the stellar-mass black-hole system V404 Cygni’. *Nature* **569**(7756):374–377.
- E. Mills, et al. (2011). ‘Properties of the Compact H II Region Complex G-0.02-0.07’. *The Astrophysical Journal* **735**(2):84.
- A. R. Minns & J. M. Riley (2000). ‘Compact radio sources variable at 151MHz - I. Catalogue of sources’. *Monthly Notices of the Royal Astronomical Society* **315**(4):839–855.
- I. F. Mirabel & L. F. Rodríguez (1994). ‘A superluminal source in the Galaxy’. *Nature* **371**(6492):46–48.

- K. P. Mooley, et al. (2018). ‘Superluminal motion of a relativistic jet in the neutron-star merger GW170817’. *Nature* **561**(7723):355–359.
- K. P. Mooley, et al. (2016). ‘The Caltech-NRAO Stripe 82 Survey (CNSS). I. The Pilot Radio Transient Survey In 50 deg<sup>2</sup>’. *The Astrophysical Journal* **818**(2):105.
- C. Motch (1998). ‘The transient jet of the galactic supersoft X-ray source RX J0925.7-4758’. *Astronomy and Astrophysics* **338**:L13–L16.
- T. Muñoz-Darias, et al. (2019). ‘Hard-state Accretion Disk Winds from Black Holes: The Revealing Case of MAXI J1820+070’. *The Astrophysical Journal Letters* **879**(1):L4.
- T. Murphy, et al. (2017). ‘A search for long-time-scale, low-frequency radio transients’. *Monthly Notices of the Royal Astronomical Society* **466**(2):1944–1953.
- T. Murphy, et al. (2007). ‘The second epoch Molonglo Galactic Plane Survey: compact source catalogue’. *Monthly Notices of the Royal Astronomical Society* **382**(1):382–392.
- S. Nakahira, et al. (2018). ‘Discovery and state transitions of the new Galactic black hole candidate MAXI J1535-571’. **70**(5):95.
- R. Nan, et al. (2011). ‘The Five-Hundred Aperture Spherical Radio Telescope (fast) Project’. *International Journal of Modern Physics D* **20**(6):989–1024.
- R. Narayan, et al. (1997a). ‘Advection-dominated Accretion Model of the Black Hole V404 Cygni in Quiescence’. *The Astrophysical Journal* **482**(1):448–464.
- R. Narayan, et al. (1997b). ‘Advection-dominated Accretion and Black Hole Event Horizons’. *The Astrophysical Journal Letters* **478**(2):L79–L82.
- R. Narayan, et al. (2003). ‘Magnetically Arrested Disk: an Energetically Efficient Accretion Flow’. **55**:L69–L72.

- R. Narayan, et al. (1996). ‘A New Model for Black Hole Soft X-Ray Transients in Quiescence’. *The Astrophysical Journal* **457**:821.
- R. Narayan, et al. (2012). ‘GRMHD simulations of magnetized advection-dominated accretion on a non-spinning black hole: role of outflows’. *Monthly Notices of the Royal Astronomical Society* **426**(4):3241–3259.
- R. Narayan & I. Yi (1994). ‘Advection-dominated Accretion: A Self-similar Solution’. *The Astrophysical Journal Letters* **428**:L13.
- R. Narayan & I. Yi (1995). ‘Advection-dominated Accretion: Underfed Black Holes and Neutron Stars’. *The Astrophysical Journal* **452**:710.
- H. Negoro, et al. (2017a). ‘MAXI/GSC discovery of a new hard X-ray transient MAXI J1535-571’. *The Astronomer’s Telegram* **10699**:1.
- H. Negoro, et al. (2017b). ‘Further brightening of the X-ray transient MAXI J1535-571, suggesting the presence of a black hole’. *The Astronomer’s Telegram* **10708**:1.
- H. Negoro, et al. (2016a). ‘MAXI/GSC detection of a new outburst from GRS 1716-249/GRO J1719-24 or a new X-ray transient MAXI J1719-254’. *The Astronomer’s Telegram* **9876**:1.
- H. Negoro, et al. (2011). ‘MAXI/GSC and Swift/BAT detect a new hard X-ray transient MAXI J1836-194’. *The Astronomer’s Telegram* **3611**:1.
- H. Negoro, et al. (2016b). ‘MAXI/GSC detection of a new X-ray outburst of 4U 1711-34’. *The Astronomer’s Telegram* **9807**:1.
- A. R. Offringa, et al. (2012). ‘Post-correlation filtering techniques for off-axis source and RFI removal’. *Monthly Notices of the Royal Astronomical Society* **422**(1):563–580.

- A. R. Offringa, et al. (2014). ‘WSCLEAN: an implementation of a fast, generic wide-field imager for radio astronomy’. *Monthly Notices of the Royal Astronomical Society* **444**(1):606–619.
- A. R. Offringa, et al. (2015). ‘The Low-Frequency Environment of the Murchison Widefield Array: Radio-Frequency Interference Analysis and Mitigation’. *Publications of the Astronomical Society of Australia* **32**:e008.
- D. E. Osterbrock & G. J. Ferland (2006). *Astrophysics of gaseous nebulae and active galactic nuclei*.
- J. A. Paice, et al. (2019). ‘A black hole X-ray binary at  $\sim 100$  Hz: multiwavelength timing of MAXI J1820+070 with HiPERCAM and NICER’. *Monthly Notices of the Royal Astronomical Society* **490**(1):L62–L66.
- A. S. Parikh, et al. (2019). ‘Rapidly Evolving DiskJet Coupling during Re-brightenings in the Black Hole Transient MAXI J1535–571’. *The Astrophysical Journal Letters* **878**(2):L28.
- B. Partridge, et al. (2016). ‘Absolute Calibration of the Radio Astronomy Flux Density Scale at 22 to 43 GHz Using Planck’. *The Astrophysical Journal* **821**(1):61.
- A. Pe’er & P. Casella (2009). ‘A Model for Emission from Jets in X-Ray Binaries: Consequences of a Single Acceleration Episode’. *The Astrophysical Journal* **699**(2):1919–1937.
- A. Pe’er & S. Markoff (2012). ‘X-Ray Emission from Transient Jet Model in Black Hole Binaries’. *The Astrophysical Journal* **753**(2):177.
- U.-L. Pen, et al. (2009). ‘The GMRT EoR experiment: limits on polarized sky brightness at 150 MHz’. *Monthly Notices of the Royal Astronomical Society* **399**(1):181–194.

- R. A. Perley (1989). ‘Wide Field Imaging II: Imaging with Non-Coplanar Arrays’. In R. A. Perley, F. R. Schwab, & A. H. Bridle (eds.), *Synthesis Imaging in Radio Astronomy*, vol. 6 of *Astronomical Society of the Pacific Conference Series*, p. 259.
- R. A. Perley & B. J. Butler (2013). ‘An Accurate Flux Density Scale from 1 to 50 GHz’. *The Astrophysical Journal Supplement Series* **204**(2):19.
- P.-O. Petrucci, et al. (2008). ‘The role of the disc magnetization on the hysteresis behaviour of X-ray binaries’. *Monthly Notices of the Royal Astronomical Society* **385**(1):L88–L92.
- R. M. Plotkin, et al. (2021). ‘Towards a larger sample of radio jets from quiescent black hole X-ray binaries’. *Monthly Notices of the Royal Astronomical Society* **503**(3):3784–3795.
- R. M. Plotkin, et al. (2013). ‘The X-Ray Spectral Evolution of Galactic Black Hole X-Ray Binaries toward Quiescence’. *The Astrophysical Journal* **773**(1):59.
- R. M. Plotkin, et al. (2017). ‘The 2015 Decay of the Black Hole X-Ray Binary V404 Cygni: Robust Disk-jet Coupling and a Sharp Transition into Quiescence’. *The Astrophysical Journal* **834**(2):104.
- P. Podsiadlowski & S. Rappaport (2000). ‘Cygnus X-2: The Descendant of an Intermediate-Mass X-Ray Binary’. *The Astrophysical Journal* **529**(2):946–951.
- P. Podsiadlowski, et al. (2002). ‘Evolutionary Sequences for Low- and Intermediate-Mass X-Ray Binaries’. *The Astrophysical Journal* **565**(2):1107–1133.
- E. Polisensky, et al. (2018). ‘VLITE meter-wavelength detection of MAXI J1820+070 at 339 MHz’. *The Astronomer’s Telegram* **11540**:1.
- E. Polisensky, et al. (2016). ‘Exploring the Transient Radio Sky with VLITE: Early Results’. *The Astrophysical Journal* **832**(1):60.

- R. A. Preston, et al. (1989). ‘The Southern Hemisphere VLBI Experiment’. *The Astronomical Journal* **98**:1.
- R. A. Preston & SHEVE Team (1993). ‘The Southern hemisphere VLBI experiment (SHEVE)’. In R. J. Davis & R. S. Booth (eds.), *Sub-arcsecond Radio Astronomy*, p. 428.
- J. E. Pringle & M. J. Rees (1972). ‘Accretion Disc Models for Compact X-Ray Sources’. *Astronomy and Astrophysics* **21**:1.
- B. Punsly (2021). ‘The Bulk Flow Velocity and Acceleration of the Inner Jet in M87’. *The Astrophysical Journal* **918**(1):4.
- B. Punsly & S. Chen (2021). ‘Did the Event Horizon Telescope Detect the Base of the Submilliarsecond Tubular Jet in M87?’. *The Astrophysical Journal Letters* **921**(2):L38.
- B. Punsly, et al. (2021). ‘Observing the Time Evolution of the Multicomponent Nucleus of 3C 84’. *The Astrophysical Journal* **911**(1):19.
- E. Quataert & A. Gruzinov (2000). ‘Convection-dominated Accretion Flows’. *The Astrophysical Journal* **539**(2):809–814.
- V. Razin (1960). ‘To the theory of radio emission spectra caused by discrete sources at frequencies lower than 30 MHz’. *Izvestiya Vysshikh Uchebnykh Zavedenii. Radiofizika* (3):584–594.
- S. H. Reddy, et al. (2017). ‘A Wideband Digital Back-End for the Upgraded GMRT’. *Journal of Astronomical Instrumentation* **6**(1):1641011–336.
- M. J. Reid, et al. (2011). ‘The Trigonometric Parallax of Cygnus X-1’. *The Astrophysical Journal* **742**(2):83.
- M. J. Reid, et al. (2014). ‘Trigonometric Parallaxes of High Mass Star Forming Regions: The Structure and Kinematics of the Milky Way’. *The Astrophysical Journal* **783**(2):130.

- R. A. Remillard & J. E. McClintock (2006). ‘X-Ray Properties of Black-Hole Binaries’. *Annual Review of Astronomy and Astrophysics* **44**(1):49–92.
- S. Repetto, et al. (2012). ‘Investigating stellar-mass black hole kicks’. *Monthly Notices of the Royal Astronomical Society* **425**(4):2799–2809.
- S. Repetto, et al. (2017). ‘The Galactic distribution of X-ray binaries and its implications for compact object formation and natal kicks’. *Monthly Notices of the Royal Astronomical Society* **467**(1):298–310.
- J. Reynolds (1994a). ‘A Revised Flux Scale for the AT Compact Array’. *AT Technical Document AT/39.3/040* .
- J. Reynolds (1994b). ‘A Revised Flux Scale for the AT Compact Array’. *AT Technical Document AT/39.3/040* .
- J. Rodi, et al. (2021). ‘A Broadband View on Microquasar MAXI J1820+070 during the 2018 Outburst’. *The Astrophysical Journal* **910**(1):21.
- G. E. Romero, et al. (2017). ‘Relativistic Jets in Active Galactic Nuclei and Microquasars’. *Space Science Reviews* **207**(1-4):5–61.
- A. P. Rushton, et al. (2017). ‘Resolved, expanding jets in the Galactic black hole candidate XTE J1908+094’. *Monthly Notices of the Royal Astronomical Society* **468**(3):2788–2802.
- D. M. Russell, et al. (2019a). ‘Optical brightening of MAXI J1348-630’. *ATel* **12439**:1.
- D. M. Russell & R. P. Fender (2010). ‘Powerful jets from accreting black holes: evidence from the optical and infrared’. *arXiv e-prints* p. arXiv:1001.1244.
- D. M. Russell, et al. (2013). ‘Jet spectral breaks in black hole X-ray binaries’. *Monthly Notices of the Royal Astronomical Society* **429**(1):815–832.

- T. Russell, et al. (2019b). ‘ATCA detects the radio brightening of the X-ray transient MAXI J1348-630’. *ATel* **12456**:1.
- T. D. Russell, et al. (2017a). ‘Radio re-brightening of MAXI J1535-571 as it transitions back towards the hard state’. *The Astronomer’s Telegram* **10899**:1.
- T. D. Russell, et al. (2020). ‘Rapid compact jet quenching in the Galactic black hole candidate X-ray binary MAXI J1535-571’. *Monthly Notices of the Royal Astronomical Society* **498**(4):5772–5785.
- T. D. Russell, et al. (2015). ‘Radio monitoring of the hard state jets in the 2011 outburst of MAXI J1836-194’. *Monthly Notices of the Royal Astronomical Society* **450**(2):1745–1759.
- T. D. Russell, et al. (2017b). ‘ATCA radio detection of MAXI J1535-571 indicates it is a strong black hole X-ray binary candidate’. *The Astronomer’s Telegram* **10711**:1.
- T. D. Russell, et al. (2014). ‘The accretion-ejection coupling in the black hole candidate X-ray binary MAXI J1836-194’. *Monthly Notices of the Royal Astronomical Society* **439**(2):1390–1402.
- T. D. Russell, et al. (2019c). ‘DiskJet Coupling in the 2017/2018 Outburst of the Galactic Black Hole Candidate X-Ray Binary MAXI J1535571’. *The Astrophysical Journal* **883**(2):198.
- M. Ruszkowski (2003). ‘Linear and Circular Polarization Properties of Jets’. *Astrophysics and Space Science* **288**(1):133–142.
- G. B. Rybicki & A. P. Lightman (1979). *Radiative processes in astrophysics*.
- J. Salvatier, et al. (2016). ‘PyMC3: Python probabilistic programming framework’.
- R. Sari, et al. (1998). ‘Spectra and Light Curves of Gamma-Ray Burst Afterglows’. *The Astrophysical Journal Letters* **497**(1):L17–L20.

- R. J. Sault, et al. (1995). ‘A Retrospective View of MIRIAD’. In R. A. Shaw, H. E. Payne, & J. J. E. Hayes (eds.), *Astronomical Data Analysis Software and Systems IV*, vol. 77 of *Astron. Soc. Pac. Conf. Ser.*, p. 433.
- A. M. M. Scaife & G. H. Heald (2012). ‘A broad-band flux scale for low-frequency radio telescopes’. *Monthly Notices of the Royal Astronomical Society* **423**(1):L30–L34.
- E. F. Schlafly & D. P. Finkbeiner (2011). ‘Measuring Reddening with Sloan Digital Sky Survey Stellar Spectra and Recalibrating SFD’. *The Astrophysical Journal* **737**(2):103.
- F. R. Schwab & W. D. Cotton (1983). ‘Global fringe search techniques for VLBI’. *The Astronomical Journal* **88**:688–694.
- E. R. Seaquist (1976). ‘A model for the radio outbursts of Cygnus X-3.’. *The Astrophysical Journal* **207**:88–95.
- E. R. Seaquist, et al. (1980). ‘The quiescent radio spectrum of SS 433.’. *The Astrophysical Journal Letters* **241**:L77–L81.
- E. R. Seaquist, et al. (1982). ‘Simultaneous radio and X-ray activity in SS 433.’. *The Astrophysical Journal* **260**:220–232.
- S. Sekhar & R. Athreya (2018). ‘Two Procedures to Flag Radio Frequency Interference in the UV Plane’. *The Astronomical Journal* **156**(1):9.
- T. Shahbaz, et al. (2013). ‘Evidence for quiescent synchrotron emission in the black hole X-ray transient Swift J1357.2-0933’. *Monthly Notices of the Royal Astronomical Society* **434**(3):2696–2706.
- N. I. Shakura & R. A. Sunyaev (1973). ‘Reprint of 1973A&A....24..337S. Black holes in binary systems. Observational appearance.’. *Astronomy and Astrophysics* **500**:33–51.

- B. J. Shappee, et al. (2014). ‘The Man behind the Curtain: X-Rays Drive the UV through NIR Variability in the 2013 Active Galactic Nucleus Outburst in NGC 2617’. *The Astrophysical Journal* **788**(1):48.
- A. W. Shaw, et al. (2021). ‘Observations of the Disk/Jet Coupling of MAXI J1820+070 during Its Descent to Quiescence’. *The Astrophysical Journal* **907**(1):34.
- M. C. Shepherd (1997). ‘Difmap: an Interactive Program for Synthesis Imaging’. In G. Hunt & H. Payne (eds.), *Astronomical Data Analysis Software and Systems VI*, vol. 125 of *Astronomical Society of the Pacific Conference Series*, p. 77.
- M. Shidatsu, et al. (2018). ‘X-Ray, Optical, and Near-infrared Monitoring of the New X-Ray Transient MAXI J1820+070 in the Low/Hard State’. *The Astrophysical Journal* **868**(1):54.
- T. R. Smith & J. Kennicutt, Robert C. (1989). ‘The H II Region Luminosity Function of the Milky Way’. **101**:649.
- A. J. Stewart, et al. (2016). ‘LOFAR MSSS: detection of a low-frequency radio transient in 400 h of monitoring of the North Celestial Pole’. *Monthly Notices of the Royal Astronomical Society* **456**(3):2321–2342.
- H. Stiele & A. K. H. Kong (2018). ‘A Spectral and Timing Study of MAXI J1535-571, Based on Swift/XRT, XMM-Newton, and NICER Observations Obtained in Fall 2017’. *The Astrophysical Journal* **868**(1):71.
- H. Stiele & A. K. H. Kong (2020). ‘A Timing Study of MAXI J1820+070 Based on Swift/XRT and NICER Monitoring in 2018/19’. *The Astrophysical Journal* **889**(2):142.
- A. M. Stirling, et al. (2001). ‘A relativistic jet from Cygnus X-1 in the low/hard

- X-ray state'. *Monthly Notices of the Royal Astronomical Society* **327**(4):1273–1278.
- G. G. Stokes (1852). 'On the Change of Refrangibility of Light'. *Philosophical Transactions of the Royal Society of London Series I* **142**:463–562.
- H. Tananbaum, et al. (1972). 'Observation of a Correlated X-Ray Transition in Cygnus X-1'. *The Astrophysical Journal Letters* **177**:L5.
- L. Tao, et al. (2018). 'Swift observations of the bright uncatalogued X-ray transient MAXI J1535-571'. *Monthly Notices of the Royal Astronomical Society* **480**(4):4443–4454.
- A. R. Taylor & M. Jarvis (2017). 'MIGHTEE: The MeerKAT International GHz Tiered Extragalactic Exploration'. In *Materials Science and Engineering Conference Series*, vol. 198 of *Materials Science and Engineering Conference Series*, p. 012014.
- A. Tchekhovskoy, et al. (2011). 'Efficient generation of jets from magnetically arrested accretion on a rapidly spinning black hole'. *Monthly Notices of the Royal Astronomical Society* **418**(1):L79–L83.
- A. J. Tetarenko, et al. (2018a). 'NOEMA Sub-millimetre Detection of MAXI J1820+070'. *The Astronomer's Telegram* **11440**:1.
- A. J. Tetarenko, et al. (2021). 'Measuring fundamental jet properties with multi-wavelength fast timing of the black hole X-ray binary MAXI J1820+070'. *Monthly Notices of the Royal Astronomical Society* .
- A. J. Tetarenko, et al. (2019). 'Radio frequency timing analysis of the compact jet in the black hole X-ray binary Cygnus X-1'. *Monthly Notices of the Royal Astronomical Society* **484**(3):2987–3003.

- A. J. Tetarenko, et al. (2018b). ‘(Sub)-millimetre Observations of MAXI J1820+070 (ASASSN-18ey) Suggest Jet Quenching on July 6’. *The Astronomer’s Telegram* **11831**:1.
- A. J. Tetarenko, et al. (2017). ‘Extreme jet ejections from the black hole X-ray binary V404 Cygni’. *Monthly Notices of the Royal Astronomical Society* **469**(3):3141–3162.
- B. E. Tetarenko, et al. (2016). ‘WATCHDOG: A Comprehensive All-sky Database of Galactic Black Hole X-ray Binaries’. *The Astrophysical Journal Supplement Series* **222**(2):15.
- A. R. Thompson, et al. (2001). *Interferometry and Synthesis in Radio Astronomy, 2nd Edition*.
- S. J. Tingay & M. de Kool (2003). ‘An Investigation of Synchrotron Self-absorption and Free-Free Absorption Models in Explanation of the Gigahertz-peaked Spectrum of PKS 1718-649’. *The Astronomical Journal* **126**(2):723–733.
- S. J. Tingay, et al. (2013). ‘The Murchison Widefield Array: The Square Kilometre Array Precursor at Low Radio Frequencies’. *Publications of the Astronomical Society of Australia* **30**:e007.
- S. J. Tingay, et al. (1995). ‘Relativistic motion in a nearby bright X-ray source’. *Nature* **374**(6518):141–143.
- M. Tominaga, et al. (2020). ‘Discovery of the Black Hole X-Ray Binary Transient MAXI J1348-630’. *The Astrophysical Journal Letters* **899**(1):L20.
- M. A. P. Torres, et al. (2020). ‘The Binary Mass Ratio in the Black Hole Transient MAXI J1820+070’. *The Astrophysical Journal Letters* **893**(2):L37.
- M. A. P. Torres, et al. (2019). ‘Dynamical Confirmation of a Black Hole in MAXI J1820+070’. *The Astrophysical Journal Letters* **882**(2):L21.

- E. Tremou, et al. (2020). ‘Radio & X-ray detections of GX 339-4 in quiescence using MeerKAT and Swift’. *Monthly Notices of the Royal Astronomical Society* **493**(1):L132–L137.
- E. Troja, et al. (2021). ‘GRB 210318A: Swift detection of a burst’. *GRB Coordinates Network* **29662**:1.
- S. A. Trushkin, et al. (2018). ‘A flat radio spectrum of MAXI J1820+070’. *The Astronomer’s Telegram* **11439**:1.
- V. Tsytovich (1951). ‘On the radiation of the rapid electrons in the magnetic field in the presence of medium’. *Bulletin of Moscow State University* **11**:27–36.
- Z.-L. Tu, et al. (2021). ‘Superflares, Chromospheric Activities, and Photometric Variabilities of Solar-type Stars from the Second-year Observation of TESS and Spectra of LAMOST’. *The Astrophysical Journal Supplement Series* **253**(2):35.
- M. A. Tucker, et al. (2018). ‘ASASSN-18ey: The Rise of a New Black Hole X-Ray Binary’. *The Astrophysical Journal Letters* **867**(1):L9.
- M. Uemura, et al. (2004). ‘Optical Observation of the 2003 Outburst of a Black Hole X-Ray Binary, V4641 Sagittarii’. **56**:823–829.
- P. Uttley, et al. (2018). ‘NICER observations of MAXI J1820+070 suggest a rapidly-brightening black hole X-ray binary in the hard state’. *The Astronomer’s Telegram* **11423**:1.
- A. Vahdat Motlagh, et al. (2019). ‘Investigating state transition luminosities of Galactic black hole transients in the outburst decay’. *Monthly Notices of the Royal Astronomical Society* **485**(2):2744–2758.
- P. H. van Cittert (1934). ‘Die Wahrscheinliche Schwingungsverteilung in Einer von Einer Lichtquelle Direkt Oder Mittels Einer Linse Beleuchteten Ebene’. *Physica* **1**(1):201–210.

- H. van der Laan (1966a). ‘A Model for Variable Extragalactic Radio Sources’. *Nature* **211**(5054):1131–1133.
- H. van der Laan (1966b). ‘A Model for Variable Extragalactic Radio Sources’. *Nature* **211**(5054):1131–1133.
- M. P. van Haarlem, et al. (2013). ‘LOFAR: The LOw-Frequency ARray’. *Astronomy and Astrophysics* **556**:A2.
- J. van Paradijs & J. E. McClintock (1995). ‘Optical and ultraviolet observations of X-ray binaries.’. In *X-ray Binaries*, pp. 58–125.
- S. van Velzen, et al. (2016). ‘A radio jet from the optical and x-ray bright stellar tidal disruption flare ASASSN-14li’. *Science* **351**(6268):62–65.
- H. K. Vedantham, et al. (2020). ‘Coherent radio emission from a quiescent red dwarf indicative of star-planet interaction’. *Nature Astronomy* **4**:577–583.
- U. R. Venkata (2010). *Parameterized Deconvolution for Wide-Band Radio Synthesis Imaging*. Ph.D. thesis, New Mexico Institute of Mining and Technology.
- R. Walter & T. J. L. Courvoisier (1992). ‘The origin of the X-ray emission in 3C 273 and 3C 120.’. *Astronomy and Astrophysics* **258**:255.
- E. B. Waltman, et al. (1994). ‘The Quiescent Level of Cygnus X-3 at 2.25 and 8.3 GHz: 1988-1992’. *The Astronomical Journal* **108**:179.
- E. B. Waltman, et al. (1996). ‘Quenched Radio Emission in Cygnus X-3’. *The Astronomical Journal* **112**:2690.
- E. B. Waltman, et al. (1995). ‘The Evolution of Outbursts in Cygnus X-3 at 2.25 and 8.3 GHz’. *The Astronomical Journal* **110**:290.
- J. Wang, et al. (2021). ‘Disk, Corona, Jet Connection in the Intermediate State of MAXI J1820+070 Revealed by NICER Spectral-timing Analysis’. *The Astrophysical Journal Letters* **910**(1):L3.

- J. F. C. Wardle, et al. (1998). ‘Electron-positron jets associated with the quasar 3C279’. *Nature* **395**(6701):457–461.
- R. B. Wayth, et al. (2018). ‘The Phase II Murchison Widefield Array: Design overview’. *Publications of the Astronomical Society of Australia* **35**.
- T. V. Wenger, et al. (2018). ‘Kinematic Distances: A Monte Carlo Method’. *The Astrophysical Journal* **856**(1):52.
- D. J. Westpfahl (1999). ‘Spectral-Line Observing I: Introduction’. In G. B. Taylor, C. L. Carilli, & R. A. Perley (eds.), *Synthesis Imaging in Radio Astronomy II*, vol. 180 of *Astronomical Society of the Pacific Conference Series*, p. 201.
- N. E. White, et al. (1995). ‘The properties of X-ray binaries.’. In *X-ray Binaries*, pp. 1–57.
- N. E. White & J. van Paradijs (1996). ‘The Galactic Distribution of Black Hole Candidates in Low Mass X-ray Binary Systems’. *The Astrophysical Journal Letters* **473**:L25.
- D. Williams, et al. (2019). ‘MeerKAT detection of EXO 1846-031 at 1.3 GHz’. *The Astronomer’s Telegram* **12992**:1.
- D. R. A. Williams, et al. (2020). ‘The 2018 outburst of BHXB H1743-322 as seen with MeerKAT’. *Monthly Notices of the Royal Astronomical Society* **491**(1):L29–L33.
- W. E. Wilson, et al. (2011). ‘The Australia Telescope Compact Array Broad-band Backend: description and first results’. *Monthly Notices of the Royal Astronomical Society* **416**(2):832–856.
- Y. Xu, et al. (2018). ‘Reflection Spectra of the Black Hole Binary Candidate MAXI J1535-571 in the Hard State Observed by NuSTAR’. *The Astrophysical Journal Letters* **852**(2):L34.

- J. Yang, et al. (2011). ‘Transient relativistic ejections and stationary core in XTE J1752-223’. *Monthly Notices of the Royal Astronomical Society* **418**(1):L25–L29.
- F. Yatabe, et al. (2019). ‘MAXI/GSC discovery of a new X-ray transient MAXI J1348-630’. *ATel* **12425**:1.
- B. A. Zauderer, et al. (2011). ‘Birth of a relativistic outflow in the unusual  $\gamma$ -ray transient Swift J164449.3+573451’. *Nature* **476**(7361):425–428.
- A. A. Zdziarski, et al. (1998). ‘Broad-band X-ray/gamma-ray spectra and binary parameters of GX 339-4 and their astrophysical implications’. *Monthly Notices of the Royal Astronomical Society* **301**(2):435–450.
- F. Zernike (1938). ‘The concept of degree of coherence and its application to optical problems’. *Physica* **5**(8):785–795.
- L. Zhang, et al. (2020a). ‘NICER observations reveal that the X-ray transient MAXI J1348-630 is a Black Hole X-ray binary’. *arXiv e-prints* p. arXiv:2009.07749.
- X. Zhang, et al. (2020b). ‘MeerKAT radio detection of the transient Galactic black hole candidate Swift J1842.5-1124’. *ATel* **13802**:1.

Every reasonable effort has been made to acknowledge the owners of copyright material. I would be pleased to hear from any copyright owner who has been omitted or incorrectly acknowledged.